

UCLA

UCLA Electronic Theses and Dissertations

Title

The Art of Contemporary Drug Discovery: Developing Novel Small Molecule Therapeutics For Neurological and Muscular Disorders

Permalink

<https://escholarship.org/uc/item/3j18q771>

Author

Johnson-Cohn, Samuel Whitaker

Publication Date

2023

Peer reviewed|Thesis/dissertation

UNIVERSITY OF CALIFORNIA

Los Angeles

The Art of Contemporary Drug Discovery:
Developing Novel Small Molecule Therapeutics
For Neurological and Muscular Disorders

A dissertation submitted in partial satisfaction of the
requirements for the degree Doctor of Philosophy
in Molecular, Cellular and Integrative Physiology

by

Samuel Whitaker Johnson-Cohn

2023

© Copyright by

Samuel Whitaker Johnson-Cohn

2023

ABSTRACT OF THE DISSERTATION

The Art of Contemporary Drug Discovery:
Developing Novel Small Molecule Therapeutics
For Neurological and Muscular Disorders

by

Samuel Whitaker Johnson-Cohn

Doctor of Philosophy in Molecular, Cellular and Integrative Physiology

University of California, Los Angeles, 2023

Professor Varghese John, Chair

The integration of basic biological research and contemporary drug discovery and development strategies stands at the forefront of scientific efforts to develop treatments for innumerable medical conditions. Advances in genomics, molecular biology, computer science and 'omics' technologies have enabled a holistic understanding of complex disease mechanisms, facilitating the identification of novel biomarkers and therapeutic targets. Modern pharmaceutical research tools have led to a well-established drug discovery workflow that often drives efforts to efficiently develop safe and effective therapeutics. This approach typically involves the use of high-throughput screening to identify “hits” that achieve a desired phenotype. This is followed by an

optimization process utilizing *in-vitro* ADME assays and medicinal chemistry to develop more selective, potent, and bioavailable compounds. Finally, *in-vivo* testing in disease-relevant models allows for proper evaluation of drug efficacy before moving into preclinical or clinical development. This dissertation focuses on the use of these approaches in the context of drug discovery programs targeting innovative therapeutic mechanisms such as increasing secreted clusterin for Alzheimer's disease, inhibiting microtubule affinity-regulating kinase 4 for vascular cognitive impairment, enhancing calcium calmodulin II kinase signaling for limb-girdle muscular dystrophy, and increasing sarcospan for Duchenne muscular dystrophy. Leveraging advanced scientific tools, the research explores the intricate mechanisms underlying these diseases and identifies promising new drug candidates and therapeutic approaches that warrant further investigation as disease treatments.

The dissertation of Samuel Whitaker Johnson-Cohn is approved.

Julian Philip Whitelegge

Igor Spigelman

Melissa J Spencer

Rachelle Hope Crosbie

Varghese John, Committee Chair

University of California, Los Angeles

2023

This thesis is dedicated to my father,

Steven Geoffrey Cohn.

May his memory serve as a constant
reminder to always enjoy life and always keep surfing.

He was the best father a kid could have.

TABLE OF CONTENTS

LIST OF TABLES AND FIGURES.....	vii
ACKNOWLEDGEMENTS.....	x
BIOGRAPHICAL SKETCH.....	xii
PREFACE.....	1
CHAPTER 1: Integrated Multiomics Analysis of Salivary Exosomes to Identify Biomarkers Associated with Changes in Mood States and Fatigue.....	6
CHAPTER 2: Multi-Omics Analysis of Microglial Extracellular Vesicles From Human Alzheimer's Disease Brain Tissue Reveals Disease-Associated Signatures.....	55
CHAPTER 3: Small Molecule Epigenetic Modulators of Secreted Clusterin Promote Synaptic Plasticity, Metabolic Homeostasis and Reduce Inflammation in an Alzheimer's Disease Mouse Model.....	98
CHAPTER 4: Developing Selective Inhibitors of Microtubule Affinity-Regulating Kinase 4 for Vascular Cognitive Impairment and Dementia.....	144
CHAPTER 5: Hit-to-Lead Optimization and Molecular Target Identification of Myosin Light Chain 2 Enhancers for Limb Girdle Muscular Dystrophy R1.....	181
CHAPTER 6: Hit-to-Lead Optimization and Molecular Target Identification of Sarcospan Enhancers for Duchenne Muscular Dystrophy.....	215
CONCLUDING REMARKS.....	256

LIST OF TABLES AND FIGURES

Preface

Figure 1: Developing secreted clusterin enhancers for Alzheimer's disease using the iterative UCLA drug discovery lab developmental strategy.

Chapter 1

Table 1.1: Antibodies used for immunoblot analysis of small EV (F2) fractions and microglial EVs isolated from human parietal cortex.

Table 12: Case information for human samples.

Figure 1.1: Small EV fraction characterization and microglial EV purification.

Figure 1.2: Proteomic analysis of microglial EVs from normal/low pathology and late-stage AD cases.

Figure 1.3: miRNA transcriptomic analysis of microglial EVs from normal/low pathology and late stage AD cases.

Figure 1.4: Lipidomic analysis of microglial EVs from normal/low pathology and late-stage AD cases.

Chapter 2

Table 2.1: Identification of differentially abundant proteins and miRNA in salivary exosomes in the Discovery group.

Figure 2.1: Difference in Total Mood Disturbance (TMD) as assessed by the Profile of Mood States (PoMS) allows separation into Discovery, Validation, and Test groups.

Figure 2.2: Multiomics analysis reveals quantifiable differences in protein and miRNA abundances

in the Test group pan- and neuron-derived exosomes.

Figure 2.3: Interconnected protein and miRNA networks regulate molecular pathways associated with increased TMD score in the Discovery group.

Table 2.1: Identification of differentially abundant proteins and miRNA in salivary exosomes in the Discovery group.

Figure 2.4: Proteins and miRNA identified in the Validation group are associated with Total Mood Disturbance (TMD), Fatigue–Inertia (FI), and Work.

Figure 2.5: PGK1 levels in Test and Discovery groups, and correlation of PGK1 to mi3185.

Figure 2.6: Study flow scheme for Profile of Mood States (PoMS) assessment, sample collection, processing, and analysis.

Chapter 3

Figure 3.1: Molecular mechanisms of secreted clusterin for preventing Alzheimer’s disease.

Figure 3.2: High-throughput screening identifies HDAC and BET inhibitors to increase sCLU levels in U-87 MG glioblastoma cells.

Table 3.1: Physiochemical Properties of Candidate sCLU Enhancers.

Figure 3.3: Synthetic scheme and biological activity of novel sCLU enhancers.

Figure 3.4: Short-term administration of DDL-357 promotes synaptic, metabolic, and protein homeostasis in E4/FAD mice.

Table 3.2: Alzheimer’s Disease-relevant proteins upregulated in E4/FAD mice following DDL-357 treatment.

Figure 3.5: DDL-357 promotes neurite outgrowth in human iPSC-derived neurons.

Chapter 4

Figure 4.1: In-silico design guides synthesis of selective MARK4 inhibitors.

Figure 4.2: Hit-to-lead optimization leads to the development of potent MARK4 inhibitors.

Table 4.1: In-vitro ADME properties of candidate MARK4 inhibitors.

Figure 4.3: DDL-662 is bioavailable and prevents MARK4-mediated tau phosphorylation.

Supplementary Figure 4.S1: Chemical structures of all new chemical entities synthesized.

Chapter 5

Figure 5.1: Synthesis and testing of novel AMBMP analogs.

Table 5.1: In-vitro ADME properties of candidate MYL2 enhancers.

Figure 5.2: Key structure-activity relationship control elements for MYL2 activity, solubility, and metabolic stability.

Figure 5.3: Identification of direct and indirect molecular targets of AMBMP.

Figure 5.4: Evaluation of S100A6 levels and AMBMP-13 efficacy in-vivo.

Chapter 6

Figure 6.1: Synthesis and testing of novel SSPN enhancers.

Table 6.1: In-vitro ADME properties of candidate SSPN enhancers.

Figure 6.2: Key structure-activity relationship control elements for SSPN activity and metabolic stability.

Figure 6.3: Lead candidates DDL-449 and DDL-472 increase SSPN in-vivo.

Figure 6.4: Identification of direct and indirect molecular targets of OT-9.

Supplementary Figure 6.S1: Chemical structures of all new chemical entities synthesized.

ACKNOWLEDGMENTS

Completing my doctoral studies has been a long journey filled with challenges, growth, and invaluable support from various individuals. It is difficult for me to summarize my immense appreciation for all of those who have supported and influenced me along the way.

Firstly, I would like to thank my doctoral advisor, Dr. Varghese John, whose mentorship has left a lasting impact on me both professionally and personally. His passion for research and profound knowledge of neurological disorders and the drug discovery process has greatly informed my interests, research, and career path. His unwavering faith in me and my abilities has given me the confidence to conduct innovative and impactful research that has become the cornerstone of my graduate degree. Perhaps most importantly, I'm grateful for his patience, kindness and camaraderie, which he extends to everyone who crosses his path.

I would also like to extend my eternal gratitude to my mentors Dr. Julian Whitelegge and Dr. Kym Francis Faull, without whom, I would have never made it this far. Time spent with them in Pasarow Mass Spectrometry Lab is what made me decide to pursue a career in biomedical research. The environment fostered in their lab is undoubtedly one-of-a-kind and one of the most enjoyable experiences of my life. Their mentorship and friendship is something that I will always cherish.

I would also like to thank my other doctoral committee members, Dr. Rachelle Crosbie, Dr. Melissa Spencer, and Dr. Igor Spigelman. Their support, influence, and feedback has been invaluable in shaping graduate research. Their willingness to collaborate has allowed to broaden the scope of my knowledge, providing me with additional perspectives and expertise in differing fields or research.

I would also like to acknowledge and thank all the members of both the Drug Discovery Lab and Pasarow Mass Spectrometry Lab, past and present. Most importantly, I would like to thank Jesus Campagna for his constant encouragement and guidance throughout my graduate studies. He has undeniably impacted my graduate training and research more than any one person. I truly could not have completed this degree without him. I would also like to show special appreciation for Travis Moller, Austin Quach, Alex Yoon, Adrian Gomez, Joe Capri, Jessica Lee, and Dongwook Wi for their friendship and support throughout my time at UCLA. Each of them are incredibly talented scientists, and even more wonderful people.

I would also like to thank all of the individuals I have had the pleasure of collaborating with during my time at UCLA. Especially those who have contributed to this work, including Ravinder Malik, Ekaterina Mokhonova, Jason Hinman, Manu Vora, Jennifer Ann, and Irina Kramerova.

Finally, I would like to thank all my friends and family. I would be absolutely nothing without you. You have always been there for me. In the good times and the bad. My experiences with you all have shaped me into the person that I am today and are memories that I will cherish forever. My appreciation for you and amount of love that you have shown me a something that cannot be put into words. I would like to give extra thanks to my parents, Katherine Cohn and Steve Cohn, my grandparents, Lester Cohn and Judy Cohn, my twin brother, William Cohn, my girlfriend, Erin Turgeon, and all members of 6533, the Plumbers, and the Great Smokey Hooligans, particularly Christoph von Ruexleben, Paul Orszag, Harrison Bernsen, Greg Yeoman, Andrew Dietz and Trent Anderson. I love you all. Thank you, always.

BIOGRAPHICAL SKETCH

Education

University of California, Los Angeles 2018 – Present
PhD Candidate: Molecular, Cellular, and Integrative Physiology

GPA: 4.00

University of California, Santa Barbara 2009 – 2013

Bachelor of Science: Biopsychology

GPA: 3.98

Employment

Staff Research Associate 2014 – 2018

University of California, Los Angeles – The Pasarow Mass Spectrometry Laboratory

Teaching

LS 7A: Cell and Molecular Biology Winter 2021

LS 7A: Cell and Molecular Biology Fall 2020

Honors and Awards

1. Muscle Cell Biology, Pathophysiology, and Therapeutics T32 Training Grant Summer 2022 – Spring 2023
2. The UCLA Molecular, Cellular & Integrative Physiology Interdepartmental PhD Program Annual Retreat - 1st place poster winner March 2022
3. The UCLA Molecular, Cellular & Integrative Physiology Interdepartmental PhD Program Summer Mentored Research Fellowship Summer 2021
4. Screening for Enhancers of Secreted Clusterin and Evaluation in AD Models R21 Grant Spring 2021 – Spring 2023
5. Best Case-Study Writing Award – C234, Ethics and Accountability in Biomedical Research Course Spring 2019

Publications

1. Jesus Campagna, Barbara Jagodzinska, Pablo Alvarez, Constance Yeun, Kathryn M Enquist, Whitaker Cohn, Pavla Fajtová, Anthony J O'Donoghue, Vaithilingaraja Arumugaswami, Melody MH Li, Robert Damoiseaux and Varghese John. Identification of a Papain-Like Protease Inhibitor with Potential for Repurposing in Combination with an Mpro Protease Inhibitor for Treatment of SARS-CoV-2. *Archives of Clinical and Biomedical Research* 6 (2022): 993-1002.
2. Qian, K., Tol, M. J., Wu, J., Uchiyama, L. F., Xiao, X., Cui, L., Bedard, A. H., Weston, T. A., Rajendran, P. S., Vergnes, L., Shimanaka, Y., Yin, Y., Jami-Alahmadi, Y., Cohn, W., Bajar, B. T., Lin, C. H., Jin, B., DeNardo, L. A., Black, D. L., Whitelegge, J. P., ... Tontonoz, P. (2022). CLSTN3 β enforces adipocyte multilocularity to facilitate lipid utilization. *Nature*, 10.1038/s41586-022-05507-1. Advance online publication. <https://doi.org/10.1038/s41586-022-05507-1>
3. Cohn, W., Zhu, C., Campagna, J., Bilousova, T., Spilman, P., Teter, B., Li, F., Guo, R., Elashoff, D., Cole, G. M., Avidan, A., Faull, K. F., Whitelegge, J., Wong, D., & John, V. (2022). Integrated Multiomics Analysis of Salivary Exosomes to Identify Biomarkers Associated with Changes in Mood States and Fatigue. *International journal of molecular sciences*, 23(9), 5257. <https://doi.org/10.3390/ijms23095257>
4. Cohn, W., Melnik, M., Huang, C., Teter, B., Chandra, S., Zhu, C., McIntire, L. B., John, V., Gylys, K. H., & Bilousova, T. (2021). Multi-Omics Analysis of Microglial Extracellular Vesicles From Human Alzheimer's Disease Brain Tissue Reveals Disease-Associated Signatures. *Frontiers in pharmacology*, 12, 766082. <https://doi.org/10.3389/fphar.2021.766082>
5. Cohn, W., Huguet, R., Zabrouskov, V., Whitelegge, J., (2021). Dissociation strategies to maximize coverage of alpha-helical domains in top-down mass spectrometry of integral membrane proteins. *Journal of the American Society for Mass Spectrometry*.
6. Zhu, C., Bilousova, T., Focht, S., Jun, M., Elias, C. J., Melnik, M., Chandra, S., Campagna, J., Cohn, W., Hatami, A., Spilman, P., Gylys, K. H., & John, V. (2021). Pharmacological inhibition of nSMase2 reduces brain exosome release and α -synuclein pathology in a Parkinson's disease model. *Molecular brain*, 14(1), 70. <https://doi.org/10.1186/s13041-021-00776-9>
7. Guo, X., Ramirez, I., Garcia, Y. A., Velasquez, E. F., Gholkar, A. A., Cohn, W., Whitelegge, J. P., Tofig, B., Damoiseaux, R., & Torres, J. Z. (2021). DUSP7 regulates the activity of ERK2 to promote proper chromosome alignment during cell division. *The Journal of biological chemistry*, 100676. Advance online publication. <https://doi.org/10.1016/j.jbc.2021.100676>
8. Bhaduri, S., Singh, S. K., Cohn, W., Hasan, S. S., Whitelegge, J. P., & Cramer, W. A. (2020). A novel chloroplast super-complex consisting of the ATP synthase and photosystem I reaction center. *PLoS one*, 15(8), e0237569. <https://doi.org/10.1371/journal.pone.0237569>
9. Gholkar, A. A., Schmollinger, S., Velasquez, E. F., Lo, Y. C., Cohn, W., Capri, J., Dharmarajan, H., Deardorff, W. J., Gao, L. W., Abdusamad, M., Whitelegge, J. P., & Torres, J. Z. (2020). Regulation of Iron Homeostasis through Parkin-Mediated Lactoferrin Ubiquitylation. *Biochemistry*, 59(32), 2916–2921. <https://doi.org/10.1021/acs.biochem.0c00504>
10. Yokota, T., McCourt, J., Ma, F., Ren, S., Li, S., Kim, T. H., Kurmangaliyev, Y. Z., Nasiri, R., Ahadian, S., Nguyen, T., Tan, X., Zhou, Y., Wu, R., Rodriguez, A., Cohn, W., ... Deb, A. (2020). Type V Collagen in Scar Tissue Regulates the Size of Scar after Heart Injury. *Cell*, S0092-8674(20)30807-2.

11. Bilousova, T., Simmons, B., Knapp, R., Elias, C., Campagna, J., Melnik, M., Cohn, W., ... & John, V. (2020). Dual Neutral Sphingomyelinase 2/Acetylcholinesterase Inhibitors for the treatment of Alzheimer 's disease. *ACS Chemical Biology*
12. Moore, T. M., Zhou, Z., Cohn, W., Norheim, F., Lin, A. J., Kalajian, N., ... & Ho, T. (2020). Age-induced mitochondrial DNA point mutations are inadequate to alter metabolic homeostasis in response to nutrient challenge. *Aging Cell*.
13. Kawahara, B., Gao, L., Cohn, W., Whitelegge, J. P., Sen, S., Janzen, C., & Mascharak, P. K. (2020). Diminished viability of human ovarian cancer cells by antigen-specific delivery of carbon monoxide with a family of photoactivatable antibody-photoCORM conjugates. *Chemical Science*, 11(2), 467-473.
14. Marcus, E. A., Tokhtaeva, E., Jimenez, J. L., Wen, Y., Naini, B. V., Heard, A. N., Cohn, W., ... & Vagin, O. (2020). Helicobacter pylori infection impairs chaperone-assisted maturation of Na, K-ATPase in gastric epithelium. *American Journal of Physiology-Gastrointestinal and Liver Physiology*.
15. Kalinec, G. M., Gao, L., Cohn, W., Whitelegge, J., Faull, K. F., & Kalinec, F. (2019). Extracellular Vesicles From Auditory Cells as Nanocarriers for Anti-inflammatory Drugs and Pro-resolving Mediators. *Frontiers in Cellular Neuroscience*, 13, 530.
16. Sarafian, T. A., Yacoub, A., Kunz, A., Aranki, B., Serobyan, G., Cohn, W., ... & Watson, J. B. (2019). Enhanced mitochondrial inhibition by 3, 4-dihydroxyphenyl-acetaldehyde (DOPAL)-oligomerized α -synuclein. *Journal of Neuroscience Research*.
17. Liu, K., Singer, E., Cohn, W., Micewicz, E. D., McBride, W. H., Whitelegge, J. P., & Loo, J. A. (2019). Time-Dependent Measurement of Nrf2-Regulated Antioxidant Response to Ionizing Radiation towards Identifying Potential Protein Biomarkers for Acute Radiation Injury. *PROTEOMICS-Clinical Applications*, 1900035.
18. Kalinec, PhD, G. M., Cohn, W. BSc, Whitelegge, PhD, J. P., Faull, PhD, K. F., & Kalinec, PhD, F. (2019). Preliminary Characterization of Extracellular Vesicles From Auditory HEI-OC1 Cells. *Annals of Otolaryngology & Laryngology*, 128(6_suppl), 52S-60S.
19. Moore, T. M., Zhou, Z., Cohn, W., Norheim, F., Lin, A. J., Kalajian, N., ... & Ho, T. (2019). The impact of exercise on mitochondrial dynamics and the role of Drp1 in exercise performance and training adaptations in skeletal muscle. *Molecular metabolism*, 21, 51-67.
20. Khachatoorian, R., Cohn, W., Buzzanco, A., Riahi, R., Arumugaswami, V., Dasgupta, A., ... & French, S. W. (2018). HSP70 Copurifies with Zika Virus Particles. *Virology*, 522, 228-233.
21. Saelices, L., Chung, K., Lee, J. H., Cohn, W., Whitelegge, J. P., Benson, M. D., & Eisenberg, D. S. (2018). Amyloid seeding of transthyretin by ex vivo cardiac fibrils and its inhibition. *Proceedings of the National Academy of Sciences*, 201805131.
22. Waldron, R. T., Su, H. Y., Piplani, H., Capri, J., Cohn, W., Whitelegge, J. P., ... & Zhou, B. (2018). Ethanol Induced Disordering of Pancreatic Acinar Cell Endoplasmic Reticulum: An ER Stress/Defective Unfolded Protein Response Model. *Cellular and molecular gastroenterology and hepatology*, 5(4), 479-497.
23. Rao, N. M., Capri, J., Cohn, W., Abdaljaleel, M., Restrepo, L., Gornbein, J. A., ... & Whitelegge, J. P. (2017). Peptide Composition of Stroke Causing Emboli Correlate with Serum Markers of Atherosclerosis and Inflammation. *Frontiers in neurology*, 8, 427.
24. Chai, H., Diaz-Castro, B., Shigetomi, E., Monte, E., Octeau, J. C., Yu, X., Cohn, W., ... & Khakh, B. S. (2017). Neural circuit-specialized astrocytes: transcriptomic, proteomic, morphological, and functional evidence. *Neuron*, 95(3), 531-549.
25. Khachatoorian, R., Cohn, W., Ganapathy, E., Liu, N., Vu, J., Lu, N., Whitelegge, J., & French, S. W. (2017). Mass spectrometry analysis of the phosphoproteome in an in vitro lipotoxicity model. *The FASEB Journal*, 31(1 Supplement), 804-6.
26. Lu, N. T., Liu, N. M., Vu, J. Q., Patel, D., Cohn, W., Capri, J., ... & Whitelegge, J. (2016). Phospho-Network Analysis Identifies and Quantifies Hepatitis C Virus (HCV)-induced Hepatocellular Carcinoma (HCC) Proteins Regulating Viral-mediated Tumor Growth. *Cancer Genomics-Proteomics*, 13(5), 339-357.
27. Singh, S. K., Hasan, S. S., Zakharov, S. D., Naurin, S., Cohn, W., Ma, J., Whitelegge, J. P., & Cramer, W. A. (2016). Trans-membrane Signaling in Photosynthetic State Transitions: REDOX- AND STRUCTURE-DEPENDENT INTERACTION IN VITRO BETWEEN STT7 KINASE AND THE CYTOCHROME b6f COMPLEX. *The Journal of biological chemistry*, 291(41), 21740-21750. <https://doi.org/10.1074/jbc.M116.732545>
28. Cheung, K., Senese, S., Kuang, J., Bui, N., Ongpipattanakul, C., Gholkar, A., Cohn, W., ... & Torres, J. Z. (2016). Proteomic Analysis of the Mammalian Katanin Family of Microtubule-severing Enzymes Defines Katanin p80 subunit B-like 1 (KATNBL1) as a Regulator of Mammalian Katanin Microtubule-severing. *Molecular & Cellular Proteomics*, 15(5), 1658-1669.
29. Dada, L. A., Bittar, H. E. T., Welch, L. C., Vagin, O., Deiss-Yehiely, N., Kelly, A. M., Cohn, W., ... & Gruenbaum, Y. (2015). High CO2 leads to Na, K-ATPase endocytosis via c-Jun amino-terminal kinase-induced LMO7b phosphorylation. *Molecular and cellular biology*, 35(23), 3962-3973.

PREFACE

The emergence of contemporary drug discovery and development approaches marks a transformative phase in the field of healthcare. Once reliant on the identification of active elements within traditional remedies or accidental discoveries such as penicillin, the field has now undergone a paradigm shift toward more systematic and powerful methodologies (Ref. 1). This revolution has led to the acceleration of therapeutic innovation, offering new hope for addressing a myriad of diseases and health conditions.

The importance of basic biological research to the advancement of pharmaceutical identification and development cannot be understated. Significant advancements in scientific disciplines like chemistry, biology, and computer science have revolutionized drug discovery by enabling the exploration of complex disease mechanisms (Ref. 2). Sequencing the human genome has been pivotal, aiding in identifying genetic variations linked to specific conditions and disease-causing genes. Advances in molecular biology tools to characterize and manipulate biological systems have allowed for a deeper understanding of disease-causing mechanisms and possible therapeutic avenues (Ref. 3). Even more recently, integration of various 'omics' technologies such as genomics, transcriptomics, proteomics, and metabolomics have allowed for a more intricate and holistic view of disease etiology (Ref.4). By simultaneously analyzing multiple layers of molecular information, this comprehensive methodology illuminates complex biochemical interactions contributing to disease progression, greatly facilitating the identification of novel biomarkers and therapeutic targets that are the basis for drug discovery programs.

Major developments in pharmaceutical research tools has dramatically improved the success of drug discovery efforts. This has led to the establishment of a contemporary drug discovery and development strategy used by pharmaceutical companies (Fig. 1). Firstly, the development of chemical libraries and high-throughput screening (HTS) has significantly expedited modern drug discovery by systematically evaluating diverse compounds against specific biological targets, streamlining selection processes and enhancing efficiency (Fig. 1A) (Ref. 5). This approach accelerates the identification of potential therapeutic candidates, enhancing the cost-effectiveness of drug development. Subsequent hit-to-lead optimization refines initial HTS hits into more potent, selective, and bioavailable lead compounds, guiding their evolution by enhancing desirable properties and minimizing undesirable attributes (Fig. 1B) (Ref. 6). This may also encompass experiments to identify drug mechanism of action, which can facilitate rational drug design or be used to identify superior therapeutic strategies, increasing the likelihood of creating effective therapeutics (Ref. 7). Finally, *in-vivo* testing in disease-relevant models is vital as it bridges the gap between promising *in-vitro* outcomes and efficacy and safety in higher organisms (Fig. 1C) (Ref. 8). This testing provides essential insights into pharmacokinetics, pharmacodynamics, toxicity, metabolism, and physiological impact, aiding researchers in evaluating compounds within complex biological systems, thereby boosting the chances of successful drug development.

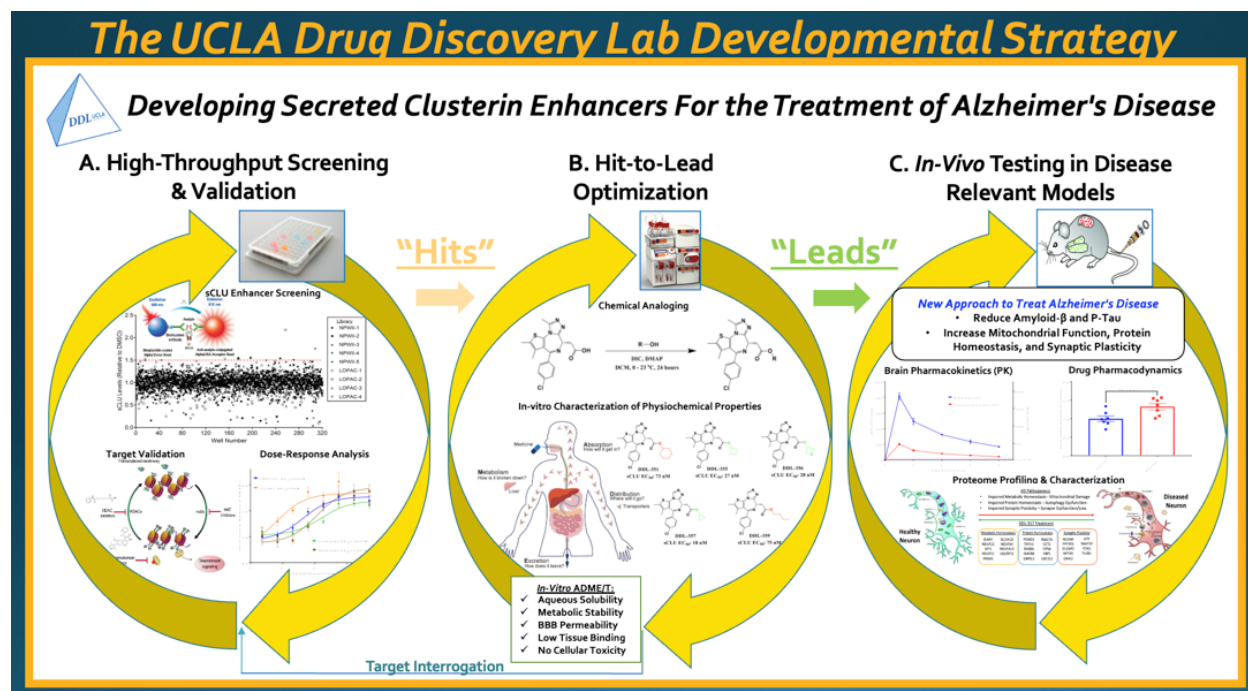


Figure 1. Developing secreted clusterin enhancers for Alzheimer's disease using the iterative UCLA Drug Discovery Lab developmental strategy. (A) The first step of the drug discovery process: the high-throughput screening to identify compounds that achieve a desired phenotype. In this case, increasing sCLU. (B) Subsequent hit-to-lead optimization uses medicinal chemistry to optimize hits into more potent, selective, and bioavailable lead compounds. (C) Finally, lead compounds are evaluated *in-vivo* in disease-relevant models.

This well-established workflow stands at the forefront of scientific efforts to develop therapies for countless diseases. This dissertation focuses on several drug discovery programs to identify groundbreaking treatments to several neurological and muscular disorders, including Alzheimer's disease, vascular cognitive impairment and dementia, limb girdle muscular dystrophy and Duchenne muscular dystrophy. Through the lens of advanced scientific tools and methodologies, we explore the cellular and molecular mechanisms underlying the cause of these diseases and the intricacies of the drug discovery process, with the ultimate goal of identifying disease modifying

therapies that alleviate symptoms and improve patients lives. I am optimistic that the research described here provides further understanding of the intricate mechanisms involved in the development and treatment of these diseases.

REFERENCES

1. Pina, A. S., Hussain, A., & Roque, A. C. A. (2010). An historical overview of drug discovery. *Ligand-Macromolecular Interactions in Drug Discovery: Methods and Protocols*, 3-12.
2. Heilbron, K., Mozaffari, S. V., Vacic, V., Yue, P., Wang, W., Shi, J., ... & Wang, X. (2021). Advancing drug discovery using the power of the human genome. *The Journal of Pathology*, 254(4), 418-429.
3. Belfield, G. P., & Delaney, S. J. (2006). The impact of molecular biology on drug discovery. *Biochemical Society Transactions*, 34(2), 313-316.
4. Matthews, H., Hanison, J., & Nirmalan, N. (2016). “Omics”-informed drug and biomarker discovery: opportunities, challenges and future perspectives. *Proteomes*, 4(3), 28.
5. Carnero, A. (2006). High throughput screening in drug discovery. *Clinical and Translational Oncology*, 8, 482-490.
6. Hoffer, L., Muller, C., Roche, P., & Morelli, X. (2018). Chemistry-driven Hit-to-lead Optimization Guided by Structure-based Approaches. *Molecular informatics*, 37(9-10), e1800059.
7. Davis R. L. (2020). Mechanism of Action and Target Identification: A Matter of Timing in Drug Discovery. *iScience*, 23(9), 101487.
8. Loewa, A., Feng, J. J., & Hedtrich, S. (2023). Human disease models in drug development. *Nature reviews bioengineering*, 1–15. Advance online publication.

CHAPTER 1

Multi-Omics Analysis of Microglial Extracellular Vesicles From Human Alzheimer's Disease Brain Tissue Reveals Disease-Associated Signatures

Whitaker Cohn¹, Mikhail Melnik ², Calvin Huang², Bruce Teter¹, Sujyoti Chandra¹, Chunni Zhu¹,
Laura Beth McIntire³, Varghese John¹, Karen H. Gyllys ² and Tina Bilousova^{1,2 *}

¹Drug Discovery Lab, Department of Neurology, University of California, Los Angeles, Los Angeles, CA, United States

²School of Nursing, University of California, Los Angeles, Los Angeles, CA, United States

³Taub Institute for Research on Alzheimer's Disease and the Aging Brain, Department of Pathology and Cell Biology, Columbia University Medical Center, New York, NY, United States

[This research was originally published by the *Frontiers in pharmacology*, 2021, 12, 766082.
<https://doi.org/10.3389/fphar.2021.766082>]

Abstract

Alzheimer's disease (AD) is the most common cause of dementia, yet there is no cure or diagnostics available prior to the onset of clinical symptoms. Extracellular vesicles (EVs) are lipid bilayer-delimited particles that are released from almost all types of cell. Genome-wide association studies have linked multiple AD genetic risk factors to microglia-specific pathways. It is plausible that microglia-derived EVs may play a role in the progression of AD by contributing to the dissemination of insoluble pathogenic proteins, such as tau and A β . Despite the potential utility of EVs as a diagnostic tool, our knowledge of human brain EV subpopulations is limited. Here we present a method for isolating microglial CD11b-positive small EVs from cryopreserved human brain tissue, as well as an integrated multiomics analysis of microglial EVs enriched from the parietal cortex of four late-stage AD (Braak V-VI) and three age-matched normal/low pathology (NL) cases. This integrated analysis revealed 1,000 proteins, 594 lipids, and 105 miRNAs using shotgun proteomics, targeted lipidomics, and NanoString nCounter technology, respectively. The results showed a significant reduction in the abundance of homeostatic microglia markers P2RY12 and TMEM119, and increased levels of disease-associated microglia markers FTH1 and TREM2, in CD11b-positive EVs from AD brain compared to NL cases. Tau abundance was significantly higher in AD brain-derived microglial EVs. These changes were accompanied by the upregulation of synaptic and neuron-specific proteins in the AD group. Levels of free cholesterol were elevated in microglial EVs from the AD brain. Lipidomic analysis also revealed a proinflammatory lipid profile, endolysosomal dysfunction, and a significant AD-associated decrease in levels of docosahexaenoic acid (DHA)-containing polyunsaturated lipids, suggesting a potential defect in acyl-chain remodeling. Additionally, four miRNAs associated with immune and cellular senescence signaling pathways were significantly upregulated in the AD group. Our data suggest

that loss of the homeostatic microglia signature in late AD stages may be accompanied by endolysosomal impairment and the release of undigested neuronal and myelin debris, including tau, through extracellular vesicles. We suggest that the analysis of microglia-derived EVs has merit for identifying novel EV-associated biomarkers and providing a framework for future larger-scale multiomics studies on patient-derived cell-type-specific EVs.

Introduction

Alzheimer's disease (AD) is the most common cause of dementia, yet there is no cure or diagnostics available prior to the onset of clinical symptoms (2021 Alzheimer's disease facts and figures, 2021). The main neuropathological hallmarks of AD include the accumulation of amyloid beta peptide (A β)-containing plaques, hyperphosphorylated tau protein (p-tau)-composed neurofibrillary tangles, extensive neuroinflammation, synaptic loss, and neuronal cell death (Serrano-Pozoe et al., 2011). Numerous anti-AD drug candidates have proven to be effective in AD animal models but subsequently failed in clinical trials (Mehta et al., 2017). These failures can be attributed to three factors: 1) limited knowledge of the complex cellular and molecular mechanisms causing disease onset; 2) late initiation of the experimental treatments; and 3) inadequate monitoring of the treatment effects due to the absence of a biomarker panel that provides accurate longitudinal information regarding disease progression (Yiannopoulou et al., 2019).

Small extracellular vesicles (EVs), originating either from the plasma membrane (microvesicles) or from multivesicular bodies (exosomes), play a role in many of the major pathological and physiological pathways altered in AD, including A β aggregation (Dinkins et al., 2014; Kokubo, et

al., 2005; Rajendran, et al., 2006; Yuyama, et al., 2014), spread of tau and A β seeds (Asai, et al., 2015; Bilousova, et al., 2018; Bilousova, et al., 2020; Joshi, et al., 2014; Sardar Sinha, et al., 2018), neuroinflammation (Pascual et al., 2020), synaptic transmission (An, et al., 2013), cell death (G. Wang, et al., 2012; Winston, et al., 2019), and senescence (D'Anca, et al., 2019). Interestingly, the two greatest genetic risk factors for late-onset AD (LOAD), apolipoprotein E (apoE) and bridging integrator-1 (Bin1), are involved in EV biogenesis and/or cargo sorting (Crotti, et al., 2019; Peng, et al., 2019), suggesting direct involvement of EVs in the development AD pathophysiology. Moreover, the molecular composition of EVs reflects the state and makeup of their cells of origin, and thus, they may be an invaluable resource for identifying important biomarkers of the disease. Indeed, brain-derived EVs cross the blood–brain barrier (BBB) harboring disease-associated molecules such as p-tau and A β . In this context, they provide an accessible reservoir of biomarkers that might predict the development of AD at the asymptomatic stage, as well as the conversion from mild cognitive impairment (MCI)/prodromal stage to clinical AD (Fiandaca, et al., 2015; Goetzl et al., 2016; Goetzl et al., 2018; Hornung et al., 2020; Winston, et al., 2016).

Genome-wide association studies (GWAS) have identified multiple AD risk loci located in or near genes preferentially expressed in microglia, suggesting that microglial dysfunction may have a causative role in disease development (Takatori et al., 2019). Moreover, single-cell and single-nuclei RNA sequencing analysis (RNA-seq) revealed the presence of disease-associated microglia (DAM) clusters near A β plaques in both animal models and in the human AD brain (Butovsky and Weiner, 2018; Del-Aguila, et al., 2019; Mathys, et al., 2019). DAM populations are characterized by the loss of a homeostatic transcriptional signature, including decreases in purinergic 2Y receptor

12 (P2RY12), P2RY13, transmembrane protein 119 (TMEM119), CX3C chemokine receptor 1 (CX3CR1), and others, and activation of genes responsible for either proinflammatory microglia activation (Stage 1 DAM) or a neurodegeneration restrictive phenotype (Stage 2 DAM). Upregulation of apoE, ferritin heavy chain-1 (FTH-1), beta-2-microglobulin (B2m), major histocompatibility complex class I (MHC class 1), and DAP12 are changes associated with the Stage 1 DAM transcriptome profile, while increases in the triggering receptor expressed on myeloid cells 2 (TREM 2) and exosomal markers CD63 and CD9 are part of the Stage 2 DAM program (Deczkowska, et al., 2018; Xue and Du, 2021). Upregulation of exosomal markers suggests that an increase in exosome production may help to resolve inflammation; on the other hand, microglial EVs, specifically the neutral sphingomyelinase 2 (nSMase2)-dependent exosomal population, take part in spreading tau pathology *in vitro* and in mouse models of tauopathy (Asai, et al., 2015; Maphis, et al., 2015).

Despite progress identifying cell-specific EVs in body fluids (Fiandaca, et al., 2015; Goetzl et al., 2016; Goetzl, Mustapic, et al., 2016; Wang, et al., 2012; Willis, et al., 2017), it is important to note that little is known about the composition of cell-type-specific EV subpopulations isolated from human brain tissue. Changes in the brain EV proteome in human AD cases and animal models suggest the enrichment of a neurodegenerative microglial signature in bulk brain EV preparations (Muraoka, et al., 2020; Muraoka, et al., 2021). Our knowledge of the miRNA transcriptome and lipidome of AD brain-derived EVs is even more limited (Cheng, et al., 2020; Su, et al., 2021). Here we specifically focus on human microglia-derived EVs isolated from cryopreserved human tissue from late AD (Braak V-VI) and normal/low pathology (NL) cases in order to characterize

their molecular profiles utilizing an integrative approach combining proteomic, transcriptomic (miRNA), and lipidomic analyses.

Materials and Methods

Purification of Small Microglial EVs From Cryopreserved Human Brain Tissue

Human brain parietal cortex samples were prepared as described (Gylys and Bilousova, 2017) using tissue from cases with postmortem interval (PMI) less than or equal to 7 h. Briefly, following harvesting of the human brain from Brodmann area A7, A39, or A40, the tissue was finely minced (1–3 mm fragments) on ice and suspended in a solution of sucrose and protease inhibitors (0.32 M sucrose, 2 mM EDTA, 2 mM EGTA, 0.2 mM PMSF, 1 mM NaPP, 5 mM NaF, 10 mM Tris-HCL, pH 8.0), with 10 ml sucrose buffer/g tissue, and then slowly frozen to -80°C ; this protocol is based on a described method (Dodd, et al., 1986). On the day of EV isolation, the cryopreserved brain tissue was quickly thawed at 37°C , centrifuged (1,000xg, 2 min, 4°C) to remove cryopreservation buffer, and weighed. The tissue was gently dissociated using an adult brain dissociation kit and a GentleMACS dissociator (Miltenyi Biotec) according to the instructions of the manufacturer (0.5 g of tissue per enzymatic reaction). In a recent study comparing six different enzyme protocols for cell dissociation from the rodent brain, this kit yielded the highest number of live cells (Hussain, et al., 2018). After the dissociation step, the cell suspension was passed through a MACS Smart strainer (70 μm ; Miltenyi Biotec). Small EV fractions were purified by sequential centrifugation steps including sucrose density gradient ultracentrifugation followed by washing steps as described (Vella, et al., 2017). This protocol for brain EV isolation has been extensively validated in our previous publications and by others, and enrichment of small EVs in the 0.6 M sucrose layer (F2) has been demonstrated (Bilousova, et al., 2020; Huang, et al., 2020; Vassileff, et al., 2020; Zhu, et

al., 2021). Final F2 pellets were resuspended in 25 mM trehalose in PBS, pH 7.4 with a protease and phosphatase inhibitor cocktail (ThermoFisher); the volume of the resuspension solution was adjusted based on the original brain tissue weight (1 g of tissue/150 μ l solution). Trehalose prevents EV aggregation and serves as a cryopreservant (Bosch, et al., 2016). Small portions of the F2 small EV fractions were frozen at -80°C for further characterization (see below), and the remainder was used for immunoprecipitation (IP) of microglial EVs using antibodies for the myeloid cell-specific marker CD11b (BioLegend; Clone M1/70) or for control IP reactions with isotype control rat IgG2b antibodies (BioLegend; Clone RTK4530). Covalent coupling of antibodies to Dynabeads M-270 epoxy beads was performed with the Dynabead antibody coupling kit (ThermoFisher; 14311D) according to the instructions of the manufacturer. F2 fractions were incubated with a human-specific FcR blocking reagent (Milteny biotec) for 5 min on ice (5 μ l of the blocking reagent per 100 μ l of F2), followed by 1:20 dilution with 1% bovine serum albumin (BSA) in PBS, pH 7.4. We used 1.25 mg of antibody-coupled Dynabeads per 2 ml of the 1:20 diluted F2 sample. IP reactions were incubated overnight at 4°C with rotation, followed by 4 consecutive 10-min washes with rotation: the first wash with 0.1% BSA/PBS, the second wash with 25 mM citrate-phosphate buffer, pH 5 to reduce the amount of nonspecifically bound material as previously described (Heinzelman et al., 2016), followed by two washes with PBS, pH 7.4. Dynabeads with bound microglial EVs were aliquoted based on the original tissue weight (microglial EVs from 1 g of tissue per aliquot) and frozen at -80°C for downstream analysis.

Transmission Electron Microscopy (TEM)

For quality control purposes, small amounts of purified brain-derived EVs were loaded on the formvar/carbon 400 mesh copper EM grids (Ted Pella, Inc.), incubated for 30 min, then fixed in

2% paraformaldehyde solution (3 min), followed by washes with distilled water, and staining with 2% uranyl acetate solution (3 min). The grids were dried for at least 1 h at room temperature, and the negative-stained EVs were imaged on a JEOL 100CX electron microscope at 60 kV and $\times 29,000$ magnification.

Tunable Resistive Pulse Sensing Analysis

Size distribution and concentrations of EV samples were measured by the Tunable Resistive Pulse Sensing (TRPS) method using the qNano Gold instrument (Izon Science). NP100 nanopore (particle size range: 50–330 nm) and CPC100 calibration particles were used for the analysis. Data analysis was performed using the qNano instrument software.

Immunoblotting

Microglial EVs were separated from Dynabeads by incubation in a Tris-Glycine SDS sample buffer without reducing agents at 95 C for 5 min after which immunoblot analysis was performed as described above. Proteins from microglial and total small EV fractions were separated by 10–20% Tris-Glycine SDS-PAGE under reducing (50 mM dithiothreitol) or nonreducing (for tetraspanins) conditions, transferred to PVDF membrane, and probed with primary antibodies (Table 1) followed by HRP-conjugated secondary antibodies (Jackson ImmunoResearch). Chemiluminescent signals were obtained with Super Signal West Femto substrate (Thermo Scientific Pierce 34095), detected using the BioSpectrum 600 imaging system, and quantified using the VisionWorks version 6.6A software (UVP; Upland, CA). Data were analyzed by Student's t-test.

Target protein	Company	Clone name	Figure number
CD9	ThermoFisher	TS9	1C, E
CD81	ThermoFisher	M38	1C
Syntenin-1	Abcam	EPR8102	1C
Calnexin	Santa Cruz Biotech	AF18	1C
GM130	Cell Signaling	D6B1	1C
CD63	ThermoFisher	TS63	1D
Tau	ThermoFisher	HT7	1E
CD11b	BioLegend	M1/70	1E
TREM2	Abcam	EPR20243	2D
apoE	Abcam	E6D7	2D

Table 1. *Antibodies used for immunoblot analysis of small EV (F2) fractions and microglial EVs isolated from human parietal cortex.*

Proteomic Analysis

One aliquot of frozen microglial EVs isolated from 1 g of parietal cortex tissue from each case presented in Table 2 was used for the proteomic analysis. Microglial EV samples were diluted in lysis buffer [200 uL, 12 mM sodium lauroyl sarcosine, 0.5% sodium deoxycholate, 50 mM triethylammonium bicarbonate (TEAB)] and Halt™ Protease and Phosphatase Inhibitor Cocktail (Thermo Scientific, Waltham, MA), and then were treated with tris(2-carboxyethyl) phosphine (10 mM, 30 min, 60°C), alkylated (chloroacetamide 40 mM, 30 min, 25°C in the dark), and digested with Sequencing Grade Modified Trypsin (Promega, Madison, WI; 1 ug, 37°C, overnight). The samples were then desalted on C18 StageTips according to Rappsilber's protocol (Rappsilber et al., 2007). The collected eluent was then chemically modified using a TMT10plex Isobaric Label Reagent Set (Thermo Fisher Scientific) per the protocol of the manufacturer. The samples were pooled according to the protein content (1 ug of peptide from each sample) and desalted again according to Rappsilber's protocol (Rappsilber, et al., 2007). The eluants were

injected onto a reverse-phase nanobore HPLC column (AcuTech Scientific, C18, 1.8-um particle size, 360 um x 20 cm, 150 um ID), equilibrated in solvent A, and eluted (300 nl/min) with an increasing concentration of solvent B (acetonitrile/water/FA, 98/2/0.1, v/v/v: min/% B; 0/0, 5/3, 18/7, 74/12, 144/24, 153/27, 162/40, 164/80, 174/80, 176/0, 180/0) using a Dionex UltiMate 3,000 RSLCnano System (Thermo Fisher Scientific). The effluent from the column was directed to a nanospray ionization source connected to an Orbitrap Fusion Lumos Tribrid mass spectrometer (Thermo Fisher Scientific) acquiring mass spectra utilizing the Synchronous Precursor Selection (SPS) MS3 method in which isolation and MS3 fragmentation of MS2 fragment ions eliminate isolation interference and dynamic range compression often observed in isobaric tandem mass tag-based proteomics experiments.

Case ID	Age, years	Sex	PMI	Diagnosis	A β plaque pathology in parietal cortex	Neurofibrillary degeneration stage (Braak)
NL1	65	F	6	MSA, Striatonigral degeneration	0	I
NL2	100	F	4	Normal (mild Braak changes)	0	III
NL3	91	F	7	Normal, multiple infarctions	0	II
AD1	86	M	6	AD, vascular dementia	Severe	V
AD2	95	F	6	AD, vascular dementia	Severe	VI
AD3	95	M	5	AD, LB in SN&LC, CAA	Moderate	V
AD4	88	M	7	AD, diffuse LB	Severe	VI

F, female; M, male; AD, Alzheimer disease; CAA, cerebral amyloid angiopathy; MSE, multiple system atrophy; SN, substantia nigra; PMI, postmortem interval; LB, Lewy bodies.

Table 2. Case information for human samples.

For statistical analysis, the raw data were searched against the Uniprot human reviewed protein database using SEQUEST-HT in Proteome Discoverer (Version 2.4, Thermo Scientific), which provided measurements of relative abundance of the identified peptides. Decoy database searching was used to generate high confidence tryptic peptides (FDR < 1%). Tryptic peptides containing amino acid sequences unique to individual proteins were used to identify and provide relative quantification between proteins in each sample. Between-group comparisons were analyzed using the abundance ratio *p*-value (Student's t-test). Gene set enrichment gene ontology (GO) and

pathway analysis was performed by the STRING database (version 11.5), which was used for functional interpretation of the proteomics data and provided p -values corrected by the FDR method (Szkłarczyk, et al., 2019).

MicroRNA Transcriptomics

Microglial EV samples isolated from 1 g of parietal cortex tissue from each case presented in Table 2 were used for RNA purification with the SerMir Exosome RNA Column Purification Kit (Systems Bioscience Inc). Purified RNA samples were run on nCounter human microRNA panel Human v3 miRNA according to the instructions of the manufacturer (NanoString). The panel contains 800 pairs of probes specific for a predefined set of biologically relevant miRNAs, which were combined with a series of internal controls to form a Human miRNA Panel CodeSet (NanoString Technologies). Raw counts for miRNA targets were analyzed using the Nanostring nCounter Digital Analyzer software according to the instructions of the manufacture. Statistical analysis of NanoString nCounter data was performed as described (Brumbaugh et al., 2011). Only miRNAs that were above background in five out of seven samples from two groups (NL and AD) were selected for the analysis, which resulted in normalized counts and a list of differentially expressed microRNAs that significantly differ between NL and AD groups. Using the miRNet software, we then identified top pathways in the Reactome pathway database, which can be controlled by the miRNAs shown to be significantly altered in the AD group compared to NL by Student's t-test; p -values were corrected by the FDR method.

Lipidomic Analysis

We interrogated 34 classes, including free cholesterol (FC), cholesteryl ester (CE), acyl carnitine (AC), monoacylglycerol (MG), diacylglycerol (DG), triacylglycerol (TG), ceramide (Cer), sphingomyelin (SM), monohexosylceramide (MhCer), sulfatides (Sulf), lactosylceramide (LacCer), monosialodihexosylganglioside (GM3), globotriaosylceramide (GB3), phosphatidic acid (PA), phosphatidylcholine (PC), ether phosphatidylcholine (PCe), phosphatidylethanolamine (PE), plasmalogen phosphatidylethanolamine (Pep), phosphatidylserine (PS), phosphatidylinositol (PI), phosphatidylglycerol (PG), bis(monoacylglycerol)phosphate (BMP), acyl phosphatidylglycerol (AcylPG), lysophosphatidylcholine (LPC), ether lysophosphatidylcholine (LPCe), lysophosphatidylethanolamine (LPE), plasmalogen lysophosphatidylethanolamine (LPEp), lysophosphatidylinositol (LPI), lysophosphatidylserine (LPS), N-Acyl phosphatidylethanolamine (NAPE), N-acyl phosphatidylserine (NAPS), and N-acyl serine (NSer), encompassing 593 individual lipid species. Immuno-isolated microglial EV preparations were subjected to modified Bligh–Dyer lipid extraction (Bligh and Dyer, 1959), dried, resuspended, and subjected to liquid-chromatography tandem mass spectrometry (LC-MS/MS) targeted lipidomics using Agilent 1,260 Infinity HPLC integrated to an Agilent 6490A QQQ mass spectrometer controlled by Masshunter v 7.0 (Agilent Technologies, Santa Clara, CA) in positive and negative ion modes as previously described (Chan, et al., 2012; Guan et al., 2007; Hsu et al., 2004). Quantification of lipid species was accomplished using multiple reaction monitoring (MRM) transitions (Chan, et al., 2012; Guan, et al., 2007; Hsu, et al., 2004) under both positive and negative ionization modes in conjunction with referencing of appropriate internal standards: PA 14:0/14:0, PC 14:0/14:0, PE 14:0/14:0, PG 15:0/15:0, PI 17:0/20:4, PS 14:0/14:0, BMP 14:0/14:0, APG 14:0/14:0, LPC 17:0, LPE 14:0, LPI 13:0, Cer d18:1/17:0, SM d18:1/12:0, dhSM d18:0/12:0, GalCer d18:1/12:0, GluCer d18:1/12:0, LacCer d18:1/12:0, D7-cholesterol, CE 17:0, MG 17:0,

4ME 16:0 diether DG, and D5-TG 16:0/18:0/16:0 (Avanti Polar Lipids, Alabaster, AL). Lipid levels for each sample were calculated by summing the total number of moles of all lipid species measured by all three LC-MS methodologies and then normalizing that total to mol%. The final data are presented as mean mol% with error bars showing mean \pm S.E. Graph-pad Prism was used to analyze the lipidomics data. For statistical analysis, two-way repeated measures (mixed model) ANOVA was completed on individual lipid classes among the lipid species using an unweighted means analysis due to the different n for LN and AD groups. Bonferroni post-test was used to compare replicate means by row (lipid species) in which microglia NL and microglia AD were compared.

Results

Microglia-Derived Small EV Isolation and Characterization

Based on a previously described method of brain EV isolation (Vella, et al., 2017), brain tissue from two late AD cases (Braak V-VI) was used for the development and standardization of the microglial EV isolation protocol. Sucrose-gradient fractions enriched in EVs were isolated from cryopreserved tissue after enzymatic digestion and ultracentrifugation. TEM and TRPS analysis confirmed the abundance of small EVs (below 200 nm in diameter) in Fraction 2 (F2) (**Figures 1A, B**). This fraction was enriched in exosomal markers CD9, CD81, and syntenin-1 and contained only trace amounts of negative control markers, such as Golgi complex protein GM130 and endoplasmic reticulum protein calnexin (CNX) (They, et al., 2018) (**Figure 1C**). The F2 fraction was further used for the isolation of microglial EVs by immunoprecipitation with antibodies against the microglia-specific marker CD11b. Immunoblot analysis demonstrated the enrichment of exosomal markers, CD63 and CD9, and the microglial marker, CD11B, in small EVs

immunoprecipitated with CD11b-conjugated Dynabeads when compared to isotype control antibody-conjugated beads (**Figures 1D, E**). We also compared the levels of the microglial marker TMEM119 between the F2 fraction and the corresponding CD11b-positive microglial fraction (Figure 1F). The data demonstrate the enrichment of TMEM119 in the IP fraction despite much higher EV load in the F2 lane as documented by the CD63 signal (**Figure 1F**). We tested relative abundances of TMEM119 and another microglial marker P2RY12 in F2 and CD11b-IP samples by proteomics. Proteomic analysis revealed the enrichment of microglia-associated proteins in CD11b-pos EVs when compared to F2 fractions from NL and AD brain tissue. Relative to other proteins in each sample, two microglia markers, TMEM119 and P2RY12, were significantly more abundant in CD11b-purified samples with 6.1- and 16.9-fold increase, respectively (**Figure 1G**). Tau was detected in some but not all microglial EV samples by immunoblotting (**Figure 1E**); however, A β peptide was not detected (data not shown) either because of low levels or difficulties relating to A β detection without prior delipidation (Perez-Gonzalez, et al., 2017).

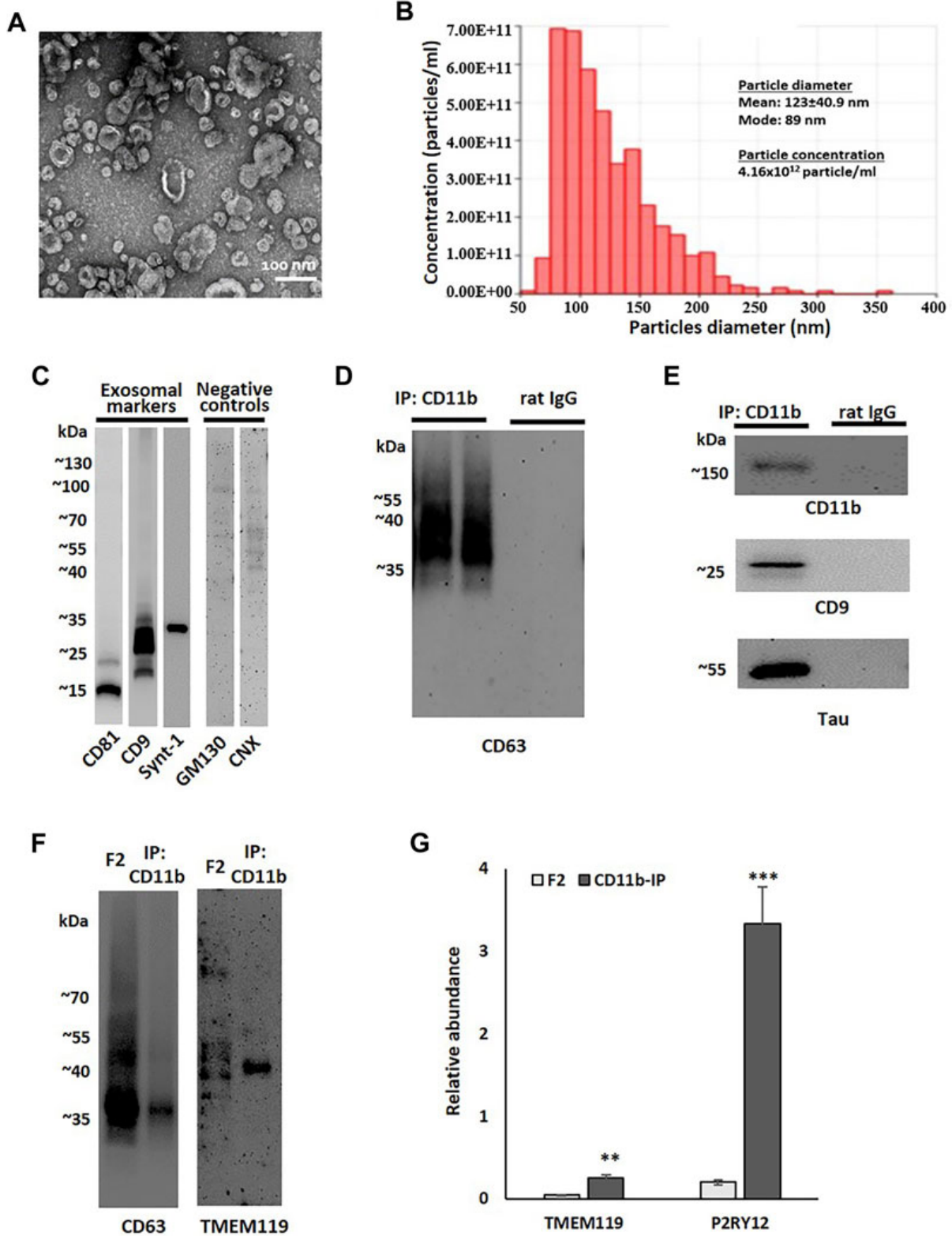


Figure 1. *Small EV fraction characterization and microglial EV purification.* (A) Representative transmission electron microscopy (TEM) image of small EV fraction (F2) isolated from the human

parietal cortex. (B) Tunable resistive pulse sensing (TRPS) analysis of the F2 fraction isolated from the human parietal cortex. (C) A representative image of immunoblot analysis of an F2 fraction using antibodies against exosomal markers (CD9, CD81, and syntaxin-1) and negative control markers (GM130 and calnexin, CNX). (D) A representative image of immunoblot analysis of two immunoprecipitation (IP) samples pull-down either with antibodies against microglial marker CD11b or with corresponding isotype control antibodies (rat IgG2b). Membrane was probed with the exosomal marker CD63. (E) Immunoblotting of CD11b-IP samples and isotype control samples probed with antibodies against a microglial marker (CD11b), an exosomal marker (CD9), and tau. (F) Immunoblotting of the F2 fraction isolated from the human parietal cortex and corresponded CD11b-IP fraction with antibodies against the exosomal marker CD63 and the microglial marker TMEM119. The sample volume was equal between CD63 and TMEM119 immunoblots. (G) Relative abundances of microglial markers, TMEM119 and P2RY12, in F2 (n = 6) and CD11b-IP samples (n = 7) as indicated by LC-MS/MS (** $p < 0.001$; *** $p < 0.0001$). For the omics analyses, microglial EVs enriched from 1 g of cryopreserved human parietal cortex tissue from three normal/low pathology cases (NL 1-3) and four late AD cases (AD 1-4) were used. Demographic information for all the cases is presented in Table 2.

Proteomic Analysis of Microglial EVs

Using Tandem Mass Tag (TMT)-based quantitative proteomics, a total of 1,000 unique proteins were identified in the microglia-derived small EV samples from the human parietal cortex. Among these, 985 were detected in both NL and AD groups. Three proteins, fatty acid binding protein 3, heart type (FABP3), mitochondrial copper transporter Solute Carrier Family 25 Member 3 (SLC25A3), and GTPase Atlastin-3(Alt3), were only detected in the NL samples. Twelve proteins

were detected only in the AD samples. These included innate immune response proteins toll-like receptor 8 (TLR8) and CX3C chemokine receptor 1 (CX3CR1), neuron-specific proteins, cell cycle exit and neuronal differentiation 1 (CEND1), synaptosomal-associated protein 25 (SNAP25) and myelin-associated glycoprotein (MAG), and two known regulators of amyloid precursor protein (APP) metabolism, calpain-2 catalytic subunit (CAPN2) (Mahaman, et al., 2019) and integral membrane protein 2B (ITM2B/BRI2) (Matsuda et al., 2008) (**Figure 2A**). A total of 469 proteins were quantified in all analyzed samples, providing relative abundances for each protein. Differences in protein abundances are illustrated via a volcano plot, which shows that 4 proteins were significantly downregulated and 23 proteins were significantly upregulated in the AD group when compared to the NL group (**Figure 2B**). A heatmap showing differential expression of the significantly altered proteins across individual samples is presented in **Figure 2C**. The protein composition of microglia EVs from AD cases reflects the loss of the homeostatic signature of their cells of origin, with a significant decrease in the abundance of two main markers of homeostatic microglia, TMEM119 and P2RY12 (2.8-fold and 1.8-fold, respectively). Abundances of the phagocytic microglial marker FCGR1A (CD64) and a known TREM2 ligand, ApoA1, were also significantly lower in the AD group (**Figures 2B, C**). There was a significant upregulation of the Stage 1 DAM (proinflammatory phenotype) marker, ferritin heavy chain-1 (FTH1; 2.7-fold) (**Figures 2B, C**). Most proteins with significantly higher abundances in AD cases can be divided into four groups: 1) neuronal and synapse-enriched proteins: synaptotagmin-2 (SYT-2; 5.5-fold), synaptotagmin-11 (SYT11; 4.4-fold), Syntaxin-1B (STX1B; 2.5-fold), Thy1 membrane glycoprotein (Thy1; 4.2 -fold), and tau protein (3.5-fold); 2) complement regulators: complement component 4B (C4B; 2.8-fold) and CD59 (2.6-fold); 3) GTPases: septin-7 (SEPT7; 4.1-fold) and G-protein complex subunits, guanine nucleotide-binding protein G(I)/G(S)/G(O) subunit gamma-

7 (GNG7; 3.8-fold), guanine nucleotide-binding protein G(I)/G(S)/G(T) subunit beta-2 (GNB2; 2-fold), guanine nucleotide-binding protein G(i) subunit alpha-1 (GNAI1; 1.7-fold), and guanine nucleotide-binding protein G(o) subunit alpha (GNAO1; 1.9-fold); and 4) members of the annexin family involved in vesicle traffic, aggregation, and membrane fusion: annexins A6 (ANXA6; 2.6-fold) and A7 (ANXA7; 4.2-fold) (Lizarbe et al., 2013). We also identified AD-related increases in toll-like receptor chaperone, heat shock protein 90B1 (HSP90B1; 3.4-fold) (Binder, 2014); antioxidant protein, DJ-1, which is coded by a gene causative for autosomal recessive Parkinson's disease (PARK7; 2.6-fold) (Hijioka et al., 2017) and has an emerging role in regulation of immune responses (Zhang, et al., 2020); neurotrophic insulin-like growth factor 2 (IGF2; 6.2-fold); contactin associated protein 1 (Caspr-1; 3.9-fold), which reduces A β production (Fan, et al., 2013) and promotes release of prosurvival secreted amyloid precursor protein (APP) domain sAPP α (Tang, et al., 2020); calcium-dependent phospholipid-binding protein copine-3 (CPNE3; 1.9-fold); and D-3-phosphoglycerate dehydrogenase (PHGDH; 3.4-fold), an enzyme essential for the synthesis of l-serine (**Figures 2B, C**). Interestingly, brain levels of the PHGDH are decreased in AD brain samples, and extracellular PHGDH mRNA was recently proposed to be an early presymptomatic blood marker for Alzheimer's disease (Yan, et al., 2020). Several proteins with mostly unknown functions, including small VCP/p97-interacting protein (SVIP; 3.6-fold) and methyltransferase-like protein 7A (METTL7A; 2.3-fold), were also significantly more abundant in microglial EVs from the AD brain (**Figures 2B, C**).

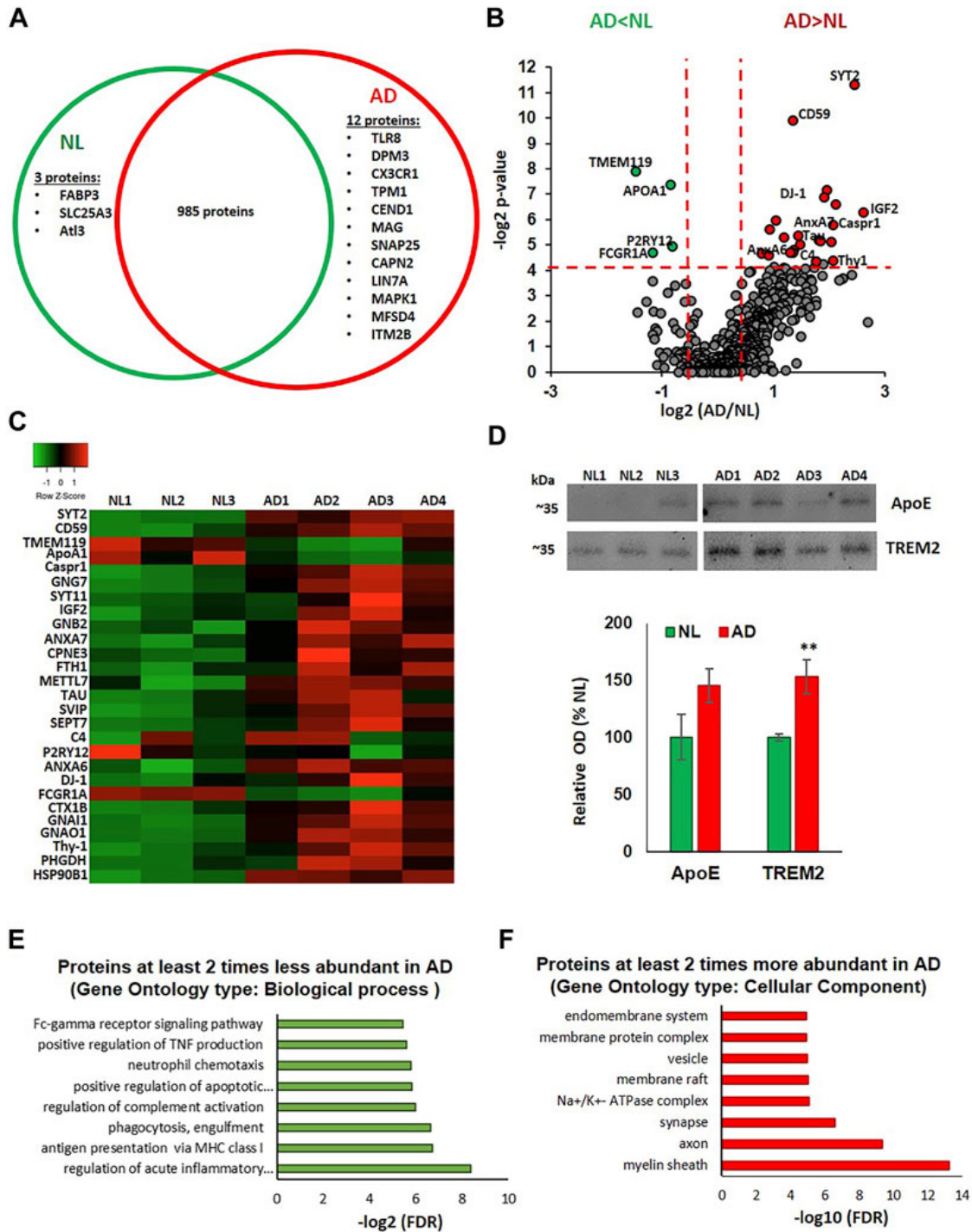


Figure 2. Proteomic analysis of microglial EVs from normal/low pathology and late-stage AD cases. (A) Venn diagram representing microglial proteins differentially detected in NL and AD groups. (B) Volcano plot showing a degree of differential expression of proteins in NL and AD groups. Vertical red dotted lines separate proteins, which are two or more times less abundant in

AD (far left segment) and two or more times more abundant in AD (far right segment). Horizontal red dotted line separates the top part of the plot containing dots representing proteins whose abundances are significantly different between NL and AD groups ($p < 0.05$) and the bottom part (no significant changes). Proteins that are significantly different between AD and NL groups are color-coded: two or more times more abundant in AD are presented in red, two or more times less abundant in green. (C) Heat map of proteins significantly up- and downregulated in AD compared to the NL group across seven evaluated human cases. (D) Immunoblotting of CD11b-IP samples with antibodies against ApoE and TREM2. Representative images are in the upper section and the composite data are in the lower section ($*p < 0.05$). (E) Gene ontology enrichment bioinformatic analysis of proteins two or more times less abundant in AD compared to NL. (F) Gene ontology enrichment bioinformatic analysis of proteins two or more times more abundant in AD compared to NL.

Notably, the abundance of ApoE, a Stage 1 DAM marker, was 1.4 times higher in microglial EVs from the AD brain when compared to NL, although this difference was not statistically significant. We subsequently confirmed this result using immunoblotting (**Figure 2D**), which also revealed an ~40% increase in ApoE levels in the AD group, validating the changes observed in the proteomics analysis. To our surprise, the mass spectrometric analysis did not detect the microglia marker TREM2. In contrast, TREM2 was detected in the same samples using immunoblotting, and average TREM2 levels were significantly higher in the AD group (**Figure 2D**). Interestingly, amyloid-beta precursor protein (APP) was detected in all samples with only one unique peptide (AA 578-589) that corresponds to a region of A β . The abundance of the APP/A β was 1.9 times

higher in the AD group when compared to NL, but this difference was not statistically significant (data not shown).

The proteomic data set was further analyzed using the STRING database for enrichment gene ontology (GO) and pathway analysis. Proteins exhibiting a decrease of twofold or greater in the AD group were enriched in several immune regulation pathways, including acute inflammatory response, antigen presentation, phagocytosis, complement regulation, TNF production, and Fc-gamma receptor signaling (**Figure 2E**). Proteins exhibiting an increase of twofold or greater in the AD group showed enrichment in the following cellular components: myelin sheath, synaptic, and endosomal vesicular related proteins (**Figure 2F**).

miRNA Profiling of Microglial EVs

We identified 105 miRNAs present in 5 or more of the analyzed human cases using the nCounter miRNA expression panel. Fold changes (AD/NL) and *p*-values corresponding to each identified miRNA were illustrated by a volcano plot, which revealed that levels of four miRNA—miR-28-5p, miR-381-3p, miR-651-5p, and miR-188-5p—were significantly higher in microglial EVs from AD cases when compared to NL cases (**Figure 3A**). Functional interpretation of these data was performed using miRNet (Fan, et al., 2016), which revealed SUMOylation, toll-like receptor (TLR), Fc epsilon receptor I (FCERI), and senescence pathways to be among those regulated by the four significantly increased miRNAs (**Figure 3B**).

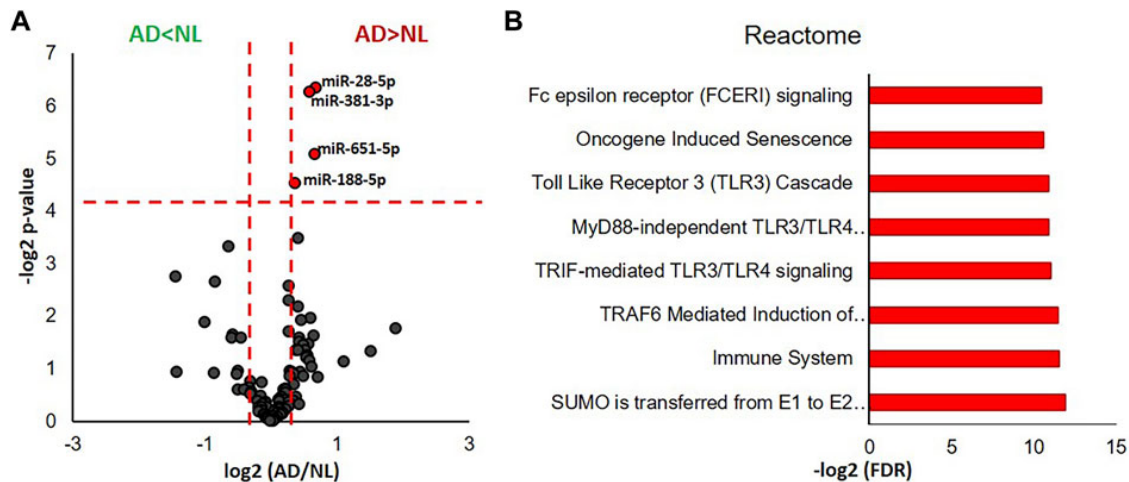


Figure 3. *miRNA transcriptomic analysis of microglial EVs from normal/low pathology and late-stage AD cases.* (A) Volcano plot showing a degree of differential expression of miRNAs in NL and AD groups. Vertical red dotted lines separate miRNA, which are 1.5 or more times less abundant in AD (far left segment) and 1.5 or more times more abundant in AD (far right segment). Horizontal red dotted line separates the top section of the plot containing dots representing proteins whose abundance is significantly different between NL and AD groups ($*p < 0.05$). MicroRNAs, which are significantly different between AD and NL groups, are color-coded: 1.5 or more times more abundant in AD are presented in red, 1.5 or more times less abundant are in green. (B) Gene ontology enrichment bioinformatic analysis of miRNAs significantly more abundant in AD compared to NL.

Lipidomics of Microglial EVs

Analysis across all lipid classes without regard to acyl chain composition indicated that only free cholesterol (FC) was increased in microglia-derived EVs from the AD brain (**Figure 4A**). Phospholipids showed acyl chain specific changes in mono- and polyunsaturated species. Microglia-derived EVs from the AD brain showed a significant deficit in phosphatidylethanolamine (PE) 38:0 and 38:1 (**Figure 4B**) and a concurrent loss of the PE

metabolites—lysoPE 2:4 and N-acyl phosphatidylethanolamine (NAPE) 16:0/18:0/20:4 (**Figures 4C, D**). Interestingly, differences in microglia-derived EVs from the AD brain were seen on phospholipids likely to harbor docosahexaenoic acid (22:6) in the sn-2 position. Specifically, microglia-derived EVs showed significant deficits in phosphatidic acid (PA) 40:6 (**Figure 4E**) and phosphatidylserine (PS) 40:6 (**Figure 4F**). A trend toward depletion of 40:6 was also detected in PE (PE 40:6) (Figure 4B) and PEp (PEp40:6) (data not shown). Specific lipid changes observed in microglial EVs included upregulation of the most abundant lipid species of BMP and monohexosylceramides (mhCer). The most abundant BMP species BMP 36:2 was enriched in EVs derived from the AD brain (**Figure 4G**). Finally, the most abundant mhCer, mhCer d18:1/24:1, was significantly upregulated in microglial-derived EVs from the AD brain (**Figure 4H**).

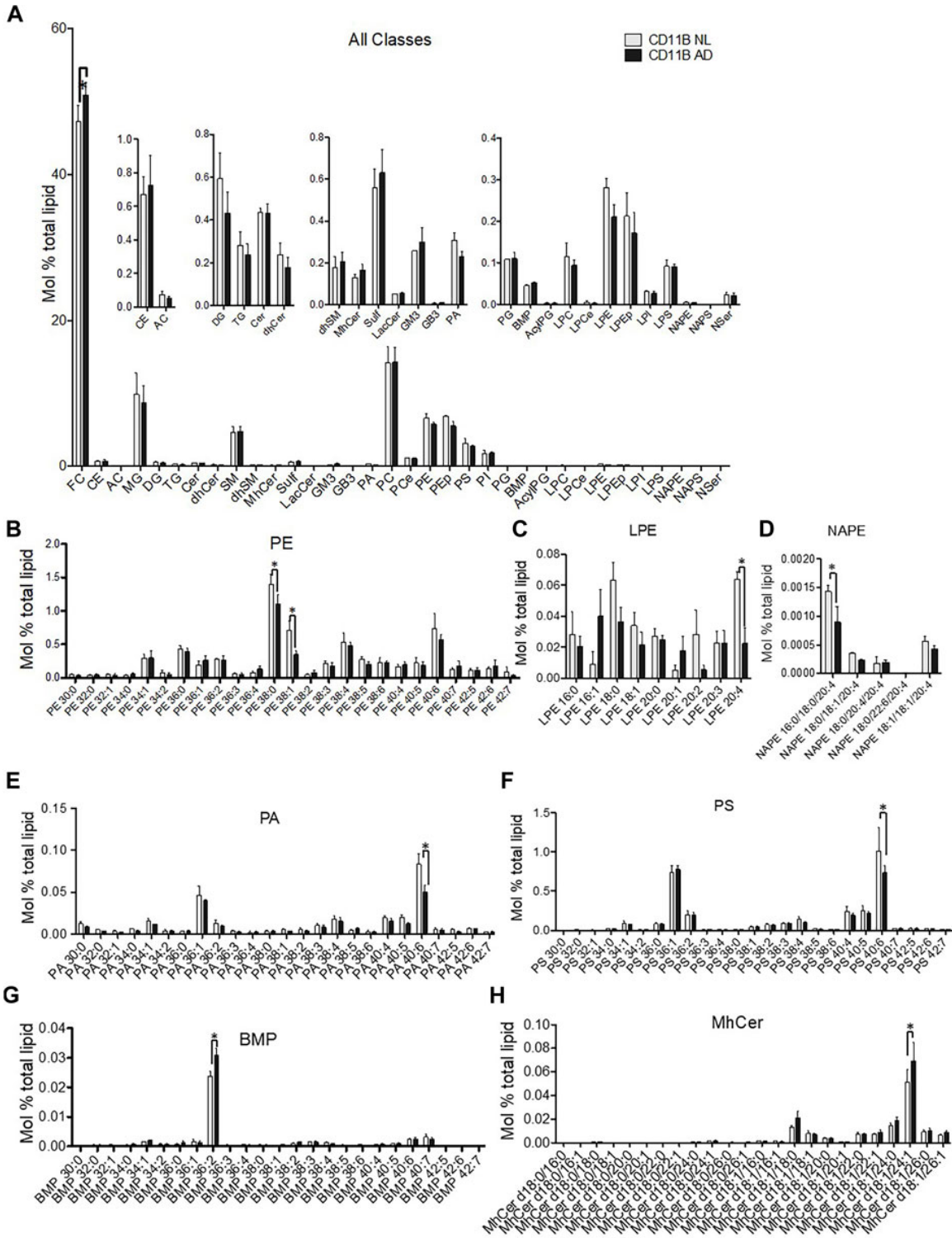


Figure 4. Lipidomic analysis of microglial EVs from normal/low pathology and late-stage AD cases. (A) Relative quantification 34 lipid classes and 593 individual lipid species in microglial EVs. Lipids are quantified as mol% total lipid by normalizing the molar amount of each lipid

species to the summed total moles of all lipid species in each sample. The inset panels show lower abundance species on the expanded y-axis. Abbreviations are free cholesterol (FC), cholesteryl ester (CE), acyl carnitine (AC), monoacylglycerol (MG), diacylglycerol (DG), triacylglycerol (TG), ceramide (Cer), sphingomyelin (SM), monohexosylceramide (MhCer), sulfatides (Sulf), lactosylceramide (LacCer), monosialodihexosylganglioside (GM3), globotriaosylceramide (GB3), phosphatidic acid (PA), phosphatidylcholine (PC), ether phosphatidylcholine (PCe), phosphatidylethanolamine (PE), plasmalogen phosphatidylethanolamine (Pep), phosphatidylserine (PS), phosphatidylinositol (PI), phosphatidylglycerol (PG), bis(monoacylglycerol)phosphate (BMP), acyl phosphatidylglycerol (AcylPG), lysophosphatidylcholine (LPC), ether lysophosphatidylcholine (LPCe), lysophosphatidylethanolamine (LPE), plasmalogen lysophosphatidylethanolamine (LPEp), lysophosphatidylinositol (LPI), lysophosphatidylserine (LPS), N-Acyl phosphatidylethanolamine (NAPE), N-acyl phosphatidylserine (NAPS), and N-acyl serine (NSer). Data are presented as mean mol% with error bars showing mean \pm S.E. FC is significantly increased shown in the primary panel ($p < 0.01$). (B) PE species were detected using mass spectrometry and are shown using relative quantification as mol%. PE 38:0 ($p < 0.05$); PE 38:1 ($p < 0.01$). (C) Most abundant LPE [LPE20:4 ($p < 0.05$)] and (D) NAPE [NAPE 16:0/18:0/20:4 ($p < 0.05$)] lipid species are shown to significantly differ between LN- and AD-derived microglia EV. (E) PA40:6 lipid species is decreased in microglia-derived EV from the AD brain (AD) compared to control (LN) ($p < 0.0001$), while no other PA species are significantly affected. (F) The most abundant PS species, PS40:6 species, is decreased in EV derived from the AD brain (AD) compared to control (LN) ($p < 0.001$) while no other PS species are significantly altered. (G) The most abundant BMP 36:2 ($p <$

0.0001) and (H) MhCer d18:1/24:1 ($p < 0.01$) lipid species are increased in AD-derived microglia EV. All data are presented as mean mol% with error bars showing mean \pm S.E.

Discussion

We evaluated the changes across the proteome, lipidome, and miRNA transcriptome of small EVs of microglial origin (positive for myeloid cell marker, CD11B) isolated from the human parietal cortex of three normal/low pathology (NL) and four late-stage AD cases (**Table 2**). We found a significant decrease in the abundance of known homeostatic microglial markers, P2RY12 and TMEM119, and a corresponding increase in DAM markers, FTH1 (Stage 1 DAM) and TREM2 (Stages 1 and 2 DAM), in microglial EVs from the AD brain when compared to NL. However, a homeostatic microglia marker, Cx3CR1, was detected in AD, but not in the NL group, and a classical Stage 1 DAM marker, ApoE, was only marginally increased in AD (**Figures 2A–D**). Overall, these changes better recapitulate the overall brain cell transcriptional signatures of DAM from mouse AD models (Deczkowska, et al., 2018), which were not reproduced in a recent human RNAseq study (Srinivasan, et al., 2020). A possible explanation for the discrepancy can be disproportional enrichment of DAM-derived EVs in the microglial secretome from the AD tissue. The burdens of cortical dense-core plaques in AD mouse models (Tg2576, APP_{Swe}PS1 Δ E9, and 5XFAD) greatly exceed the cortical plaque burdens in human AD cases (P. Liu, et al., 2017). As a result, the proportion of DAM cells surrounding dense-core plaques (Keren-Shaul, et al., 2017) may be higher in the mouse models when compared with the human disease, and a DAM-specific transcriptomic signature may be easier to detect. It has been recently demonstrated that small EV secretion is highly upregulated in mouse DAM cells (Clayton, et al., 2021). Moreover, mouse and human DAM display a transcriptional signature characteristic of senescent cells (Hu, et al., 2021),

which are known to secrete vast numbers of EVs as a part of the senescence-associated secretory phenotype (SASP). In agreement with this, our miRNA transcriptome data revealed senescence as one of the top pathways controlled by four miRNAs identified to be significantly upregulated in AD microglial EVs (**Figure 3B**). Thus, it is possible that analysis of human microglial EVs may more specifically address changes in the A β -plaque-associated DAM population when compared to cell RNAseq analysis.

Microglial EVs either contain low levels of tau protein or a composition of tau species that cannot be easily detected by immunoblotting analysis. Yet, tau was detected in all samples by mass spectrometry, and tau abundance was significantly higher in AD when compared to NL samples (**Figures 2B, C**). These data confirmed a potential role of microglia-derived EVs in the spread of tau pathology in the human AD brain, as it was previously described *in vitro* and in mouse tauopathy and AD models (Asai, et al., 2015; Clayton, et al., 2021; Maphis, et al., 2015). The specific microglial EV-associated tau species and their proteopathic seeding potential still need to be defined.

In addition to the increase in abundance of tau protein in AD brain-derived microglial EVs, we found that levels of neuron-specific and synapse-enriched proteins were either exclusively detected (CEND1 and SNAP25) or significantly upregulated (SYT-1, SYT-11, STX1B, and Thy1) in the AD group (**Figures 2A, B**). Myelin-specific protein MAG was only found in microglial EVs from AD, but not in NL samples (**Figure 2A**). Moreover, myelin sheath was the cellular component most enriched in proteins that were increased twofold or greater in the AD group (**Figure 2F**). Increases in synaptic protein VGlut1 in microglial cells from the 5xFAD mouse model and in

TDP43-depleted microglia with a hyperphagocytic phenotype have been described (Brioschi, et al., 2020), so it is likely that synaptic and myelin-specific proteins have been phagocytosed prior to entering microglial exosomes. In this regard, elevated levels of complement protein, C4, in microglial EVs from AD cases (**Figure 2B**) may suggest that the process of complement-dependent engulfment of synapses by microglia may be involved (Thion and Garel, 2018; Yilmaz, et al., 2021). On the other hand, C4-coated EVs may play a role as scavengers and thus may protect cells from complement attack (Karasu et al., 2018). Interestingly, we also observed an increase in membrane attack complex (MAC)-inhibitory protein, CD59, which is known to negatively regulate complement-mediated phagocytosis (Schartz and Tenner, 2020; Tenner, 2020).

Our lipidomic analysis revealed an increase in cholesterol in AD microglial EVs (**Figure 4A**), which is consistent with the phagocytosis of neuronal debris by microglial cells. Cholesterol metabolism has also been associated with immune activation (Deczkowska, et al., 2018; Orre, et al., 2014; Simon, 2014; Spann and Glass, 2013; Wong, et al., 2020). A recent study reported cholesteryl ester accumulation in TREM2-deficient microglia that fails to mount an immune response (Nugent, et al., 2020). However, we did not find significant changes in CE species levels in microglia-derived EVs in the AD cases reported here.

We also found a significant increase in the major bis(monoacylglycerol)phosphate (BMP) and monohexosylceramide (MhCer) lipid species (**Figures 4G,H**). An increase of this species of BMP, a lysosome-specific lipid, suggests increased lysosomal lipid content in AD microglia (Showalter, et al., 2020). Elevated levels of MhCer may play a role in microglial activation and immune response (Brennan, et al., 2017; Miltenberger-Miltenyi, et al., 2020; Niimura et al., 2010), as well

as be a precursor of more complex gangliosides (Merrill, 2011). Interestingly, enrichment of BMP and MhCer in EVs has been previously linked to the impairment of endolysosomal function induced by Vsp34 kinase inhibition, which causes phosphatidylinositol-3-phosphate (PI3P) deficiency (Miranda, et al., 2018). Thus, endolysosomal impairment can explain the elevated levels of neuronal and myelin molecules in microglial EVs from the AD brain and potentially lead to the disruption of microglial pathways as suggested by the bioinformatic analysis in **Figure 2E**.

We observed that a reduction in phospholipids is likely to harbor docosahexaenoic acid (DHA, 22:6) in the sn-2 position in microglial EVs from the AD brain. One likely acyl chain configuration for PS40:6 and PA40:6 is sn-1 18:0, sn-2 22:6. These data echo the previously described DHA decrease in the bulk preparations of human AD brain EVs and global AD-related brain DHA deficiency, which has a proinflammatory effect and may also disrupt A β clearance (H. Su, et al., 2021). The selective loss of DHA among PA and PS (**Figures 4E, F**) as well as the trend in PE (Figure 2B) suggests the overactivation of DHA-selective phospholipase A 2 (PLA2) and a deficit in acyl chain remodeling (Abdullah, et al., 2017; Calon, et al., 2004; Fernandez, et al., 2018; Fernandez, et al., 2021; Fonteh, et al., 2013; Granger, et al., 2019).

The loss of LPE20:4 in EVs derived from AD microglia (**Figure 4C**) may represent exhaustion of acyl chain remodeling of PE. Since 20:4 is cleaved from PE20:4 to liberate the free fatty acid, arachidonate, it may represent loss of this proinflammatory fatty acid due to overactivation of PLA2, which has previously been reported in AD (Sanchez-Mejia, et al., 2008; Wang, et al., 2021). Interestingly, NAPE is an important precursor to endocannabinoid synthesis, which is dysregulated in AD (Bisogno and Di Marzo, 2008; Fonteh, et al., 2013; Liu, et al., 2006). Even though previous

studies have reported global loss of PE and plasmalogen, our analyses show only a trend for PE depletion and no loss in plasmalogen from AD brain microglia-derived EVs (Han et al., 2001; Han et al., 2002).

We did not find AD-associated changes in key modulators of immune responses—miR-146a-5p, miR-155-5p, and miR-124-3p (Su et al., 2016); miR-124-3p was not detected in our samples, while miR-146a-5p and miR-155-5p levels were above background but did not show any significant differences between NL and AD groups (data not shown). Two out of four miRNAs upregulated in the AD group, miR-188-5p and miR-381-3p (**Figure 3A**), are known to have neuroprotective effects. MiR-188-5p restores synaptic and cognitive deficits in 5xFAD mice (Lee, et al., 2016), and miR-381-3p promotes the recovery of spinal cord injury in rats (Chen et al., 2018). In addition to a neuroprotective miRNA signature, proteomics revealed increases in the abundance of IGF2, ITM2B and CASPR-1, and DJ-1 in microglial EVs from AD cases (**Figures 2A–B**). Neurotrophic factor IGF2 was shown to reduce A β amyloidosis, reverse synaptic deficits, and improve memory in AD animal models (Mellott et al., 2014; Pascual-Lucas, et al., 2014). ITM2B and CASPR-1 are known to regulate APP metabolism and suppress A β production (Fan, et al., 2013; Matsuda, et al., 2008; Tang, et al., 2020), and DJ-1 is an important antioxidant with newly discovered immune regulation functions (Zhang, et al., 2020). The presence of both neuroprotective and pathology-related miRNA and proteins in AD cases, a seemingly contradictory result, may represent both a consequence of, and a response to, disease pathogenesis. It is interesting to surmise that the response and consequence may be present as the cargo in different EV subpopulations, either derived from the same cells or from microglia at different stages of activation. Further evaluation of EV subpopulations and the molecular mechanisms dictating their release may provide a new

avenue for AD therapeutic development with the aim to suppress subpopulations containing pathogenic cargo, while promoting the release of neuroprotective EVs.

In conclusion, our data suggest that loss of a homeostatic signature and the deterioration of functional microglia in late AD stages may accompany endolysosomal impairment and the release of undigested neuronal and myelin debris, including tau, through extracellular vesicles. We also found a significant AD-associated decrease in levels of DHA-containing polyunsaturated lipids of different classes, which may be associated with global DHA deficiency in AD and indicate a potential defect in the acyl-chain remodeling by PLA2 and lysophospholipid acyltransferases. On the other hand, the AD-specific microglial EV signature also includes increases in some miRNAs and proteins with neuroprotective properties. It is currently unknown if those “harmful” vs. “protective” molecular signatures represent different subpopulations of microglial EVs. Results from our study support the hypothesis that the molecular composition of EVs reflects functional changes in microglia consistent with a diseased state. To the best of our knowledge, this is the first study analyzing proteins, lipids, and miRNAs in cell-type specific EVs from human brain tissue. The main limitation of the study is the small number of cases, and our results require further validation in larger cohorts, and when possible inclusion of samples from earlier disease stages. Despite these limitations, this proof-of-concept study clearly demonstrates the feasibility of using multiple omics analyses on small microglial EVs isolated from cryopreserved human brain tissue. Our results exemplify the superiority of an integrative approach when compared to individual proteomics, lipidomics, or microRNA analyses, and suggest that new AD biomarkers may arise from all three different classes of biomolecules.

Data Availability Statement

The datasets presented in this study can be found in online repositories. The names of the repository/repositories and accession number(s) can be found below: PRIDE, accession no: PXD028898.

Author Contributions

LM, VJ, KG, and TB participated in the research design. WC, MM, CH, LM, BT, SC, CZ, and TB conducted experiments. WC, MM, LM, and TB performed data analysis. WC, MM, BT, LM, SC, VJ, KG, and TB wrote or contributed to the writing of the manuscript.

Funding

The work was supported by the following grants: NIH AG063767 to TB and KG, NIH AG051386 and AFOSR FA9550-17-1-0399 to VJ, and NIH R56 High Priority, Short-Term Project Award, NIH 1R56AG062271-01A1 and Department of Defense, W81XWH-19-1-0817, GRANT12727289 for LM.

Conflict of Interest

The authors declare that the research was conducted in the absence of any commercial or financial relationships that could be construed as a potential conflict of interest.

Publisher's Note

All claims expressed in this article are solely those of the authors and do not necessarily represent those of their affiliated organizations, or those of the publisher, the editors and the reviewers. Any

product that may be evaluated in this article, or claim that may be made by its manufacturer, is not guaranteed or endorsed by the publisher.

Acknowledgments

We thank the AD Research Center Neuropathology Cores of USC, UCLA, and UC Irvine for human autopsy brain samples and neuropathology reports. We also would like to acknowledge the Brain Research Institute electron microscopy core facility, the UCLA-DOE Biochemistry core facility, and the UCLA Center for Systems Biomedicine. We would also like to acknowledge Kym Francis Faull and Julian Whitelegge from the UCLA Pasarow Mass Spectrometry Laboratory for the use of their instrumentation and their contributions in editing the manuscript.

References

1. 2021 Alzheimer's disease facts and figures, 2021 2021 Alzheimer's disease facts and figures (2021). *Alzheimers Dement* 17, 327–406. doi:10.1002/alz.12328
2. Abdullah, L., Evans, J. E., Emmerich, T., Crynen, G., Shackleton, B., Keegan, A. P., et al. (2017). APOE ϵ 4 Specific Imbalance of Arachidonic Acid and Docosahexaenoic Acid in Serum Phospholipids Identifies Individuals with Preclinical Mild Cognitive Impairment/Alzheimer's Disease. *Aging (Albany NY)* 9, 964–985. doi:10.18632/aging.101203
3. An, K., Klyubin, I., Kim, Y., Jung, J. H., Mably, A. J., O'Dowd, S. T., et al. (2013). Exosomes Neutralize Synaptic-Plasticity-Disrupting Activity of A β Assemblies *In Vivo*. *Mol. Brain* 6, 47. doi:10.1186/1756-6606-6-47
4. Asai, H., Ikezu, S., Tsunoda, S., Medalla, M., Luebke, J., Haydar, T., et al. (2015). Depletion of Microglia and Inhibition of Exosome Synthesis Halt Tau Propagation. *Nat. Neurosci.* 18, 1584–1593. doi:10.1038/nn.4132
5. Bilousova, T., Elias, C., Miyoshi, E., Alam, M. P., Zhu, C., Campagna, J., et al. (2018). Suppression of Tau Propagation Using an Inhibitor that Targets the DK-Switch of nSMase2. *Biochem. Biophys. Res. Commun.* 499, 751–757. doi:10.1016/j.bbrc.2018.03.209
6. Bilousova, T., Simmons, B. J., Knapp, R. R., Elias, C. J., Campagna, J., Melnik, M., et al. (2020). Dual Neutral Sphingomyelinase-2/Acetylcholinesterase Inhibitors for the Treatment of Alzheimer's Disease. *ACS Chem. Biol.* 15, 1671. doi:10.1021/acscchembio.0c00311

7. Binder, R. J. (2014). Functions of Heat Shock Proteins in Pathways of the Innate and Adaptive Immune System. *J. Immunol.* 193, 5765–5771. doi:10.4049/jimmunol.1401417
8. Bisogno, T., and Di Marzo, V. (2008). The Role of the Endocannabinoid System in Alzheimer's Disease: Facts and Hypotheses. *Curr. Pharm. Des.* 14, 2299–3305. doi:10.2174/138161208785740027
9. Bligh, E. G., and Dyer, W. J. (1959). A Rapid Method of Total Lipid Extraction and Purification. *Can. J. Biochem. Physiol.* 37, 911–917. doi:10.1139/o59-099
10. Bosch, S., de Beaufort, L., Allard, M., Mosser, M., Heichette, C., Chrétien, D., et al. (2016). Trehalose Prevents Aggregation of Exosomes and Cryodamage. *Sci. Rep.* 6, 36162. doi:10.1038/srep36162
11. Brennan, P. J., Cheng, T. Y., Pellicci, D. G., Watts, G. F. M., Veerapen, N., Young, D. C., et al. (2017). Structural Determination of Lipid Antigens Captured at the CD1d-T-Cell Receptor Interface. *Proc. Natl. Acad. Sci. U S A.* 114, 8348–8353. doi:10.1073/pnas.1705882114
12. Brioschi, S., d'Errico, P., Amann, L. S., Janova, H., Wojcik, S. M., Meyer-Luehmann, M., et al. (2020). Detection of Synaptic Proteins in Microglia by Flow Cytometry. *Front. Mol. Neurosci.* 13, 149. doi:10.3389/fnmol.2020.00149
13. Brumbaugh, C. D., Kim, H. J., Giovacchini, M., and Pourmand, N. (2011). NanoStriDE: Normalization and Differential Expression Analysis of NanoString nCounter Data. *BMC Bioinformatics.* 12, 479. doi:10.1186/1471-2105-12-479
14. Butovsky, O., and Weiner, H. L. (2018). Microglial Signatures and Their Role in Health and Disease. *Nat. Rev. Neurosci.* 19, 622–635. doi:10.1038/s41583-018-0057-5

15. Calon, F., Lim, G. P., Yang, F., Morihara, T., Teter, B., Ubeda, O., et al. (2004). Docosahexaenoic Acid Protects from Dendritic Pathology in an Alzheimer's Disease Mouse Model. *Neuron* 43, 633–645. doi:10.1016/j.neuron.2004.08.013
16. Chan, R. B., Oliveira, T. G., Cortes, E. P., Honig, L. S., Duff, K. E., Small, S. A., et al. (2012). Comparative Lipidomic Analysis of Mouse and Human Brain with Alzheimer Disease. *J. Biol. Chem.* 287, 2678–2688. doi:10.1074/jbc.M111.274142
17. Chen, W. C., Luo, J., Cao, X. Q., Cheng, X. G., and He, D. W. (2018). Overexpression of miR-381-3p Promotes the Recovery of Spinal Cord Injury. *Eur. Rev. Med. Pharmacol. Sci.* 22, 5429–5437. doi:10.26355/eurrev_201809_15802
18. Cheng, L., Vella, L. J., Barnham, K. J., McLean, C., Masters, C. L., and Hill, A. F. (2020). Small RNA Fingerprinting of Alzheimer's Disease Frontal Cortex Extracellular Vesicles and Their Comparison with Peripheral Extracellular Vesicles. *J. Extracell Vesicles* 9, 1766822. doi:10.1080/20013078.2020.1766822
19. Clayton, K., Delpech, J. C., Herron, S., Iwahara, N., Ericsson, M., Saito, T., et al. (2021). Plaque Associated Microglia Hyper-Secrete Extracellular Vesicles and Accelerate Tau Propagation in a Humanized APP Mouse Model. *Mol. Neurodegener* 16, 18. doi:10.1186/s13024-021-00440-9
20. Crotti, A., Sait, H. R., McAvoy, K. M., Estrada, K., Ergun, A., Szak, S., et al. (2019). BIN1 Favors the Spreading of Tau via Extracellular Vesicles. *Sci. Rep.* 9, 9477. doi:10.1038/s41598-019-45676-0
21. D'Anca, M., Fenoglio, C., Serpente, M., Arosio, B., Cesari, M., Scarpini, E. A., et al. (2019). Exosome Determinants of Physiological Aging and Age-Related

- Neurodegenerative Diseases. *Front. Aging Neurosci.* 11, 232. doi:10.3389/fnagi.2019.00232
22. Deczkowska, A., Keren-Shaul, H., Weiner, A., Colonna, M., Schwartz, M., and Amit, I. (2018). Disease-Associated Microglia: A Universal Immune Sensor of Neurodegeneration. *Cell* 173, 1073–1081. doi:10.1016/j.cell.2018.05.003
23. Del-Aguila, J. L., Li, Z., Dube, U., Mihindikulasuriya, K. A., Budde, J. P., Fernandez, M. V., et al. (2019). A Single-Nuclei RNA Sequencing Study of Mendelian and Sporadic AD in the Human Brain. *Alzheimers Res. Ther.* 11, 71. doi:10.1186/s13195-019-0524-x
24. Dinkins, M. B., Dasgupta, S., Wang, G., Zhu, G., and Bieberich, E. (2014). Exosome Reduction *In Vivo* Is Associated with Lower Amyloid Plaque Load in the 5XFAD Mouse Model of Alzheimer's Disease. *Neurobiol. Aging* 35, 1792–1800. doi:10.1016/j.neurobiolaging.2014.02.012
25. Dodd, P. R., Hardy, J. A., Baig, E. B., Kidd, A. M., Bird, E. D., Watson, W. E., et al. (1986). Optimization of Freezing, Storage, and Thawing Conditions for the Preparation of Metabolically Active Synaptosomes from Frozen Rat and Human Brain. *Neurochem. Pathol.* 4, 177–198. doi:10.1007/BF02834357
26. Fan, L. F., Xu, D. E., Wang, W. H., Yan, K., Wu, H., Yao, X. Q., et al. (2013). Caspr Interaction with Amyloid Precursor Protein Reduces Amyloid- β Generation *In Vitro*. *Neurosci. Lett.* 548, 255–260. doi:10.1016/j.neulet.2013.05.055
27. Fan, Y., Siklenka, K., Arora, S. K., Ribeiro, P., Kimmins, S., and Xia, J. (2016). miRNet - Sissecting miRNA-Target Interactions and Functional Associations Through Network-Based Visual Analysis. *Nucleic Acids Res.* 44, W135–W141. doi:10.1093/nar/gkw288

28. Fernandez, R. F., Kim, S. Q., Zhao, Y., Foguth, R. M., Weera, M. M., Counihan, J. L., et al. (2018). Acyl-CoA Synthetase 6 Enriches the Neuroprotective omega-3 Fatty Acid DHA in the Brain. *Proc. Natl. Acad. Sci. U S A.* 115, 12525–12530. doi:10.1073/pnas.1807958115
29. Fernandez, R. F., Pereyra, A. S., Diaz, V., Wilson, E. S., Litwa, K. A., Martínez-Gardeazabal, J., et al. (2021). Acyl-CoA Synthetase 6 Is Required for Brain Docosahexaenoic Acid Retention and Neuroprotection during Aging. *JCI Insight* 6. doi:10.1172/jci.insight.144351
30. Fiandaca, M. S., Kapogiannis, D., Mapstone, M., Boxer, A., Eitan, E., Schwartz, J. B., et al. (2015). Identification of Preclinical Alzheimer's Disease by a Profile of Pathogenic Proteins in Neurally Derived Blood Exosomes: A Case-Control Study. *Alzheimers Dement* 11, 600–e1. doi:10.1016/j.jalz.2014.06.008
31. Fonteh, A. N., Chiang, J., Cipolla, M., Hale, J., Diallo, F., Chirino, A., et al. (2013). Alterations in Cerebrospinal Fluid Glycerophospholipids and Phospholipase A2 Activity in Alzheimer's Disease. *J. Lipid Res.* 54, 2884–2897. doi:10.1194/jlr.M037622
32. Goetzl, E. J., Goetzl, L., Karliner, J. S., Tang, N., and Pulliam, L. (2016). Human Plasma Platelet-Derived Exosomes: Effects of Aspirin. *FASEB J.* 30, 2058–2063. doi:10.1096/fj.201500150R
33. Goetzl, E. J., Mustapic, M., Kapogiannis, D., Eitan, E., Lobach, I. V., Goetzl, L., et al. (2016). Cargo Proteins of Plasma Astrocyte-Derived Exosomes in Alzheimer's Disease. *FASEB J.* 30, 3853–3859. doi:10.1096/fj.201600756R

34. Goetzl, E. J., Schwartz, J. B., Abner, E. L., Jicha, G. A., and Kapogiannis, D. (2018). High Complement Levels in Astrocyte-Derived Exosomes of Alzheimer Disease. *Ann. Neurol.* 83, 544–552. doi:10.1002/ana.25172
35. Granger, M. W., Liu, H., Fowler, C. F., Blanchard, A. P., Taylor, M. W., Sherman, S. P. M., et al. (2019). Distinct Disruptions in Land's Cycle Remodeling of Glycerophosphocholines in Murine Cortex Mark Symptomatic Onset and Progression in Two Alzheimer's Disease Mouse Models. *J. Neurochem.* 149, 499–517. doi:10.1111/jnc.14560
36. Guan, Z., Li, S., Smith, D. C., Shaw, W. A., and Raetz, C. R. (2007). Identification of N-Acylphosphatidylserine Molecules in Eukaryotic Cells. *Biochemistry* 46, 14500–14513. doi:10.1021/bi701907g
37. Gylys, K. H., and Bilousova, T. (2017). Flow Cytometry Analysis and Quantitative Characterization of Tau in Synaptosomes from Alzheimer's Disease Brains. *Methods Mol. Biol.* 1523, 273–284. doi:10.1007/978-1-4939-6598-4_16
38. Han, X., Holtzman, D. M., and McKeel, D. W. (2001). Plasmalogen Deficiency in Early Alzheimer's Disease Subjects and in Animal Models: Molecular Characterization Using Electrospray Ionization Mass Spectrometry. *J. Neurochem.* 77, 1168–1180. doi:10.1046/j.1471-4159.2001.00332.x
39. Han, X., M Holtzman, D., McKeel, D. W., Kelley, J., and Morris, J. C. (2002). Substantial Sulfatide Deficiency and Ceramide Elevation in Very Early Alzheimer's Disease: Potential Role in Disease Pathogenesis. *J. Neurochem.* 82, 809–818. doi:10.1046/j.1471-4159.2002.00997.x

40. Heinzelman, P., Bilousova, T., Campagna, J., and John, V. (2016). Nanoscale Extracellular Vesicle Analysis in Alzheimer's Disease Diagnosis and Therapy. *Int. J. Alzheimers Dis.* 2016, 8053139. doi:10.1155/2016/8053139
41. Hijioka, M., Inden, M., Yanagisawa, D., and Kitamura, Y. (2017). DJ-1/PARK7: A New Therapeutic Target for Neurodegenerative Disorders. *Biol. Pharm. Bull.* 40, 548–552. doi:10.1248/bpb.b16-01006
42. Hornung, S., Dutta, S., and Bitan, G. (2020). CNS-derived Blood Exosomes as a Promising Source of Biomarkers: Opportunities and Challenges. *Front. Mol. Neurosci.* 13, 38. doi:10.3389/fnmol.2020.00038
43. Hsu, F. F., Turk, J., Shi, Y., and Groisman, E. A. (2004). Characterization of Acylphosphatidylglycerols from *Salmonella typhimurium* by Tandem Mass Spectrometry with Electrospray Ionization. *J. Am. Soc. Mass. Spectrom.* 15, 1–11. doi:10.1016/j.jasms.2003.08.006
44. Hu, Y., Fryatt, G. L., Ghorbani, M., Obst, J., Menassa, D. A., Martin-Estebane, M., et al. (2021). Replicative Senescence Dictates the Emergence of Disease-Associated Microglia and Contributes to A β Pathology. *Cell Rep* 35, 109228. doi:10.1016/j.celrep.2021.109228
45. Huang, Y., Cheng, L., Turchinovich, A., Mahairaki, V., Troncoso, J. C., Pletniková, O., et al. (2020). Influence of Species and Processing Parameters on Recovery and Content of Brain Tissue-Derived Extracellular Vesicles. *J. Extracell Vesicles* 9, 1785746. doi:10.1080/20013078.2020.1785746
46. Hussain, R. Z., Miller-Little, W. A., Doelger, R., Cutter, G. R., Loof, N., Cravens, P. D., et al. (2018). Defining Standard Enzymatic Dissociation Methods for Individual Brains and

- Spinal Cords in EAE. *Neurol. Neuroimmunol Neuroinflamm* 5, e437. doi:10.1212/NXI.0000000000000437
47. Joshi, P., Turola, E., Ruiz, A., Bergami, A., Libera, D. D., Benussi, L., et al. (2014). Microglia Convert Aggregated Amyloid- β into Neurotoxic Forms through the Shedding of Microvesicles. *Cell Death Differ* 21, 582–593. doi:10.1038/cdd.2013.180
48. Karasu, E., Eisenhardt, S. U., Harant, J., and Huber-Lang, M. (2018). Extracellular Vesicles: Packages Sent With Complement. *Front Immunol* 9, 721. doi:10.3389/fimmu.2018.00721
49. Keren-Shaul, H., Spinrad, A., Weiner, A., Matcovitch-Natan, O., Dvir-Szternfeld, R., Ulland, T. K., et al. (2017). A Unique Microglia Type Associated with Restricting Development of Alzheimer's Disease. *Cell* 169, 1276–e17. doi:10.1016/j.cell.2017.05.018
50. Kokubo, H., Saido, T. C., Iwata, N., Helms, J. B., Shinohara, R., and Yamaguchi, H. (2005). Part of Membrane-Bound Abeta Exists in Rafts within Senile Plaques in Tg2576 Mouse Brain. *Neurobiol. Aging* 26, 409–418. doi:10.1016/j.neurobiolaging.2004.04.008
51. Lee, K., Kim, H., An, K., Kwon, O. B., Park, S., Cha, J. H., et al. (2016). Replenishment of microRNA-188-5p Restores the Synaptic and Cognitive Deficits in 5XFAD Mouse Model of Alzheimer's Disease. *Sci. Rep.* 6, 34433. doi:10.1038/srep34433
52. Liu, J., Wang, L., Harvey-White, J., Osei-Hyiaman, D., Razdan, R., Gong, Q., et al. (2006). A Biosynthetic Pathway for Anandamide. *Proc. Natl. Acad. Sci. U S A.* 103, 13345–13350. doi:10.1073/pnas.0601832103
53. Liu, P., Reichl, J. H., Rao, E. R., McNellis, B. M., Huang, E. S., Hemmy, L. S., et al. (2017). Quantitative Comparison of Dense-Core Amyloid Plaque Accumulation in Amyloid- β

- Protein Precursor Transgenic Mice. *J. Alzheimers Dis.* 56, 743–761. doi:10.3233/JAD-161027
54. Lizarbe, M. A., Barrasa, J. I., Olmo, N., Gavilanes, F., and Turnay, J. (2013). Annexin-phospholipid Interactions. Functional Implications. *Int. J. Mol. Sci.* 14, 2652–2683. doi:10.3390/ijms14022652
55. Mahaman, Y. A. R., Huang, F., Kessete Afewerky, H., Maibouge, T. M. S., Ghose, B., and Wang, X. (2019). Involvement of Calpain in the Neuropathogenesis of Alzheimer's Disease. *Med. Res. Rev.* 39, 608–630. doi:10.1002/med.21534
56. Maphis, N., Xu, G., Kokiko-Cochran, O. N., Jiang, S., Cardona, A., Ransohoff, R. M., et al. (2015). Reactive Microglia Drive Tau Pathology and Contribute to the Spreading of Pathological Tau in the Brain. *Brain* 138, 1738–1755. doi:10.1093/brain/awv081
57. Mathys, H., Davila-Velderrain, J., Peng, Z., Gao, F., Mohammadi, S., Young, J. Z., et al. (2019). Single-cell Transcriptomic Analysis of Alzheimer's Disease. *Nature* 570, 332–337. doi:10.1038/s41586-019-1195-2
58. Matsuda, S., Giliberto, L., Matsuda, Y., McGowan, E. M., and D'Adamio, L. (2008). BRI2 Inhibits Amyloid Beta-Peptide Precursor Protein Processing by Interfering with the Docking of Secretases to the Substrate. *J. Neurosci.* 28, 8668–8676. doi:10.1523/JNEUROSCI.2094-08.2008
59. Mehta, D., Jackson, R., Paul, G., Shi, J., and Sabbagh, M. (2017). Why Do Trials for Alzheimer's Disease Drugs Keep Failing? A Discontinued Drug Perspective for 2010–2015. *Expert Opin. Investig. Drugs* 26, 735–739. doi:10.1080/13543784.2017.1323868
60. Mellott, T. J., Pender, S. M., Burke, R. M., Langley, E. A., and Blusztajn, J. K. (2014). IGF2 Ameliorates Amyloidosis, Increases Cholinergic Marker Expression and Raises

- BMP9 and Neurotrophin Levels in the hippocampus of the APP^{swe}PS1^{dE9} Alzheimer's Disease Model Mice. *PLoS One* 9, e94287. doi:10.1371/journal.pone.0094287
61. Merrill, A. H. (2011). Sphingolipid and Glycosphingolipid Metabolic Pathways in the Era of Sphingolipidomics. *Chem. Rev.* 111, 6387–6422. doi:10.1021/cr2002917
62. Miltenberger-Miltenyi, G., Cruz-Machado, A. R., Saville, J., Conceição, V. A., Calado, Â., Lopes, I., et al. (2020). Increased Monohexosylceramide Levels in the Serum of Established Rheumatoid Arthritis Patients. *Rheumatology (Oxford)* 59, 2085–2089. doi:10.1093/rheumatology/kez545
63. Miranda, A. M., Lasiecka, Z. M., Xu, Y., Neufeld, J., Shahriar, S., Simoes, S., et al. (2018). Neuronal Lysosomal Dysfunction Releases Exosomes Harboring APP C-Terminal Fragments and Unique Lipid Signatures. *Nat. Commun.* 9, 291. doi:10.1038/s41467-017-02533-w
64. Muraoka, S., DeLeo, A. M., Sethi, M. K., Yukawa-Takamatsu, K., Yang, Z., Ko, J., et al. (2020). Proteomic and Biological Profiling of Extracellular Vesicles from Alzheimer's Disease Human Brain Tissues. *Alzheimers Dement* 16, 896–907. doi:10.1002/alz.12089
65. Muraoka, S., Jedrychowski, M. P., Iwahara, N., Abdullah, M., Onos, K. D., Keezer, K. J., et al. (2021). Enrichment of Neurodegenerative Microglia Signature in Brain-Derived Extracellular Vesicles Isolated from Alzheimer's Disease Mouse Models. *J. Proteome Res.* 20, 1733–1743. doi:10.1021/acs.jproteome.0c00934
66. Niimura, Y., Moue, T., Takahashi, N., and Nagai, K. (2010). Modification of Sphingoglycolipids and Sulfolipids in Kidney Cell Lines under Heat Stress: Activation of Monohexosylceramide Synthesis as a Ceramide Scavenger. *Glycobiology* 20, 710–717. doi:10.1093/glycob/cwq018

67. Nugent, A. A., Lin, K., van Lengerich, B., Lianoglou, S., Przybyla, L., Davis, S. S., et al. (2020). TREM2 Regulates Microglial Cholesterol Metabolism upon Chronic Phagocytic Challenge. *Neuron* 105, 837–e9. doi:10.1016/j.neuron.2019.12.007
68. Orre, M., Kamphuis, W., Osborn, L. M., Jansen, A. H. P., Kooijman, L., Bossers, K., et al. (2014). Isolation of Glia from Alzheimer's Mice Reveals Inflammation and Dysfunction. *Neurobiol. Aging* 35, 2746–2760. doi:10.1016/j.neurobiolaging.2014.06.004
69. Pascual, M., Ibáñez, F., and Guerri, C. (2020). Exosomes as Mediators of Neuron-Glia Communication in Neuroinflammation. *Neural Regen. Res.* 15, 796–801. doi:10.4103/1673-5374.268893
70. Pascual-Lucas, M., Viana da Silva, S., Di Scala, M., Garcia-Barroso, C., González-Aseguinolaza, G., Mulle, C., et al. (2014). Insulin-like Growth Factor 2 Reverses Memory and Synaptic Deficits in APP Transgenic Mice. *EMBO Mol. Med.* 6, 1246–1262. doi:10.15252/emmm.201404228
71. Peng, K. Y., Pérez-González, R., Alldred, M. J., Goulbourne, C. N., Morales-Corraliza, J., Saito, M., et al. (2019). Apolipoprotein E4 Genotype Compromises Brain Exosome Production. *Brain* 142, 163–175. doi:10.1093/brain/awy289
72. Pérez-González, R., Gauthier, S. A., Kumar, A., Saito, M., Saito, M., and Levy, E. (2017). A Method for Isolation of Extracellular Vesicles and Characterization of Exosomes from Brain Extracellular Space. *Methods Mol. Biol.* 1545, 139–151. doi:10.1007/978-1-4939-6728-5_10
73. Rajendran, L., Honsho, M., Zahn, T. R., Keller, P., Geiger, K. D., Verkade, P., et al. (2006). Alzheimer's Disease Beta-Amyloid Peptides Are Released in Association with Exosomes. *Proc. Natl. Acad. Sci. USA.* 103, 11172–11177. doi:10.1073/pnas.0603838103

74. Rappsilber, J., Mann, M., and Ishihama, Y. (2007). Protocol for Micro-purification, Enrichment, Pre-fractionation and Storage of Peptides for Proteomics Using StageTips. *Nat. Protoc.* 2, 1896–1906. doi:10.1038/nprot.2007.261
75. Sanchez-Mejia, R. O., Newman, J. W., Toh, S., Yu, G. Q., Zhou, Y., Halabisky, B., et al. (2008). Phospholipase A2 Reduction Ameliorates Cognitive Deficits in a Mouse Model of Alzheimer's Disease. *Nat. Neurosci.* 11, 1311–1318. doi:10.1038/nn.2213
76. Sardar Sinha, M., Ansell-Schultz, A., Civitelli, L., Hildesjö, C., Larsson, M., Lannfelt, L., et al. (2018). Alzheimer's Disease Pathology Propagation by Exosomes Containing Toxic Amyloid-Beta Oligomers. *Acta Neuropathol.* 136, 41–56. doi:10.1007/s00401-018-1868-1
77. Scharz, N. D., and Tenner, A. J. (2020). The Good, the Bad, and the Opportunities of the Complement System in Neurodegenerative Disease. *J. Neuroinflammation* 17, 354. doi:10.1186/s12974-020-02024-8
78. Serrano-Pozo, A., Frosch, M. P., Masliah, E., and Hyman, B. T. (2011). Neuropathological Alterations in Alzheimer Disease. *Cold Spring Harb Perspect. Med.* 1, a006189. doi:10.1101/cshperspect.a006189
79. Showalter, M. R., Berg, A. L., Nagourney, A., Heil, H., Carraway, K. L., and Fiehn, O. (2020). The Emerging and Diverse Roles of Bis(monoacylglycero) Phosphate Lipids in Cellular Physiology and Disease. *Int. J. Mol. Sci.* 21. doi:10.3390/ijms21218067
80. Simon, A. (2014). Cholesterol Metabolism and Immunity. *N. Engl. J. Med.* 371, 1933–1935. doi:10.1056/NEJMcibr1412016
81. Spann, N. J., and Glass, C. K. (2013). Sterols and Oxysterols in Immune Cell Function. *Nat. Immunol.* 14, 893–900. doi:10.1038/ni.2681

82. Srinivasan, K., Friedman, B. A., Etxeberria, A., Huntley, M. A., van der Brug, M. P., Foreman, O., et al. (2020). Alzheimer's Patient Microglia Exhibit Enhanced Aging and Unique Transcriptional Activation. *Cel Rep* 31, 107843. doi:10.1016/j.celrep.2020.107843
83. Su, H., Rustam, Y. H., Masters, C. L., Makalic, E., McLean, C. A., Hill, A. F., et al. (2021). Characterization of Brain-Derived Extracellular Vesicle Lipids in Alzheimer's Disease. *J. Extracell Vesicles* 10, e12089. doi:10.1002/jev2.12089
84. Su, W., Aloji, M. S., and Garden, G. A. (2016). MicroRNAs Mediating CNS Inflammation: Small Regulators with Powerful Potential. *Brain Behav. Immun.* 52, 1–8. doi:10.1016/j.bbi.2015.07.003
85. Szklarczyk, D., Gable, A. L., Lyon, D., Junge, A., Wyder, S., Huerta-Cepas, J., et al. (2019). STRING v11: Protein-Protein Association Networks With Increased Coverage, Supporting Functional Discovery in Genome-Wide Experimental Datasets. *Nucleic Acids Res.* 47, D607–D13. doi:10.1093/nar/gky1131
86. Takatori, S., Wang, W., Iguchi, A., and Tomita, T. (2019). Genetic Risk Factors for Alzheimer Disease: Emerging Roles of Microglia in Disease Pathomechanisms. *Adv. Exp. Med. Biol.* 1118, 83–116. doi:10.1007/978-3-030-05542-4_5
87. Tang, S.-Y., Liu, D.-X., Li, Y., Wang, K.-J., Wang, X.-F., Su, Z.-K., et al. (2020). Caspr1 Facilitates sAPP α Production by Regulating α -Secretase ADAM9 in Brain Endothelial Cells. *Front. Mol. Neurosci.* 13, 23. doi:10.3389/fnmol.2020.00023
88. Tenner, A. J. (2020). Complement-Mediated Events in Alzheimer's Disease: Mechanisms and Potential Therapeutic Targets. *J. Immunol.* 204, 306–315. doi:10.4049/jimmunol.1901068

89. Théry, C., Witwer, K. W., Aikawa, E., Alcaraz, M. J., Anderson, J. D., Andriantsitohaina, R., et al. (2018). Minimal Information for Studies of Extracellular Vesicles 2018 (MISEV2018): a Position Statement of the International Society for Extracellular Vesicles and Update of the MISEV2014 Guidelines. *J. Extracell Vesicles* 7, 1535750. doi:10.1080/20013078.2018.1535750
90. Thion, M. S., and Garel, S. (2018). Microglia Under the Spotlight: Activity and Complement-Dependent Engulfment of Synapses. *Trends Neurosci* 41, 332–34. doi:10.1016/j.tins.2018.03.017
91. Vassileff, N., Vella, L. J., Rajapaksha, H., Shambrook, M., Kenari, A. N., McLean, C., et al. (2020). Revealing the Proteome of Motor Cortex Derived Extracellular Vesicles Isolated from Amyotrophic Lateral Sclerosis Human Postmortem Tissues. *Cells* 9, 1709. doi:10.3390/cells9071709
92. Vella, L. J., Scicluna, B. J., Cheng, L., Bawden, E. G., Masters, C. L., Ang, C. S., et al. (2017). A Rigorous Method to Enrich for Exosomes from Brain Tissue. *J. Extracell Vesicles* 6, 1348885. doi:10.1080/20013078.2017.1348885
93. Wang, B., Wu, L., Chen, J., Dong, L., Chen, C., Wen, Z., et al. (2021). Metabolism Pathways of Arachidonic Acids: Mechanisms and Potential Therapeutic Targets. *Signal. Transduct Target. Ther.* 6, 94. doi:10.1038/s41392-020-00443-w
94. Wang, G., Dinkins, M., He, Q., Zhu, G., Poirier, C., Campbell, A., et al. (2012). Astrocytes Secrete Exosomes Enriched with Proapoptotic Ceramide and Prostate Apoptosis Response 4 (PAR-4): Potential Mechanism of Apoptosis Induction in Alzheimer Disease (AD). *J. Biol. Chem.* 287, 21384–21395. doi:10.1074/jbc.M112.340513

95. Willis, C. M., Ménoret, A., Jellison, E. R., Nicaise, A. M., Vella, A. T., and Crocker, S. J. (2017). A Refined Bead-free Method to Identify Astrocytic Exosomes in Primary Glial Cultures and Blood Plasma. *Front. Neurosci.* 11, 335. doi:10.3389/fnins.2017.00335
96. Winston, C. N., Goetzl, E. J., Akers, J. C., Carter, B. S., Rockenstein, E. M., Galasko, D., et al. (2016). Prediction of Conversion from Mild Cognitive Impairment to Dementia with Neuronally Derived Blood Exosome Protein Profile. *Alzheimers Dement (Amst)* 3, 63–72. doi:10.1016/j.dadm.2016.04.001
97. Winston, C. N., Romero, H. K., Ellisman, M., Nauss, S., Julovich, D. A., Conger, T., et al. (2019). Assessing Neuronal and Astrocyte Derived Exosomes from Individuals with Mild Traumatic Brain Injury for Markers of Neurodegeneration and Cytotoxic Activity. *Front. Neurosci.* 13, 1005. doi:10.3389/fnins.2019.01005
98. Wong, M. Y., Lewis, M., Doherty, J. J., Shi, Y., Cashikar, A. G., Amelianchik, A., et al. (2020). 25-Hydroxycholesterol Amplifies Microglial IL-1 β Production in an apoE Isoform-dependent Manner. *J. Neuroinflammation* 17, 192. doi:10.1186/s12974-020-01869-3
99. Xue, F., and Du, H. (2021). TREM2 Mediates Microglial Anti-inflammatory Activations in Alzheimer's Disease: Lessons Learned from Transcriptomics. *Cells* 10, 321. doi:10.3390/cells10020321
100. Yan, Z., Zhou, Z., Wu, Q., Chen, Z. B., Koo, E. H., and Zhong, S. (2020). Presymptomatic Increase of an Extracellular RNA in Blood Plasma Associates with the Development of Alzheimer's Disease. *Curr. Biol.* 30, 1771–e3. doi:10.1016/j.cub.2020.02.084

101. Yiannopoulou, K. G., Anastasiou, A. I., Zachariou, V., and Pelidou, S. H. (2019). Reasons for Failed Trials of Disease-Modifying Treatments for Alzheimer Disease and Their Contribution in Recent Research. *Biomedicines* 7, 97. doi:10.3390/biomedicines7040097
102. Yilmaz, M., Yalcin, E., Presumey, J., Aw, E., Ma, M., Whelan, C. W., et al. (2021). Overexpression of Schizophrenia Susceptibility Factor Human Complement C4A Promotes Excessive Synaptic Loss and Behavioral Changes in Mice. *Nat Neurosci*, 24, 214–224. doi:10.1038/s41593-020-00763-8
103. Yuyama, K., Sun, H., Sakai, S., Mitsutake, S., Okada, M., Tahara, H., et al. (2014). Decreased Amyloid- β Pathologies by Intracerebral Loading of Glycosphingolipid-Enriched Exosomes in Alzheimer Model Mice. *J. Biol. Chem.* 289, 24488–24498. doi:10.1074/jbc.M114.577213
104. Zhang, L., Wang, J., Wang, J., Yang, B., He, Q., and Weng, Q. (2020). Role of DJ-1 in Immune and Inflammatory Diseases. *Front. Immunol.* 11, 994. doi:10.3389/fimmu.2020.00994
105. Zhu, C., Bilousova, T., Focht, S., Jun, M., Elias, C. J., Melnik, M., et al. (2021). Pharmacological Inhibition of nSMase2 Reduces Brain Exosome Release and α -synuclein Pathology in a Parkinson's Disease Model. *Mol. Brain* 14, 70. doi:10.1186/s13041-021-00776-9

CHAPTER 2

Integrated Multiomics Analysis of Salivary Exosomes to Identify Biomarkers Associated with Changes in Mood States and Fatigue

Whitaker Cohn,¹ Chunni Zhu,¹ Jesus Campagna,¹ Tina Bilousova,¹ Patricia Spilman,¹ Bruce Teter,¹ Feng Li,² Rong Guo,³ David Elashoff,³ Greg M. Cole,⁴ Alon Avidan,⁴ Kym Francis Faull,⁵ Julian Whitelegge,⁵ David T. W. Wong,² and Varghese John^{1,*}

¹The Drug Discovery Lab, Department of Neurology, David Geffen School of Medicine, 710 Westwood Plaza, University of California Los Angeles, Los Angeles, CA 90095, USA

²Center for Oral/Head & Neck Oncology Research, Laboratory of Salivary Diagnostics, School of Dentistry, 10833 Le Conte Avenue, University of California Los Angeles, Los Angeles, CA 90095, USA

³Department of Medicine Statistics Core, David Geffen School of Medicine, 1100 Glendon Avenue, University of California Los Angeles, Los Angeles, CA 90095, USA

⁴Department of Neurology, David Geffen School of Medicine, 710 Westwood Plaza, University of California Los Angeles, Los Angeles, CA 90095, USA

⁵Pasarow Mass Spectrometry Laboratory, Jane and Terry Semel Institute for Neuroscience and Human Behavior, David Geffen School of Medicine, 760 Westwood Plaza, University of California Los Angeles, Los Angeles, CA 90095, USA

[This is a reprint of research originally published by the *International journal of molecular sciences* (2022), 23(9), 5257. <https://doi.org/10.3390/ijms23095257>]

Abstract

Fatigue and other deleterious mood alterations resulting from prolonged efforts such as a long work shift can lead to a decrease in vigilance and cognitive performance, increasing the likelihood of errors during the execution of attention-demanding activities such as piloting an aircraft or performing medical procedures. Thus, a method to rapidly and objectively assess the risk for such cognitive fatigue would be of value. The objective of the study was the identification in saliva-borne exosomes of molecular signals associated with changes in mood and fatigue that may increase the risk of reduced cognitive performance. Using integrated multiomics analysis of exosomes from the saliva of medical residents before and after a 12 h work shift, we observed changes in the abundances of several proteins and miRNAs that were associated with various mood states, and specifically fatigue, as determined by a Profile of Mood States questionnaire. The findings herein point to a promising protein biomarker, phosphoglycerate kinase 1 (PGK1), that was associated with fatigue and displayed changes in abundance in saliva, and we suggest a possible biological mechanism whereby the expression of the PGK1 gene is regulated by miR3185 in response to fatigue. Overall, these data suggest that multiomics analysis of salivary exosomes has merit for identifying novel biomarkers associated with changes in mood states and fatigue. The promising biomarker protein presents an opportunity for the development of a rapid saliva-based test for the assessment of these changes.

Keywords: fatigue; cognitive impairment; exosomes; biomarkers; saliva; multiomics; proteomics; microRNA

1. Introduction

The onset of fatigue confers an increased risk of impaired cognitive performance, resulting in what is referred to as cognitive fatigue (CF) [1,2]. This is characterized by an inability to maintain optimal performance during prolonged cognitive effort [3]; it can manifest after long-duration cognitive activity, sleep deprivation [4], or excessive exercise [5]. CF is of particular concern for those involved in attention-demanding occupations such as surgeons performing extended operations and pilots navigating long flights and may result in catastrophic accidents. Typically, the extent of fatigue and thus the risk of CF is determined by self-reported assessments, which are subjective and unreliable. Thus, a method for objectively assessing physiological alterations that are associated with an increased risk of CF would be of value, and the identification of biomarkers associated with fatigue has the potential to be the first step in the development of rapid tests to determine the risk of CF.

Fatigue-associated changes may be due, in part, to biochemical changes in cellular signaling processes and observed in the molecular composition of saliva. While saliva is obtained easily and noninvasively in sufficient quantities for analyses, the ability to identify fatigue biomarkers is hindered by the complexity and concentration dynamic range of the salivary proteome and transcriptome. Here, we have attempted to overcome this challenge by assessing biomarkers in exosomes, a subset of extracellular vesicles (EVs), in saliva.

Exosomes are 50–100 nm diameter [6] particles of endosomal origin that occur in body fluids and the extracellular space of tissues. They are comprised of a lipid bilayer that carries cargo in their interior and is attached to their surface. Like other exosomes, the surface of salivary exosomes is

enriched in tetraspanin marker proteins CD9, CD63, and CD81 [7,8], important for the organization of membrane domains. Exosomes also contain tumor susceptibility gene 101 (Tsg101) and ALG-2-interacting protein X (ALIX) that are part of the Endosomal Sorting Complexes Required for Transport (ESCRT) machinery involved in intracellular vesicle formation and sorting of cargo [6].

In a process still being elucidated, during the formation, exosomes are loaded with cytoplasmic proteins, nucleic acids, including microRNAs, and membrane constituents that reflect the biochemistry and status of the parent cell at the time of the exosome biogenesis [9]. Exosomes are released from all cell types, including neurons, and can act as intercellular signal carriers. Sleep deprivation is associated with a decline in cognitive function and alterations in levels of intracellular proteins and nucleic acids [10,11], as well as circulating signaling molecules [12]. Thus, exosomes derived from individuals experiencing sleep deprivation may carry molecular signals reflective of changes in the physiology of the central nervous system (CNS) associated with the onset of fatigue-associated cognitive impairment [13].

We hypothesize that the potential for salivary exosomes to reflect changes in cognitive function is due to the presence of anatomical connections from the CNS, specifically innervation of Cranial Nerves VII and IX from the superior and inferior salivary nuclei to the oral cavity and the parotid and submandibular glands [14], or directly from the blood through the oral cavity vasculature. The hypothesis that salivary exosomes carry signals that influence and are indicative of the changes in brain function is supported by reports on salivary exosome proteins changing with HIV-associated cognitive deficits, in traumatic brain injury concussion-related cognitive fatigue, and in

monozygotic twins discordant for chronic fatigue syndrome [15,16,17]. Further, proteins such as beta-amyloid [18] and tau [19], implicated in the impaired cognitive function associated with Alzheimer's disease, change in abundance in the total saliva protein pool and are present in bloodborne brain-derived EVs [20]. These findings make it reasonable to postulate that other proteins and biomarkers related to cognitive function may be contained in salivary exosomes.

Autonomic nervous system alterations also play a role in the manifestation of fatigue [21] and saliva production [22]; therefore, it is also likely that exosomes released by neurons of the autonomic nervous system are present in salivary exosomes.

To test our hypothesis that exosomes originating from neuronal cells are present in saliva and carry biomarkers reflecting physiological states of fatigue, saliva from medical and dental resident participants was collected before and after a 12 h work shift. Participants were asked to complete a modified Profile of Mood States (PoMS) questionnaire both before and after their work shift, and the changes in subscale scores for self-assessed mood states such as fatigue were used to generate Total Mood Disturbance (TMD) scores. The PoMS method of assessment was chosen because, in Fogt et al. [2], increased fatigue, as reflected by the PoMS score, was directly correlated with decreased cognitive performance as determined by the Stroop Color-Word Conflict Test.

Exosomes isolated from the collected saliva were subjected to multiomics analyses, including quantitative proteomics and miR-omics, to identify proteins and microRNAs associated with changes in TMD scores.

2. Results

PoMS Analysis and Assignment to Study Groups

Participant answers on the PoMS questionnaire were used to calculate pre- and post-work shift TMD scores. Each of the mood state subscales—TA, DD, AH, FI, CB, and VA (**Figure 1A**)—contributed to the TMD score (**Figure 1B, Supplementary Table S1, Supplementary Figure S1**), with only the VA being subtracted from the total of the others because increased vigor and activity are associated with an improved, rather than worsening, mood. Therefore, an increase in TMD indicated a decline in mood states post shift. Significantly increased scores were observed for CB and FI and a decreased score for VA (**Supplementary Table S1, Figure 1A**). The TMD score also significantly increased from pre-shift (53.07 ± 20.21) to post shift (65.99 ± 24.83) ($p < 0.05$), indicating that the mood of most participants worsened during the shift (**Figure 1B**). Not all participants recorded a positive TMD. A decrease in TMD score was observed for 12 of the 36 (33%) participants, indicative of no change or an elevated mood post shift (**Figure 1C**). As described in *Methods* Section, the TMD score was subsequently used to segregate saliva samples into three groups: Test, Discovery, and Validation (**Figure 1C**).

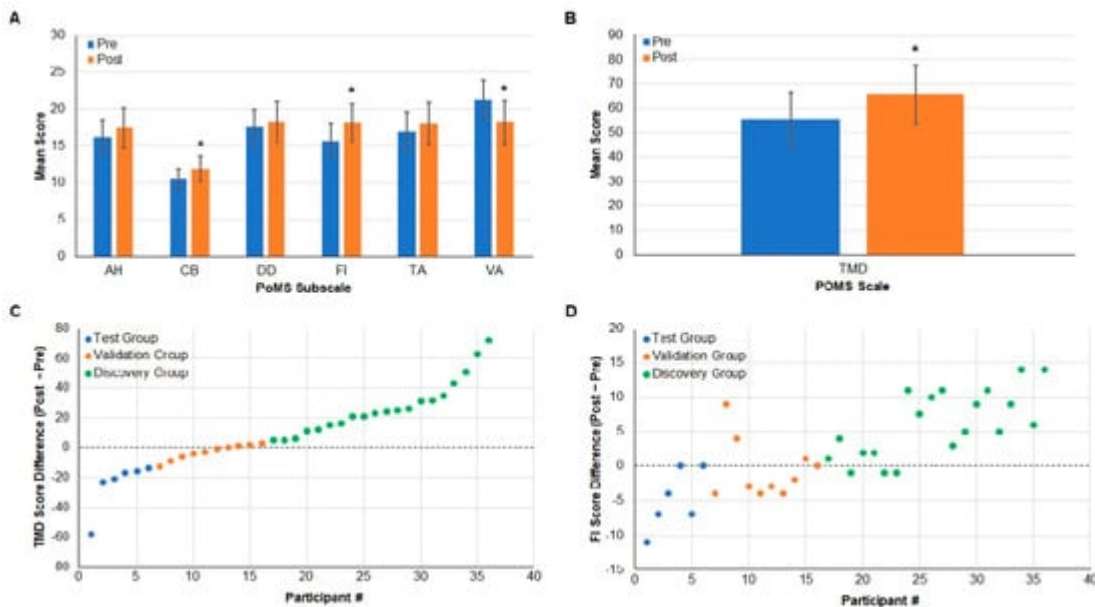


Figure 1. *Difference in Total Mood Disturbance (TMD) as assessed by the Profile of Mood States (PoMS) allows separation into Discovery, Validation, and Test groups.* (A) The PoMS scores for anger–hostility (AH), confusion–bewilderment (CB), depression–dejection (DD), fatigue–inertia (FI), tension–anxiety (TA), and vigor–activity (VA) are shown pre- and post-work shift. CB * $p = 0.003$, FI * $p = 0.0393$, and VA * $p = 0.0047$. (B) The combined TMD score for all participants’ pre- and post-work shifts is shown; * $p = 0.0200$. (C) The number of participants sorted into each group (x-axis), and the difference between pre- and post-work shift TMD (y-axis) is shown. The 6 participants with the greatest decrease in TMD score are in the Test group (blue), the 20 participants with the greatest increase in the Discovery group (green), and 10 intermediate participants in the Validation group (orange). (D) The number of participants sorted into each group (x-axis), and the difference between pre- and post-work shift FI (y-axis) is shown.

The purpose of the Test group was to establish the validity of analytical methods and testing of potential biomarker candidates using six participants with a negative TMD difference whose saliva would not be predicted to harbor biomarkers associated with deteriorating mood. The Discovery group focused on participants with self-reported increased fatigue (**Figure 1D**) and a decline in mood and consisted of the 20 individuals with the largest increase in TMD. The Discovery group would also be expected to exhibit physiological changes associated with fatigue and an increased risk for CF. The Validation group included participants with only slightly positive and negative changes in TMD and FI, whose saliva samples underwent proteomics and qPCR analysis. A narrower group of proteins and miRNAs identified from the larger Discovery group analysis were measured in the Validation group, and any correlations to PoMS subscales were determined.

3. Multiomics Analysis of Test Group Salivary Exosomes

3.1. Quantitative Global Proteomics on Salivary Exosomes

Bottom-up proteomics analysis identified a total of 118 unique proteins in exosomes enriched from the saliva of Test group participants. Reporter ion-based quantification of proteins using Tandem Mass Tags (TMT) revealed quantifiable differences in the abundance of 98 proteins extracted from the salivary exosomes of residents before and after 12 h work shifts (**Figure 2A**). While changes in the abundance of only two proteins, BPI fold-containing family A member 2 (BPIFA2; fold change = 1.91, $p = 0.02$) and small proline-rich protein 3 (SPRR3; fold change = -2.58 , $p = 0.05$) were statistically significant, many other proteins showed trends and were close to reaching significance ($p < 0.05$; **Supplementary Table S2**). GO classifications revealed an abundance of exosome-associated proteins (**Supplementary Table S3**), including four altered membrane-bound proteins (**Supplementary Table S2**).

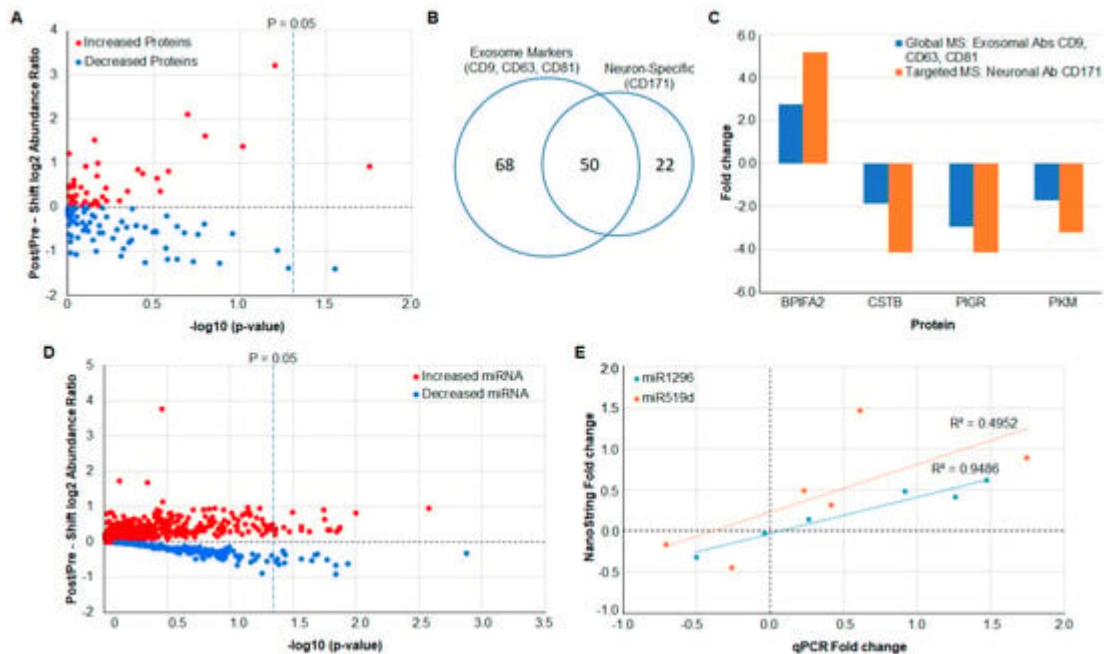


Figure 2. *Multiomics analysis reveals quantifiable differences in protein and miRNA abundances in the Test group pan- and neuron-derived exosomes.* (A) Differences in the abundances of proteins present in the salivary exosomes of Test group participants pre- and post-work shifts are illustrated via a volcano plot. The \log_{10} (abundance ratio: post-work/pre-work) is plotted against $-\log_{10}$ (p value). (B) A Venn diagram shows the overlap of proteins found in exosomes isolated with pan-exosomal or neuron-selective exosomal markers for a single participant. (C) The protein fold change for the single Test group participant is shown when using global proteomics on exosomes isolated by a pan-exosome set of antibodies (Global MS (exosome abs: CD9, CD63, CD81); blue bars) or targeted MS on four corresponding to the four proteins (STVSSLLQK/BPIFA2, SQVVAGTNYFIK/CSTB, TVTINCPFK/PIGR, LDIDSPITAR/PKM) present in exosomes isolated using an antibody to a neuron-specific exosome marker (Targeted MS (neuronal ab: CD171); orange bars). (D) Differences in the abundances of miRNAs present in the salivary exosomes of participants pre- and post-work shift are illustrated via a volcano plot. The \log_{10} (abundance ratio: post-work/pre-work) is plotted against $-\log_{10}$ (p -value). (E) Fold change of miR-519d and miR-1296 as measured using the NanoString platform (y -axis) shows a moderate and strong positive correlation (miR-519d $R^2 = 0.50$, $r(5) = 0.70$, $p = 0.01881$; miR-1296 $R^2 = 0.95$, $r(5) = 0.97$, $p = 0.0062$) with fold change as measured by qPCR (x -axis).

3.2. Verification of Protein Measurements in Neuron-Derived Exosomes by Targeted MS

In the single Test group of participants from which neuron-derived exosomes were isolated, as many as 50 of the proteins identified from the immunoprecipitation using exosomal cell surface markers CD9, CD63, CD81 (**Supplementary Table S2**) were subsequently also identified using targeted MS for neuron-derived exosomes after isolation of salivary exosomes using neuron cell

surface marker (CD171) (**Figure 2B, Supplementary Table S4**). The targeted MS was performed for proteins with abundant peptides that contained no post-translational modifications. Four proteins—BPIFA2, CSTB, PIGR, and PKM—in neuron-derived exosomes correlated well with global proteomics used for exosomes isolated using pan-exosomal markers, but the protein fold change observed in the targeted MS was higher compared with global proteomics (**Figure 2C**).

3.3. MicroRNA Analysis Using NanoString

The NanoString platform was used to determine the abundance of a panel of 800 biologically relevant miRNAs. While not all the miRNA species were quantifiable above background in salivary exosomes, the analysis revealed 22 miRNAs to be significantly changed between pre- and post-work shifts (absolute fold change ≥ 1.2 , $p < 0.05$) (**Figure 2D, Supplementary Table S5**). Several of the significantly altered miRNA were found to target genes encoding proteins that were also determined to change in abundance between pre- and post-work shifts (Supplementary Table S2). An inverse relationship between some identified miRNAs and their associated protein was observed.

3.4. Verification of miRNA Measurements Using qPCR

NanoString abundance measurements were validated for two select miRNAs (miR1296-3p and miR519d-3p) using qPCR. Values of % change between pre- and post-work shift for the miRNAs in the 6 Test group participants show that measurements made using the NanoString platform were qualitatively verified by qPCR (**Figure 2E**). This result provided the reassurance of the reliability of NanoString miRNA abundance measurements needed for subsequent analysis of the Discovery group saliva samples. The raw qPCR results are presented in **Supplementary Table S6**.

4. Biomarker Identification in Discovery Group Saliva

Identification of Additional Significantly Altered Protein and miRNA

Quantitative, bottom-up proteomics analyses on the salivary exosomes from the larger Discovery group ($n = 20$) resulted in the identification of an increased number of proteins when compared with the Test group. Among the 309 proteins quantified (**Supplementary Table S7**), the abundance of 7 of these was determined to be significantly altered between pre- and post- work shifts (absolute fold change ≥ 1.2 with a p value < 0.05), and 7 additional proteins displayed trends that were close to reaching statistical significance (**Figure 3A**). All of the proteins that exhibited a difference in absolute fold change ≥ 1.2 with a p value < 0.1 and their associated miRNA are displayed in **Table 1**.

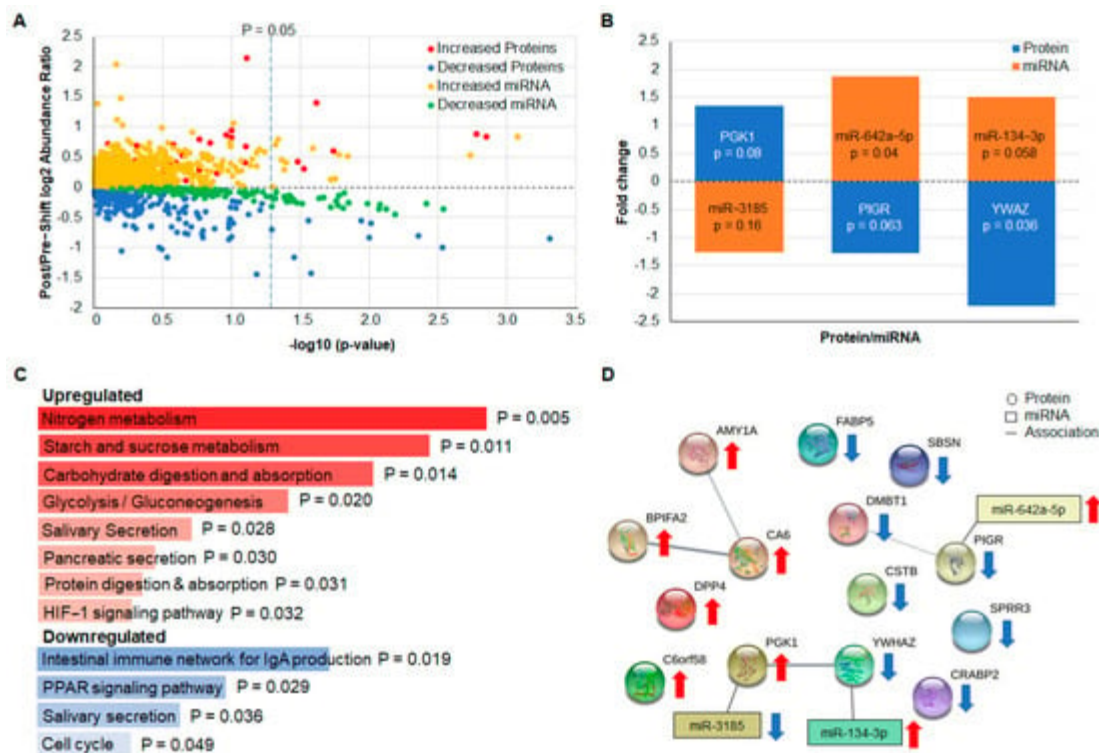


Figure 3. *Interconnected protein and miRNA networks regulate molecular pathways associated with increased TMD score in the Discovery group.* (A) Differences in the abundances of proteins and miRNAs present in the salivary exosomes of Discovery group participants ($n = 20$) pre- and post-work shift are illustrated via volcano plot; significant differences are points to the right of the vertical line marked $p = 0.05$. The \log_{10} (abundance ratio: post-work/pre-work) is plotted against the $-\log_{10}$ (p -value). (B) The mean fold change of three significantly altered miRNA (miR-3185, miR-642-5p, miR-134-3p) is shown to inversely relate to the abundances of proteins encoded by one of their target genes (PGK1, PIGR, YWHAZ). (C) Gene set enrichment analysis of upregulated and downregulated proteins using Enrichr [23] shows enrichment of KEGG database [24] molecular pathways after a 12 h work shift. Results are ranked according to p value. (D) Functional protein association network analysis using STRING [25] shows that associated and interacting protein networks are differentially regulated after a 12 h work shift.

Gene Symbol	Protein Description	Protein Fold Change: Post-/Pre-Work	Protein p-Value: Post-/Pre-Work	miRNA	miRNA Fold Change: Post-/Pre-Work	miRNA p-Value: Post-/Pre-Work
LEG1	Liver-enriched gene 1 protein	4.46	0.079			
AMY1A	Alpha-amylase 1 ^{n,c}	1.85	0.002			
BPIFA2	BPI fold-containing family A member ⁿ	1.64	0.006			
CA6	Carbonic anhydrase 6 ⁿ	1.5	0.083			
PGK1	Phosphoglycerate kinase 1 ⁿ	1.34	0.08	hsa-miR-3185	0.79	0.016
DPP4	Dipeptidyl peptidase 4	1.24	0.03			
SBSN	Suprabasin	-1.23	0.06			
PIGR	Polymeric immunoglobulin receptor ^{m,n,c}	-1.28	0.063	hsa-miR-642a-5p	1.9	0.04
CSTB	Cystatin-B ^{n,c}	-1.34	0.057			
SPRR3	Small proline-rich protein 3	-1.49	0.01			
CRABP2	Cellular retinoic acid-binding protein 2	-1.49	0.098			
FABP5	Fatty acid-binding protein 5	-1.72	0.004			
YWHAZ	14-3-3 protein zeta/delta ^{n,c}	-2.22	0.036	hsa-miR-134-3p	1.5	0.058
DMBT1	Deleted in malignant brain tumors 1 ^{n,c}	-2.63	0.027			

^m = Membrane Protein; ⁿ = Experimentally identified using neuron-specific marker (CD171); ^c = Relevant in Chronic Fatigue Syndrome.

Table 1. *Identification of differentially abundant proteins and miRNA in salivary exosomes in the Discovery group. The protein–miRNA pairs are listed in the same row.*

NanoString miRNA analysis showed that 22 miRNAs significantly changed between pre- and post-work shifts (absolute fold change ≥ 1.2 , $p < 0.05$, **Supplementary Table S8, Figure 3A**). In addition, 69 miRNAs changed in correlation with changes in either the PoMS TMD (32 miRNAs) or FI (37 miRNAs) subscale (**Supplementary Tables S9, S10**). As in the Test group, the abundance of several miRNAs, miR-3185, miR-642-5p, and miR-134-3p, was found to inversely correlate with the protein encoded by one of their target genes (**Figure 3B, Table 1**). This relationship highlights three potential proteins (Phosphoglycerate Kinase, gene PGK1; Polymeric Immunoglobulin Receptor, gene PIGR; and Tryptophan 5-Monooxygenase Activation Protein Zeta, gene YWHAZ) and miRNA (miR-3185, miR-642a-5p, miR-134-3p) biomarkers to be quantified in Validation group saliva. One of these miRNAs, miR-642a-5p, weakly correlated with changes in the PoMS FI subscale (Supplementary Figure S2). Additional bioinformatic approaches, including gene set enrichment, GO classification and pathway analysis (Figure 3C), and functional protein network analysis (Figure 3D), were utilized to elucidate the potential biological roles of the identified proteins in increased TMD score. In addition, correlations of NanoString and qPCR analyses were determined for miR642a, miR3185, and miR3185 (**Supplementary Figure S3**). Of the six proteins that were increased and the eight proteins that were decreased in the Discovery group (**Table 1**), three are encoded by genes that could be a target of three of the miRNAs that changed in abundance in the opposite direction to that of the protein (as expected for the normal downregulation of gene expression by a miRNA).

5. Confirmation of Biomarkers and Fold Change in Validation Group Salivary Exosomes

5.1. Validation of Protein Biomarkers

Proteomic analysis of salivary exosomes from Validation group participants confirmed the presence of 12 of the 14 candidate biomarkers identified in the Discovery group (**Table 1, Figure 4A**). As observed in the Discovery group, the mean fold change in the abundances of five proteins CSTB, DDP4, FABP5, PIGR, and YWAZ maintained an inverse relationship with changes in TMD score. We note, however, that none of these changes were statistically significant ($p < 0.05$). The abundance of six proteins identified in the Validation group (DPP4, BPIFA2, CA6, AMY1A, LEG1, and DMBT1) did not correlate with changes in TMD or FI score but exhibited mean fold changes similar to what was observed in the Discovery group. One protein, PGK1, identified in the Discovery group was also identified in the Validation group, and its fold change showed a positive but weak correlation with changes in FI score (**Figure 4B**).

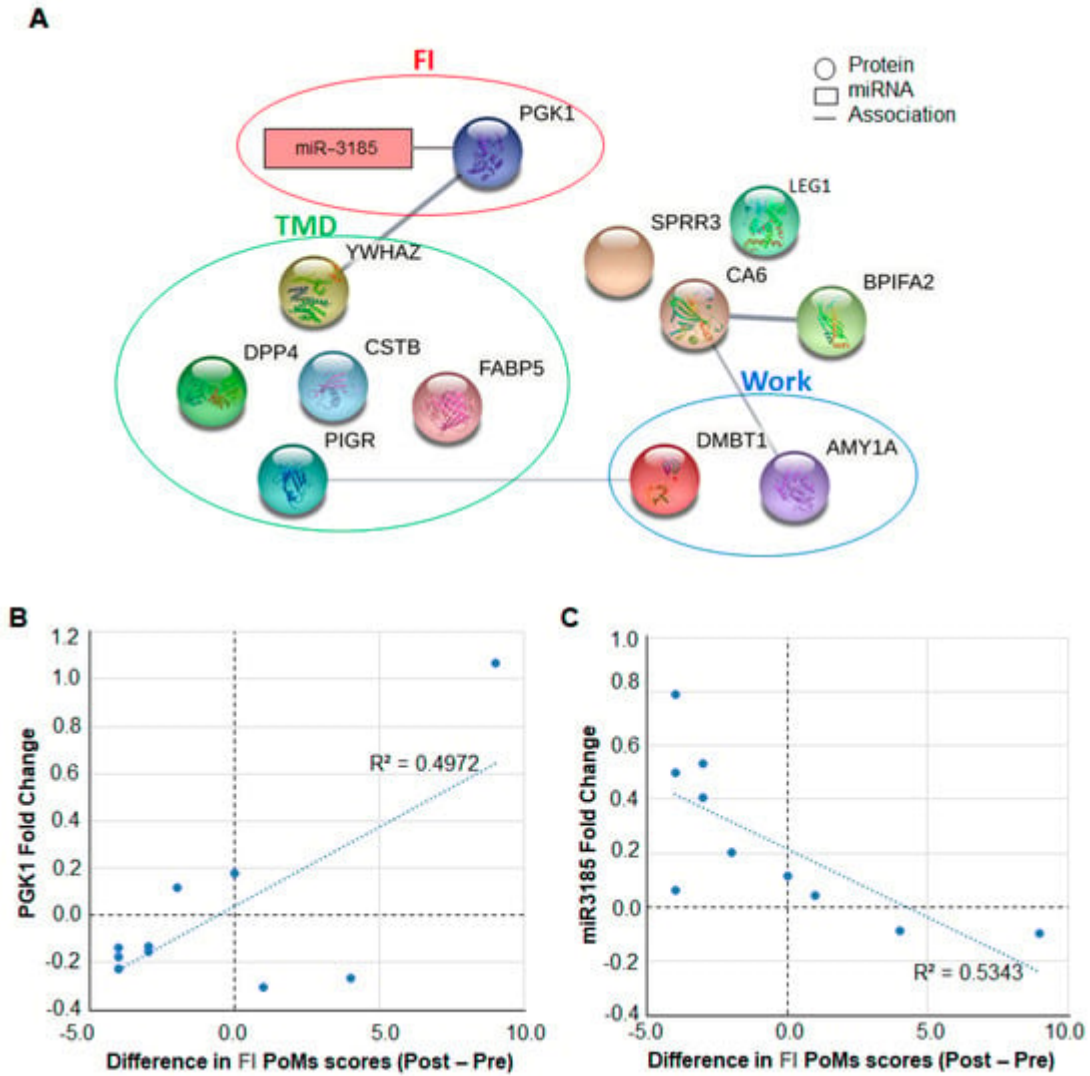


Figure 4. Proteins and miRNA identified in the Validation group are associated with Total Mood Disturbance (TMD), Fatigue–Inertia (FI), and Work, and (A) 12 of the 14 proteins identified as significantly altered in the Discovery group were also identified in the Validation group. The abundance of one protein (PGK1) correlates with FI (red circle), and those of the five proteins (DPP4, PIGR, CSTB, FABP5, and YWHAZ) are associated with TMD (green circle). Of the remaining six proteins, two (AMY1A and DMBT1) were altered significantly ($p < 0.05$) after a 12 h work shift (blue circle), while the remaining four (BPIFA2, CA6, SPRR3, and LEG1) were not altered. (B) PGK1 fold change (y -axis) shows a weak positive correlation ($R^2 = 0.50$, $r(10) =$

0.70, $p = 0.0242$) and (C) miR3185 fold change (y -axis) shows a weak negative correlation ($R^2 = 0.53$, $r(10) = -0.73$, $p = 0.0165$) with FI difference in Validation group participants after a work shift.

5.2. Validation of miRNA Biomarkers

The Validation Group samples were assessed for a total of 13 miRNAs using qPCR. These miRNAs were chosen based on the Discovery group. NanoString results which showed either large or highly significant changes in their levels with either pre-shift/post shift or change with PoMS subscales TMD or FI (**Supplementary Tables S9, S10**), specifically 13 miRNAs, were miR3185, miR28, miR1296, miR182, miR614, miR4536, miR140, miR1257, miR518e, miR105, miR126, miR642a, and miR134. The abundance of one miRNA in the validation group—miR3185—was found to moderately correlate with PoMS FI subscale score differences (**Figure 4C**).

5.3. PGK1 Protein and miR3185 in Saliva as Potential Biomarkers of Fatigue

In the Test group participants' salivary exosomes (with a lower rather than increased TMD score post shift), the fold change in PGK1 was negative, and in the Discovery group, with participants who recorded increased TMD and FI scores, it was positive (**Figure 5A**). In 15 of 30 participants in either the Discovery or Validation groups, wherein PGK1 was identified, there was an inverse correlation with miR3185 in both positive and negative abundance ratios (**Figure 5B**).

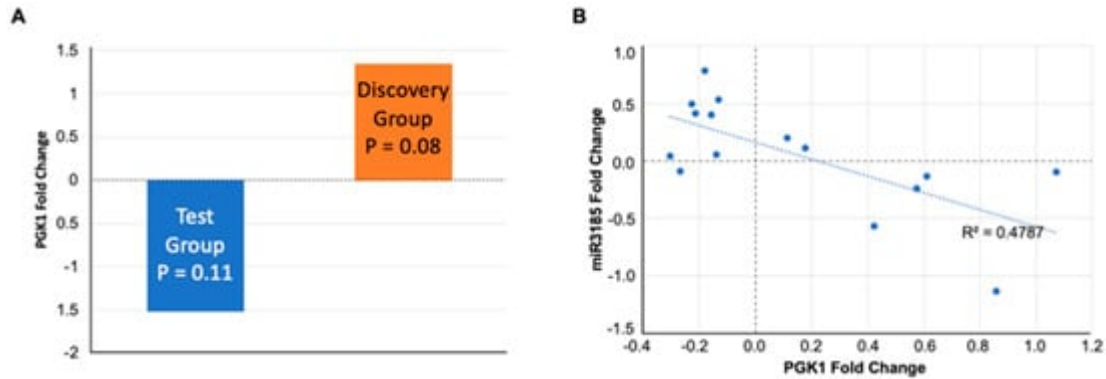


Figure 5. *PGK1* levels in Test and Discovery groups, and correlation of *PGK1* to *mi3185*. (A) The *PGK1* fold change for the Test and Discovery groups is shown. (B) The relative *PGK1* (x-axis) and *miR3185* levels (y-axis) display an inverse relationship. The correlation coefficient is $R^2 = 0.48$ $r(15) = 0.69$, $p = 0.0044$).

5.4. Integration of Test, Discovery, and Validation Data Reveals Proteins Associated with Work

When changes in protein abundances from the Test, Discovery, and Validation groups are combined, five proteins (*AMY1A*, *BPIFA2*, *CA6*, *DPP4*, and *LEG1*) significantly increase, and two proteins (*SBSN* and *DMBT1*) significantly decrease after a 12 h work shift (absolute fold change ≥ 1.2 , $p < 0.05$) (**Supplementary Figure S4**).

6. Discussion

Proteomics analysis of Test group saliva confirmed successful enrichment of exosome populations and identified changes in the abundance of several proteins pre- and post-work shift. Some of the proteins with altered abundances are known to be associated with Chronic Fatigue Syndrome (CFS), including alpha amylase 1 (*AMY1A*), cystatin-B (*CSTB*), polymeric immunoglobulin receptor (*PIGR*), deleted in malignant brain tumors 1 protein (*DMBT1*), lysozyme C (*LYZ*), and ras-related C3 botulinum toxin substrate 1 (*RAC1*) [17,26,27,28]. The abundance of these CFS-

associated proteins increased in some instances and decreased in others without correlation to the ‘improved’ mood reported by the Test group (Supplementary Table S2). It is significant that two biomarkers, protein PGK1 and miR3185, show abundance in saliva exosomes and change directions when the TMD score difference (**Figure 2C**) switches from negative to positive (Figure 4B,C); this shows that these biomarkers are responsive to changes in mood state and fatigue.

A subset of proteins with altered abundance in the Test group are membrane-bound proteins (**Supplementary Table S2**), an appealing characteristic as these potential biomarkers could possibly be identified without requiring exosome lysis in future studies.

In a single Test group participant, four of the proteins (BPIFA2, CSTB, PIGR, and PKM) with altered abundance identified from pan-exosome-isolated samples were qualitatively validated using global proteomics/Proteome Discoverer in neuron-derived exosomes (**Supplementary Tables S2, S4**). A notable increase in fold change was observed when using a targeted mass spectrometry approach for the neuron-derived exosomes. This discrepancy most likely results from a systematic underestimation of quantitative ratios caused by co-fragmentation of undesirable peptides when using isobaric mass tags such as those used in the untargeted proteomic analysis [29]. This ratio compression does not occur when using targeted, label-free quantification strategies resulting in more pronounced fold changes. Taking this into account, smaller fold changes need to be considered significant when using isobaric mass tags for quantitative proteomics in the discovery group analysis, and proteins of interest should be further analyzed using targeted approaches. Alternatively, these augmented fold change results may also be due to enhanced protein responses in neuron-derived exosomes, which become reduced in magnitude when diluted in total exosomes.

miRNA analysis on the Test group using the NanoString platform identified 22 miRNAs as significantly changed between pre- and post-work shifts, 12 of which were also found to change in the Discovery and Validation groups. These measurements were subsequently validated for two miRNAs (miR1296-3p and miR519d-3p) using qPCR, providing reassurance of the reliability of the NanoString platform. Several of these miRNAs were also found to exhibit changes in abundance opposite to that of the identified protein encoded by their target genes, suggesting a mechanism of gene regulation that is influencing the abundances of identified proteins. Omics analyses in the Test group confirmed our ability to identify exosomal proteins and their associated miRNAs that are detectable and may be altered pre- and post-work shift.

Global proteomic analysis of the larger Discovery group samples identified a considerably greater number of significantly changed proteins, including increases in AMY1A, BPI fold-containing family A member (BPIFA2), dipeptidyl peptidase 4 (DPP4), and decreases in small proline-rich protein 3 (SPRR3), fatty acid-binding protein 5 (FABP5), 14-3-3 protein zeta/delta (YWHAZ), and DMBT1. Four proteins that were altered—AMY1A (increased), CSTB (decreased), PIGR (decreased), and DMBT1 (decreased)—are known to be associated with CFS. Several other proteins, including liver-enriched gene 1 (LEG1), carbonic anhydrase 6 (CA6), suprabasin (SBSN), phosphoglycerate kinase 1 (PGK1), and cellular retinoic acid-binding protein 5, demonstrated close to significant changes in abundance and were also considered potential biomarkers. Gene set enrichment, GO classification and pathway analysis, and functional protein network analysis were utilized to help understand the potential biological roles of the identified proteins. These analyses highlighted the potential existence of regulated fatigue-associated protein networks that generate

ATP in response to energy demand or cellular stress. PGK1 catalyzes the formation of ATP from ADP and 1,3-diphosphoglycerate, playing an important role in glycolysis and energy homeostasis [30]. AMY1A hydrolyzes 1,4-alpha-glucosidic bonds in oligosaccharides and polysaccharides, yielding glucose that is then available to generate ATP [31]. DPP4 also influences glucose levels by deactivating incretins, which normally stimulate the release of pancreatic insulin [32].

NanoString miRNA analysis on the Discovery group identified 69 miRNAs that significantly changed and correlated with PoMS TMD or FI (**Supplementary Tables S9, S10**). Interestingly, some of these miRNAs exhibit changes in other CNS pathologies. For example, hsa-miR-142-3p is increased in individuals who have experienced a mild traumatic brain injury [33]. We hypothesize that the expression of these miRNAs is sensitive to changes in cognitive function and that they regulate the expression of biologically relevant proteins and pathways. Integrated analysis of the two-omics datasets was used to determine if any significantly altered miRNAs were known to regulate target genes encoding significantly altered proteins. miRNA-protein/gene pairs were selected if the direction of change in the miRNA was in the opposite direction of the change in the protein, considering the typical mechanism of downregulation of a gene mRNA by upregulated miRNA. This analysis identified three miRNA-protein/gene pairs: miR-3185—PGK1, miR-642a—PIGR, and miR-134—YWHAZ.

Validation group saliva was used to determine if the candidate biomarkers identified in the Discovery group analysis correlated with TMD or FI. Proteomic analysis identified 12 of the 14 proteins altered in the Discovery group to be present in Validation group exosomes and, while not statistically significant, the mean fold change in CSTB, DDP4, FABP5, PIGR, and YWAZ

maintained an inverse relationship with changes in TMD score. Additionally, PGK1 maintained and positive but weak correlation with changes in FI score. It should be noted that the magnitude of TMD and FI difference scores in the validation group was significantly smaller than those of the Discovery group, which may make biomarker validation more challenging and is most likely evidenced by a lack of statistical significance. When the magnitude of FI score differences is considered, PGK1 would be an interesting protein for continued evaluation as a biomarker of cognitive fatigue. When the Validation group and Discovery group data were combined, the abundance of the other six candidate biomarkers (DPP4, BPIFA2, CA6, AMY1A, LEG1, and DMBT1) were still significantly altered between pre- and post-work saliva but were not determined to be associated with either TMD or FI. This notable observation highlights that many of the originally identified potential biomarkers may be associated with biological processes altered by work alone that are not impacted by changes in TMD or FI score. Therefore, these proteins may still have value as biomarkers of biologically relevant phenomena unrelated to mood- and fatigue-associated cognitive impairment.

Of 13 miRNAs selected for continued evaluation in Validation group samples, the abundance of miR3185 was correlated with TMD and FI. miR3185 is of particular interest because it regulates the target gene PGK1, a protein identified as a potential biomarker correlated with fatigue [34]. The relation between miR3185 and PGK1 was strengthened by their inverse correlation, suggesting a potential biological mechanism for regulation of the PGK1 gene by miR3185 may be induced by fatigue. The inversely correlated levels of miR3185 and PGK1 could represent a coregulated set that is not only a biomarker of fatigue but could possibly contribute to a mechanism of fatigue induction or relief. The levels of miR3185 and PGK1 not only correlated with the degree

of mood disturbance assessed by the POMS FI subscale, but the correlation extended beyond increased FI to decreased FI; among subjects whose PoMS FI difference was negative (reduced fatigue), miR3185 increased, and PGK1 decreased.

PGK1 deficiency is associated with anemia syndromes that include the progressive onset of weakness, fatigue, and lassitude [35] and motor neuron vulnerability in spinal muscular atrophy (SMA) [36]. The increase in PGK1 with increased mood disturbance may represent a compensatory response to boost energy levels, but this is speculative and might be elucidated by following PGK1 levels in salivary exosomes over time during a demanding work shift.

Little is known about miR3185, other than it is specific to primate genomes [37] and reported to be increased in cardiac tissues in cases of mechanical asphyxia [38] as well as associated with increased survival in liver cancer [39]. PGK1 and miR3185 are both attractive biomarker targets that could potentially be used to detect the onset of mood- and fatigue-associated cognitive impairment in salivary exosomes.

There were some important limitations to this exploratory study for saliva biomarkers. The PoMS questionnaire determines total mood disturbance, and not specifically CF, but two subscales—fatigue–inertia (FI) and confusion–bewilderment (CB)—that were significantly worsened in the Discovery group very likely affect cognitive performance, as previously reported for PoMS-determined fatigue [2]. Confirmation of this association will require further study and the use of objective CF-specific testing. We further note that work shifts were not controlled for time of day, that is, the impact of circadian rhythm on exosomal content or for the activity levels of each of the

participants, which could affect their reported PoMS scores. We did not calculate effect sizes for comparison in the present study. Additionally, while the findings from neuron-derived exosomes suggest concordance/overlap with findings from global analysis of exosomes isolated without neuron-specific markers, these selected exosomes were from a single participant, and the findings require validation with greater *n* numbers. Similarly, the miRNA/protein biomarkers described require validation. Further, while some of the candidate biomarkers have interesting reported roles in fatigue or CFS, the analysis performed here does not establish a causal relationship between the PoMS TMD score/fatigue-inertia score and the changes in exosomal content pre- and post-shift. In conclusion, our study identified proteins and miRNAs in salivary exosomes that correlate with changes in mood state and fatigue as measured by the PoMS questionnaire. They represent possible biomarkers that can be quantified using saliva with the potential to reveal an increased risk for loss of vigilance and decline in cognitive performance. These results add to the growing knowledge of detectable changes in the biomolecular composition of exosomes in various pathologies and point to a promising candidate biomarker, PGK1, in saliva, as well as suggest a possible mechanism in which expression of the PGK1 gene is regulated by miR3185 in response to changes in fatigue. This salivary biomarker requires further clinical validation in larger well-defined cohorts. The limitations of the current study were the small sample size and the potential inaccuracies associated with subjective self-assessment of mood states. Despite these limitations, this study demonstrates the value of using an integrated multiomics approach to the identification of novel mechanisms and biomarkers in salivary exosomes, with the possibility of developing a rapid saliva-based antigen test for cognitive fatigue.

7. Methods

7.1. Participants

Donors were recruited from UCLA medical and dental residents. A total of 36 residents participated. The research was approved by the UCLA IRB committee (UCLA IRB # 17-000317). Residents were given information about the research, and they gave oral consent for participation in this study.

7.2. Whole Saliva Collection

Saliva samples were collected over a period of 60 min immediately before and following a 12 h work shift in 50 mL conical tubes. Samples were centrifuged (2600 ref, 4 °C, 15 min), and the supernatants were aliquoted (1 mL) in microcentrifuge tubes containing Superase RNase inhibitor (1 µL, Thermo Fisher Scientific, Cat #AM2694, Waltham, MA, USA) and stored at –80 °C until processing.

7.3. The Profile of Mood States (PoMS) Questionnaire

Mood states were accessed using a modified version of the PoMS questionnaire [40,41,42,43]. This consisted of a 62-item inventory of six subscales: tension–anxiety (TA), depression–dejection (DD), anger–hostility (AH), vigor–activity (VA), fatigue–inertia (FI), and confusion–bewilderment (CB). Responses were provided on a 5-point scale ranging from 1 (not at all) to 5 (extremely). The global indicator Total Mood Disturbance (TMD) is defined as: $TMD = (AH + CB + DD + FI + TA) - VA$. An increase in TMD suggests the onset of mood disturbances that would be considered unfavorable for optimum vigilance and cognitive performance, such as increased fatigue which has been associated with increased cognitive fatigue and decreased

cognitive performance [2]; decreases in TMD reflect positive changes in mood, for example, a decrease in tension and anxiety.

7.4. Separation of Saliva Samples by PoMS TMD Score

Based on TMD scores, subject saliva samples were assigned to 3 groups, the Test group, Discovery group, or Validation group (Figure 6), similarly to a previously reported approach used for the analysis of saliva samples for biomarkers of traumatic brain injury [16]. The Test group comprised saliva from 6 participants with a negative TMD difference, that is, those who reported no change or an improvement in mood as a result of the work shift. The Discovery group comprised 20 subjects with the greatest increase in TMD score post shift. Saliva samples from both groups underwent exosome isolation followed by proteomics and Nanostring miRNA analyses. The Validation group consisted of 10 subjects with nearly unchanged or slightly increased or decreased TMD post-shift scores. For the Validation group, the same methods were used as for the other two groups, but proteomics were targeted for select proteins, and qPCR was performed for select genes. These groups were established based on the hypothesis that potential biomarkers of fatigue ‘discovered’ in individuals reporting fatigue (Discovery group) could be tested for their potential as biomarkers in the group that reported an opposite ‘improved’ change in mood (Test group) based on the supposition that these biomarkers would either be unchanged or change in the opposite direction in the Test group. The potential biomarkers were again ‘validated’ in the group with a mix of scores (Validation group).

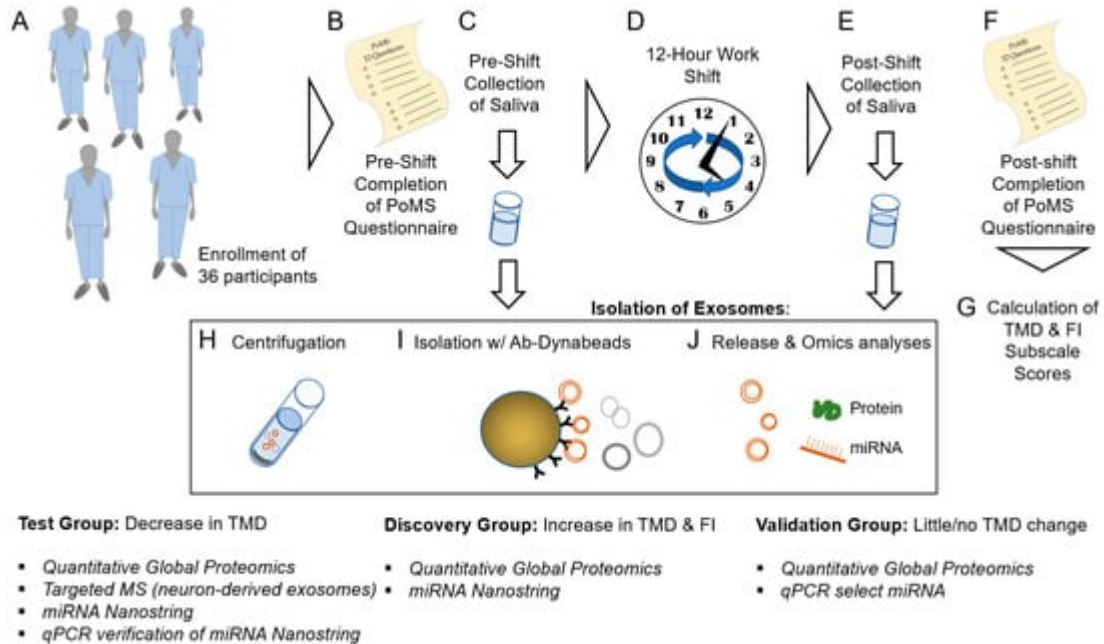


Figure 6. Study flow scheme for Profile of Mood States (PoMS) assessment, sample collection, processing, and analysis. (A) Resident participants ($n = 36$) were enrolled. (B) Participants completed the PoMS questionnaire and (C) collected saliva before a (D) 12 h work shift. (E) Saliva was collected, and the (F) PoMS questionnaire completed again after the work shift. (G) Total Mood Disturbance (TMD) and subscale (for example, fatigue–inertia, FI) scores were calculated. Isolation of exosomes comprised (H) centrifugation, (I) binding of exosomes to exosome marker-specific (and in one instance, neuronal-marker specific) antibody-conjugated Dynabeads, (J) release of exosomes for processing, and omics analyses. Based on TMD, participant samples were separated into Test (decrease in TMD or ‘improved’ mood), Discovery (increased in TMD or mood disturbance), and Validation (little/no change in TMD) groups. Exosomes from each group underwent the analyses shown.

7.5. EV Isolation and Enrichment for Exosomes

Salivary EVs were isolated using magnetic microsphere-based immunoprecipitation (IP) modified from established methods [44]. Frozen saliva aliquots were thawed at 37 °C, spiked with HALT Protease and Phosphatase Inhibitor Cocktail (Thermo Fisher Scientific, Cat # 78440, Waltham, MA, USA), and diluted threefold with ice-cold phosphate-buffered saline (PBS) and centrifuged (13,000 rcf, 20 min, 4 °C). Supernatants were then incubated (overnight, 4 °C) with a mixture of antibodies specific for various exosomal surface markers, including tetraspanins CD9, CD63, and CD81 (all Thermo Fisher Scientific, Cat # 10626D, 10628D, and 10630D, respectively, Waltham, MA, USA) that were previously desalted (Zeba™ Spin Desalting Columns, 7K MWCO, 0.5 mL, Thermo Fisher Scientific Cat # 89882, Waltham, MA, USA) and conjugated to Dynabeads (Invitrogen DYNAL Dynabeads M-270 Epoxy, Thermo Fisher Scientific Cat # 14301, Waltham, MA, USA) according to the manufacturer's protocols. The isolated exosomes were used for bottom-up proteomics by mass spectroscopy (MS) and miRNA analysis.

For isolation of salivary exosomes originating from neurons (performed for a single participant in the Test Group), Dynabeads conjugated to antibodies specific for a neuronal surface marker CD171 (Thermo Fisher Scientific, Cat # MA5-14140, Waltham, MA, USA) was used. After incubation, the diluted saliva samples with Dynabeads were set on a magnetic bar for 1 min, after which supernatant was discarded. The beads destined for proteomics analysis were subsequently washed once with 1× PBS, twice with 0.15 M citrate phosphate buffer (pH 5.2), and once again with 1× PBS. For beads destined for miRNA analysis, 0.1% BSA was added to both 1× PBS washes. The isolated exosomes were used for targeted proteomics by MS.

7.6. Quantitative Global Proteomics Analysis

Preliminary protein quantification assays indicated that the amount of total protein in samples post immunoprecipitation-based EV enrichment from saliva was very low (<2 µg). Because of the limited amount of protein in each sample, protein levels were normalized after the proteomic analysis. After the proteins were digested with trypsin, peptides from each sample were chemically modified with different isobaric tandem mass tag (TMT) labeling reagents. Upon isolation and subsequent fragmentation of each peptide, reporter ions corresponding to each TMT reagent provide relative abundances for those peptides in each sample. Thermo Scientific Proteome Discoverer software uses this data to calculate the relative amount of total protein in each sample, which is used to normalize the data post analysis via liquid chromatography-tandem mass spectrometry

Immunoprecipitated exosomes were eluted from the Dynabeads at 95 °C for 5 min in lysis buffer (100 µL, 12 mM sodium lauroyl sarcosine, 0.5% sodium deoxycholate, 50 mM triethylammonium bicarbonate (TEAB), Halt™ Protease, and Phosphatase Inhibitor Cocktail), then subjected to bath sonication (10 min, Bioruptor Pico, Diagenode Inc.; Denville, NJ, USA). The samples were treated with tris (2-carboxyethyl) phosphine (10 µL, 55 mM in 50 mM TEAB, 30 min, 37 °C), followed by treatment with chloroacetamide (10 µL, 120 mM in 50 mM TEAB, 30 min, 25 °C in the dark). They were then diluted fivefold with aqueous 50 mM TEAB and incubated overnight with Sequencing Grade Modified Trypsin (1 µg in 10 µL of 50 mM TEAB; Promega, Cat # V511A, Madison, WI, USA). Following this, an equal volume of ethyl acetate/trifluoroacetic acid (TFA, 100/1, v/v) was added, and after vigorous mixing (5 min) and centrifugation (13,000× g, 5 min), the supernatants were discarded, and the lower phases were dried in a centrifugal vacuum concentrator. The samples were then desalted using a modified version of Rappsilber's protocol

[45], in which the dried samples were reconstituted in acetonitrile/water/TFA (solvent A, 100 μ L, 2/98/0.1, v/v/v) and then loaded onto a small portion of a C18-silica disk (3M, Maplewood, MN, USA) placed in a 200 μ L pipette tip. Prior to sample loading, the C18 disk was prepared by sequential treatment with methanol (20 μ L), acetonitrile/water/TFA (solvent B, 20 μ L, 80/20/0.1, v/v/v), and finally with solvent A (20 μ L). After loading the sample, the disc was washed with solvent A (20 μ L, eluent discarded) and eluted with solvent B (40 μ L). The collected eluent was dried in a centrifugal vacuum concentrator. The samples were then chemically modified using a TMT11plex Isobaric Label Reagent Set (Thermo Fisher Scientific, Cat # A34808, Waltham, MA, USA) as per the manufacturer's protocol. The TMT-labeled peptides were dried and reconstituted in solvent A (50 μ L), and an aliquot (2 μ L) was taken for measurement of total peptide concentration (Pierce Quantitative Colorimetric Peptide, Thermo Fisher Scientific, Waltham, MA, USA). The samples were then pooled and desalted again using the modified Rappsilber's protocol. The eluants were then dried and reconstituted in water/acetonitrile/FA (solvent B, 10 μ L, 98/2/0.1, v/v/v), and aliquots (5 μ L) were injected onto a reverse-phase nanobore HPLC column (AcuTech Scientific, C18, 1.8 μ m particle size, 360 μ m \times 20 cm, 150 μ m ID, San Diego, CA, USA), equilibrated in solvent E, and eluted (500 nL/min) with an increasing concentration of solvent F (acetonitrile/water/FA, 98/2/0.1, v/v/v: min/% F; 0/0, 5/3, 18/7, 74/12, 144/24, 153/27, 162/40, 164/80, 174/80, 176/0, 180/0) using an Eksigent NanoLC-2D system (Sciex, Framingham, MA, USA)). The effluent from the column was directed to a nanospray ionization source connected to a hybrid quadrupole-Orbitrap mass spectrometer (Q Exactive Plus, Thermo Fisher Scientific, Waltham, MA, USA), acquiring mass spectra in a data-dependent mode alternating between a full scan (350–1700 m/z, automated gain control (AGC) target 3×10^6 , 50 ms maximum injection time, FWHM resolution 70,000 at 200 m/z) and up to 15 MS/MS scans (quadrupole isolation of charge

states 2–7, isolation window 0.7 m/z) with previously optimized fragmentation conditions (normalized collision energy of 32, dynamic exclusion of 30 s, AGC target 1×10^5 , 100 ms maximum injection time, FWHM resolution 35,000 at 200 m/z).

7.7. Proteomics Analysis

Raw proteomic data were searched against the Uniprot human-reviewed protein database using SEQUEST-HT in Proteome Discoverer (Version 2.4, Thermo Scientific, Waltham, MA, USA), which provided measurements of abundances for identified peptides in each sample that were normalized to total protein amount. Decoy database searching was used to identify high confidence tryptic peptides (FDR < 1%). Tryptic peptides containing amino acid sequences unique to individual proteins were used to identify and provide relative quantification between proteins in each sample. Normalized protein abundances for pre- and post-work samples from each participant were scaled so that the average abundance was 100. Median abundance values of all replicates from each condition were used to generate abundance ratios for each protein (post-work/pre-work).

7.8. Protein Bioinformatics Analysis

Proteins exhibiting a fold change with a magnitude ≥ 1.2 and a p value ≤ 0.1 were subject to comprehensive gene-set enrichment-analysis gene ontology (GO) classification and KEGG [24] pathway analysis using Enrichr (Chen et al., 2013), as well as functional protein association network analysis using the STRING database (version 11.5), which was used for functional interpretation of the proteomics data and provided p -values corrected by the FDR method [25]. The relatively high p value of ≤ 0.1 was set due to the limited number of samples that were available for analysis; the selection of a higher significance threshold allowed us to expand the

number of proteins to be assessed as potential biomarkers of fatigue in the Validation group so that potential biomarkers would not be excluded. We note that this significance value was only used for the selection of proteins for the additional analyses reported above and not for the final presentation of findings of potential biomarkers.

7.9. Targeted LC-MS/MS Protein Quantification

Proteins isolated by antibody-conjugated microbeads were reduced, alkylated, and treated with trypsin as described in *Global Proteomics Analysis*; however, in contrast with that sample processing protocol, no isotopically labeled chemical tags were utilized to provide relative quantification between peptides in different samples. Furthermore, the data were acquired with the mass spectrometer utilizing a customized target-selected ion monitoring/data-dependent MS/MS (t-SIM/dd-MS²) method in which an inclusion list was used to isolate and fragment select peptides corresponding to specific proteins and measure precursor ion peak areas. Data from the global proteomic analysis were used to identify unique peptides for this analysis and select the correct m/z (Da) and charge state (Z) of each peptide targeted. The sensitivity gained by the targeted analysis using the SIM scan (AGC target 2×10^5 , 130 ms maximum injection time, FWHM resolution 70,000 at m/z 200, isolation window 2.0 m/z) permitted modification of the LC gradient (min/% F; 0/0, 5/3, 55/22, 61/35, 63/80, 73/80, 75/0, 79/0) and shortening of mass spectrometer acquisition time.

7.10. Global miRNA Analysis

RNA was extracted from the immunoprecipitated salivary exosomes using the SeraMir Exosome RNA Column Purification Kit (System Biosciences, Palo Alto, CA, USA) according to the

manufacturer's protocol. The quality of the RNA was assessed via electrophoresis using the Small RNA Kit (Agilent Technologies, Santa Clara, CA, USA) on a 2100 Bioanalyzer System (Agilent Technologies) according to the manufacturer's instructions. Global profiling of miRNA from Test and Discovery group samples was completed at the UCLA Center for Systems Biomedicine with the nCounter Human v3 miRNA Expression Assay (NanoString Technologies; Seattle, WA, USA), in which 800 pairs of probes specific for a predefined set of biologically relevant miRNAs were combined with a series of internal controls to form a Human miRNA Panel CodeSet (NanoString Technologies, Seattle, WA, USA). miRNA (100 ng) targets of interest were hybridized overnight with two juxta-positioned probes: a biotinylated capture probe and a uniquely fluorescently labeled reporter probe for each target. The hybridized samples were then transferred to the nCounter Prep Station, where excess probes were removed, and the target–probe complexes were immobilized and aligned on the surface of a flow cell using an automated liquid handler. The unique sequences of the reporter probes were counted using the nCounter Digital Analyzer and translated into the number of counts per miRNA target. nSolver Analysis Software (NanoString Technologies, Seattle, WA, USA) was used to facilitate data extraction and analysis. In Nanostring analysis, the raw miRNA counts were normalized (corrected for multiple testing) using positive control (spike-in) normalization and the geometric mean of the top 100 expressed miRNAs, performed using the Benjamini–Hochberg method within the Nanostring nSolver software.

7.11. Targeted miRNA Analysis

Quantitative polymerase chain reaction (qPCR) was used to verify the miRNA levels detected in the NanoString analysis. For verification, the same RNA samples that were used in the NanoString analysis were assayed for select miRNAs using the TaqMan Advanced miRNA Assay (Thermo

Fisher Scientific, Cat # A25576, Waltham, MA, USA) according to the manufacturer's protocol. qPCR amplification Ct values for each resident's pre- and post-shift samples were compared using the $\Delta\Delta C_t$ method and converted to a % change in miRNA levels (post-work—pre-work) for each subject. The RNA yield from exosomes isolated from 1 mL of saliva was, on average, 208 +/- 44 ng. This yield is comparable to published reports of saliva exosome RNA yields, specifically 209–274 ng/mL of salivary exosomes [46].

7.12. Identification of miRNA Target Genes

Target genes associated with miRNAs exhibiting significant changes in abundance in response to work shifts were identified using miRNet [47]. Proteins corresponding to these genes were subsequently checked for and identified in the list of proteins identified in the global proteomics analysis. Potential miRNA target genes were identified when the direction of change in the abundance of a miRNA was opposite that of a protein encoded by its regulated gene.

7.13. Statistical Analysis

PoMS analysis. Both pre- and post-shift PoMS scores from all 36 residents were included in the analysis. Wilcoxon signed-rank test was used for the paired comparison between pre- and post-work shifts. The analysis was performed using SAS version 9.4 (SAS Institute Inc., Cary, NC, USA).

Proteomics analysis. A Student's *t*-test was used to determine if the observed differences in protein abundances between pre- vs. post-work for each group were statistically significant ($p < 0.05$).

The p value of ≤ 0.1 described above was solely used to select proteins for further analysis and assessment in the Validation group and not for the identification of potential biomarkers of fatigue. miRNA analysis. A paired t -test was used to identify miRNAs exhibiting significant changes in abundance in response to work shifts (fold change magnitude ≥ 1.2 ; p value < 0.05). For identifying miRNA associated with PoMS scales in the discovery group, median values of FI and TMD pre- and post-work were calculated, and candidate miRNA biomarkers were determined using the Wilcoxon ranked-sum test with a false discovery rate (q) of < 0.05 .

7.14. Study Design

The study design and flow scheme, including enrollment, saliva collection, and PoMS assessment pre- and post-work shift, calculation of TMD and subscales scores for separation into Test, Discovery, and Validation groups, and exosome isolation and analyses are shown in **Figure 1**.

Supplementary Materials

The following supporting information can be downloaded at: <https://www.mdpi.com/article/10.3390/ijms23095257/s1>.

Author Contributions

W.C. performed proteomics analysis and cowrote the manuscript; C.Z. recruited participants and performed exosome isolation; J.C. recruited participants and collected samples/questionnaires; T.B. performed exosome isolation and electron microscopy; F.L. and D.T.W.W. recruited participants, collected samples/questionnaires, performed saliva sample initial processing; R.G. and D.E. modified the PoMS questionnaire, adapted it to a digital format and analyzed PoMS data

that enabled segregation of saliva specimens in groups; P.S. cogenerated figures and cowrote the manuscript; G.M.C. contributed to the study design, specifically methods of exosome isolation); A.A. provided expert advice on the PoMS questionnaire analysis, segregation of saliva specimens into groups, and constructing the salivary nsEV intercellular signaling network and cellular response map; K.F.F. and J.W. provided MS instrumentation and helped with proteomics experimental design and edited the manuscript; B.T. performed qPCR for miR assessment and cowrote the manuscript; V.J. codesigned the study, provided resources and supervision, and edited the manuscript. All authors have read and agreed to the published version of the manuscript.

Funding

This Research was funded by the Air Force Office of Scientific Research (AFOSR) Grant, FA9550-17-1-0399, to the John Drug Discovery Lab and the APC was funded by unrestricted funds from the John lab. Funding from PHS grant UG3/UH3 TR002978 supported Drs Wong and Li.

Institutional Review Board Statement

The study was conducted in accordance with the Declaration of Helsinki, and approved by UCLA Institutional Board (UCLA IRB #17-000317 approved on 22 March 2017).

Informed Consent Statement

Informed oral consent was obtained from all subjects involved in the study.

Acknowledgments

We would like to thank Patrick Bradshaw, Program Officer of the AFOSR grant, for valuable insights on the design of the study. We would also like to thank Emmanuelle Faure-Kumar of the UCLA Molecular Technologies Core for advice and assistance with NanoString analysis of the salivary exosomes and Swapna Joshi for statistical analysis of NanoString results. We would like to thank Pete Heinzelman for his contribution to the submission of the AFOSR grant. We would like to thank Asa Hatami for his assistance in developing protocols for exosome isolation from saliva.

Conflicts of Interest

Author David Wong has equity in Liquid Diagnostics LLC and RNAmETRIX Inc. He is consultant to Colgate Palmolive and GlaxoSmithKline. Other authors declare no conflict of interest.

References

1. Lorist, M.M.; Boksem, M.A.; Ridderinkhof, K.R. Impaired cognitive control and reduced cingulate activity during mental fatigue. *Cogn. Brain Res.* 2005, *24*, 199–205.
2. Fogt, D.L.; Kalns, J.E.; Michael, D.J. A comparison of cognitive performance decreases during acute, progressive fatigue arising from different concurrent stressors. *Mil. Med.* 2010, *175*, 939–944.
3. Holtzer, R.; Shuman, M.; Mahoney, J.R.; Lipton, R.; Verghese, J. Cognitive fatigue defined in the context of attention networks. Neuropsychology, development, and cognition. *Aging Neuropsychol. Cogn.* 2011, *18*, 108–128.
4. Hudson, A.N.; Van Dongen, H.P.A.; Honn, K.A. Sleep deprivation, vigilant attention, and brain function: A review. *Neuropsychopharmacology* 2020, *45*, 21–30.
5. Meeusen, R.; Van Cutsem, J.; Roelands, B. Endurance exercise-induced mental fatigue and the brain. *Exp. Physiol.* 2021, *106*, 2294–2298.
6. Cocucci, E.; Meldolesi, J. Ectosomes and exosomes: Shedding the confusion between extracellular vesicles. *Trends Cell Biol.* 2015, *25*, 364–372.
7. Multhoff, G.; Hightower, L.E. Distinguishing integral and receptor-bound heat shock protein 70 (Hsp70) on the cell surface by Hsp70-specific antibodies. *Cell Stress Chaperones* 2011, *16*, 251–255.
8. Ghosh, A.; Davey, M.; Chute, I.C.; Griffiths, S.G.; Lewis, S.; Chacko, S.; Barnett, D.; Crapoulet, N.; Fournier, S.; Joy, A.; et al. Rapid isolation of extracellular vesicles from cell culture and biological fluids using a synthetic peptide with specific affinity for heat shock proteins. *PLoS ONE* 2014, *9*, e110443.

9. Yáñez-Mó, M.; Siljander, P.R.; Andreu, Z.; Zavec, A.B.; Borràs, F.E.; Buzas, E.I.; Buzas, K.; Casal, E.; Cappello, F.; Carvalho, J.; et al. Biological properties of extracellular vesicles and their physiological functions. *J. Extracell. Vesicles* 2015, 4, 27066.
10. Irwin, M.R.; Wang, M.; Campomayor, C.O.; Collado-Hidalgo, A.; Cole, S. Sleep deprivation and activation of morning levels of cellular and genomic markers of inflammation. *Arch. Intern. Med.* 2006, 166, 1756–1762.
11. Carroll, J.E.; Cole, S.W.; Seeman, T.E.; Breen, E.C.; Witarama, T.; Arevalo, J.M.; Ma, J.; Irwin, M.R. Partial sleep deprivation activates the DNA damage response (DDR) and the senescence-associated secretory phenotype (SASP) in aged adult humans. *Brain Behav. Immun.* 2016, 51, 223–229.
12. Zhu, B.; Dong, Y.; Xu, Z.; Gompf, H.S.; Ward, S.A.; Xue, Z.; Miao, C.; Zhang, Y.; Chamberlin, N.L.; Xie, Z. Sleep disturbance induces neuroinflammation and impairment of learning and memory. *Neurobiol. Dis.* 2012, 48, 348–355.
13. Gottshall, J.L.; Guedes, V.A.; Pucci, J.U.; Brooks, D.; Watson, N.; Sheth, P.; Gabriel, A.; Mithani, S.; Leete, J.L.; Lai, C.; et al. Poor Sleep Quality is linked to elevated extracellular vesicle-associated inflammatory cytokines in warfighters with chronic mild traumatic brain injuries. *Front. Pharmacol.* 2022, 12, 762077.
14. Ferreira, J.N.; Hoffman, M.P. Interactions between developing nerves and salivary glands. *Organogenesis* 2013, 9, 199–205.
15. Dominy, S.S.; Brown, J.N.; Ryder, M.I.; Gritsenko, M.; Jacobs, J.M.; Smith, R.D. Proteomic analysis of saliva in HIV-positive heroin addicts reveals proteins correlated with cognition. *PLoS ONE* 2014, 9, e89366.

16. Di Pietro, V.D.; Porto, E.; Ragusa, M.; Barbagallo, C.; Davies, D.; Forcione, M.; Logan, A.; Di Pietro, C.; Purrello, M.; Grey, M.; et al. Salivary MicroRNAs: Diagnostic Markers of Mild Traumatic Brain Injury in Contact-Sport. *Front. Mol. Neurosci.* 2018, *11*, 290.
17. Ciregia, F.; Giusti, L.; Valle, Y.D.; Donadio, E.; Consensi, A.; Giacomelli, C.; Sernissi, F.; Scarpellini, P.; Maggi, F.; Lucacchini, A.; et al. A multidisciplinary approach to study a couple of monozygotic twins discordant for the chronic fatigue syndrome: A focus on potential salivary biomarkers. *J. Transl. Med.* 2013, *11*, 243–257.
18. Bermejo-Pareja, F.; Antequera, D.; Vargas, T.; Molina, J.; Carro, E. Saliva levels of Aβ₁₋₄₂ as potential biomarker of Alzheimer's disease: A pilot study. *BMC Neurol.* 2010, *10*, 108.
19. Shi, M.; Sui, Y.T.; Peskind, E.R.; Li, G.; Hwang, H.; Devic, I.; Gingham, C.; Edgar, J.S.; Pan, C.; Goodlett, D.R.; et al. Salivary tau species are potential biomarkers of Alzheimer's disease. *J. Alzheimers Dis.* 2011, *27*, 299–305.
20. Fiandaca, M.S.; Kapogiannis, D.; Mapstone, M.; Boxer, A.; Eitan, E.; Schwartz, J.B.; Abner, E.L.; Petersen, R.C.; Federoff, H.J.; Miller, B.L.; et al. Identification of preclinical Alzheimer's disease by a profile of pathogenic proteins in neurally derived blood exosomes: A case-control study. *Alzheimers Dement.* 2015, *11*, 600–607.
21. Tanaka, M.; Mizuno, K.; Yamaguti, K.; Kuratsune, H.; Fujii, A.; Baba, H.; Matsuda, K.; Nishimae, A.; Takesaka, T.; Watanabe, Y. Autonomic nervous alterations associated with daily level of fatigue. *Behav. Brain Funct.* 2011, *7*, 46.
22. Proctor, G.B.; Carpenter, G.H. Regulation of salivary gland function by autonomic nerves. *Auton. Neurosci.* 2007, *133*, 3–18.

23. Chen, E.Y.; Tan, C.M.; Kou, Y.; Duan, Q.; Wang, Z.; Meirelles, G.V.; Clark, N.R.; Ma'ayan, A. Enrichr: Interactive and collaborative HTML5 gene list enrichment analysis tool. *BMC Bioinform.* 2013, *14*, 128.
24. Kanehisa, M.; Goto, S. KEGG: Kyoto encyclopedia of genes and genomes. *Nucleic Acids Res.* 2000, *28*, 27–30.
25. Szklarczyk, D.; Gable, A.L.; Lyon, D.; Junge, A.; Wyder, S.; Huerta-Cepas, J.; Simonovic, M.; Doncheva, N.T.; Morris, J.H.; Bork, P.; et al. STRING v11: Protein-protein association networks with increased coverage, supporting functional discovery in genome-wide experimental datasets. *Nucleic Acids Res.* 2019, *47*, D607–D613.
26. Pihur, V.; Datta, S.; Datta, S. Meta analysis of Chronic Fatigue Syndrome through integration of clinical, gene expression, SNP and proteomic data. *Bioinformatics* 2011, *6*, 120–124.
27. Casado, B. and Baraniuk, J.N. Abstract: Decreased Mucosal Protein Secretion in the Nonallergic Rhinitis of Chronic Fatigue Syndrome. *J. Allergy Clin. Immunol.* 2009, *123*, S260.
28. Maes, M.; Twist, F.N.; Kubera, M.; Ringel, K. Evidence for inflammation and activation of cell-mediated immunity in myalgic encephalomyelitis/chronic fatigue syndrome (ME/CFS): Increased interleukin-1, tumor necrosis factor- α , PMN-elastase, lysozyme and neopterin. *J. Affect. Disord.* 2012, *136*, 933–939.
29. Savitski, M.M.; Mathieson, T.; Zinn, N.; Sweetman, G.; Doce, C.; Becher, I.; Pachel, F.; Kuster, B.; Bantscheff, M. Measuring and managing ratio compression for accurate iTRAQ/TMT quantification. *J. Proteome Res.* 2013, *12*, 3586–3598.

30. Nie, H.; Ju, H.; Fan, J.; Shi, X.; Cheng, Y.; Cang, X.; Zheng, Z.; Duan, X.; Yi, W. O-GlcNAcylation of PGK1 coordinates glycolysis and TCA cycle to promote tumor growth. *Nat. Commun.* 2020, *11*, 36.
31. Barber, T.M.; Bhatti, A.A.; Elder, P.J.D.; Ball, S.P.; Calvez, R.; Ramsden, D.B.; Cuthbertson, D.J.; Pfeiffer, A.F.; Burnett, D.; Weickert, M.O. AMY1 Gene Copy Number Correlates with Glucose Absorption and Visceral Fat Volume, but Not with Insulin Resistance. *J. Clin. Endocrinol. Metab.* 2020, *105*, dgaa473.
32. Love, K.M.; Liu, Z. DPP4 Activity, Hyperinsulinemia, and Atherosclerosis. *J. Clin. Endocrinol. Metab.* 2021, *106*, 1553–1565.
33. Mitra, B.; Rau, T.F.; Surendran, N.; Brennan, J.H.; Thaveenthiran, P.; Sorich, E.; Fitzgerald, M.C.; Rosenfeld, J.V.; Patel, S.A. Plasma micro-RNA biomarkers for diagnosis and prognosis after traumatic brain injury: A pilot study. *J. Clin. Neurosci.* 2017, *38*, 37–42.
34. Vissing, J.; Akman, H.O.; Aasly, J.; Kahler, S.G.; Bacino, C.A.; DiMauro, S.; Haller, R.G. Level of residual enzyme activity modulates the phenotype in phosphoglycerate kinase deficiency. *Neurology* 2018, *91*, e1077–e1082.
35. David, D.; Almeida, L.S.; Maggi, M.; Araújo, C.; Imreh, S.; Valentini, G.; Fekete, G.; Haltrich, I. Clinical Severity of PGK1 Deficiency Due To a Novel p.E120K Substitution Is Exacerbated by Co-inheritance of a Subclinical Translocation t(3;14)(q26.33;q12), Disrupting NUBPL Gene. *JIMD Rep.* 2015, *23*, 55–65.
36. Boyd, P.J.; Tu, W.-Y.; Shorrock, H.K.; Groen, E.J.N.; Carter, R.N.; Powis, R.A.; Thomson, S.R.; Thomson, D.; Graham, L.C.; Motyl, A.A.L.; et al. Bioenergetic status modulates motor neuron vulnerability and pathogenesis in a zebrafish model of spinal muscular atrophy. *PLoS Genet.* 2017, *13*, e1006744.

37. Du, Z.-Q.; Yang, C.-X.; Rothschild, M.F.; Ross, J.W. Novel microRNA families expanded in the human genome. *BMC Genom.* 2013, *14*, 98.
38. Han, L.; Zhang, H.; Zeng, Y.; Lv, Y.; Tao, L.; Ma, J.; Xu, H.; Ma, K.; Shi, Q.; Xiao, B.; et al. Identification of the miRNA-3185/CYP4A11 axis in cardiac tissue as a biomarker for mechanical asphyxia. *Forensic Sci. Int.* 2020, *311*, 110293.
39. Pascut, D.; Pratama, M.Y.; Gilardi, F.; Giuffrè, M.; Crocè, L.S.; Tiribelli, C. Weighted miRNA co-expression networks analysis identifies circulating miRNA predicting overall survival in hepatocellular carcinoma patients. *Sci. Rep.* 2020, *10*, 18967.
40. McNair, D.; Lorr, M.; Droppleman, L. *Manual for the Profile of Mood States*; Educational and Industrial Testing Service: San Diego, CA, USA, 1971.
41. McNair, D.M. *Profile of Mood States*; Educational and Industrial Testing Service: San Diego, CA, USA, 1992.
42. Heuchert, J.P.; McNair, D.M. Profile of Mood States 2. Multi-Health Systems. APA Psych Tests Database. 2012.
43. Albrecht, R.R.; Ewing, S.J. Standardizing the administration of the Profile of Mood States (POMS): Development of alternative word lists. *J. Pers. Assess* 1989, *53*, 31–39.
44. Heinzelman, P.; Powers, D.; Wohlschlegel, J.; John, V. Shotgun Proteomic Profiling of Bloodborne Nanoscale Extracellular Vesicles. *Methods Mol. Biol.* 2019, *1897*, 403–416.
45. Rappsilber, J.; Mann, M.; Ishihama, Y. Protocol for micro-purification, enrichment, pre-fractionation and storage of peptides for proteomics using StageTips. *Nat. Protoc.* 2007, *2*, 1896–1906.

46. Michael, A.; Bajracharya, S.D.; Yuen, P.S.T.; Zhou, H.; Star, R.A.; Illei, G.G.; Alevizos, I. Exosomes from Human Saliva as a Source of microRNA Biomarkers. *Oral Dis.* 2010, *16*, 34–38.
47. Fan, Y.; Siklenka, K.; Arora, S.K.; Ribeiro, P.; Kimmins, S.; Xia, J. miRNet-dissecting miRNA-target interactions and functional associations through network-based visual analysis. *Nucleic Acids Res.* 2016, *44*, W135–W141.

CHAPTER 3

Small Molecule Epigenetic Modulators of Secreted Clusterin Promote Mitochondrial Function, Synaptic Plasticity and Proteostasis in an Alzheimer's Disease Mouse Model

Whitaker Cohn^{1,2}, Jesus Campagna¹, Jessica Tracy Lee¹, Dongwook Wi¹, Jose Angelo Grajeda¹, Ainsley Jackman¹, Jennifer An³, Chunni Zhu¹, Barbara Jagodzinska¹, Patricia Spilman¹, Brandon Han³, Robert Damoiseaux³, Julian Whitelegge², Varghese John¹

¹The Drug Discovery Lab, Mary S. Easton Center for Alzheimer's Disease Research, Department of Neurology, David Geffen School of Medicine, 710 Westwood Plaza, University of California Los Angeles, Los Angeles, CA 90095, USA

²Pasarow Mass Spectrometry Laboratory, Jane and Terry Semel Institute for Neuroscience and Human Behavior, David Geffen School of Medicine, 760 Westwood Plaza, University of California Los Angeles, Los Angeles, CA 90095, USA

³The Hinman Lab, Department of Neurology, David Geffen School of Medicine, 710 Westwood Plaza, University of California Los Angeles, Los Angeles, CA 90095, USA

⁴California NanoSystems Institute, 570 Westwood Plaza, University of California Los Angeles, Los Angeles, CA 90095, USA

ABSTRACT

Alzheimer's Disease (AD) is the most common form of dementia and is characterized by the gradual accumulation of amyloid- β (A β) plaques and tau neurofibrillary tangles in the brain, leading to significant inflammation, synaptic injury, and progressive neuronal degeneration. Though, despite a myriad of therapeutic approaches, disease-modifying treatment options for AD patients remain severely limited. Clusterin (CLU) is the third strongest genetic risk factor for late-onset Alzheimer's disease (LOAD). The secreted isoform (sCLU) mediates numerous cytoprotective functions with the ability to slow or reverse the various molecular mechanisms underlying AD pathophysiology. A "pharma" drug discovery model was used to identify potent, brain-permeable small molecules that increase levels of sCLU and to evaluate their effect on AD pathology. A high-throughput screening (HTS) campaign identified several 'hits' that increase sCLU levels, including histone deacetylase and bromodomain inhibitors. Various *in-vitro* ADME assays were utilized to assess the drug-like properties of these compounds and select candidates for pharmacokinetic/pharmacodynamic (PK/PD) analyses *in-vivo*. Exploratory medicinal chemistry was used to design novel sCLU enhancers with increased potency and oral brain bioavailability. Treatment of 5XFAD-ApoE4 (E4FAD) AD mice with the lead candidate, DDL-357, resulted in increased expression of sCLU as well as proteins integral to maintaining mitochondrial function, synaptic plasticity, and protein homeostasis. While additional research is needed to evaluate the full extent of sCLU's involvement, this drug discovery effort has undoubtedly shed light on a valuable therapeutic approach that warrants further evaluation as a treatment for AD.

Key Words: Clusterin, Alzheimer's Disease, BET Inhibitor, Drug Discovery

INTRODUCTION

Alzheimer's Disease (AD) is the most common form of dementia and is characterized by the gradual accumulation of amyloid- β ($A\beta$) plaques and tau neurofibrillary tangles in the brain, leading to significant inflammation, synaptic injury, and progressive neuronal degeneration (Ref. 1, 2). Currently, more than 50 million people worldwide are living with AD, making it the seventh leading cause of death in the United States. In 2021 alone, AD cost the nation \$355 billion, and it is projected that this number of cases will triple by 2050, imposing an unprecedented burden on society and the healthcare system (Ref. 3, 4). Despite numerous therapeutic approaches, including 143 agents in clinical trials as of 2022, treatment options for AD patients remain severely limited (Ref. 3). Of the three classes of FDA-approved drugs, namely acetylcholinesterase inhibitors and N-methyl D-aspartyl (NMDA) receptor antagonists, only provide temporary symptomatic relief without halting disease progression (Ref. 5, 6). Recently, two $A\beta$ -directed antibodies, aducanumab and lecanemab, demonstrated the ability to reduce $A\beta$ plaques and slow cognitive decline in clinical trials (Ref. 3). These therapies received authorization under the FDA's accelerated approval pathway, highlighting the urgent need for novel disease-modifying therapeutic targets. Furthermore, it may be necessary to develop multifaceted therapies that target both the primary disease pathogenesis and the additional cellular stress responses associated with AD pathophysiology.

While familial forms of the disease typically result from mutations in genes for amyloid precursor protein (APP), presenilin (PSEN1), and presenilin 2 (PSEN2), the etiology of sporadic or late-onset Alzheimer's disease (LOAD) is still largely unknown (Ref. 1, 7). LOAD, accounting for approximately 95% of all AD cases, is considered a multifactorial disease that depends on the

complex interaction of both genetic and environmental risk factors (Ref. 7). The third strongest genetic risk factor for LOAD is a single nucleotide polymorphism (SNP) in a gene that encodes clusterin (CLU), a multifunctional chaperone protein directly involved in a wide range of AD-associated biological processes, including A β and Tau metabolism, lipid transport, immune modulation, oxidative stress, and cell apoptosis (Ref. 8-10). Interestingly, seven CLU gene variants have been associated with AD, and individuals carrying the C allele of the rs11136000 SNP show increased A β and Tau deposition, faster cognitive decline, and decreased expression of the secreted clusterin isoform (sCLU) compared to other isoforms (Ref. 9, 11-19). Consequently, extensive research on CLU in different disease states, including neurodegeneration, cardiovascular disease, and cancer, has led to the prevailing hypothesis that sCLU promotes cytoprotection, while intracellular isoforms have pro-apoptotic properties (Ref. 8).

The most significant protective function of sCLU is its role in regulating protein homeostasis within the central nervous system (CNS) (**Fig. 1**). Extensive research has demonstrated its ability to bind and prevent the aggregation of toxic, misfolded proteins, including α -synuclein, TDP-43, A β , and Tau (**Fig. 1A**) (Ref. 20-23). Moreover, sCLU is recognized as a crucial mediator of A β clearance from the brain. Its strong affinity for A β and endocytic receptors such as LRP2 and TREM2 enables efficient transportation of toxic A β species across the blood-brain barrier (BBB) or into glial cells for lysosomal degradation (**Fig. 1B, 1C**) (Ref. 24-26). Additionally, sCLU exhibits high binding affinity with ApoER2 and VLDLR, inducing reelin signaling and a corresponding decrease in tau phosphorylation (p-tau) (**Fig. 1D**) (Ref. 27-29). Extensive evidence supports the role of sCLU in protecting against oxidative stress, harmful immunological changes, and synaptic deficits, all of which are prominent pathological features contributing to the

progression of AD (**Fig. 1E, 1F, 1G**) (Ref. 30-37). Notably, peripheral administration of human recombinant sCLU in an AD mouse model has been shown to reduce A β accumulation in the brain and cerebral arteries, as well as alleviate associated hippocampal neuronal loss and pro-inflammatory markers (Ref. 38). As scientific literature continues to accumulate, the therapeutic potential of sCLU in preventing the molecular processes underlying AD becomes increasingly apparent. It has not escaped our notice that the mechanisms described here immediately suggest that increasing sCLU levels could represent a broader therapeutic approach for treating additional proteinopathies, such as Parkinson's disease and amyotrophic lateral sclerosis.

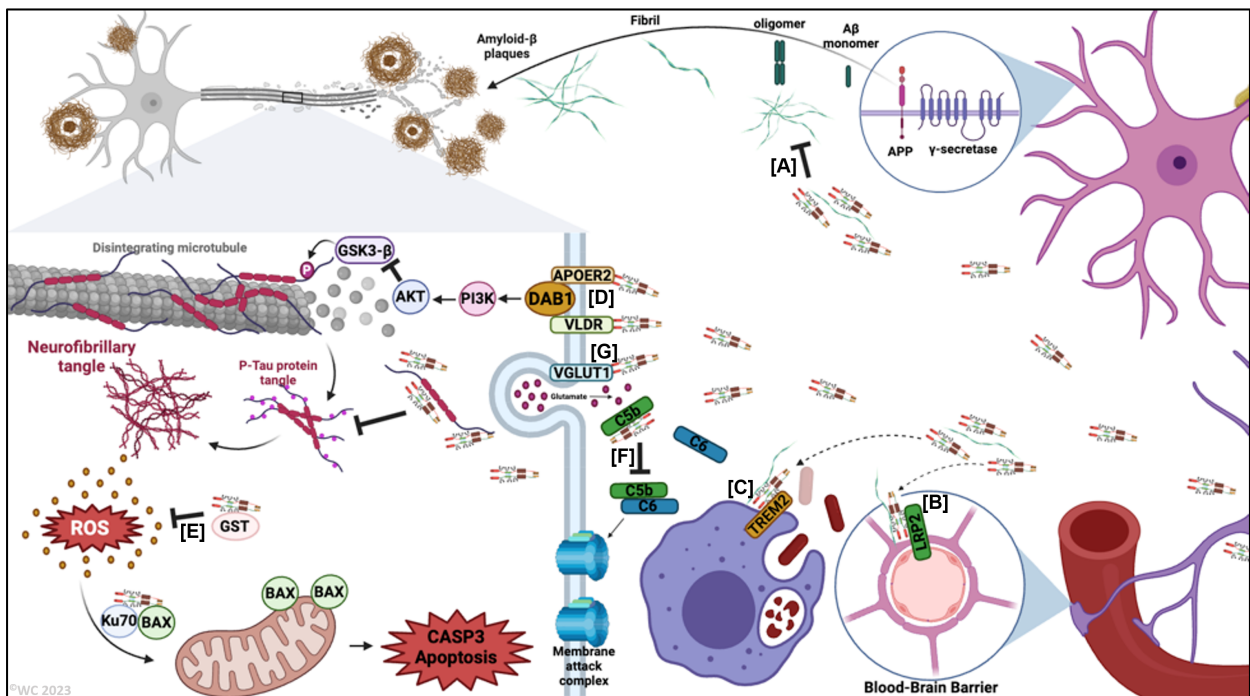


Figure 1. *Molecular mechanisms of secreted clusterin for preventing Alzheimer's disease.* (A) sCLU binds and prevent the aggregation of A β . (B) sCLU interacts with LRP2 to transports A β species across the blood-brain barrier into the periphery. (C) sCLU interacts with TREM2 to transport A β into glial cells for lysosomal degradation. (D) sCLU interacts with APOER2 and VLDR to induce reelin signaling, which decreases tau phosphorylation by inhibiting GSK3 β . (E)

sCLU prevents oxidative stress and associated CASP3-mediated apoptosis. (F) sCLU prevents assembly of the membrane attack complex and associated apoptosis. (G) sCLU interacts with VGLUT1 to stimulate excitatory neurotransmission.

This manuscript describes a comprehensive research program to identify potent, brain permeable, small molecules that increase levels of sCLU and to evaluate their effect on AD pathology. This was accomplished using a well-established drug discovery and development strategy involving high-throughput screening (HTS) to identify compounds or ‘hits’ with potent sCLU enhancing ability, *in-vitro* absorption, distribution, metabolism, excretion and toxicity (ADMET) assays and *in-vivo* pharmacokinetics (PK) analyses to assess drug-likeness and guide hit selection, exploratory medicinal chemistry to design novel sCLU enhancers, and further efficacy testing in AD patient-derived neural cells and 5XFAD-ApoE4 (E4FAD) mice. This study demonstrates the value using this approach to identify novel therapeutics and to determine which are likely to be effective *in-vivo*. The lead drug candidates described here represent a promising new therapeutic paradigm with the potential to prevent AD progression through numerous mechanisms, including, but not limited to the reducing disease-causing A β plaques and Tau neurofibrillary tangles, as well as promoting mitochondrial function, synaptic plasticity, and protein homeostasis.

METHODS

Human sCLU AlphaLISA

Cell culture supernatant (2 μ L) was added to a 384-well proxy plate preloaded with AlphaLISA HiBlock buffer (2 μ L, 1X, CAT#AL004C, Perkin Elmer). Then an anti-sCLU antibody mixture (2 μ L, mAb J84, biotinylated (10 nM, Cat# 3717-6-1000, Mabtech) and mAb CLU aa 22-227

(Cat#AF7084, R&D Systems), Acceptor bead conjugated (50 $\mu\text{g}/\text{mL}$, Cat#6772001, Perkin Elmer) was added and incubated at room temperature for 1 hour. AlphaScreen Streptavidin Donor beads (2 μL , Cat#6760002S, Perkin Elmer) were added, incubated for an additional 30 minutes in the dark, and the plate was read in an Envision plate reader.

Mouse sCLU ELISA

Brain tissue was homogenized and diluted to a protein concentration of 50 ng/mL . The Mouse Clusterin ELISA Kit (Cat#ab199079, Abcam) was performed according to the manufacturer's protocol.

High Throughput Screening

Human glioblastoma U-87 MG cells were proliferated in EMEM with 10% FBS and 1% P/S (complete medium) in 10 cm dishes until approximately 90% confluent. Following trypsinization, a suspension of 2×10^5 cells/mL (25 μL) were added to 384-well plates containing complete medium (25 μL) and library compounds from 9 plates (5 μM). After incubation for 30 hours at 37 $^\circ\text{C}$ and 5% CO_2 , 2 μL of cell culture supernatant were analyzed via human sCLU AlphaLISA as described above. Cell culture medium and cells were added to the 384-well plates using the MultiDrop. The BioMek FX was used to pin the drugs and transfer the cell culture supernatant. The MANTIS liquid handler was used to added human sCLU AlphaLISA reagents.

Dose Response Analysis

Human glioblastoma U-87 MG cells were proliferated in EMEM with 10% FBS and 1% P/S (complete medium) in 10 cm dishes until approximately 90% confluent. Following trypsinization,

a suspension of 2×10^5 cells/mL (25 μ L) were added to 384-well plates containing complete medium (25 μ L) with various concentrations of compounds (5, 14, 41, 123, 370, 1111, 3333, 10000 nM). After incubation for 30 hours at 37 °C and 5% CO₂, 2 μ L of cell culture supernatant were analyzed via human sCLU AlphaLISA as described above.

Cell Viability and Toxicity Analysis

Cell viability and toxicity were simultaneously assessed using the MultiTox-Fluor Multiplex Cytotoxicity Assay (Cat# PRG9200, Fisher Scientific) according to the manufacturer's protocol.

Compound Synthesis via Amide Coupling

(S)-2-(4-(4-chlorophenyl)-2,3,9-trimethyl-6H-thieno[3,2-f][1,2,4]triazolo[4,3-a][1,4]diazepin-6-yl)acetic acid (1 equiv), amine-containing reagent (2 equiv), 1-Ethyl-3-(3-dimethylaminopropyl)carbodiimide (EDC; 2 equiv.), Hydroxybenzotriazole (HOBT; 2 equiv.), and N-N, Diisopropylethylamine (DIPEA; 2.5 equiv.) were added to a round bottom flask. The reagents were solubilized using methylene chloride and the reaction mixture was stirred at room temperature for 16 hours. The crude product was concentrated in vacuo and then purified via flash column chromatography. A mobile phase of hexanes:ethyl acetate (time/% ethyl acetate: 0/0, 2/0, 7/50, 15/100, 20/0) was first utilized to elute any existing impurities, and the product was eluted in the DCM:MeOH mobile phase (time/%MeOH: 0/0, 4/0, 35/15, 42/20, 45/50, 50/0). Identity and purity of each compound was confirmed via LC-MS, LC-UV/Vis, and ¹H NMR.

Compound Synthesis via Ester Coupling

(S)-2-(4-(4-chlorophenyl)-2,3,9-trimethyl-6H-thieno[3,2-f][1,2,4]triazolo[4,3-a][1,4]diazepin-6-yl)acetic acid (1 equiv), alcohol-containing reagent (3 equiv), and 4-Dimethylaminopyridine (DMAP; 2 equiv) were added to a round bottom flask. The reagents were solubilized using methylene chloride (800 μ L) and was brought to 0 $^{\circ}$ C in an ice bath. A solution of diisopropylcarbodiimide (DIC; 2 equiv) in methylene chloride (200 μ L) was added dropwise over the course of 30 minutes and then slowly brought to room temperature. After stirring for 24 hours, the reaction mixture was filtered through a filter funnel and concentrated in vacuo. The crude product was purified via flash column chromatography. A mobile phase of hexanes:ethyl acetate (time/% ethyl acetate: 0/0, 2/0, 7/50, 15/100, 20/0) was first utilized to elute any existing impurities, and the product was eluted in the DCM:MeOH mobile phase (time/%MeOH: 0/0, 4/0, 35/15, 42/20, 45/50, 50/0). Identity and purity of each compound was confirmed via LC-MS, LC-UV/Vis, and 1 H NMR .

Liver Microsome Stability Assay

An aliquot (1 μ L) of test compound (1 mM, 100% DMSO) was added to an aqueous liver microsome solution (1000 μ L, PBS pH 7.4, 0.5mg/mL human liver microsomes (Thermo Fisher Scientific, Cat#HMMPL), 2 mM NADPH, 2 mM MgCl₂) and incubated at 37 $^{\circ}$ C for 120 min. Aliquots (50 μ L) of the microsome solution were taken at various time points (0, 5, 10, 15, 30, 60, 90, 120 min) and added to a reaction quenching solution (200 μ L 100% Acetonitrile) containing an internal standard. Solutions were clarified by centrifugation (16,000 x g, 5 min), and the supernatants were transferred to new tubes and lyophilized. Samples were reconstituted in 100 μ L of 50/50/0.1 (Water/Acetonitrile/Formic Acid) prior to analysis via liquid chromatography-tandem mass spectrometry (LC-MS/MS). Chromatographic peak areas normalized to the internal standard

were plotted at each time point and the half-life ($t_{1/2}$) of compound in liver microsomes was determined by using the trendline equation to calculate the time at which compound abundance was 50% of that at time point 0 (t_0).

Plasma and Brain Tissue Binding Assays

Brain tissue was homogenized in PBS (pH 7.4) (1: 3 weight(mg)/volume(μ L)) and the protein concentration was determined using the Micro BCA™ Protein Assay Kit (Thermo Fisher Scientific, Cat#23235). Brain homogenate was clarified and diluted to 20 mg/mL in PBS (pH 7.4). Either brain homogenate or plasma was and added to Slide-A-Lyzer™ MINI Dialysis Devices, 10K MWCO dialysis cups (Thermo Fisher Scientific, Cat#PI88401) in a 48-well plate containing PBS (500 μ L; pH 7.4). 1 μ L of 1 mM compound was added to the brain homogenate (Final Concentration: 2 μ M compound, 0.5% DMSO) and incubated on a rocker for 4.5 hours at 37 °C. 50 μ L of brain homogenate or plasma (within the dialysis cup) and PBS (within the 48-well plate) were transferred to new microcentrifuge tubes containing 400 μ L of quenching reagent (100% Acetonitrile) containing internal standard. Solutions were clarified by centrifugation (16,000 x g, 5 min), and the supernatants were transferred to new tubes and lyophilized. Samples were reconstituted in 100 μ L of 50/50/0.1 (Water/Acetonitrile/Formic Acid) prior to analysis via liquid chromatography-tandem mass spectrometry (LC-MS/MS). The % of the unbound drug ($f_{u, \text{bound}}$) was calculated using the following equation:

$$\% \text{ Bound} = [1 - (\text{PBS chromatographic peak area} / \text{brain homogenate or plasma chromatographic peak area})] \times 100$$

Blood-Brain Barrier (BBB) Permeability Assay

A liquid chromatography-ultraviolet/visible spectroscopy (LC-UV/Vis) assay was performed on a 1290 Infinity HPLC system (Agilent Technologies) with an HPLC column containing immobilized phosphatidylcholine (IAM.PC.DD, Regis Technologies, Cat#774011, 5 μ m 300 Å 100 x 4.6 mm). The HPLC method was a mixture of 6.7 mM phosphate buffer saline (pH 7.4; solvent A) and acetonitrile (solvent B), and a gradient was used for the elution of the compounds (min/%B: 0/20, 20/60, 21/20, 30/20). The retention time of the compound (t_r) and void volume time of the column (t_0) were recorded. Blood-brain barrier (BBB) permeability (P_m) was calculated using the following equations as described by Yoon et al (DOI: 10.1177/1087057105281656):

$$K_{IAM} = (t_r - t_0) / t_0 ; P_m = (K_{IAM} / MW^4) \times 10^{10}$$

Compounds with a $P_m > 0.85$ were determined to be BBB permeable (CNS+) at pH 7.

In-Vivo Pharmacokinetics

Following oral administration of compound via pipette feeding, mice brain tissue and plasma were collected after euthanasia and perfusion at 1, 2, 4, 6 and 8 hours. Brain tissue were homogenized in a bead beater using 5 volumes of ice-cold 80% acetonitrile (1/5; mg of brain/ μ L of 80% ACN). Plasma analytes were extracted using 4 volumes of ice-cold acetonitrile (1/4; μ L of plasma/ μ L of ACN). Solutions were clarified by centrifugation (16,000 x g, 5 min) and the supernatants were transferred to new tubes and lyophilized. Samples were reconstituted in 100 μ L of 50/50/0.1 (Water/Acetonitrile/Formic Acid) prior to analysis via liquid chromatography-tandem mass spectrometry (LC-MS/MS). An internal standard (IS) was added to every sample to account for compound loss during sample processing. Standards were made in drug naïve plasma and brain lysates with increasing amounts of analyte (S1,S2: 0 pmol/ S3,S4: 1 pmol/ S5,S6: 10 pmol/ S7,S8: 100 pmol, S9,S10: 1000 pmol). The standard curve was made by plotting the known amount of

analyte per standard vs. the ratio of measured chromatographic peak areas corresponding to the analyte over that of the IS (analyte/IS). The trendline equation was then used to calculate the absolute concentrations of each compound in plasma and brain tissue.

Kinetic Solubility

Test compound (10 mM, 100% DMSO) was diluted separately into aqueous buffer (100 μ M; PBS pH 7.4) and DMSO at various concentrations (500, 250, 125, 62.5, 31.3, 15.6, 7.8, 3.9, 2, 1 μ M). The solutions were then incubated at 37 ° C for 90 min and centrifuged (16000xg, 5 min). An aliquot of each supernatant is analyzed by UV/Vis (if possible) or LC-MS/MS. A standard curve was made by plotting the known amount of analyte per standard in DMSO vs. absorbance or chromatographic peak area. Kinetic solubility (mM) was calculated using the trendline equation with maximum absorbance or chromatographic peak area observed in the aqueous sample.

Liquid Chromatography-Tandem Mass Spectrometry

Analysis of compound levels was done at the UCLA Pasarow Mass Spectrometry Lab (PMSL; Julian Whitelegge, Ph.D., Director). A targeted LC-MS/MS assay was developed for each compound using the multiple reaction monitoring (MRM) acquisition method on a 6460 triple quadrupole mass spectrometer (Agilent Technologies) coupled to a 1290 Infinity HPLC system (Agilent Technologies) with a Phenomenex analytical column (Kinetex 1.7 μ m C18 100 Å 100 x 2.1 mm). The HPLC method utilized a mixture of solvent A (99.9/1 Water/Formic Acid) and solvent B (99.9/1 Acetonitrile/Formic Acid) and a gradient was used for the elution of the compounds (min/%B: 0/1, 3/1, 19/99, 20/1, 30/1). Two fragment ions originating from each compound were monitored at specific LC retention times to ensure specificity and accurate

quantification in the complex biological samples. The normalized chromatographic peak areas were determined by taking the ratio of measured chromatographic peak areas corresponding to each compound over that of the internal standard (Analyte/IS).

Proteomics

Hippocampus were homogenized in lysis buffer (12 mM sodium lauroyl sarcosine, 0.5% sodium deoxycholate, 50 mM triethylammonium bicarbonate (TEAB), Halt™ Protease and Phosphatase Inhibitor Cocktail (Thermo Fisher Scientific)), the samples were reduced and alkylated with tris(2-carboxyethyl)phosphine (10 mM) and chloroacetamide (40 mM) for 30 minutes at 95 °C, and then digested with trypsin (20 ug) for 16 hours at 37 °C. The samples were then isotopically labeled (TMT18plex Isobaric Label Reagent Set, Thermo Fisher Scientific) according to the manufacturer's protocol to provide relative quantitation between samples. The samples were then fractionated separately via high pH reversed-phase chromatography (Pierce™ High pH Reversed-Phase Peptide Fractionation Kit) as per manufacturer's protocol for increased proteome coverage. Aliquots of each fraction were injected onto a reverse phase nanobore HPLC column (AcuTech Scientific, C18, 1.8um particle size, 360 um x 20 cm, 150 um ID), equilibrated in solvent A (water/acetonitrile/FA, 98/2/0.1, v/v/v) and eluted (300 nL/min) with an increasing concentration of solvent B (acetonitrile/water/FA, 98/2/0.1, v/v/v: min/% F; 0/0, 5/3, 18/7, 74/12, 144/24, 153/27, 162/40, 164/80, 174/80, 176/0, 180/0) using an EASY-nLC II (Thermo Fisher Scientific). The effluent from the column was directed to a nanospray ionization source connected to a hybrid quadrupole-Orbitrap mass spectrometer (Q Exactive Plus, Thermo Fisher Scientific) acquiring mass spectra in a data-dependent mode alternating between a full scan (m/z 350-1700, automated gain control (AGC) target 3 x 10⁶, 50 ms maximum injection time, FWHM resolution 70,000 at

m/z 200) and up to 15 MS/MS scans (quadrupole isolation of charge states 2-7, isolation window 0.7 m/z) with previously optimized fragmentation conditions (normalized collision energy of 32, dynamic exclusion of 30 s, AGC target 1×10^5 , 100 ms maximum injection time, FWHM resolution 35,000 at m/z 200). Raw proteomic data were searched against a Uniprot database containing the complete human proteome using SEQUEST-HT (including dynamic modifications: oxidation (+15.995) on M, deamidation (+0.984) on N/Q, and carbamidomethyl (+57.021), phosphorylation (+79.966) on S/T/Y) in Proteome Discoverer (Version 2.4, Thermo Scientific), which provided measurements of relative abundance of the identified peptides. Decoy database searching was used to generate high confidence tryptic peptides (FDR < 1%). Tryptic peptides containing amino acid sequences unique to individual proteins were used to identify and provide relative quantification between different proteins in each sample. Post-translationally modified peptides from each protein were normalized to protein abundance and peptides exhibiting a p-value ≤ 0.05 with a log₂-fold change ≥ 0.5 were analyzed using a series of bioinformatics tools including functional protein association network analysis, comprehensive gene set enrichment gene ontology (GO) classification and pathway analysis, as well as kinase substrate enrichment analyses.

Neurite Outgrowth Assay in iPSC-Derived Human Neurons.

The iPSC derived human neurons were provided by the Kornblum lab to be cultured in normal growth conditions (37°C, 5% CO₂) for 2-3 days. Cells were cultured in CELLSTAR uClear 384 well plates, PS, F bottom at seeding density of 5000 cells per well coated overnight with 30ug/mL poly-D-lysine and 2 ug/mL laminin. Media was replaced every 3 days with Lonza Primary Neuron Basal Medium (PNBM) supplemented with 2mM L-glutamine, GA-1000, and 2% NSF-1. On day

3, cells were treated with DDL357 in doses ranging from 15,000nM to 0.76 nM for 48 hours. All compounds were diluted in 0.5% DMSO and pinned to 384 well plates with 25 μ L of cell media per well with pin size of 250 nL using BioMek FX (Beckman Coulter, CA). After 48 hours, media was replaced twice to ensure removal of any remaining compound residues before imaging for neurite outgrowth with Calcein-AM and Hoescht. Imaging was done at UCLA Molecular Screening Shared Resource core facility (MSSR; Robert Damoiseaux, Ph.D., Director) with ImageXpress Confocal (Molecular Devices, CA) using a 10x objective. Total neurite outgrowth was measured via a MetaXpress (Molecular Devices, CA) neurite outgrowth analysis algorithm. Neurite outgrowth was set to detect cell bodies with approximate width of $\geq 20\mu\text{m}$ and outgrowth with maximal width of $5\mu\text{m}$ and length of $\geq 100\mu\text{m}$ with intensity of 1000 grey scales over background. Mean neurite outgrowth per drug exposure was determined by normalizing to vehicle control (n = 60). Neurite outgrowth assay data were compared using a two-way ANOVA for drug effect and concentration. Internal standards were designed in each plate with controls of untreated neurons (n = 24) and vehicle controls of neurons treated with 0.5% DMSO (n = 60) since all compounds were dissolved in 0.5% DMSO - the concentration that showed no signs of cell toxicity from previous studies.

RESULTS

HTS Identifies HDAC and BET Inhibitors to Increase sCLU Levels in U-87 MG cells

A customized AlphaLISA immunoassay developed and optimized to quantify sCLU secreted from human U-87 MG glioblastoma cells in a 384-well plate format was utilized to screen nine UCLA drug libraries consisting of 2,880 FDA-approved compounds at a concentration of 5 μM (**Fig. 2A**). Three of the thirty-two compounds chosen for confirmatory retesting in triplicate significantly

increased sCLU relative to DMSO treated controls (**Fig. 2B**). The validated hits comprised of the histone deacetylase (HDAC) inhibitor, vorinostat, the bromodomain and extraterminal protein (BET) inhibitor, I-BET151, and the naturally occurring alkaloid, piperlongumine that are known to inhibit the activity of proteins that recognize acetylated histone motifs (**Fig. 2C**). Further testing of additional structurally diverse compounds confirmed that HDAC and BET inhibitors increase sCLU in U-87 MG cells (**Fig. 2D**). A dose response analysis identified the BET inhibitors to be significantly more potent than the HDAC inhibitors (**Fig. 2E**). I-BET151 and (+)-JQ1 both demonstrated low nanomolar potency, increasing sCLU with EC_{50} 's of 234 nM and 70 nM, respectively. Vorinostat and belinostat, on the other hand, both had EC_{50} 's in the micromolar range at 1626 nM and 1164 nM, respectively. Testing of selective HDAC inhibitors determined HDAC1, HDAC3, and HDAC6 to be capable of increasing sCLU levels, but not as much as pan HDAC inhibitor, vorinostat (**Fig. 2F**). Testing of bromodomain (BD) selective inhibitors identified BD2 of BET proteins to be essential to the mechanism of enhancing sCLU (**Fig. 2G**). BD2 selective inhibitor, ABBV744, increased sCLU levels significantly at all tested concentrations. BD1 selective inhibitor, MS436, only increased sCLU at 5 μ M, a concentration at which it is no longer selective for just BD1. Dual treatment with both inhibitors did not have an additive effect on enhancing sCLU. Though, dual inhibition of both HDAC and BET proteins with vorinostat and I-BET151 did result in a significant synergistic increase in sCLU levels (**Fig. 2H**). Evaluation of both compounds in a cytotoxicity assay identified vorinostat to be significantly toxic to U-87 MG cells at concentrations greater than 5 μ M, while I-BET151 was well tolerated up to 50 μ M (**Fig. 2I**).

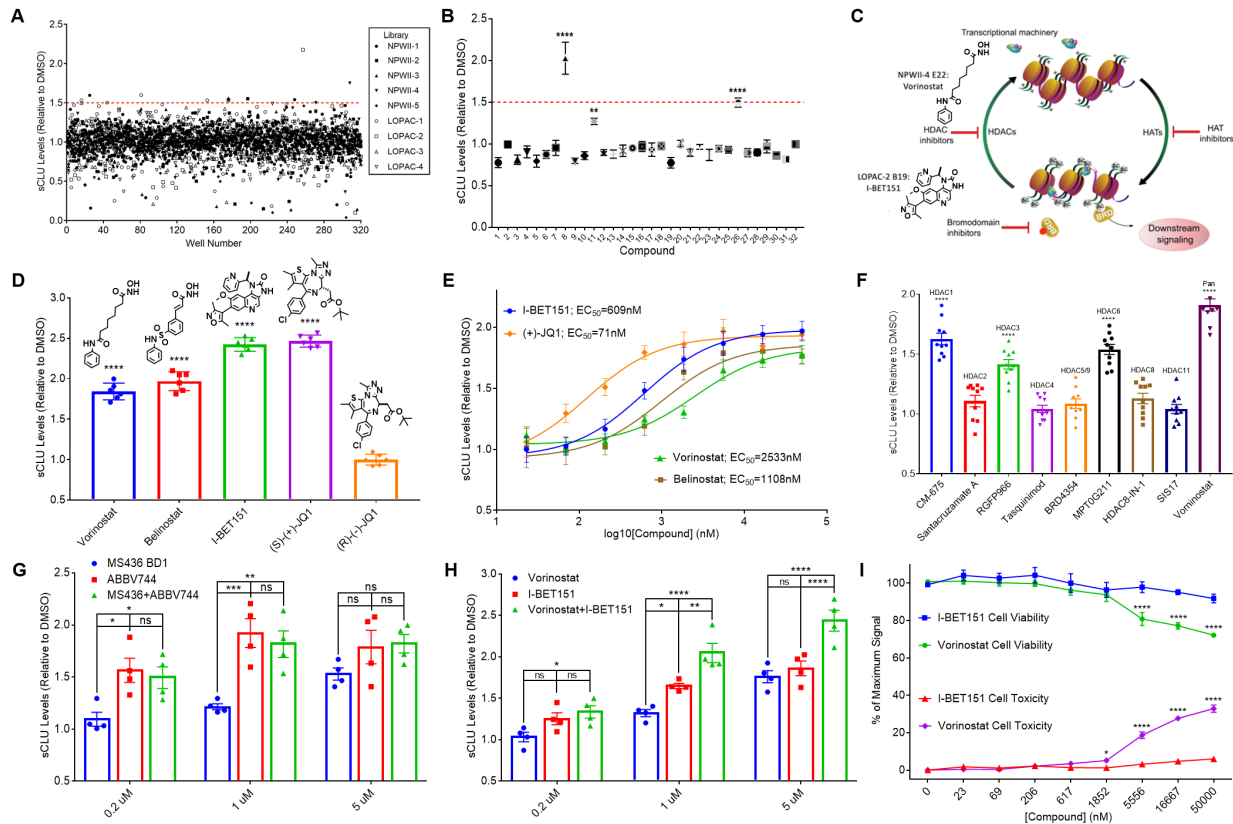


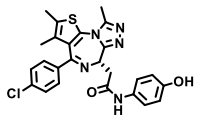
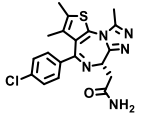
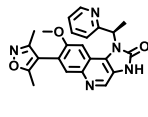
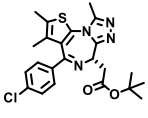
Figure 2. High-throughput screening identifies HDAC and BET inhibitors to increase sCLU levels in U-87 MG glioblastoma cells. (A) sCLU levels from a high-throughput screening of LOPAC and Prestwick chemical libraries at a concentration of 5 μ M in U-87 MG glioblastoma cells. (B) sCLU levels from the retesting of 32 compounds selected from the high-throughput screen in triplicate. (C) Schematic showing the molecular relationship between HDAC inhibitor, vorinostat, and BET inhibitor, I-BET151. (D) sCLU levels following treatment with HDAC inhibitors (vorinostat and belinostat), BET inhibitors (I-BET151 and (+)-JQ1), and the inactive enantiomer of (+)-JQ1 ((-)-JQ1). (E) Dose-response curves showing sCLU levels and calculated EC_{50} values for vorinostat (2533 nM), belinostat (1108 nM), I-BET151 (609 nM), and (+)-JQ1 (71 nM), following treatment at concentrations of 2, 7, 206, 62, 185, 556, 1667 and 5000 nM. (F) sCLU levels following testing of isoform selective HDAC inhibitors (CM-675, santacruzamate A, RGFP966, tasquinimod, BRD4354, MPT0G211, HDAC8-IN-1, SIS17) and vorinostat at a concentration of 5 μ M.

(G) sCLU following testing of bromodomain selective inhibitors, MS436 and ABBV744, independently and jointly at concentrations of 0.2, 1 and 5 μ M. (H) sCLU following testing of vorinostat and I-BET151 independently and jointly at concentrations of 0.2, 1 and 5 μ M. (I) Live and dead U-87 MG cell measures following treatment with vorinostat or I-BET151 at 23, 69, 206, 617, 1852, 5556, 16667 and 50000 nM. All results graphed as mean \pm SEM. All statistics were performed with a two-way ANOVA (* p < 0.05; ** p < 0.001; *** p < 0.0001; **** p < 0.00001).

Hit-to-Lead Optimization Identifies Candidates with Good ADME Properties

Optimization efforts led to the synthesis of ten new chemical entities (NCEs) and physiochemical evaluation of nineteen different BET inhibitors for the purposes of identifying the sCLU enhancers likely to be successful therapeutics *in-vivo* (**Table 1**). Two general synthetic approaches were utilized to synthesize novel analogs of the known BET inhibitor (+)-JQ1. The synthesis of the validated analogs DDL-351, -355, -356, -357, and -358, was made possible by performing an ester coupling reaction between the commercially available (+)-JQ1 carboxylic acid (1 equiv) and an alcohol-containing substituent (2 equiv), in the presence of 4-Dimethylaminopyridine (DMAP; 2 equiv) and diisopropylcarbodiimide (DIC; 2 equiv) (**Fig. 3A**). The synthesis of DDL-352, -353, -354, and -359, was made possible by performing an amide coupling reaction between the (+)-JQ1 carboxylic acid (1 equiv) and an amide-containing substituent (2 equiv), in the presence of 1-Ethyl-3-(3-dimethylaminopropyl)carbodiimide (EDC; 2 equiv.), Hydroxybenzotriazole (HOBt; 2 equiv.), and N-N, Diisopropylethylamine (DIPEA; 2.5 equiv.) (**Fig. 3B**). Bromodomain-containing protein 2 and 4 (BRD2/4) inhibition assays and sCLU levels were subsequently used to identify the ester-containing analogs as significantly more potent (**Fig. 3C, 3D**). Of these compounds, DDL-357 exhibited the greatest potency *in-vitro* with BRD2/4 IC₅₀'s of 161 and 20

nM and a sCLU EC₅₀ of 18 nM (**Fig. 3C**). Assessment of biological activity of each analog, it was clear that the ester-containing analogs were significantly more potent than the amide-containing analogs (**Fig. 3C, 3D**). To determine which compounds were likely to demonstrate therapeutic efficacy *in-vivo*, various *in-vitro* assays were used to assess physiochemical properties that influence compound absorption, distribution, metabolism, excretion (ADME). This included the assessment of compound solubility, liver microsome stability, plasma binding, brain tissue binding and blood-brain-barrier permeability (**Table 1**). Desired *in-vitro* ADME property values and go/no go criteria for continued evaluation *in-vivo* are as follows: Aqueous Kinetic Solubility > 50 μM; Liver Microsomal Stability t_{1/2} > 1 hours; Plasma Binding < 90%; Brain Tissue Binding < 80%; BBB Permeability P_m > 0.85 = CNS+; *In-Vitro* Efficacious Dose < 100 nM. Only one known BET inhibitor, (+)-JQ1 PA, and three NCEs, DDL-356, DDL-357, and DLL-360, met these strict ADME criteria. Of these compounds, DDL-357 exhibited the greatest potency *in-vitro* with an EC₅₀ of 18 nM, and was therefore chosen as lead candidate for further efficacy testing *in-vivo*.

Compound	Structure	Molecular Weight [Da]	Kinetic Solubility [μM]	Microsomal Stability [t _{1/2} (min)]	Plasma Binding [% Bound]	Brain Tissue Binding [% Bound]	BBB Permeability PAMPA [P _m]	In-Vitro Efficacious Dose [sCLU EC ₅₀ (nM)]
Birabresib		491.99	77.7	116	95.36	88.5	0.95	56
CPI-203		399.9	>100	>120	76.59	46.41	1.4	52
I-BET 151		415.44	>100	>120	93.63	68.46	1.28	609
(+)-JQ1		456.99	86.5	27	85.44	87.06	1.44	71

(+)-JQ1 PA		437.95	>100	116	87.44	63.56	1.2	61
MS417		414.91	>100	113	96.22	65.86	1.64	38
PFI-1		347.4	>100	>120	76.78	47.53	1.25	1170
PLX51107		438.48	>100	>120	74.82	66.99	0.39	162
DDL-351		483.03	57.5	3	99.04	94.11	1.35	73
DDL-352		468.02	>100	62	96.15	64.92	0.98	134
DDL-353		468.02	>100	8	93.88	79.08	1.08	105
DDL-354		500.01	91.1	12	91.11	67.06	0.76	97
DDL-355		454.97	63.7	27	86.16	88.64	1.42	27
DDL-356		456.95	>100	75	79.28	57.3	0.96	28
DDL-357		440.95	80	61	88.72	75.28	1.66	18

DDL-358		456.99	59.3	14	98.78	93.68	1.42	75
DDL-359		514.04	>100	13	94.9	44.96	0.7	162
DDL-360		415.9	>100	>120	88.85	59.3	1.09	81

*Desired physiochemical property values: Kinetic Solubility > 50 μM ; Microsomal Stability $t_{1/2}$ > 1 hours; Plasma Binding < 90%; Brain Tissue Binding < 80%; PAMPA P_m > 0.85 = CNS+; *In-Vitro* Efficacious Dose < 100 nM

Table 1. *Physiochemical Properties of Candidate sCLU Enhancers.*

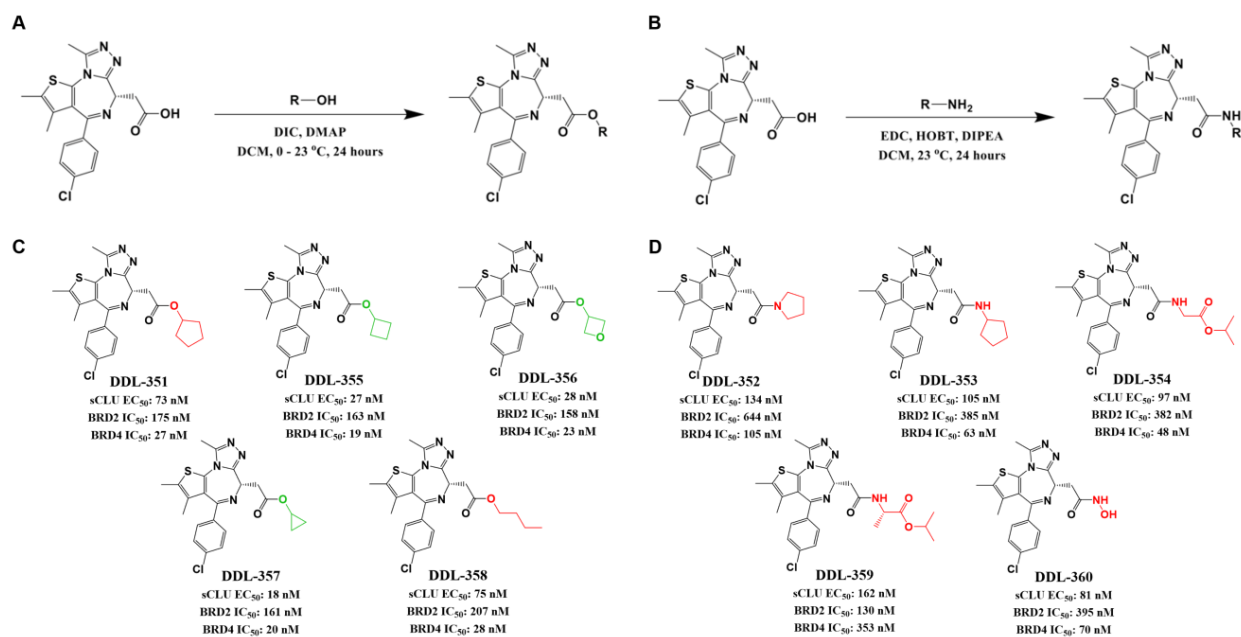


Figure 3. *Synthetic scheme for the synthesis of novel sCLU enhancers.* (A) General synthetic scheme used for the synthesis of ester-containing (+)-JQ1 analogs. (B) General synthetic scheme used for the synthesis of amide-containing (+)-JQ1 analogs. (C) The chemical structure and biological activity (sCLU EC₅₀, BRD2/4 IC₅₀'s) for ester-containing analogs, DDL-351, - 355, - 356, -357, and -358. The chemical structure and biological activity (sCLU EC₅₀, BRD2/4 IC₅₀'s) for amide-containing analogs, DDL-352, - 353, -354, -358, and -360. Green indicates a

modification that results in increase potency, relative to (+)-JQ-1. Red indicates a modification that results in decreased potency, relative to (+)-JQ-1.

Short-Term Administration of DDL-357 Promotes Mitochondrial Function, Synaptic Plasticity and Protein Homeostasis E4/FAD Mice

Proof-of-concept pharmacokinetic/pharmacodynamic (PK/PD) analyses were performed to see if the DDL-357 was orally brain bioavailable and capable of increasing sCLU levels in E4/FAD mice. *In-vivo* pharmacokinetics confirmed DDL-357 to brain bioavailable following oral administration via pipette feeding, reached a maximum brain concentration of 1850 nM, 1-hour post administration at a dose of 30 mg/kg (**Fig. 4A**). When brain tissue binding is considered (75.3%), the unbound brain concentration of DDL-357 is still 457 nM, which is almost 10-fold greater than the predetermined *in-vitro* efficacious dose ($EC_{50} = 50$ nM) (**Fig. 4A**). Based on these results, DDL-357 was chosen for short-term preclinical efficacy testing in four-month-old E4/FAD mice. Two-weeks of bidaily treatments at a dose of 15 mg/kg was determined to significantly increase sCLU levels in the hippocampus by approximately 1.3-fold, relative to vehicle treated controls (**Fig. 4B**). Interestingly, levels of Amyloid β 1-42 ($A\beta_{42}$) in the hippocampus were found to be decreased by approximately 1.3-fold (**Fig. 4C**). Though, unfortunately, due to high variability in $A\beta_{42}$ levels in this mouse model, this change was not significant. Subsequent mass-spectrometry-based proteomics analysis comparing DDL-357 and vehicle-treated hippocampal lysates identified many additional differentially expressed proteins (**Fig. 4D**). A gene-set enrichment gene ontology analysis was utilized to identify biological processes associated with proteins that were significantly upregulated at least 1.3-fold (**Fig. 4E**). There was notable enrichment of many AD-relevant biological processes such as but not limited to: Amyloid β

clearance by transcytosis, WNT signaling pathway, synaptic vesicle recycling, and protein localization to mitochondrion. The enrichment was used to identify disease-relevant genes that play a role in promoting synaptic plasticity, metabolic homeostasis, and/or protein homeostasis - biological processes that are well-known for being disrupted during the development of AD pathogenesis. (**Fig. 4F, Table 2**). Notably, many of the upregulated proteins have been previously identified to be decreased in AD patients (**Table 2**). The results of this analysis prompted the assessment of DDL-357 as a mediator of neurite outgrowth in Human iPSC-derived neurons. The extent of neurite outgrowth can be clearly visualized in images taken of DMSO and DDL-357 treated wells after 48 hours (**Fig. 5A, 5B**). Excitingly, DDL-357 exhibited a concentration-dependent increase in neurite outgrowth that plateaued at 1.5-fold at a concentration of only 7 nM, when compared to DMSO-treated controls (**Fig. 5C**).

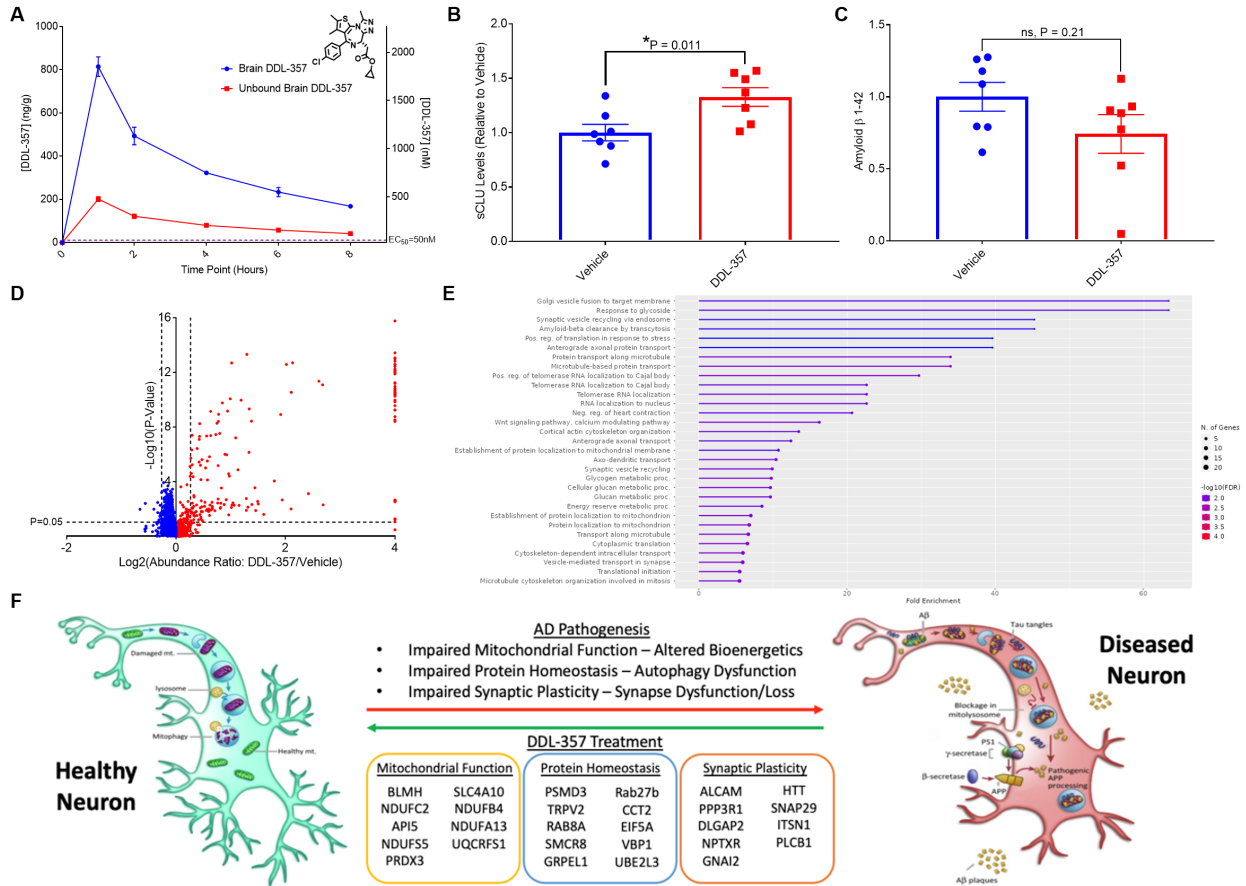


Figure 4. Short-term administration of DDL-357 promotes synaptic, metabolic, and protein homeostasis in E4/FAD mice. (A) DDL-357 brain concentrations (total and unbound), 1, 2, 4, 6 and 8 hours following oral administration at a dose of 30 mg/kg. (B) sCLU levels in the hippocampus of E4/FAD mice following administration of DDL-357 at a dose of 15 mg/kg or vehicle, bidaily, for two weeks. (C) Amyloid β 1-42 levels in the hippocampus of E4/FAD mice following administration of DDL-357 at a dose of 15 mg/kg or vehicle, bidaily, for two weeks. (D) Differences in the abundances of proteins, illustrated via volcano plot, in the hippocampus of E4/FAD mice following administration of DDL-357 at a dose of 15 mg/kg or vehicle, bidaily, for two weeks. The $-\log_{10}(p\text{-value})$ is plotted against $\log_{10}(\text{abundance ratio: DDL-357/Vehicle})$. (E) Gene ontology enrichment analysis using proteins significantly upregulated in the hippocampus of DDL-357 treated E4/FAD mice, relative to vehicle treated controls. (F) A schematic illustrating

the DDL-357-upregulated genes important for maintaining AD-relevant biological functions, including mitochondrial function, protein homeostasis, and synaptic plasticity. All results graphed as mean \pm SEM. All statistics were performed with a two-way ANOVA ($*p < 0.05$; $**p < 0.001$; $***p < 0.0001$; $****p < 0.00001$).

Gene	Description	Abundance Ratio (DDL357/Veh)	P-Value	Expression in AD	Biological Function
BLMH	Bleomycin hydrolase	6.40	8.14E-12		Metabolic Homeostasis, Synaptic plasticity and Anti-Neuroinflammation
NDUFC2	NADH:ubiquinone oxidoreductase subunit C2	4.29	1.02E-02	Down	Metabolic Homeostasis - Mitochondrial Membrane Respiratory Chain NADH Dehydrogenase (C1) Subunit
API5	Apoptosis Inhibitor-5	3.83	2.19E-03		Metabolic Homeostasis - Anti-Apoptotic Regulator of E2F1
NDUFS5	NADH:ubiquinone oxidoreductase subunit S5	2.45	4.81E-14	Down	Metabolic Homeostasis - Mitochondrial Membrane Respiratory Chain NADH Dehydrogenase (C1) Subunit
PRDX3	Peroxisiredoxin 3	1.80	1.74E-10	Down	Metabolic Homeostasis; Anti-Neuroinflammation - Mitochondrial Antioxidant Protein
SLCA410	Solute carrier family 4 member 10	1.74	2.96E-08	Down	Metabolic Homeostasis - Modulates Mitochondrial/Glycolytic Enzymes; Synaptic Plasticity - Modulates Short Term Plasticity
NDUFB4	NADH:Ubiquinone Oxidoreductase Subunit B4	1.49	3.10E-06	Down	Metabolic Homeostasis - Mitochondrial Membrane Respiratory Chain NADH Dehydrogenase (C1) Subunit
NDUFA13	NADH:Ubiquinone Oxidoreductase Subunit A13	1.37	7.18E-05	Down	Metabolic Homeostasis - Mitochondrial Membrane Respiratory Chain NADH Dehydrogenase (C1) Subunit
UQCRCF51	Cytochrome b-c1 complex subunit Rieske, mitochondrial	1.34	3.67E-06	Down	Metabolic Homeostasis - Mitochondrial Membrane Respiratory Chain Ubiquinol-Cytochrome C Oxidoreductase (CIII) Subunit
PSMD3	26S proteasome non-ATPase regulatory subunit 3	100.00	1.51E-13	Up	Protein Homeostasis - Proteasomal Protein
TRPV2	Transient receptor potential cation channel subfamily V member 2	100.00	3.70E-14	down	Protein Homeostasis - Receptor Promoting $\text{A}\beta$ Phagocytosis/Clearance via Microglia
RAB8A	Ras-related protein Rab-8A	100.00	5.63E-10	down	Protein Homeostasis - Reduces α -synuclein aggregation; Synaptic Plasticity - Postsynaptic Receptor Trafficking
SMCR8	Guanine nucleotide exchange protein	4.30	2.92E-11		Protein Homeostasis - Autophagosome/Lysosome Regulator
GRPSEL1	GrpE protein homolog 1, mitochondrial	2.74	1.31E-02		Protein/Metabolic Homeostasis - Mitochondrial UPR Regulator
Rab27b	Ras-related protein Rab-27B	2.19	1.38E-05	Up	Protein Homeostasis - Autophagy Regulator - Reduces α -synuclein Toxicity; Synaptic Plasticity - Promotes Presynaptic LTP
CCT2	T-complex protein 1 subunit beta	1.96	3.98E-05		Protein Homeostasis - Protein Aggregate Receptor/Chaperone
EIF5A	eukaryotic initiation factor 5A	1.89	2.11E-03		Protein Homeostasis - Inhibits TDP-43 Aggregation/UPR Regulator
VBP1	VHL Binding Protein 1	1.70	1.87E-03	Mutation Associated	Protein Homeostasis - Facilitates Proteasomal Protein Degradation; Synaptic Plasticity - Modulates Wnt Signaling
UBE2L3	ubiquitin conjugating enzyme E2 L3	1.52	1.38E-02	Mutation Associated	Protein Homeostasis - Protein Ubiquitination; Anti-Neuroinflammation - Reduces IL-1 β
ALCAM	Activated leukocyte cell adhesion molecule	3.48	9.02E-05	Up in Plasma	Synaptic Plasticity - Promotes Axon Elongation and Navigation
PPP3R1	Calcineurin subunit B	2.52	4.79E-10	Down	Synaptic Plasticity - Modulates Axon Guidance, Glutamatergic Synapse, LTP, and MAPK Signaling Pathways
DLGAP2	Disks large-associated protein 2	2.09	5.45E-03	Down	Synaptic Plasticity - Critically Regulates Dendritic Spine Density and Morphology & Memory
NPTXR	Neuronal pentraxin receptor	2.02	2.04E-13	Down	Synaptic Plasticity - Mediates Uptake of Synaptic Material and Clustering of AMPA Glutamate Receptors. Crucial for LTP
GNAI2	Guanine nucleotide-binding protein G(i) subunit alpha-2	1.90	1.09E-06	Down	Synaptic Plasticity - Associated with LTP
HTT	Huntingtin Protein	1.69	3.70E-03	Up	Synaptic Plasticity - Increases BDNF; Metabolic Homeostasis - Traffics Mitochondrial Proteins; Protein Homeostasis - Scaffold for Autophagy
SNAP29	neuronal synaptosome associated protein 29	1.53	1.53E-06	Down	Synaptic Plasticity - Presynaptic Maintenance is Crucial for Cognitive Function; Autophagy - Mediates Autophagosome-Lysosome Fusion
ITSN1	Intersectin 1	1.47	4.54E-08		Synaptic Plasticity - Activates Reelin Signaling Through VLDLR
PLCB1	1-Phosphatidylinositol-4,5-bisphosphate phospholipase beta-1	1.44	3.28E-03		Synaptic Plasticity - Enhances endocannabinoid mobilization and NMDAR-mediated LTP

Table 2. Alzheimer's Disease-relevant proteins upregulated in E4/FAD mice following DDL-357 treatment.

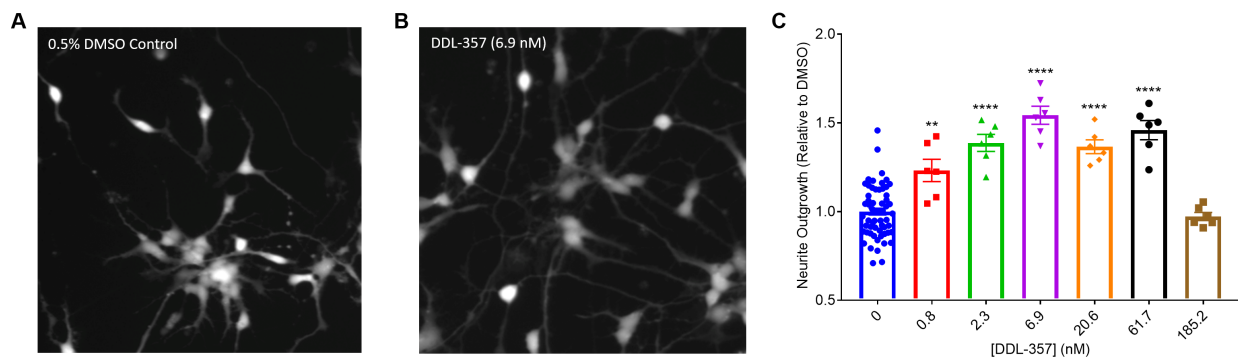


Figure 5. *DDL-357 promotes neurite outgrowth in human iPSC-derived neurons.* (A) Confocal image of Calcein-AM stained iPSC-derived neurons 48 hours after treatment with 0.5% DMSO. (B) Confocal image of Calcein-AM stained iPSC-derived neurons 48 hours after treatment with DDL-357 at a concentration of 6.9 nM. (C) Measurements of neurite outgrowth in iPSC-derived neurons following treatment with 0.5% DMSO or DDL-357 at a concentrations of 0.8, 2.3, 6.9, 20.6, 61.7, and 185.2 nM. All results graphed as mean \pm SEM. All statistics were performed with a two-way ANOVA (* $p < 0.05$; ** $p < 0.001$; *** $p < 0.0001$; **** $p < 0.00001$).

DISCUSSION

To the best of our knowledge, this study represents the first description of a drug discovery effort aimed at identifying potent, brain-permeable small molecules that increase levels of sCLU, and evaluating their effects on AD. A high-throughput screening (HTS) approach successfully identified three compounds (vorinostat, I-BET151, piperlongumine) that significantly increased sCLU levels secreted from glioblastoma cells. Interestingly, all three compounds shared a common theme of inhibiting proteins that recognize acetyl functional groups on lysine residues. Two of these compounds, vorinostat and piperlongumine, had been classified as HDAC inhibitors. HDACs are enzymes that regulate the transcription process by removing acetyl groups from lysine residues of histones and transcription factors and have been associated with various

neurodegenerative diseases, including AD (Ref. 39-40). Interestingly, HDAC inhibition has been described as a promising therapeutic strategy offering neuroprotection by reversing the hypoacetylation commonly observed in AD, preventing A β -induced hyperphosphorylation of tau, and promoting the expression of crucial genes associated with synaptic plasticity, learning, and memory (Ref. 39-40). Not surprisingly, vorinostat is already being tested in phase 1 clinical trials for treating AD (Ref. 3). The other compound identified in the HTS was the well-known BET inhibitor, I-BET151. Similar to HDACs, BET proteins are widely acknowledged as master transcriptional regulators in response to physiological and pathophysiological cues (Ref. 41). This function is facilitated by two acetyl lysine-recognizing bromodomains (BDs) that recruit transcription factors and coactivators to target gene sites, activating the transcriptional machinery (Ref. 41). With this in mind, it is easy to conceive how pharmacological inhibition of HDACs could exert downstream effects on BET proteins. Accordingly, the inhibition of BET proteins has also been recognized as a potential therapeutic strategy for treating AD (Ref. 42). BET inhibitors have been shown to reduce neuroinflammation and tau phosphorylation, while also promoting brain plasticity and cognitive function (Ref. 42-45). Many of the molecular mechanisms underlying these neurotrophic changes are not well characterized and may be mediated by sCLU. Needless to say, these findings reveal a shared molecular pathway connecting impaired protein acetylation with sCLU and AD pathogenesis.

Through testing a structurally diverse array of HDAC and BET inhibitors, a comprehensive investigation was conducted into the molecular mechanisms underlying sCLU expression. While the availability of entirely selective inhibitors somewhat constrained the experiments, the results suggest that three HDACs (HDAC1, HDAC3, HDAC6) and BD2 of BRD4 are involved in

regulating sCLU expression. This information could be utilized in the pursuit of developing more selective sCLU-enhancing therapeutics that avoid disrupting the normal homeostatic functions of all HDAC or BET proteins simultaneously. Limiting drug promiscuity is often critical in preventing adverse reactions/effects that contribute to drug attrition (Ref. 46). Most notably, the findings also revealed BET inhibitors to be considerably more potent and less toxic than HDAC inhibitors, effectively elevating sCLU levels at low nanomolar concentrations without causing any significant cellular toxicity. Consequently, it was concluded that BET inhibition represents a more valuable therapeutic approach, as pharmacologically relevant drug levels were much more attainable *in-vivo*, and less likely to cause unwanted side effects.

In pursuit of identifying BET inhibitors likely to be successful therapeutics for treating CNS disorders *in-vivo*, various *in-vitro* assays were used to evaluate physicochemical properties that influence drug ADME. While a compound may exhibit good *in-vitro* drug activity, it does not automatically guarantee favorable *in-vivo* activity unless it also possesses good bioavailability and half-life (Ref. 47). Moreover, the escalating costs associated with the development of novel therapeutics and the high rate of candidate attrition have prompted a shift in drug discovery strategies towards the simultaneous evaluation of comprehensive drug physicochemical and ADME properties alongside efficacy (Ref. 48). This comprehensive assessment holds particular significance for CNS disorders due to the selective exclusion of nearly 100% of large-molecule neurotherapeutics and over 98% of all small-molecule drugs by the blood-brain barrier (BBB) (Ref. 49). Additional optimization efforts also resulted in the design and synthesis of ten novel JQ1 analogs. Of the nineteen compounds assessed, only one known BET inhibitor and three NCEs met the stringent go/no-go ADME criteria required for further evaluation *in-vivo*. Moreover, DDL-

357 exhibited enhanced potency, BBB permeability, and metabolic stability, along with decreased brain tissue and plasma binding. As a result, it was selected as the lead sCLU enhancing drug candidate moving forward.

Proof-of-concept pharmacokinetic and pharmacodynamic analyses were subsequently conducted to determine if DDL-357 could reach therapeutically relevant concentrations in the brain and effectively increase sCLU levels. As predicted by the *in-vitro* ADME assessment, DDL-357 exhibited excellent brain bioavailability, reaching micromolar concentrations one-hour post-administration at a dose of 30 mg/kg. Even after brain tissue binding is considered, the unbound concentration of DDL-357 that is free to interact with the pharmacological target is still more than 20-fold greater *in-vitro* EC₅₀. Following this, DDL-357 demonstrated a significant increase in hippocampal sCLU levels in the E4/FAD AD mouse model after two weeks of treatment. Interestingly, a corresponding decrease in A β 42 levels was also observed, but due to large variability, it was not deemed statistically significant. It is possible that a longer study in a larger cohort of mice would yield different results. Unfortunately, the effects of DDL-357 on p-tau levels were unable to be assessed, as the mice do not express the human form of tau.

To further characterize the pharmacological effects of DDL-357 *in-vivo*, an unbiased proteomics analysis was utilized to identify additional differentially expressed proteins. This approach revealed increased expression of various proteins critical to mitochondrial function, synaptic plasticity, and protein homeostasis - processes known to be disrupted during AD pathogenesis (Ref. 50-52). This included several proteins from complex I, NADH:ubiquinone oxidoreductase (NDUFA13, NDUFC2, NDUFS5, NDUFB4), and complex III, ubiquinol-cytochrome c

oxidoreductase (UQCRC1), of the mitochondrial respiratory chain. These proteins are notably decreased in AD patient brains, and in some cases, this decrease has been suggested to be causative of the disease (Ref. 53-59). Increasing these proteins has important implications for maintaining mitochondrial bioenergetics vital to supporting neuronal function and preventing oxidative damage in AD (Ref. 58-59). Interestingly, there was also an upregulation of several autophagy-regulating proteins (SMCR8, TRPV2, RAB8A, RAB27B, GRPEL1) known to enhance autophagic-lysosomal clearance of protein aggregates, including A β and alpha-synuclein (*αsyn*) (Ref. 60-64). This was accompanied by increases in important molecular chaperones (CCT2, CCT3, VBP1), as well as additional components of the endo-lysosome autophagy pathway (VSP39) and the ubiquitin-proteasome system degradation pathway (UBE2L3, PSMD3) (Ref. 65-71). Several proteins critical for maintaining synaptic function, dendritic spine morphology, long-term potentiation, and associated learning and memory processes were also upregulated (SNAP29, ALCAM, ITSN1, DLGAP2, NPTXR) (Ref. 72-79). Interestingly, one of these proteins, ITSN1, is a prominent component of the reelin signaling pathway and should, therefore, work in conjunction with sCLU to reduce levels of p-tau (Ref. 27-29, 74-75). Encouraged by these findings, DDL-357 was tested on human iPSC-derived neurons and shown to significantly enhance neurite outgrowth. While the effects of DDL-357 on mitochondrial respiration have yet to be tested in these cells, it is hypothesized that a Seahorse-based bioenergetics analysis will show pronounced increases in ATP production.

This discovery of a novel class of sCLU enhancers presents an opportunity for further evaluation and development of these compounds as novel therapeutics for treating Alzheimer's disease. The results described provide evidence of numerous disease-relevant biological processes mediated by

BET proteins. Moreover, it provides evidence that BET inhibition may represent a mechanistically-related, yet superior therapeutic approach when compared to HDAC inhibition, which is currently being evaluated in clinical trials. The lead drug candidate, DDL-357, specifically shows promise as a potent, multifaceted therapeutic that may inhibit primary disease pathogenesis while also promoting various neuroprotective functions such as mitochondrial function, synaptic plasticity, and protein homeostasis. We are confident that a long-term *in-vivo* study in a different AD mouse model (containing three mutations associated with familial Alzheimer's disease: APP Swedish, MAPT P301L, and PSEN1 M146V), the 3xTg-AD mouse model, will provide further evidence of drug efficacy and spawn the emergence of a promising new clinical candidate that may, one day, be used to treat MCI and AD patients. While additional research is needed to evaluate the full extent of sCLU's involvement, this drug discovery effort has undoubtedly shed light on a valuable therapeutic approach that warrants further evaluation as a treatment for AD.

AUTHOR CONTRIBUTIONS

WC, VJ, JW, JC, PS, BJ, RD participated in research design. WC, JC, AG, AJ, JA conducted experiments. WC, JL, DW synthesized compounds. WC performed data analysis. WC wrote the manuscript. VJ edited the manuscript.

FUNDING

The work was supported by the following grant: NIH R21AG072150 to VJ

SUPPLEMENTARY ANALYTICAL MATERIAL

DDL-351:

^1H NMR (400 MHz, CDCl_3) δ 7.41 (m, 2H), 7.32 (m, 2H), 5.25 (m, 1H), 4.12 (q, $J = 6.47$ Hz, 1H), 3.57 (m, 1H), 2.68 (s, 3H), 2.41 (s, 3H), 1.90 (m, 2H), 1.77 (m, 2H), 1.69 (s, 3H), 1.60 (m, 2H), 1.25 (t, $J = 7.06$ Hz, 2H). LC-MS m/z $[\text{M}+\text{H}]^+$ 483.17.

DDL-352:

^1H NMR (400 MHz, CDCl_3) δ 7.39 (d, $J = 8$ Hz, 2H), 7.31 (d, $J = 8$ Hz, 2H), 4.80 (t, $J = 4$ Hz, 1H), 3.69 – 3.49 (m, 4H), 2.95 (s, 3H), 2.88 (d, $J = 0.6$ Hz, 2H), 2.66 (s, 3H), 2.39 (s, 3H), 2.09 – 1.85 (m, 4H). LC-MS m/z $[\text{M}+\text{H}]^+$ 468.17.

DDL-353:

^1H NMR (400 MHz, CDCl_3) δ 7.46 – 7.32 (m, 4H), 4.68 (t, $J = 7.1$ Hz, 1H), 4.22 (h, $J = 6.9$ Hz, 1H), 3.54 (dd, $J = 14.3, 7.3$ Hz, 1H), 3.38 (dd, $J = 14.3, 6.8$ Hz, 1H), 2.72 (s, 3H), 2.41 (s, 3H), 2.23 (s, 3H), 2.06 – 1.88 (m, 2H), 1.65 – 1.46 (m, 6H). LC-MS m/z $[\text{M}+\text{H}]^+$ 468.17.

DDL-354:

^1H NMR (300 MHz, CDCl_3) δ 7.50 – 7.32 (m, 4H), 5.08 (t, $J = 7.1$ Hz, 1H), 4.74 (m, 1H), 3.62 (s, 2H), 3.12 (d, $J = 6.7$ Hz, 2H), 2.73 (s, 3H), 2.45 (s, 3H), 1.73 (s, 3H), 1.39-1.51 (d, $J = 6.9$ Hz, 6H). LC-MS m/z $[\text{M}+\text{H}]^+$ 500.16. LC-MS m/z

DDL-355:

^1H NMR (300 MHz, CDCl_3) δ 7.50 – 7.32 (m, 4H), 5.16 – 5.04 (m, 1H), 4.64 (dd, $J = 7.5, 6.6$ Hz, 1H), 3.70 – 3.59 (m, 2H), 2.73 (s, 3H), 2.45 (s, 3H), 2.26 – 2.11 (m, 2H), 1.93 – 1.79 (m,

1H), 1.73 (s, 3H), 1.69 – 1.59 (m, 1H), 1.30 (dt, $J = 7.1, 4.1$ Hz, 1H), 0.90 (dd, $J = 14.6, 6.8$ Hz, 1H). LC-MS m/z $[M+H]^+$ 455.14.

DDL-356:

^1H NMR (400 MHz, CDCl_3) δ 7.44 – 7.36 (m, 2H), 7.36 – 7.30 (m, 2H), 5.52 (tt, $J = 6.4, 5.3$ Hz, 1H), 4.91 (tdd, $J = 7.5, 6.3, 1.0$ Hz, 2H), 4.72 (dddd, $J = 7.5, 5.0, 3.8, 0.9$ Hz, 2H), 4.60 (t, $J = 6.3$ Hz, 1H), 3.77 – 3.60 (m, 2H), 2.72-2.67 (s, 3H), 2.46-2.39 (s, 3H), 1.71-1.65 (s, 3H). LC-MS m/z $[M+H]^+$ 457.12.

DDL-357:

δ ^1H NMR (400 MHz, CDCl_3) δ ^1H NMR (300 MHz, CDCl_3) δ 7.50 – 7.32 (m, 4H), 4.65 (t, $J = 7.0$ Hz, 1H), 4.30 – 4.17 (m, 1H), 3.63 (d, $J = 7.1$ Hz, 2H), 2.73 (s, 3H), 2.46 (d, $J = 0.8$ Hz, 3H), 1.73 (s, 3H), 0.95 – 0.72 (m, 4H). LC-MS m/z $[M+H]^+$ 441.12.

DDL-358:

δ ^1H NMR (400 MHz, CDCl_3) δ 7.44 – 7.30 (m, 4H), 4.63 (t, $J = 6.7$ Hz, 1H), 4.18 (t, $J = 6.6$ Hz, 2H), 3.62 (d, $J = 1.4$ Hz, 2H), 2.73 (s, 3H), 2.42 (s, 3H), 1.69 (s, 3H), 1.68 – 1.62 (m, 2H), 1.47 – 1.34 (m, 2H), 0.94 (t, $J = 7.4$ Hz, 3H). LC-MS m/z $[M+H]^+$ 457.15.

DDL-359

^1H NMR (400 MHz, CDCl_3) δ 7.39 (d, $J = 4$ Hz, 2H), 7.32 (d, $J = 4$ Hz, 2H), 5.03 (t, $J = 8$ Hz, 1H), 4.54 (sept, $J = 4$ Hz, 1H), 3.54 (q, 4Hz, 1H), 2.66 (s, 2H), 2.61 (s, 6H), 2.39 (s, 3H) 1.45 (d, $J = 4$ Hz, 3H), 1.23 (d, $J = 4$ Hz, 3H), 1.205 (d, $J = 2$ Hz, 3H). LC-MS m/z $[M+H]^+$ 514.17.

DDL-360

^1H NMR (400 MHz, CDCl_3) δ 7.46 (d, $J = 8$ Hz, 2H), 7.41 (d, $J = 8$ Hz, 2H), 4.46 (t, $J = 8$ Hz, 1H), 3.09 (d, $J = 8$ Hz), 2.56 (s, 3H), 2.38 (s, 3H), 1.59 (s, 3H), 1.20 (s, 1H). LC-MS m/z $[\text{M}+\text{H}]^+$ 416.10.

REFERENCES

1. DeTure MA and Dickson DW. The neuropathological diagnosis of Alzheimer's disease. *Mol Neurodegener.* 2019;14:32. PMID:31375134; PMCID:PMC6679484.
2. Serrano-Pozo A, Frosch MP, Masliah E and Hyman BT. Neuropathological alterations in Alzheimer disease. *Cold Spring Harb Perspect Med.* 2011;1:a006189. PMID:22229116; PMCID:PMC3234452.
3. Cummings J, Lee G, Nahed P, Kambar MEZN, Zhong K, Fonseca J, Taghva K. Alzheimer's disease drug development pipeline: 2022. *Alzheimers Dement (N Y).* 2022 May 4;8(1):e12295. doi: 10.1002/trc2.12295. PMID: 35516416; PMCID: PMC9066743.
4. Scheltens P, De Strooper B, Kivipelto M, Holstege H, Chételat G, Teunissen CE, Cummings J, van der Flier WM. Alzheimer's disease. *Lancet.* 2021 Apr 24;397(10284):1577-1590. doi: 10.1016/S0140-6736(20)32205-4. Epub 2021 Mar 2. PMID: 33667416; PMCID: PMC8354300.
5. Racchi M, Mazzucchelli M, Porrello E, Lanni C, Govoni S. Acetylcholinesterase inhibitors: novel activities of old molecules. *Pharmacol Res.* 2004 Oct;50(4):441-51. doi: 10.1016/j.phrs.2003.12.027. PMID: 15304241.
6. Robinson DM, Keating GM. Memantine: a review of its use in Alzheimer's disease. *Drugs.* 2006;66(11):1515-34. doi: 10.2165/00003495-200666110-00015. PMID: 16906789.
7. Dorszewska J, Prendecki M, Oczkowska A, Dezor M and Kozubski W. Molecular Basis of Familial and Sporadic Alzheimer's Disease. *Curr Alzheimer Res.* 2016;13:952-63. PMID:26971934.
8. Foster EM, Dangla-Valls A, Lovestone S, Ribe EM and Buckley NJ. Clusterin in Alzheimer's Disease: Mechanisms, Genetics, and Lessons From Other Pathologies. *Front Neurosci.* 2019;13:164. PMID:30872998; PMCID:PMC6403191.
9. Roussotte FF, Gutman BA, Madsen SK, Colby JB, Thompson PM and Alzheimer's Disease Neuroimaging I. Combined effects of Alzheimer risk variants in the CLU and ApoE genes on ventricular expansion patterns in the elderly. *J Neurosci.* 2014;34:6537-45. PMID:24806679; PMCID:PMC4012312.

10. Lenzi C, Ramazzina I, Russo I, Filippini A, Bettuzzi S, Rizzi F. The Down-Regulation of Clusterin Expression Enhances the α Synuclein Aggregation Process. *Int J Mol Sci.* 2020 Sep 29;21(19):7181. doi: 10.3390/ijms21197181. PMID: 33003328; PMCID: PMC7582711.
11. Harold D, Abraham R, Hollingworth P, Sims R, Gerrish A, Hamshere ML, Pahwa JS, Moskvina V, Dowzell K, Williams A, Jones N, Thomas C, Stretton A, Morgan AR, Lovestone S, Powell J, Proitsi P, Lupton MK, Brayne C, Rubinsztein DC, Gill M, Lawlor B, Lynch A, Morgan K, Brown KS, Passmore PA, Craig D, McGuinness B, Todd S, Holmes C, Mann D, Smith AD, Love S, Kehoe PG, Hardy J, Mead S, Fox N, Rossor M, Collinge J, Maier W, Jessen F, Schurmann B, Heun R, van den Bussche H, Heuser I, Kornhuber J, Wiltfang J, Dichgans M, Frolich L, Hampel H, Hull M, Rujescu D, Goate AM, Kauwe JS, Cruchaga C, Nowotny P, Morris JC, Mayo K, Sleegers K, Bettens K, Engelborghs S, De Deyn PP, Van Broeckhoven C, Livingston G, Bass NJ, Gurling H, McQuillin A, Gwilliam R, Deloukas P, Al-Chalabi A, Shaw CE, Tsolaki M, Singleton AB, Guerreiro R, Muhleisen TW, Nothen MM, Moebus S, Jockel KH, Klopp N, Wichmann HE, Carrasquillo MM, Pankratz VS, Younkin SG, Holmans PA, O'Donovan M, Owen MJ and Williams J. Genome-wide association study identifies variants at CLU and PICALM associated with Alzheimer's disease. *Nat Genet.* 2009;41:1088-93. PMID:19734902; PMCID:PMC2845877.
12. Lambert JC, Heath S, Even G, Champion D, Sleegers K, Hiltunen M, Combarros O, Zelenika D, Bullido MJ, Tavernier B, Letenneur L, Bettens K, Berr C, Pasquier F, Fievet N, Barberger-Gateau P, Engelborghs S, De Deyn P, Mateo I, Franck A, Helisalmi S, Porcellini E, Hanon O, European Alzheimer's Disease Initiative I, de Pancorbo MM, Lendon C, Dufouil C, Jaillard C, Leveillard T, Alvarez V, Bosco P, Mancuso M, Panza F, Nacmias B, Bossu P, Piccardi P, Annoni G, Seripa D, Galimberti D, Hannequin D, Licastro F, Soininen H, Ritchie K, Blanche H, Dartigues JF, Tzourio C, Gut I, Van Broeckhoven C, Alperovitch A, Lathrop M and Amouyel P. Genome-wide association study identifies variants at CLU and CR1 associated with Alzheimer's disease. *Nat Genet.* 2009;41:1094-9. PMID:19734903.

13. Seshadri S, Fitzpatrick AL, Ikram MA, DeStefano AL, Gudnason V, Boada M, Bis JC, Smith AV, Carassquillo MM, Lambert JC, Harold D, Schrijvers EM, Ramirez-Lorca R, Debette S, Longstreth WT, Jr., Janssens AC, Pankratz VS, Dartigues JF, Hollingworth P, Aspelund T, Hernandez I, Beiser A, Kuller LH, Koudstaal PJ, Dickson DW, Tzourio C, Abraham R, Antunez C, Du Y, Rotter JJ, Aulchenko YS, Harris TB, Petersen RC, Berr C, Owen MJ, Lopez-Arrieta J, Varadarajan BN, Becker JT, Rivadeneira F, Nalls MA, Graff-Radford NR, Champion D, Auerbach S, Rice K, Hofman A, Jonsson PV, Schmidt H, Lathrop M, Mosley TH, Au R, Psaty BM, Uitterlinden AG, Farrer LA, Lumley T, Ruiz A, Williams J, Amouyel P, Younkin SG, Wolf PA, Launer LJ, Lopez OL, van Duijn CM, Breteler MM, Consortium C, Consortium G and Consortium E. Genome-wide analysis of genetic loci associated with Alzheimer disease. *JAMA*. 2010;303:1832-40. PMID:20460622; PMCID:PMC2989531.
14. Thambisetty M, Beason-Held LL, An Y, Kraut M, Nalls M, Hernandez DG, Singleton AB, Zonderman AB, Ferrucci L, Lovestone S and Resnick SM. Alzheimer risk variant CLU and brain function during aging. *Biol Psychiatry*. 2013;73:399-405. PMID:22795969; PMCID:PMC3488132.
15. Zhou Y, Hayashi I, Wong J, Tugusheva K, Renger JJ and Zerbinatti C. Intracellular clusterin interacts with brain isoforms of the bridging integrator 1 and with the microtubule-associated protein Tau in Alzheimer's disease. *PLoS One*. 2014;9:e103187. PMID:25051234; PMCID:PMC4106906.
16. Braskie MN, Jahanshad N, Stein JL, Barysheva M, McMahon KL, de Zubicaray GI, Martin NG, Wright MJ, Ringman JM, Toga AW and Thompson PM. Common Alzheimer's disease risk variant within the CLU gene affects white matter microstructure in young adults. *J Neurosci*. 2011;31:6764-70. PMID:21543606; PMCID:PMC3176803.
17. Erk S, Meyer-Lindenberg A, Opitz von Boberfeld C, Esslinger C, Schnell K, Kirsch P, Mattheisen M, Muhleisen TW, Cichon S, Witt SH, Rietschel M, Nothen MM and Walter H. Hippocampal

- function in healthy carriers of the CLU Alzheimer's disease risk variant. *J Neurosci*. 2011;31:18180-4. PMID:22159129; PMCID:PMC6634131.
18. Tan L, Wang HF, Tan MS, Tan CC, Zhu XC, Miao D, Yu WJ, Jiang T, Tan L, Yu JT and Alzheimer's Disease Neuroimaging I. Effect of CLU genetic variants on cerebrospinal fluid and neuroimaging markers in healthy, mild cognitive impairment and Alzheimer's disease cohorts. *Sci Rep*. 2016;6:26027. PMID:27229352; PMCID:PMC4882617.
 19. Ling IF, Bhongsatiern J, Simpson JF, Fardo DW and Estus S. Genetics of clusterin isoform expression and Alzheimer's disease risk. *PLoS One*. 2012;7:e33923. PMID:22506010; PMCID:PMC3323613.
 20. Gregory JM, Whiten DR, Brown RA, Barros TP, Kumita JR, Yerbury JJ, Satapathy S, McDade K, Smith C, Luheshi LM, Dobson CM and Wilson MR. Clusterin protects neurons against intracellular proteotoxicity. *Acta Neuropathol Commun*. 2017;5:81. PMID:29115989; PMCID:PMC5678579.
 21. Matsubara E, Soto C, Governale S, Frangione B and Ghiso J. Apolipoprotein J and Alzheimer's amyloid beta solubility. *Biochem J*. 1996;316 (Pt 2):671-9. PMID:8687416; PMCID:PMC1217400.
 22. Narayan P, Orte A, Clarke RW, Bolognesi B, Hook S, Ganzinger KA, Meehan S, Wilson MR, Dobson CM and Klenerman D. The extracellular chaperone clusterin sequesters oligomeric forms of the amyloid-beta(1-40) peptide. *Nat Struct Mol Biol*. 2011;19:79-83. PMID:22179788; PMCID:PMC4979993.
 23. Wojtas AM, Carlomagno Y, Sens JP, Kang SS, Jensen TD, Kurti A, Baker KE, Berry TJ, Phillips VR, Castanedes MC, Awan A, DeTure M, De Castro CHF, Librero AL, Yue M, Daugherty L, Jansen-West KR, Cook CN, Dickson DW, Petrucelli L, Fryer JD. Clusterin ameliorates tau pathology in vivo by inhibiting fibril formation. *Acta Neuropathol Commun*. 2020 Dec 1;8(1):210. doi: 10.1186/s40478-020-01079-1. PMID: 33261653; PMCID: PMC7708249.
 24. Bell RD, Sagare AP, Friedman AE, Bedi GS, Holtzman DM, Deane R and Zlokovic BV. Transport pathways for clearance of human Alzheimer's amyloid beta-peptide and apolipoproteins E and J in

- the mouse central nervous system. *J Cereb Blood Flow Metab.* 2007;27:909-18. PMID:17077814; PMCID:PMC2853021.
25. Yeh FL, Wang Y, Tom I, Gonzalez LC and Sheng M. TREM2 Binds to Apolipoproteins, Including APOE and CLU/APOJ, and Thereby Facilitates Uptake of Amyloid-Beta by Microglia. *Neuron.* 2016;91:328-40. PMID:27477018.
 26. Zlokovic BV, Martel CL, Matsubara E, McComb JG, Zheng G, McCluskey RT, Frangione B and Ghiso J. Glycoprotein 330/megalin: probable role in receptor-mediated transport of apolipoprotein J alone and in a complex with Alzheimer disease amyloid beta at the blood-brain and blood-cerebrospinal fluid barriers. *Proc Natl Acad Sci U S A.* 1996;93:4229-34. PMID:8633046; PMCID:PMC39517.
 27. Leeb C, Eresheim C, Nimpf J. Clusterin is a ligand for apolipoprotein E receptor 2 (ApoER2) and very low density lipoprotein receptor (VLDLR) and signals via the Reelin-signaling pathway. *J Biol Chem.* 2014 Feb 14;289(7):4161-72. doi: 10.1074/jbc.M113.529271. Epub 2013 Dec 31. PMID: 24381170; PMCID: PMC3924281.
 28. Bock HH, May P. Canonical and Non-canonical Reelin Signaling. *Front Cell Neurosci.* 2016 Jun 30;10:166. doi: 10.3389/fncel.2016.00166. PMID: 27445693; PMCID: PMC4928174.
 29. Hiesberger T, Trommsdorff M, Howell BW, Goffinet A, Mumby MC, Cooper JA, Herz J. Direct binding of Reelin to VLDL receptor and ApoE receptor 2 induces tyrosine phosphorylation of disabled-1 and modulates tau phosphorylation. *Neuron.* 1999 Oct;24(2):481-9. doi: 10.1016/s0896-6273(00)80861-2. PMID: 10571241.
 30. Kim JH, Kim JH, Jun HO, Yu YS, Min BH, Park KH and Kim KW. Protective effect of clusterin from oxidative stress-induced apoptosis in human retinal pigment epithelial cells. *Invest Ophthalmol Vis Sci.* 2010;51:561-6. PMID:19710412.
 31. Pratico D, Clark CM, Liun F, Rokach J, Lee VY and Trojanowski JQ. Increase of brain oxidative stress in mild cognitive impairment: a possible predictor of Alzheimer disease. *Arch Neurol.* 2002;59:972-6. PMID:12056933.

32. Strocchi P, Smith MA, Perry G, Tamagno E, Danni O, Pession A, Gaiba A and Dozza B. Clusterin up-regulation following sub-lethal oxidative stress and lipid peroxidation in human neuroblastoma cells. *Neurobiol Aging*. 2006;27:1588-94. PMID:16464517.
33. Viard I, Wehrli P, Jornot L, Bullani R, Vechietti JL, Schifferli JA, Tschopp J and French LE. Clusterin gene expression mediates resistance to apoptotic cell death induced by heat shock and oxidative stress. *J Invest Dermatol*. 1999;112:290-6. PMID:10084304.
34. Cunin P, Beauvillain C, Miot C, Augusto JF, Preisser L, Blanchard S, Pignon P, Scotet M, Garo E, Fremaux I, Chevailler A, Subra JF, Blanco P, Wilson MR, Jeannin P and Delneste Y. Clusterin facilitates apoptotic cell clearance and prevents apoptotic cell-induced autoimmune responses. *Cell Death Dis*. 2016;7:e2215. PMID:27148688; PMCID:PMC4917652.
35. Heneka MT, Carson MJ, El Khoury J, Landreth GE, Brosseron F, Feinstein DL, Jacobs AH, Wyss-Coray T, Vitorica J, Ransohoff RM, Herrup K, Frautschy SA, Finsen B, Brown GC, Verkhratsky A, Yamanaka K, Koistinaho J, Latz E, Halle A, Petzold GC, Town T, Morgan D, Shinohara ML, Perry VH, Holmes C, Bazan NG, Brooks DJ, Hunot S, Joseph B, Deigendesch N, Garaschuk O, Boddeke E, Dinarello CA, Breitner JC, Cole GM, Golenbock DT and Kummer MP. Neuroinflammation in Alzheimer's disease. *Lancet Neurol*. 2015;14:388-405. PMID:25792098; PMCID:PMC5909703.
36. Urbich C, Fritzenwanger M, Zeiher AM and Dimmeler S. Laminar shear stress upregulates the complement-inhibitory protein clusterin : a novel potent defense mechanism against complement-induced endothelial cell activation. *Circulation*. 2000;101:352-5. PMID:10653823.
37. Chen F, Swartzlander DB, Ghosh A, Fryer JD, Wang B, Zheng H. Clusterin secreted from astrocyte promotes excitatory synaptic transmission and ameliorates Alzheimer's disease neuropathology. *Mol Neurodegener*. 2021 Jan 31;16(1):5. doi: 10.1186/s13024-021-00426-7. PMID: 33517893; PMCID: PMC7849119.
38. de Retana SF, Marazuela P, Sole M, Colell G, Bonaterra A, Sanchez-Quesada JL, Montaner J, MasPOCH D, Cano-Sarabia M and Hernandez-Guillamon M. Peripheral administration of human

- recombinant ApoJ/clusterin modulates brain beta-amyloid levels in APP23 mice. *Alzheimers Res Ther.* 2019;11:42. PMID:31077261; PMCID:PMC6511153.
39. Xu K, Dai XL, Huang HC, Jiang ZF. Targeting HDACs: a promising therapy for Alzheimer's disease. *Oxid Med Cell Longev.* 2011;2011:143269. doi: 10.1155/2011/143269. Epub 2011 Sep 20. PMID: 21941604; PMCID: PMC3177096.
40. Shukla S, Tekwani BL. Histone Deacetylases Inhibitors in Neurodegenerative Diseases, Neuroprotection and Neuronal Differentiation. *Front Pharmacol.* 2020 Apr 24;11:537. doi: 10.3389/fphar.2020.00537. PMID: 32390854; PMCID: PMC7194116.
41. Cheung KL, Kim C, Zhou MM. The Functions of BET Proteins in Gene Transcription of Biology and Diseases. *Front Mol Biosci.* 2021 Sep 3;8:728777. doi: 10.3389/fmolb.2021.728777. PMID: 34540900; PMCID: PMC8446420.
42. Singh MB, Sartor GC. BET bromodomains as novel epigenetic targets for brain health and disease. *Neuropharmacology.* 2020 Dec 15;181:108306. doi: 10.1016/j.neuropharm.2020.108306. Epub 2020 Sep 15. PMID: 32946883; PMCID: PMC7655633.
43. Magistri M, Velmeshev D, Makhmutova M, Patel P, Sartor GC, Volmar CH, Wahlestedt C, Faghihi MA. The BET-Bromodomain Inhibitor JQ1 Reduces Inflammation and Tau Phosphorylation at Ser396 in the Brain of the 3xTg Model of Alzheimer's Disease. *Curr Alzheimer Res.* 2016;13(9):985-95. doi: 10.2174/1567205013666160427101832. PMID: 27117003; PMCID: PMC5026248.
44. Nikkar R, Esmaeili-Bandboni A, Badrikoohi M, Babaei P. Effects of inhibiting astrocytes and BET/BRD4 chromatin reader on spatial memory and synaptic proteins in rats with Alzheimer's disease. *Metab Brain Dis.* 2022 Apr;37(4):1119-1131. doi: 10.1007/s11011-022-00940-7. Epub 2022 Mar 4. PMID: 35244824.
45. Benito E, Ramachandran B, Schroeder H, Schmidt G, Urbanke H, Burkhardt S, Capece V, Dean C, Fischer A. The BET/BRD inhibitor JQ1 improves brain plasticity in WT and APP mice. *Transl*

- Psychiatry. 2017 Sep 26;7(9):e1239. doi: 10.1038/tp.2017.202. PMID: 28949335; PMCID: PMC5639246.
46. Sun D, Gao W, Hu H, Zhou S. Why 90% of clinical drug development fails and how to improve it? *Acta Pharm Sin B*. 2022 Jul;12(7):3049-3062. doi: 10.1016/j.apsb.2022.02.002. Epub 2022 Feb 11. PMID: 35865092; PMCID: PMC9293739.
 47. Lipinski CA. Drug-like properties and the causes of poor solubility and poor permeability. *J Pharmacol Toxicol Methods*. 2000;44:235-49. PMID:11274893.
 48. Lin JH and Lu AY. Role of pharmacokinetics and metabolism in drug discovery and development. *Pharmacol Rev*. 1997;49:403-49. PMID:9443165.
 49. Wang J and Skolnik S. Recent advances in physicochemical and ADMET profiling in drug discovery. *Chem Biodivers*. 2009;6:1887-99. PMID:19937823.
 50. Wang W, Zhao F, Ma X, Perry G, Zhu X. Mitochondria dysfunction in the pathogenesis of Alzheimer's disease: recent advances. *Mol Neurodegener*. 2020 May 29;15(1):30. doi: 10.1186/s13024-020-00376-6. PMID: 32471464; PMCID: PMC7257174.
 51. Benarroch EE. Glutamatergic synaptic plasticity and dysfunction in Alzheimer disease: Emerging mechanisms. *Neurology*. 2018 Jul 17;91(3):125-132. doi: 10.1212/WNL.0000000000005807. Epub 2018 Jun 13. PMID: 29898976.
 52. Morawe T, Hiebel C, Kern A, Behl C. Protein homeostasis, aging and Alzheimer's disease. *Mol Neurobiol*. 2012 Aug;46(1):41-54. doi: 10.1007/s12035-012-8246-0. Epub 2012 Feb 24. PMID: 22361852; PMCID: PMC3443483.
 53. Adav SS, Park JE, Sze SK. Quantitative profiling brain proteomes revealed mitochondrial dysfunction in Alzheimer's disease. *Mol Brain*. 2019 Jan 28;12(1):8. doi: 10.1186/s13041-019-0430-y. PMID: 30691479; PMCID: PMC6350377.
 54. Reddy PH, Tonk S, Kumar S, Vijayan M, Kandimalla R, Kuruva CS, Reddy AP. A critical evaluation of neuroprotective and neurodegenerative MicroRNAs in Alzheimer's disease. *Biochem*

- Biophys Res Commun. 2017 Feb 19;483(4):1156-1165. doi: 10.1016/j.bbrc.2016.08.067. Epub 2016 Aug 12. PMID: 27524239; PMCID: PMC5343756.
55. Marmolejo-Garza A, Medeiros-Furquim T, Rao R, Eggen BJL, Boddeke E, Dolga AM. Transcriptomic and epigenomic landscapes of Alzheimer's disease evidence mitochondrial-related pathways. *Biochim Biophys Acta Mol Cell Res.* 2022 Oct;1869(10):119326. doi: 10.1016/j.bbamcr.2022.119326. Epub 2022 Jul 14. PMID: 35839870.
56. Wang XL, Li L. Cell type-specific potential pathogenic genes and functional pathways in Alzheimer's Disease. *BMC Neurol.* 2021 Oct 2;21(1):381. doi: 10.1186/s12883-021-02407-1. PMID: 34600516; PMCID: PMC8487122.
57. Chen F, Bai J, Zhong S, Zhang R, Zhang X, Xu Y, Zhao M, Zhao C, Zhou Z. Molecular Signatures of Mitochondrial Complexes Involved in Alzheimer's Disease via Oxidative Phosphorylation and Retrograde Endocannabinoid Signaling Pathways. *Oxid Med Cell Longev.* 2022 Apr 5;2022:9565545. doi: 10.1155/2022/9565545. PMID: 35432724; PMCID: PMC9006080.
58. Yao J, Irwin RW, Zhao L, Nilsen J, Hamilton RT, Brinton RD. Mitochondrial bioenergetic deficit precedes Alzheimer's pathology in female mouse model of Alzheimer's disease. *Proc Natl Acad Sci U S A.* 2009 Aug 25;106(34):14670-5. doi: 10.1073/pnas.0903563106. Epub 2009 Aug 10. PMID: 19667196; PMCID: PMC2732886.
59. Ashleigh T, Swerdlow RH, Beal MF. The role of mitochondrial dysfunction in Alzheimer's disease pathogenesis. *Alzheimers Dement.* 2023 Jan;19(1):333-342. doi: 10.1002/alz.12683. Epub 2022 May 6. PMID: 35522844.
60. Jung J, Behrends C. Multifaceted role of SMCR8 as autophagy regulator. *Small GTPases.* 2020 Jan;11(1):53-61. doi: 10.1080/21541248.2017.1346553. Epub 2017 Oct 3. PMID: 28696821; PMCID: PMC6959302.
61. Yang S, Du Y, Zhao X, Tang Q, Su W, Hu Y, Yu P. Cannabidiol Enhances Microglial Beta-Amyloid Peptide Phagocytosis and Clearance via Vanilloid Family Type 2 Channel Activation. *Int*

- J Mol Sci. 2022 May 11;23(10):5367. doi: 10.3390/ijms23105367. PMID: 35628181; PMCID: PMC9140666.
62. Kiral FR, Kohrs FE, Jin EJ, Hiesinger PR. Rab GTPases and Membrane Trafficking in Neurodegeneration. *Curr Biol*. 2018 Apr 23;28(8):R471-R486. doi: 10.1016/j.cub.2018.02.010. PMID: 29689231; PMCID: PMC5965285.
63. Underwood R, Wang B, Carico C, Whitaker RH, Placzek WJ, Yacoubian TA. The GTPase Rab27b regulates the release, autophagic clearance, and toxicity of α -synuclein. *J Biol Chem*. 2020 Jun 5;295(23):8005-8016. doi: 10.1074/jbc.RA120.013337. Epub 2020 Apr 29. PMID: 32350025; PMCID: PMC7278354.
64. Ma C, Gao B, Wang Z, You W, Yu Z, Shen H, Li X, Li H, Zhang X, Wang Z, Chen G. GrpEL1 regulates mitochondrial unfolded protein response after experimental subarachnoid hemorrhage in vivo and in vitro. *Brain Res Bull*. 2022 Apr;181:97-108. doi: 10.1016/j.brainresbull.2022.01.014. Epub 2022 Jan 29. PMID: 35093469.
65. Zhang Z, Klionsky DJ. CCT2, a newly identified aggrephagy receptor in mammals, specifically mediates the autophagic clearance of solid protein aggregates. *Autophagy*. 2022 Jul;18(7):1483-1485. doi: 10.1080/15548627.2022.2083305. Epub 2022 Jun 14. PMID: 35699934; PMCID: PMC9298431.
66. Pavel M, Imarisio S, Menzies FM, Jimenez-Sanchez M, Siddiqi FH, Wu X, Renna M, O'Kane CJ, Crowther DC, Rubinsztein DC. CCT complex restricts neuropathogenic protein aggregation via autophagy. *Nat Commun*. 2016 Dec 8;7:13821. doi: 10.1038/ncomms13821. PMID: 27929117; PMCID: PMC5155164.
67. Liang J, Xia L, Oyang L, Lin J, Tan S, Yi P, Han Y, Luo X, Wang H, Tang L, Pan Q, Tian Y, Rao S, Su M, Shi Y, Cao D, Zhou Y, Liao Q. The functions and mechanisms of prefoldin complex and prefoldin-subunits. *Cell Biosci*. 2020 Jul 20;10:87. doi: 10.1186/s13578-020-00446-8. PMID: 32699605; PMCID: PMC7370476.

68. Schedin-Weiss S, Nilsson P, Sandebring-Matton A, Axenus M, Sekiguchi M, Saito T, Winblad B, Saido T, Tjernberg LO. Proteomics Time-Course Study of App Knock-In Mice Reveals Novel Presymptomatic A β 42-Induced Pathways to Alzheimer's Disease Pathology. *J Alzheimers Dis.* 2020;75(1):321-335. doi: 10.3233/JAD-200028. PMID: 32280097; PMCID: PMC7902969.
69. Davegårdh C, Säll J, Benrick A, Broholm C, Volkov P, Perfilyev A, Henriksen TI, Wu Y, Hjort L, Brøns C, Hansson O, Pedersen M, Würthner JU, Pfeffer K, Nilsson E, Vaag A, Stener-Victorin E, Pircs K, Scheele C, Ling C. VPS39-deficiency observed in type 2 diabetes impairs muscle stem cell differentiation via altered autophagy and epigenetics. *Nat Commun.* 2021 Apr 23;12(1):2431. doi: 10.1038/s41467-021-22068-5. PMID: 33893273; PMCID: PMC8065135.
70. Chen XY, Xu F, Chen JQ, Landeck L, Chen SQ, Zhou Y, Wang Z, Fu NC, Zheng M, Zhang X, Man XY. UBE2L3 Reduces TRIM21 Expression and IL-1 β Secretion in Epidermal Keratinocytes and Improves Psoriasis-Like Skin. *J Invest Dermatol.* 2023 May;143(5):822-831.e4. doi: 10.1016/j.jid.2022.10.016. Epub 2022 Dec 9. PMID: 36502938.
71. Mirzaei M, Pushpitha K, Deng L, Chitranshi N, Gupta V, Rajput R, Mangani AB, Dheer Y, Godinez A, McKay MJ, Kamath K, Pascovici D, Wu JX, Salekdeh GH, Karl T, Haynes PA, Graham SL, Gupta VK. Upregulation of Proteolytic Pathways and Altered Protein Biosynthesis Underlie Retinal Pathology in a Mouse Model of Alzheimer's Disease. *Mol Neurobiol.* 2019 Sep;56(9):6017-6034. doi: 10.1007/s12035-019-1479-4. Epub 2019 Feb 1. PMID: 30707393.
72. Thelen K, Maier B, Faber M, Albrecht C, Fischer P, Pollerberg GE. Translation of the cell adhesion molecule ALCAM in axonal growth cones - regulation and functional importance. *J Cell Sci.* 2012 Feb 15;125(Pt 4):1003-14. doi: 10.1242/jcs.096149. Epub 2012 Mar 15. PMID: 22421359.
73. Chen J, Dai AX, Tang HL, Lu CH, Liu HX, Hou T, Lu ZJ, Kong N, Peng XY, Lin KX, Zheng ZD, Xu SL, Ying XF, Ji XY, Pan H, Wu J, Zeng X, Wei NL. Increase of ALCAM and VCAM-1 in the plasma predicts the Alzheimer's disease. *Front Immunol.* 2023 Jan 4;13:1097409. doi: 10.3389/fimmu.2022.1097409. PMID: 36685605; PMCID: PMC9846483.

74. Jakob B, Kochlamazashvili G, Jäpel M, Gauhar A, Bock HH, Maritzen T, Haucke V. Intersectin 1 is a component of the Reelin pathway to regulate neuronal migration and synaptic plasticity in the hippocampus. *Proc Natl Acad Sci U S A*. 2017 May 23;114(21):5533-5538. doi: 10.1073/pnas.1704447114. Epub 2017 May 8. PMID: 28484035; PMCID: PMC5448185.
75. Malakooti N, Pritchard MA, Chen F, Yu Y, Sgambelloni C, Adlard PA, Finkelstein DI. The Long Isoform of Intersectin-1 Has a Role in Learning and Memory. *Front Behav Neurosci*. 2020 Feb 25;14:24. doi: 10.3389/fnbeh.2020.00024. PMID: 32161523; PMCID: PMC7052523.
76. Yan W, Fan J, Zhang X, Song H, Wan R, Wang W, Yin Y. Decreased neuronal synaptosome associated protein 29 contributes to poststroke cognitive impairment by disrupting presynaptic maintenance. *Theranostics*. 2021 Mar 4;11(10):4616-4636. doi: 10.7150/thno.54210. PMID: 33754017; PMCID: PMC7978312.
77. Ouellette AR, Neuner SM, Dumitrescu L, Anderson LC, Gatti DM, Mahoney ER, Bubier JA, Churchill G, Peters L, Huentelman MJ, Herskowitz JH, Yang HS, Smith AN, Reitz C, Kunkle BW, White CC, De Jager PL, Schneider JA, Bennett DA, Seyfried NT; Alzheimer's Disease Genetics Consortium; Chesler EJ, Hadad N, Hohman TJ, Kaczorowski CC. Cross-Species Analyses Identify *Dlgap2* as a Regulator of Age-Related Cognitive Decline and Alzheimer's Dementia. *Cell Rep*. 2020 Sep 1;32(9):108091. doi: 10.1016/j.celrep.2020.108091. PMID: 32877673; PMCID: PMC7502175.
78. Dulewicz M, Kulczyńska-Przybik A, Słowik A, Borawska R, Mroczko B. Neurogranin and Neuronal Pentraxin Receptor as Synaptic Dysfunction Biomarkers in Alzheimer's Disease. *J Clin Med*. 2021 Oct 2;10(19):4575. doi: 10.3390/jcm10194575. PMID: 34640593; PMCID: PMC8509697.
79. Gómez de San José N, Massa F, Halbgebauer S, Oeckl P, Steinacker P, Otto M. Neuronal pentraxins as biomarkers of synaptic activity: from physiological functions to pathological changes in neurodegeneration. *J Neural Transm (Vienna)*. 2022 Feb;129(2):207-230. doi: 10.1007/s00702-021-02411-2. Epub 2021 Aug 30. PMID: 34460014; PMCID: PMC8866268.

CHAPTER 4

Developing Selective Inhibitors of Microtubule Affinity-Regulating Kinase 4 to Prevent Phosphorylation of Tau at Serine 262 for Vascular Cognitive Impairment and Dementia

Whitaker Cohn^{1,3}, Manu Vora², Nicole Katzaroff¹, Jessica Tracy Lee¹, Jennifer An², Jesus Campagna¹, Barbara Jagodzinska¹, Tina Bilousova¹, Chunni Zhu¹, Julian Whitelegge³, Jason D. Hinman², Varghese John¹

¹The Drug Discovery Lab, Mary S. Easton Center for Alzheimer's Disease Research, Department of Neurology, David Geffen School of Medicine, 710 Westwood Plaza, University of California Los Angeles, Los Angeles, CA 90095, USA

²The Hinman Lab, Department of Neurology, David Geffen School of Medicine, 710 Westwood Plaza, University of California Los Angeles, Los Angeles, CA 90095, USA

³Pasarow Mass Spectrometry Laboratory, Jane and Terry Semel Institute for Neuroscience and Human Behavior, David Geffen School of Medicine, 760 Westwood Plaza, University of California Los Angeles, Los Angeles, CA 90095, USA

ABSTRACT

Vascular cognitive impairment and dementia (VCID) is the second leading cause of dementia worldwide and commonly occurs after a stroke. Many patients with clinical Alzheimer's disease (AD) also show pathological evidence of vascular brain injury, further increasing its consequence. Accumulating literature suggests that destabilization of the neuronal cytoskeleton and the aggregation of hyperphosphorylated tau (p-tau) drive VCID pathogenesis post-stroke injury, and that this is mediated by microtubule affinity-regulating kinase 4 (MARK4). MARK4 is significantly up-regulated in stroke-injured cortical neurons, leading to selective axonal remodeling and phosphorylation of tau at the gateway site, serine 262. The present study investigates MARK4 inhibition as a novel therapeutic approach to prevent p-tau associated with vascular cognitive impairment. A molecular hybridization approach, utilizing molecular docking within the catalytic domain of the MARK4 crystal structure, facilitated the *de novo* design of novel inhibitors with favorable protein-ligand interactions. Subsequent testing of the compounds in a MARK4 inhibition assay enabled the identification of key structural elements for biological activity, further guiding optimization efforts. This led to the design and synthesis of twenty-four new chemical entities and ultimately DDL-662, a potent and selective MARK4 inhibitor capable of inhibiting MARK4-mediated phosphorylation of Ser262 on full-length human tau *in-vitro*. Importantly, DDL-662 also demonstrated limited toxicity and physicochemical properties consistent with good drug-likeness for treating central nervous system (CNS) disorders. This discovery represents a promising, first-in-class therapeutic strategy for preventing tau-mediated cortical disconnection following vascular brain injury that warrants further evaluation *in-vivo*.

Key Words: Microtubule Affinity-Regulating Kinase, Tau, Phosphorylation, Stroke, Cognitive Impairment, Vascular Injury, Alzheimer's Disease

INTRODUCTION

Stroke stands as a leading cause of adult disability in the United States, with vascular cognitive impairment and dementia (VCID) ranking as the second most prevalent dementia form, only surpassed by Alzheimer's disease (AD). In the United States alone, around 795,000 individuals experience either new or recurrent strokes annually (Ref. 1). The economic consequences of stroke are substantial, resulting in medical care expenses exceeding \$18 billion, alongside an additional \$15 billion attributed to post-stroke disability and reduced productivity (Ref. 2). The occurrence of cognitive impairment following a stroke ranges from 15% to 70%, and it can manifest either immediately after a stroke event or gradually due to chronic cerebral microvascular disease (Ref. 3-11).

The primary neuropathological manifestation in VCID is the presence of microvascular ischemia in the brain's white matter, which accumulates progressively over time (Ref. 12). Similar to AD, white matter injury in VCID is a progressive phenomenon, and the currently established stroke prevention strategies have proven unsuccessful in clinical trials (Ref. 13-14). Autopsy findings reveal that approximately 50% of dementia patients exhibit mixed dementia, characterized by features of chronic cerebrovascular disease, such as white matter injury, in addition to AD pathology (Ref. 15). Magnetic resonance imaging demonstrates a correlation between the degree of AD pathology and the presence of white matter hyperintensities in patients, and cerebrovascular pathology was significantly more pronounced in a cohort of sporadic AD subjects compared to those with autosomal dominant AD (Ref. 12, 16). Furthermore, cortical tau burden is associated with white matter hyperintensities on MRI, suggesting a relationship between axonal injury in the white matter and pathological changes in the connected cortex (Ref. 17, 18). Currently, there are

no therapeutic strategies specifically developed to target VCID and prevent neuronal pathology after a stroke.

The family of enzymes known as microtubule affinity-regulating kinases (MARK) plays a crucial role in regulating the cellular cytoskeleton (Ref. 19). In both humans and rodents, there are four MARK enzymes, all of which have been implicated in Alzheimer's disease (AD) and are associated with hyperphosphorylated tau (p-tau) found in neurofibrillary tangles (NFTs) (Ref. 20). Single nucleotide polymorphisms near the genetic loci of MARK4, identified through genetic linkage analysis, have been associated with sporadic dementia (Ref. 21). Among the MARK enzymes, MARK4 is most closely correlated with Braak stage pathology in the AD brain (Ref. 22). Its primary function as a kinase is to phosphorylate tau at a specific residue, serine 262 (Ser262), within the KXGS motif located in tau's microtubule-binding domain. Phosphorylation at Ser262 precedes the formation of NFTs and has the potential to induce neuronal cell death (Ref. 23-24). The role of tau phosphorylation at Ser262 remains controversial, but the majority of evidence suggests that phosphorylation at this site within the tau repeat domains acts as a gateway phosphorylation event, facilitating additional phosphorylation events, tau aggregation, and sensitization of neurons to β -amyloid-induced tau aggregation (Ref. 25-28). Interestingly, MARK4-mediated phosphorylation of tau at Ser262 has also been closely associated with vascular cognitive impairment and dementia (VCID) (Ref. 29). Specifically, the increased expression of MARK4 in deep layer cortical neurons following a stroke strongly suggests that p-tau-mediated reorganization of the neuronal cytoskeleton contributes to the shortening and/or loss of the axon initial segment (AIS), the primary regulator of neuronal excitability (Ref. 29). These findings reveal a shared molecular pathway mediated by MARK4, which connects subcortical vascular

injury in the form of axonal ischemia to the predominant pathology observed in AD: tau phosphorylation.

The present study investigates the inhibition of MARK4 as a novel therapeutic approach to prevent the phosphorylation of tau at Ser262, which is associated with vascular cognitive impairment. In this study, we describe the design, optimization, and characterization of potent, bioavailable, and selective inhibitors targeting MARK4. Through *in-silico* techniques, novel MARK4 inhibitors were designed *de novo* using a molecular hybridization approach followed by molecular docking of small molecules in the catalytic domain of the MARK4 crystal structure. Subsequent testing of biological activity in a MARK4 inhibition assay and structure-activity relationship analyses guided optimization efforts, leading to the design and synthesis of twenty-four new chemical entities, including DDL-662, a potent and selective inhibitor capable of inhibiting MARK4-mediated phosphorylation of Ser262 on full-length human tau *in-vitro*. Various *in-vitro* ADME assays were then used to assess the drug-like properties of candidate inhibitors. This accurately predicted the good brain bioavailability of the lead candidate DDL-662, which awaits evaluation in mouse models that reliably induce MARK4-mediated increases in tau phosphorylation at serine 262. The selective MARK4 inhibitors presented in this study hold promise as a first-in-class therapeutic strategy for preventing p-tau-mediated pathogenesis and cognitive impairment following vascular brain injury.

METHODS

Molecular Docking and Scoring of Protein-Ligand Binding Energy

Molecular docking and scoring was performed in Flare (Cresset, v.7) using the Lead Finder docking algorithm (Ref. 30). Lead Finder combines a generic algorithm search with local optimization procedures. Three different scoring functions are employed and optimized for the accurate prediction of 3D docked ligand poses, protein-ligand binding energy and rank-ordering of active and inactive compounds in virtual screening experiments. Pocket Detection in Flare is based on the fpocket and MDpocket methods, and can be used to identify and characterize pockets and cavities within a protein structure, enabling the identification of possible drug binding active sites, water binding pockets, channels and small cavities, large solvent-exposed sites (Ref. 31-32).

Compound Synthesis via Amide Coupling

Carboxylic acid-containing substituent (1 equiv.), amine-containing substituent (2 equiv.), 1-ethyl-3-(3-dimethylaminopropyl)carbodiimide (EDC; 1.1 equiv.), hydroxybenzotriazole (HOBt; 1.1 equiv.), and N,N, diisopropylethylamine (DIPEA; 2 equiv.) were added to a round bottom flask. The reagents were solubilized using anhydrous tetrahydrofuran and the reaction mixture was stirred at 23 °C for 16 hours. The crude product was concentrated in vacuo, reconstituted with ethyl acetate, and an aqueous work-up was performed in a separatory funnel using a saturated sodium bicarbonate solution. The retained organic phase was dried with anhydrous sodium sulphate, concentrated in vacuo, and then purified via flash column chromatography using a 4 g silica flash column with a mobile phase of hexanes:ethyl acetate (time/% ethyl acetate: 0/0, 3/0, 30/100, 40/100). The tert-butyloxycarbonyl (BOC) amine protecting group was removed by the addition of 4.0 N hydrochloric acid (HCl) in Dioxane at 4 °C for 30 minutes. Identity and purity of each compound was confirmed via LC-MS and ¹H NMR.

Purity Analysis via Liquid Chromatography-Mass Spectrometry (LC-MS)

Analysis of purity by liquid chromatography-mass spectrometry (LC-MS) was done at the UCLA Pasarow Mass Spectrometry Lab (PMSL; Julian Whitelegge, Ph.D., Director). Compounds were diluted to 10 mM in DMSO, then diluted 100-fold in 50/50/0.1 Water/Acetonitrile/Formic Acid (100 μ M final concentration). An aliquot (10 μ L) was analyzed using a LTQ Orbitrap XL mass spectrometer (Thermo Fisher Scientific) coupled to an UltiMate 3000 HPLC (Thermo Fisher Scientific) with a Phenomenex analytical column (Kinetex 1.7 μ m C18 100 Å 100 x 2.1 mm). The mass spectrometer acquisition method scanned a mass range from 100 – 2000 m/z . The HPLC method utilized a mixture of solvent A (99.9/1 Water/Formic Acid) and solvent B (99.9/1 Acetonitrile/Formic Acid) and a gradient was used for the elution of the compounds (min/%B: 0/0, 3/0, 19/99, 20/99, 21/0, 30/0). An ion extracted chromatogram (IEC) using the m/z corresponding to the $[M+H]^+$ ion was utilized to identify the chromatographic peak for each compound. Purity was calculated by dividing the chromatographic peak area for each compound by the sum of all the non-background peak areas in the total ion chromatogram (TIC).

Purity Analysis via Proton Nuclear Magnetic Resonance Spectroscopy (1H NMR)

Analysis of purity by magnetic resonance spectroscopy was done at the UCLA Molecular Instrumentation Center (MIC; Ignacio Martini, Ph.D., Director). ~4 mg of compound were diluted in 750 μ L of MeOH-D₄ and analyzed using a AV400 nmr spectrometer (Bruker) containing a 5 mm broadband Z-gradient probe with Automatic Tune and Match (ATM). The analysis method consisted of a 64-scan proton nmr (1H -NMR) utilizing default parameters. Predicted 1H -NMR spectra were obtained using the ChemNMR 1H estimation function in ChemDraw (PerkinElmer). The experimental data was visualized and interpreted using Mnova (Mestrelab Research).

HotSpot Kinase Assay:

Enzyme activity and compound IC₅₀'s were determined using a radiometric kinase inhibition assay. Compounds were tested in range of ten concentrations from 100 μM to 0.0017 μM using 3-fold serial dilutions. Enzymes were incubated for one hour with each compound and 10 μM radioisotope-labelled ATP (³³P-ATP), and kinase activity was subsequently detected using (³³P) phosphorylation of an appropriately selected peptide substrate. IC₅₀ curve fits were performed for compounds that inhibited enzyme activity greater than 50%.

Kinetic Solubility

Test compound (10 mM, 100% DMSO) was diluted separately into aqueous buffer (100 μM; PBS pH 7.4) and DMSO at various concentrations (0.1, 1, 10, 100 μM). The solutions were then incubated at 37 °C for 90 min and centrifuged (16000xg, 5 min). An aliquot of each supernatant is analyzed by LC-MS/MS. A standard curve was made by plotting the known amount of analyte per standard in DMSO vs. absorbance or chromatographic peak area. Kinetic solubility (mM) was calculated using the trendline equation with maximum absorbance or chromatographic peak area observed in the aqueous sample.

Liver Microsome Stability Assay

An aliquot (1 μL) of test compound (1 mM, 100% DMSO) was added to an aqueous liver microsome solution (1000 μL, PBS pH 7.4, 0.5mg/mL human liver microsomes (Thermo Fisher Scientific, Cat#HMMPL), 2 mM NADPH, 2 mM MgCl₂) and incubated at 37 °C for 120 min. Aliquots (50 μL) of the microsome solution were taken at various time points (0, 5, 10, 15, 30, 60,

90, 120 min) and added to a reaction quenching solution (400 μ L 100% Acetonitrile) containing an internal standard. Solutions were clarified by centrifugation (16,000 x g, 5 min), and the supernatants were transferred to new tubes and lyophilized. Samples were reconstituted in 100 μ L of 50/50/0.1 (Water/Acetonitrile/Formic Acid) prior to analysis via liquid chromatography-tandem mass spectrometry (LC-MS/MS). Chromatographic peak areas normalized to the internal standard were plotted at each time point and the half-life ($t_{1/2}$) of compound in liver microsomes was determined by using the trendline equation to calculate the time at which compound abundance was 50% of that at time point 0 (t_0).

Plasma and Brain Tissue Binding Assays

Brain tissue was homogenized in PBS (pH 7.4) (1: 3 weight(mg)/volume(μ L)) and the protein concentration was determined using the Micro BCA™ Protein Assay Kit (Thermo Fisher Scientific, Cat#23235). Brain homogenate was clarified and diluted to 20 mg/mL in PBS (pH 7.4). Either brain homogenate or plasma was added to Slide-A-Lyzer™ MINI Dialysis Devices, 10K MWCO dialysis cups (Thermo Fisher Scientific, Cat#PI88401) in a 48-well plate containing PBS (500 μ L; pH 7.4). 1 μ L of 1 mM compound was added to the brain homogenate (Final Concentration: 2 μ M compound, 0.5% DMSO) and incubated on a rocker for 4.5 hours at 37 °C. 50 μ L of brain homogenate or plasma (within the dialysis cup) and PBS (within the 48-well plate) were transferred to new microcentrifuge tubes containing 400 μ L of quenching reagent (100% Acetonitrile) containing internal standard. Solutions were clarified by centrifugation (16,000 x g, 5 min), and the supernatants were transferred to new tubes and lyophilized. Samples were reconstituted in 100 μ L of 50/50/0.1 (Water/Acetonitrile/Formic Acid) prior to analysis via liquid

chromatography-tandem mass spectrometry (LC-MS/MS). The % of the unbound drug ($f_{u, \text{bound}}$) was calculated using the following equation:

$$\% \text{ Bound} = [1 - (\text{PBS chromatographic peak area} / \text{brain homogenate or plasma chromatographic peak area})] \times 100$$

Blood-Brain Barrier (BBB) Permeability Assay

A liquid chromatography-ultraviolet/visible spectroscopy (LC-UV/Vis) assay was performed on a 1290 Infinity HPLC system (Agilent Technologies) with an HPLC column containing immobilized phosphatidylcholine (IAM.PC.DD, Regis Technologies, Cat#774011, 5 μm 300 \AA 100 x 4.6 mm). The HPLC method was a mixture of 6.7 mM phosphate buffer saline (pH 7.4; solvent A) and acetonitrile (solvent B), and a gradient was used for the elution of the compounds (min/%B: 0/20, 20/60, 21/20, 30/20). The retention time of the compound (t_r) and void volume time of the column (t_0) were recorded. Blood-brain barrier (BBB) permeability (P_m) was calculated using the following equations as described by Yoon et al (DOI: 10.1177/1087057105281656):

$$K_{\text{IAM}} = (t_r - t_0) / t_0; P_m = (K_{\text{IAM}} / \text{MW}^4) \times 10^{10}$$

Compounds with a $P_m > 0.85$ were determined to be BBB permeable (CNS+) at pH 7.

In-Vivo Pharmacokinetics

Following oral administration of compound, mice brain tissue and plasma were collected after euthanasia and perfusion at 1, 2, 4, and 6 hours. Brain tissue were homogenized in a bead beater using 5 volumes of ice-cold 80% acetonitrile (1/5; mg of brain/ μL of 80% ACN). Plasma analytes were extracted using 4 volumes of ice-cold acetonitrile (1/4; μL of plasma/ μL of ACN). Solutions were clarified by centrifugation (16,000 x g, 5 min) and the supernatants were transferred to new

tubes and lyophilized. Samples were reconstituted in 100 μ L of 50/50/0.1 (Water/Acetonitrile/Formic Acid) prior to analysis via liquid chromatography-tandem mass spectrometry (LC-MS/MS). An internal standard (IS) was added to every sample to account for compound loss during sample processing. Standards were made in drug naïve plasma and brain lysates with increasing amounts of analyte (S1, S2: 0 pmol/ S3, S4: 1 pmol/ S5, S6: 10 pmol/ S7, S8: 100 pmol, S9, S10: 1000 pmol). The standard curve was made by plotting the known amount of analyte per standard vs. the ratio of measured chromatographic peak areas corresponding to the analyte over that of the IS (analyte/IS). The trendline equation was then used to calculate the absolute concentrations of each compound in plasma and brain tissue.

Liquid Chromatography-Tandem Mass Spectrometry

Analysis of compound levels was done at the UCLA Pasarow Mass Spectrometry Lab (PMSL; Julian Whitelegge, Ph.D., Director). A targeted LC-MS/MS assay was developed for each compound using the multiple reaction monitoring (MRM) acquisition method on a 6460 triple quadrupole mass spectrometer (Agilent Technologies) coupled to a 1290 Infinity HPLC system (Agilent Technologies) with a Phenomenex analytical column (Kinetex 1.7 μ m C18 100 Å 100 x 2.1 mm). The HPLC method utilized a mixture of solvent A (99.9/1 Water/Formic Acid) and solvent B (99.9/1 Acetonitrile/Formic Acid) and a gradient was used for the elution of the compounds (min/%B: 0/1, 3/1, 19/99, 20/1, 30/1). Two fragment ions originating from each compound were monitored at specific LC retention times to ensure specificity and accurate quantification in the complex biological samples. The normalized chromatographic peak areas were determined by taking the ratio of measured chromatographic peak areas corresponding to each compound over that of the internal standard (Analyte/IS).

Intracerebroventricular (ICV) injection with IL-1 β

Tau P301S (PS19 line) tauopathy mice received unilateral intracerebroventricular (ICV) injections of either 0.2 ng of IL-1 β or vehicle (0.1% BSA/PBS, pH 7.4) for control (n=4 animals per group). During the surgical procedure animals were deeply anesthetized with isoflurane and injections were performed at rate 0.6 μ l/min by Hamilton syringe at a depth of 1.8 mm, -0.2 mm posterior to bregma and 1 mm to the right of midline using a small animal stereotactic frame. Mice were sacrificed 2 hours after the injections with overdose of pentobarbital, and brain tissue were collected after transcardial perfusion with normal saline. Cerebellum tissue were dissected, weighted, snap frozen on dry ice, and stored at -80 °C until further analysis.

RESULTS

In-Silico Design Guides Synthesis of Selective MARK4 Inhibitors

Using molecular hybridization of isatin-triazole hydrazones (Ref. 33) to the pyrazolone pyrimidine inhibitor (Ref. 34), we designed *de novo* a novel series of MARK4 inhibitors. Computer-aided molecular docking of these small molecules in the catalytic domain of the MARK4 crystal structure PDB: 5ES1 (Ref. 34) were used to model potential protein-ligand physiochemical interactions and facilitate *de novo* design of novel structures with favorable binding energies (**Fig. 1A**). The general synthetic approach utilized to synthesize novel MARK4 inhibitors consisted of two consecutive reactions (**Fig. 1B**). Briefly, each intermediate was synthesized by performing a coupling reaction between a carboxylic acid-containing substituent (1 equiv) and an amine-containing substituent (2 equiv) in the presence of 1-ethyl-3-(3-dimethylaminopropyl)carbodiimide (EDC; 1.15 equiv) and hydroxybenzotriazole (HOBt; 1 equiv)

at 23 °C for 16 hours. Next, each analog was synthesized by removing the tert-butyloxycarbonyl (BOC) amine protecting group by the addition of 4.0 N hydrochloric acid (HCl) in Dioxane at 4 °C for 30 minutes. Optimization efforts led to the design and synthesis of twenty-four new chemical entities (NCEs) with chemical alterations in three different regions of the molecule (A, B, C) (**Fig. 1B, Supplementary Fig. S1**). Six of these analogs (DDL-652, -661, -662, -663, -672, -673) were determined to inhibit MARK4 activity more than 50% at a concentration of 100 μM in a radiometric kinase inhibition assay using a short peptide substrate (**Fig. 1C, 1D**). A dose response analysis identified DDL-662 as the most potent MARK4 inhibitor, with an IC_{50} of 1.8 μM (**Fig. 1D**). DDL-662 was also determined to be partially selective for MARK4 over other MARK enzymes, inhibiting MARK2 and MARK3 with a IC_{50} 's of 8.6 μM and 25.1 μM , respectively (**Fig. 1E**).

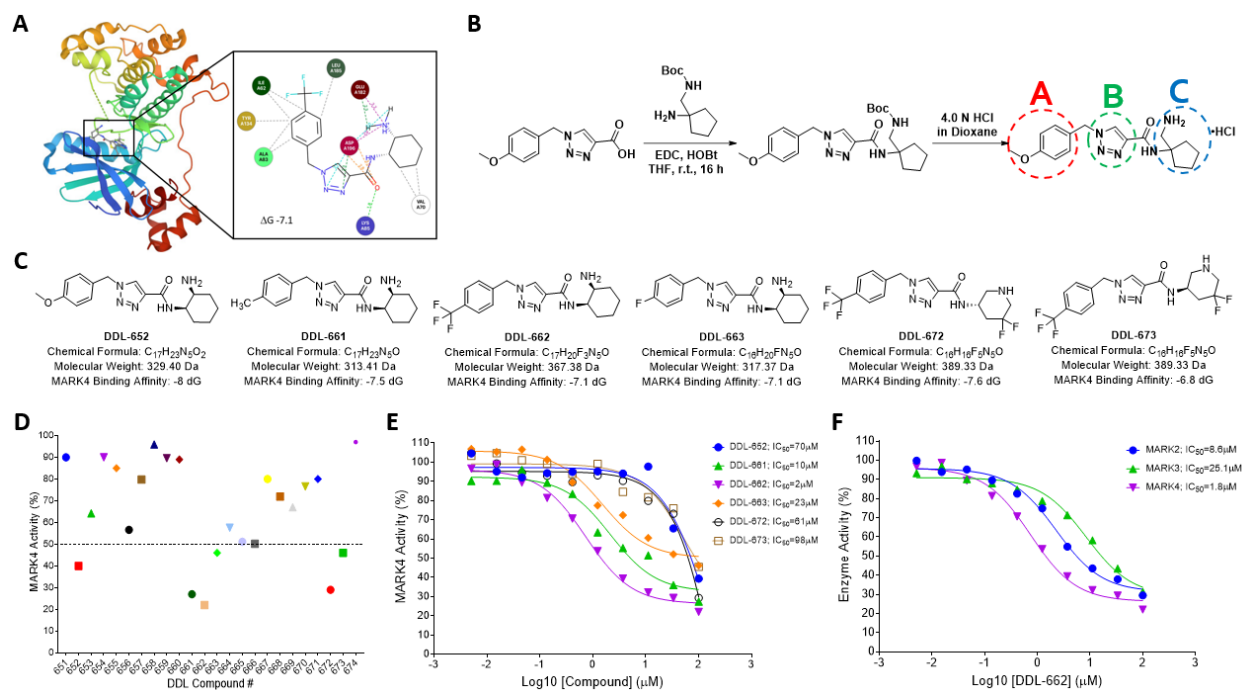


Figure 1. *In-Silico* design guides synthesis of selective MARK4 inhibitors. (A) A schematic showing molecular docking of DDL-662 in the catalytic domain MARK4 crystal structure PDB:5ES1 (Ref. 34) and predicted protein-ligand physiochemical interactions. (B) General synthetic scheme used to synthesize novel MARK4 inhibitors. Different regions of the molecule to be modified are A (red), B (green) and C (blue). (C) Structures of new chemical entities that inhibit MARK4 activity greater than 50%. (D) MARK4 activity (%) following treatment with each compound at a concentration of 100 μ M (E) Dose-response curves showing MARK4 activity (%) and calculated IC₅₀ values for DDL-652 (70 μ M), -661 (10 μ M), -662 (2 μ M), -663 (23 μ M), -672 (61 μ M), -673 (98 μ M), following treatment at concentrations of 5, 15, 45, 137, 412, 1235, 3703, 11111, 33333 and 100000 nM. (F) Dose-response curves showing enzyme activity (%) and calculated IC₅₀ values for DDL-662 and MARK2 (8.6 μ M), MARK3 (25.1 μ M) and MARK4 (1.8 μ M), following treatment at concentrations of 5, 15, 45, 137, 412, 1235, 3703, 11111, 33333 and 100000 nM.

Hit-to-Lead Optimization Identifies Candidates with Good ADME Properties

A structure-activity relationship analysis of the synthesized analogs revealed structural elements required for compound activity and/or enhanced MARK4 inhibition (**Fig. 2**). While the first analog designed, DDL-651, only marginally inhibited MARK4 by approximately 10% at a concentration of 100 μ M, substantial improvements in potency were achieved by systematically modifying chemical subgroups in regions A, B or C, followed by testing of biological activity in a MARK4 inhibition assay. Substitution of a cyclopentane ring with a cyclohexane in region C dramatically increased potency, improving the IC₅₀ from greater than 100 μ M to 70 μ M. Additional improvements in MARK4 inhibitory activity were achieved through iteratively modifying

functional groups in the para position on the benzyl group in region A. Ultimately, replacement of the hydrogen bond accepting methoxy group with a trifluoromethyl resulted in the identification of the most potent MARK inhibitor, DDL-662, which has an IC_{50} of 1.8 μM .

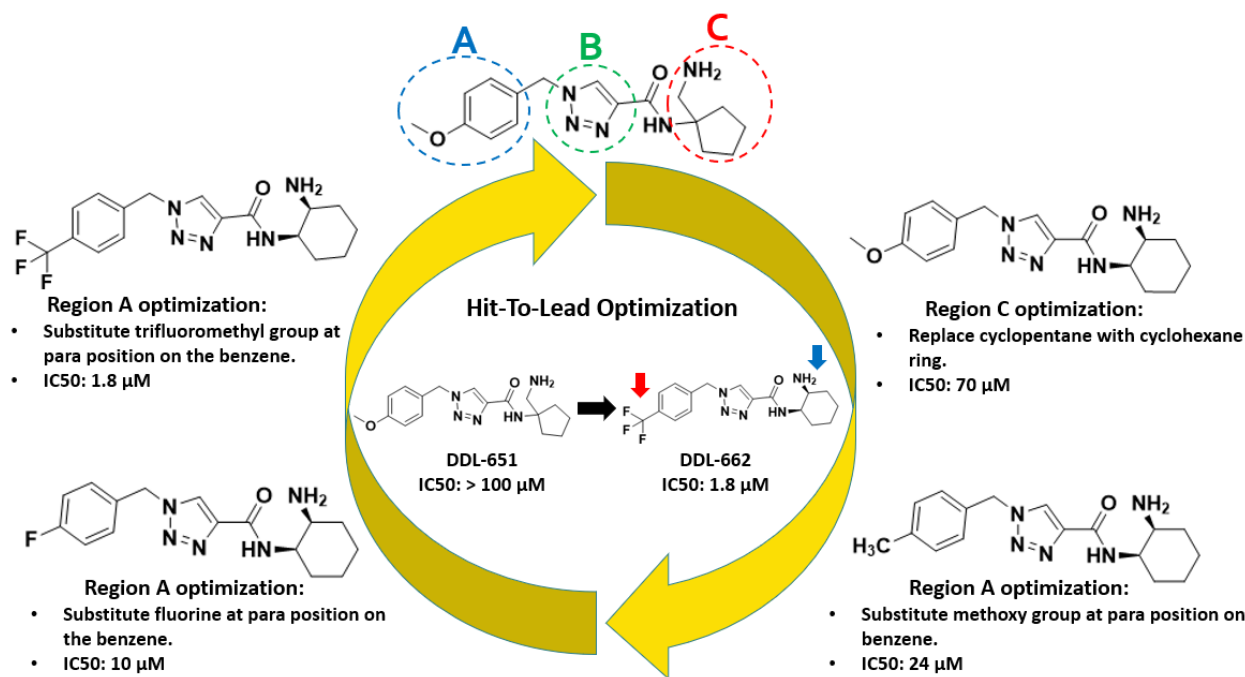


Figure 2. Hit-to-lead optimization of MARK4 inhibitors. A schematic showing hit-to-lead optimization of MARK4 inhibitors through systematic altering of chemical subgroups in regions A, B and C, which ultimately led to the identification of potent lead candidate, DDL-662.

To determine which compounds were likely to be successful therapeutics *in-vivo*, various *in-vitro* assays were used to determine physicochemical properties that influence compound absorption, distribution, metabolism, excretion (ADME) (**Table 1**). This included the assessment of compound solubility, metabolic stability, plasma binding, brain tissue binding, and blood-brain barrier (BBB) permeability. Desired *in-vitro* ADME property values are as follows: Aqueous Kinetic Solubility > 100 μM ; Liver Microsomal Stability $t_{1/2}$ > 1 hour; Plasma Binding < 90%; Brain Tissue Binding

< 80%, BBB Permeability $P_m > 0.85$. All six candidate MARK4 inhibitors tested in these ADME assays demonstrated favorable physiochemical properties, indicating that they should display good *in-vivo* brain bioavailability. Due to its favorable physiochemical properties as well as significantly enhanced potency, DDL-662 was selected as the lead MARK4 inhibitor for further evaluation in an *in-vitro* tau phosphorylation assay and *in-vivo*.

Compound	Structure	Molecular Weight [Da]	Kinetic Solubility [μM]	Microsomal Stability [$t_{1/2}$ (min)]	Plasma Binding [% Bound]	Brain Tissue Binding [% Bound]	BBB Permeability PAMPA [P_m]	In-Vitro Efficacious Dose (nM)]
DDL-652		329.4	>100	>120	68.5	32.4	2.55	70
DDL-661		313.41	>100	>120	68.4	40.1	3.86	10
DDL-662		367.38	>100	>120	83.6	65.2	2.79	2
DDL-663		317.37	>100	>120	48.4	34.2	3.18	23
DDL-672		389.33	>100	>120	85.3	41.6	1.27	61
DDL-673		389.33	>100	>120	85.1	43	1.23	98

*Desired ADME property values: Kinetic Solubility > 100 μM ; Microsomal Stability $t_{1/2}$ > 1 hrs; Plasma Binding < 90%; Brain Tissue Binding < 80%; PAMPA $P_m > 0.85$ = CNS+; *in-vitro* efficacious dose < 5 μM

Table 1. *In-vitro* ADME properties of candidate MARK4 inhibitors.

Lead Candidate, DDL-662, is Bioavailable and Prevents MARK4-mediated Tau Phosphorylation

An *in-vitro* tau phosphorylation assay was developed and utilized to determine that lead candidate, DDL-662, significantly decreased MARK4-mediated increases in p-tau at serine 262 at

concentration of 10 μM (**Fig. 3A**). DDL-662 was also shown to be well-tolerated in a cell toxicity assay in primary mouse cortical neurons and human hepatoma cells (HepG2) (**Fig. 3B**). Though, there was a significant decline in the survival of the human embryonic kidney cells (HEK293T) at a concentration of 10 μM (**Fig. 3B**). A subsequent pharmacokinetics analysis confirmed DDL-662 to be orally bioavailable following oral administration via pipette feeding. DDL-662 reached a maximum brain concentration of approximately 1 μM , 2-hours post administration at a dose of 20 mg/kg, which is close to the predetermined *in-vitro* efficacious dose ($\text{EC}_{50} = 1.8 \mu\text{M}$) (**Fig. 3C**). Next, a rapid p-tau ser262 *in-vivo* assay was established employing intracerebroventricular (ICV) injection of interleukin-1 β (IL-1 β) into the frontal cortex of the PS19 transgenic mouse model expressing mutant human tau, inducing approximately a 1.7-fold increase in phosphorylation after only two hours (**Fig. 3D**).

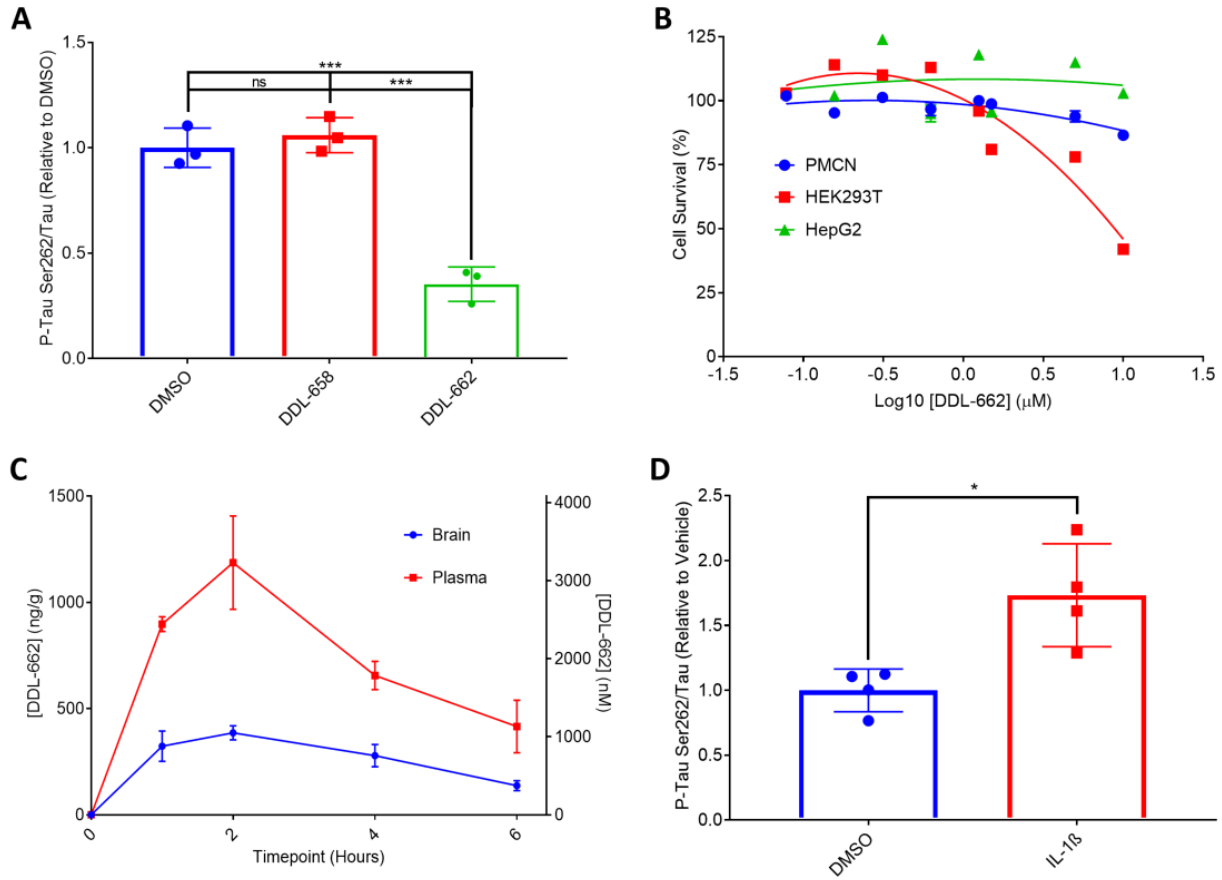


Figure 3. *DDL-662 is Bioavailable and Prevents MARK4-mediated Tau Phosphorylation.* (A) Levels of tau phosphorylation at serine 262, following incubation with MARK4 in the presence of 0.1% DMSO, DDL-58 (10 µM), or DDL-662 (10 µM). (B) Cell Survival (%) of primary mouse cortical neurons (PMCN), human embryonic kidney cells (HEK293T) and human hepatoma cells (HepG2), following treatment with DDL-662 at concentrations of 0.078, 0.156, 0.313, 0.625, 1.25, 2.5, 5, 10 µM. (C) DDL-662 brain and plasma concentrations, 1, 2, 4 and 6 hours following oral administration at a dose of 20 mg/kg. (D) Levels of tau phosphorylation at serine 262, relative to total tau, in the frontal cortex 2 hours after intracerebroventricular injection of vehicle or IL-1β (0.2 ng).

DISCUSSION

To the best of our knowledge, this study represents the first description of the design, optimization, and characterization of MARK4-selective inhibitors aimed at preventing site-specific phosphorylation of tau at Serine 262, which is associated with the onset of VCID. A molecular hybridization approach utilizing molecular docking within the catalytic domain of the MARK4 crystal structure facilitated the *de novo* design of novel inhibitors with favorable protein-ligand interactions. While this was fundamental to defining the general structure of this novel class of inhibitors, testing of these compounds in a MARK4 inhibition assay and subsequent structure-activity-relationship analyses were needed to identify key structural elements for biological activity that guided further optimization efforts. This led to the design and synthesis of twenty-four novel MARK4 inhibitors and ultimately DDL-662, the most potent inhibitor with an IC₅₀ of 1.8 μ M. Remarkably, DDL-662 also demonstrated approximately 5-fold and 14-fold selectivity for MARK4 over MARK2 and MARK3, respectively. This potentially allows its use as a MARK4-specific therapeutic, as proper dose-setting could be utilized to achieve DDL-662 concentrations high enough to inhibit MARK4 without affecting the activity of the other MARK enzymes. While MARK2 and MARK3 have also been implicated in the pathological phosphorylation of tau, it has not been shown to be linked to or initiated by vascular brain injury. Hence, the development of selective therapeutics targeting MARK4 represents a valuable approach, as it avoids disrupting the normal homeostatic functions of other MARK enzymes. Limiting drug promiscuity is critical in preventing adverse reactions/effects that often contribute to drug attrition (Ref. 35).

Importantly, DDL-662 also demonstrated physicochemical properties consistent with good drug-likeness for treating central nervous system (CNS) disorders. It is crucial to note that while a compound may exhibit good in-vitro drug activity, it does not automatically guarantee favorable

in-vivo activity unless it also possesses good bioavailability and half-life (Ref. 36). Moreover, the escalating costs associated with the development of novel therapeutics and the high rate of candidate attrition have prompted a shift in drug discovery strategies towards the simultaneous evaluation of comprehensive drug physicochemical and ADME properties alongside efficacy (Ref. 37). This comprehensive assessment holds particular significance for CNS disorders due to the selective exclusion of nearly 100% of large-molecule neurotherapeutics and over 98% of all small-molecule drugs by the blood-brain barrier (BBB) (Ref. 38). *In-vitro* ADME assays, indicating a high degree of aqueous solubility ($>100 \mu\text{M}$), metabolic stability ($>120 \text{ min}$), BBB permeability (CNS+), as well as low plasma binding (83.6%) and brain tissue binding (65.2%), accurately predicted good brain bioavailability *in-vivo*. A pharmacokinetic analysis revealed that DDL-662 could reach therapeutically relevant micromolar concentrations in the brain, achieving a maximum concentration of $1 \mu\text{M}$ following oral administration at a dose of 20 mg/kg . Based on this information, one could assume that doubling the dose to 40 mg/kg would result in a brain concentration greater than the DDL-662 IC_{50} ($1.8 \mu\text{M}$) and inhibit the phosphorylation of tau at serine 262 *in-vivo*. Given that drug toxicity is a key contributor to drug attrition in preclinical and clinical development, and a reasonable concern at micromolar concentrations, DDL-662 cytotoxicity was evaluated in primary mouse cortical neurons and two cell lines commonly used to assess nephrotoxicity and hepatotoxicity (Ref. 39-40). Encouragingly, there was no significant toxicity observed at concentrations necessary for therapeutic efficacy. However, there was some indication that DDL-662 may be toxic to kidney cells at higher concentrations, highlighting the importance of pharmacokinetics and toxicology studies for establishing proper dosing and ensuring patient (or mouse) safety. Overall, the potency, selectivity, bioavailability, and toxicology of DDL-662 support its use as a safe MARK4-specific therapeutic *in-vivo*.

Prior to further evaluation *in-vivo*, DDL-662 was tested in an *in-vitro* phosphorylation assay using a recombinant human tau substrate. Not surprisingly, significant inhibition of tau phosphorylation at serine 262 was observed following DDL-662 treatment at a concentration of 10 μ M. This provided additional confidence that the designed inhibitors not only prevented the interaction between the radiometric kinase assay substrate and MARK4, but, as predicted, also likely occupied the catalytic domain of MARK4, effectively inhibiting MARK4 phosphorylation of any substrate, including tau. To assess the efficacy of DDL-662 *in-vivo*, a rapid *in-vivo* tau phosphorylation assay was developed based on previous evidence that IL-1 β exacerbates tau pathology (Ref. 38-39). As expected, the injection of IL-1 β into the frontal cortex of the PS19 tauopathy mice induced significant increases in tau phosphorylation at serine 262 after only two hours. While it is yet to be tested, we are optimistic that the administration of DDL-662 prior to ICV injection will prevent IL-1 β -induced phosphorylation of serine 262. We also plan to evaluate DDL-662 in a more disease-relevant, chronic *in-vivo* study, utilizing a mouse model of subcortical white matter ischemic injury known to increase MARK4-mediated phosphorylation of tau at serine 262 (Ref. 29, 41-42).

In conclusion, the results presented here highlight the usefulness of *in-silico* approaches such as molecular docking for de novo drug design and structure-activity-relationship analyses to guide lead optimization. This approach led to the development of DDL-662, a potent, selective, and bioavailable MARK4 inhibitor that prevents MARK4-induced tau phosphorylation at serine 262 *in-vitro*. This discovery presents an opportunity for further development and evaluation of these inhibitors as a new therapeutic approach to prevent the pathological accumulation of

hyperphosphorylated tau associated with the onset of VCID and AD. The ultimate goal is to develop more potent candidates targeting MARK4 and assess them in more advanced models of stroke and VCID.

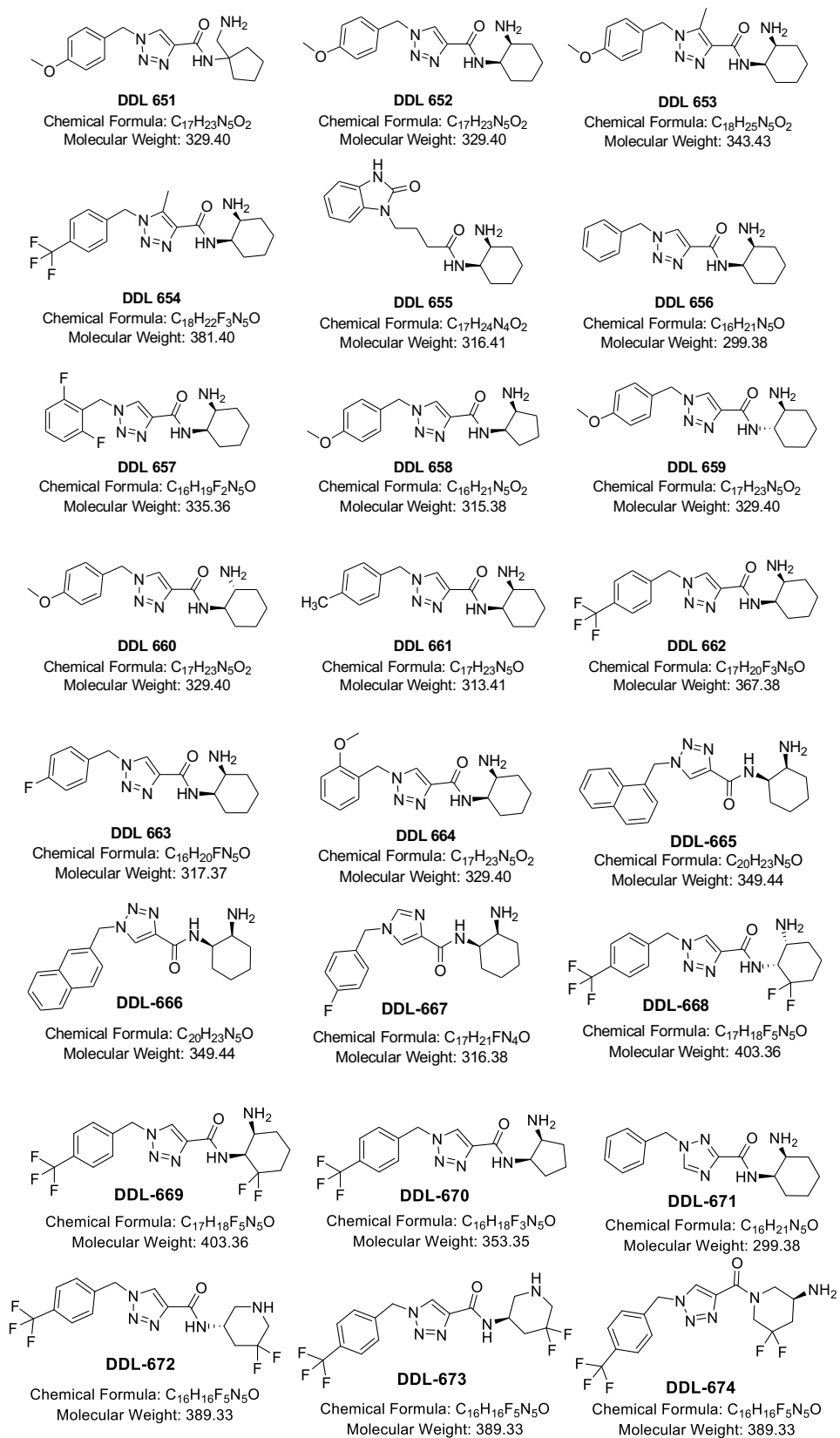
Author Contributions

WC, VJ, JH, JW, JC, BJ participated in research design. WC, MV, JA conducted experiments. WC, NK synthesized compounds. TB and CZ perform IL-1 β surgeries. WC, MV, JL performed data analysis. WC wrote the manuscript. VJ, JH, JC edited the manuscript.

Acknowledgement

Thanks to the support of the Easton Center for Alzheimer's Disease Research and Care to the Drug Discovery Lab on this project.

SUPPLEMENATRY FIGURES



Supplementary Figure S1. Chemical structures of all new chemical entities synthesized.

SUPPLEMENATRY ANALYTICAL MATERIAL

DDL-651:

^1H NMR ($(\text{CD}_3)_2\text{SO}$) δ 1.65 (m, 6H), δ 2.11 (m, 2H), δ 3.22 (s, 2H), δ 3.73 (s, 3H), δ 5.57 (s, 2H), δ 6.92 (s, 2H), δ 7.34 (s, 2H), δ 7.81 (s, 1H), δ 8.07 (s, 2H), δ 8.65 (s, 1H). LC-MS m/z $[\text{M}+\text{H}]^+ = 330.19$

DDL-652:

^1H NMR (400 MHz, MeOD) δ 8.46 (s, 1H), 7.31 (d, $J = 63.1$ Hz, 2H), 6.95 (d, $J = 12.6$ Hz, 2H), 5.58 (s, 2H), 4.49 (s, 1H), 3.78 (s, 3H), 3.74 (d, $J = 0.0$ Hz, 1H), 3.67 (d, $J = 0.0$ Hz, 2H), 3.58 (s, 1H), 1.74 (dd, $J = 4434.5, 2126.0$ Hz, 8H). LC-MS m/z $[\text{M}+\text{H}]^+ = 330.19$

DDL-653

^1H NMR (400 MHz, DMSO) δ 7.99 (s, 1H), 7.90 (s, 2H), 7.17 (d, $J = 95.2$ Hz, 2H), 6.94 (d, $J = 32.8, 0.0$ Hz, 2H), 5.56 (d, $J = 0.0$ Hz, 2H), 3.73 (s, 3H), 3.70 (dd, $J = 6.8, 1.4$ Hz, 1H), 3.68 – 3.64 (m, 1H), 2.47 (s, 3H), 1.67 (d, $J = 64.0$ Hz, 9H). LC-MS m/z $[\text{M}+\text{H}]^+ = 344.20$

DDL-654

^1H NMR (400 MHz, DMSO) δ 8.04 (d, $J = 8.0$ Hz, 1H), 7.94 (s, 3H), 7.78 (d, $J = 8.1$ Hz, 2H), 7.41 (d, $J = 8.0$ Hz, 2H), 5.80 (s, 2H), 4.27 (d, $J = 7.6$ Hz, 1H), 3.76 – 3.63 (m, 2H), 3.55 – 3.39 (m, 3H), 2.49 (s, 10H), 1.88 – 1.35 (m, 10H), 0.07 (d, $J = 3.6$ Hz, 1H). LC-MS m/z $[\text{M}+\text{H}]^+ = 382.18$

DDL-655

^1H NMR (400 MHz, DMSO) δ 10.95 (s, 1H), 7.85 (s, 4H), 7.08 (d, J = 61.0 Hz, 4H), 4.25 (d, J = 80.7 Hz, 4H), 3.69 (d, J = 97.6 Hz, 10H), 3.23 (s, 1H), 2.22 (s, 2H), 2.05 – 1.12 (m, 12H). LC-MS m/z $[\text{M}+\text{H}]^+ = 317.19$

DDL-656

^1H NMR (400 MHz, MeOD) δ 8.47 (s, 1H), 7.37 (s, 6H), 5.67 (s, 2H), 4.49 (dd, J = 355.8, 332.2 Hz, 1H), 3.74 (d, J = 0.0 Hz, 1H), 3.66 (dd, J = 289.8, 0.0 Hz, 2H), 3.61 – 3.55 (m, 1H), 1.83 (s, 8H). LC-MS m/z $[\text{M}+\text{H}]^+ = 300.18$

DDL-657

^1H NMR (400 MHz, MeOD) δ 8.49 (s, 1H), 7.55 – 7.44 (m, 1H), 7.14 – 7.01 (m, 2H), 5.79 (s, 2H), 4.50 (s, 1H), 3.67 (dd, J = 1519.1, 0.0 Hz, 1H), 3.50 (dd, J = 8.3, 4.7 Hz, 1H), 1.83 (s, 8H). LC-MS m/z $[\text{M}+\text{H}]^+ = 336.16$

DDL-658

^1H NMR (400 MHz, MeOD) δ 8.40 (s, 1H), 7.32 (d, 2H), 6.94 (d, 2H), 5.58 (s, 2H), 4.51 (s, 1H), 3.78 (s, 3H), 3.74 (ddd, J = 6.0, 5.0, 0.9 Hz, 2H), 3.69 – 3.64 (m, 2H), 3.60 – 3.56 (m, 1H), 2.19 (s, 2H), 1.76 (s, 4H). LC-MS m/z $[\text{M}+\text{H}]^+ = 316.17$

DDL-659

^1H NMR (400 MHz, DMSO) δ 8.65 (s, 1H), 7.36 (d, 2H), 6.93 (d, 2H), 5.57 (s, 2H), 3.84 (s, 1H), 3.73 (s, 3H), 3.43 (s, 2H), 3.11 (s, 1H), 2.12 – 1.15 (m, 8H). LC-MS m/z $[\text{M}+\text{H}]^+ = 330.19$

DDL-660

^1H NMR (400 MHz, DMSO) δ 8.65 (s, 1H), 8.53 (s, 1H), 7.98 (s, 3H), 7.36 (s, 2H), 6.95 (s, 2H), 5.57 (s, 2H), 4.23 (s, 2H), 3.73 (s, 3H), 3.10 (s, 1H), 2.10 – 1.99 (m, 1H), 1.74 (dd, J = 36.7, 12.1 Hz, 3H), 1.45 (dt, J = 30.8, 11.8 Hz, 2H), 1.29 – 1.12 (m, 3H). LC-MS m/z $[\text{M}+\text{H}]^+$ = 330.19

DDL-661

^1H NMR (300 MHz, DEUTERIUM OXIDE) δ ppm 8.33 (s, 1 H) 7.17 (s, 4H) 5.51 (s, 2 H) 4.33 - 4.45 (m, 1 H) 3.66 - 3.76 (m, 1 H) 2.21 (s, 4 H) 1.58- 1.82 (m, 6 H) 1.43 - 1.55 (m, 2 H). LC-MS m/z $[\text{M}+\text{H}]^+$ = 314.19

DDL-662

^1H NMR (300 MHz, DEUTERIUM OXIDE) δ ppm 8.45 (s, 1 H) 7.69 (d, J =8.2 Hz, 2 H) 7.45 (d, J =8.2 Hz, 2 H) 5.71 (s, 2 H) 4.40 - 4.52 (m, 1 H).71 - 3.82 (m, 1 H) 1.63 - 1.92 (m, 6 H) 1.47 - 1.61 (m, 3 H). LC-MS m/z $[\text{M}+\text{H}]^+$ = 368.17

DDL-663

^1H NMR (300 MHz, DEUTERIUM OXIDE) δ ppm 8.41 (d, J =1.2 Hz, 1 H) 7.25 - 7.46 (m, 2 H) 6.97 - 7.20 (m, 2 H) 5.60 (s, 2 H) 4.39 - 4.51 (m, 2 H) 3.61 - 3.73 (m, 1 H) 1.63 - 1.92 (m, 6 H) 1.51 - 1.62 (m, 2 H). LC-MS m/z $[\text{M}+\text{H}]^+$ = 318.17

DDL-664

^1H NMR (400 MHz, MeOD) δ 8.49 (s, 1H), 7.33 – 7.18 (m, 1H), 6.97 – 6.89 (m, 3H), 6.89 – 6.82 (m, 1H), 5.63 (s, 2H), 4.49 (s, 1H), 3.75 – 3.72 (m, 1H), 3.69 – 3.63 (m, 2H), 3.61 – 3.54 (m, 1H), 1.95 – 1.60 (m, 8H). LC-MS m/z $[\text{M}+\text{H}]^+ = 330.19$

DDL-665:

^1H NMR: δ 7.81-8.00 (m, 4H), 7.37-7.71 (m, 4H), 5.42 (s, 1H), 2.98 (dt, $J = 10.3, 2.8$ Hz, 1H), 1.33-1.85 (8H). LC-MS m/z $[\text{M}+\text{H}]^+ = 350.19$

DDL-666:

^1H NMR: δ 7.58-8.04 (m, 6H), 7.37-7.53 (m, 2H), 5.40 (s, 2H), 3.92 (q, $J = 2.8$ Hz, 1H), 2.98 (dt, $J = 10.3, 2.8$ Hz, 1H), 1.33-1.85 (m, 8H). LC-MS m/z $[\text{M}+\text{H}]^+ = 350.19$

DDL-667:

^1H NMR: δ 7.77 (d, $J = 1.6$ Hz, 1H), 7.56 (d, $J = 1.6$ Hz, 1H), 7.21 (ddd, $J = 8.4, 1.3, 0.6$ Hz, 2H), 6.93 (ddd, $J = 8.4, 1.2, 0.6$ Hz, 2H), 5.16 (s, 2H), 4.52 (q, $J = 2.8$ Hz, 1H), 2.98 (dt, $J = 10.3, 2.8$ Hz, 1H), 1.33-1.85 (m, 8H). LC-MS m/z $[\text{M}+\text{H}]^+ = 317.17$

DDL-668:

^1H NMR: δ 7.86 (s, 1H), 7.65 (ddd, $J = 8.6, 1.9, 0.5$ Hz, 2H), 7.50 (ddd, $J = 8.6, 1.5, 0.5$ Hz, 2H), 5.36 (s, 2H), 4.09 (d, $J = 2.8$ Hz, 1H), 3.01 (m, 1H), 1.43-1.83 (m, 6H). LC-MS m/z $[\text{M}+\text{H}]^+ = 404.15$

DDL-669:

^1H NMR: δ 7.86 (s, 1H), 7.65 (ddd, $J = 8.6, 1.9, 0.5$ Hz, 2H), 7.50 (ddd, $J = 8.6, 1.5, 0.5$ Hz, 2H), 5.26 (s, 2H), 4.09 (d, $J = 2.8$ Hz, 1H), 3.01 (dt, $J = 10.3, 2.8$ Hz, 1H), 1.43-1.83 (m, 6H). LC-MS m/z $[\text{M}+\text{H}]^+ = 404.15$

DDL-670:

^1H NMR: δ 7.83 (1H, s), 6.49 (d, $J = 11.2$ Hz, 1H), 5.81 (d, $J = 1.9$ Hz, 1H), 5.47 (s, 2H), 4.36-4.48 (m, 2H), 4.03 (ddd, $J = 8.1, 7.6, 7.0$ Hz, 1H), 3.65 (m, 1H), 2.47-2.59 (m, 2H), 1.53-1.96 (m, 6H). LC-MS m/z $[\text{M}+\text{H}]^+ = 354.15$

DDL-671:

^1H NMR: δ 8.73 (s, 1H), 7.22-7.45 (m, 5H), 5.31 (s, 2H), 3.96 (q, $J = 2.8$ Hz, 1H), 2.97 (dt, $J = 10.3, 2.8$ Hz, 1H), 1.33-1.75 (8H). LC-MS m/z $[\text{M}+\text{H}]^+ = 299.38$

DDL-672:

^1H NMR: δ 7.85 (s, 1H), 7.65 (ddd, $J = 8.6, 1.9, 0.5$ Hz, 2H), 7.50 (ddd, $J = 8.6, 1.5, 0.5$ Hz, 2H), 5.42 (s, 2H), 4.05 (tdd, $J = 10.2, 3.3, 2.6$ Hz, 1H), 2.87 (d, $J = 6.0$ Hz, 1H), 2.54-2.77 (m, 3H), 1.85-2.10 (m, 2H). LC-MS m/z $[\text{M}+\text{H}]^+ = 390.13$

DDL-673:

^1H NMR: δ 7.85 (s, 1H). 7.65 (ddd, $J = 8.6, 1.9, 0.5$ Hz, 2H), 7.50 (ddd, $J = 8.6, 1.5, 0.5$ Hz, 2H), 5.36 (s, 2H), 4.05 (m, 1H), 2.87 (d, $J = 6.0$ Hz, 1H), 2.54-2.77 (m, 3H), 1.85-2.10 (m, 2H). LC-MS m/z $[\text{M}+\text{H}]^+ = 390.13$

DDL-674:

^1H NMR: δ 7.86 (s, 1H). 7.65 (ddd, $J = 8.6, 1.9, 0.5$ Hz, 2H), 7.50 (ddd, $J = 8.6, 1.5, 0.5$ Hz, 2H), 5.36 (s, 2H), 3.83-4.01 (m, 2H), 3.54 (dd, $J = 14.7, 10.2$ Hz, 1H), 3.18-3.43 (m, 2H), 1.65-1.93 (m, 2H). LC-MS m/z $[\text{M}+\text{H}]^+ = 390.13$

REFERENCES

1. Benjamin EJ, Muntner P, Alonso A, Bittencourt MS, Callaway CW, Carson AP, Chamberlain AM, Chang AR, Cheng S, Das SR, Delling FN, Djousse L, Elkind MSV, Ferguson JF, Fornage M, Jordan LC, Khan SS, Kissela BM, Knutson KL, Kwan TW, Lackland DT, Lewis TT, Lichtman JH, Longenecker CT, Loop MS, Lutsey PL, Martin SS, Matsushita K, Moran AE, Mussolino ME, O'Flaherty M, Pandey A, Perak AM, Rosamond WD, Roth GA, Sampson UKA, Satou GM, Schroeder EB, Shah SH, Spartano NL, Stokes A, Tirschwell DL, Tsao CW, Turakhia MP, VanWagner LB, Wilkins JT, Wong SS, Virani SS, American Heart Association Council on E, Prevention Statistics C, Stroke Statistics S. Heart Disease and Stroke Statistics-2019 Update: A Report From the American Heart Association. *Circulation*. 2019;139(10):e56-e528. Epub 2019/02/01. doi: 10.1161/CIR.0000000000000659. PubMed PMID: 30700139.
2. Fang J, Shaw KM, George MG. Prevalence of stroke—United States. In: *Prevention CfDCa*, editor. 2012. p. 379-82.
3. Ivan CS, Seshadri S, Beiser A, Au R, Kase CS, Kelly-Hayes M, Wolf PA. Dementia after stroke: the Framingham Study. *Stroke*. 2004;35(6):1264-8. Epub 2004/05/01. doi: 10.1161/01.STR.0000127810.92616.78. PubMed PMID: 15118167.
4. Rabadi MH. Progressive dementia after first-ever stroke: a community-based follow-up study. *Neurology*. 2005;64(5):932-3; author reply -3. Epub 2005/03/09. doi: 10.1212/wnl.64.5.932-a. PubMed PMID: 15753452.
5. Gutierrez Perez C, Savborg M, Pahlman U, Cederfeldt M, Knopp E, Nordlund A, Astrand R, Wallin A, Frojd K, Wijk H, Tarkowski E. High frequency of cognitive dysfunction before stroke among older people. *Int J Geriatr Psychiatry*. 2011;26(6):622-9. Epub 2010/10/06. doi: 10.1002/gps.2573. PubMed PMID: 20922768.
6. Sachdev PS, Brodaty H, Valenzuela MJ, Lorentz L, Looi JC, Berman K, Ross A, Wen W, Zagami AS. Clinical determinants of dementia and mild cognitive impairment following ischaemic stroke:

- the Sydney Stroke Study. *Dement Geriatr Cogn Disord*. 2006;21(5-6):275-83. Epub 2006/02/18. doi: 10.1159/000091434. PubMed PMID: 16484805.
7. Rist PM, Chalmers J, Arima H, Anderson C, Macmahon S, Woodward M, Kurth T, Tzourio C. Baseline cognitive function, recurrent stroke, and risk of dementia in patients with stroke. *Stroke*. 2013;44(7):1790-5. Epub 2013/05/21. doi: 10.1161/STROKEAHA.111.680728. PubMed PMID: 23686974; PMCID: PMC3695012.
 8. Douiri A, Rudd AG, Wolfe CD. Prevalence of poststroke cognitive impairment: South London Stroke Register 1995-2010. *Stroke*. 2013;44(1):138-45. Epub 2012/11/15. doi: 10.1161/STROKEAHA.112.670844. PubMed PMID: 23150656.
 9. Rasquin SM, Verhey FR, van Oostenbrugge RJ, Lousberg R, Lodder J. Demographic and CT scan features related to cognitive impairment in the first year after stroke. *J Neurol Neurosurg Psychiatry*. 2004;75(11):1562-7. Epub 2004/10/19. doi: 10.1136/jnnp.2003.024190. PubMed PMID: 15489388; PMCID: PMC1738816.
 10. Ihle-Hansen H, Thommessen B, Wyller TB, Engedal K, Oksengard AR, Stenset V, Loken K, Aaberg M, Fure B. Incidence and subtypes of MCI and dementia 1 year after first-ever stroke in patients without pre-existing cognitive impairment. *Dement Geriatr Cogn Disord*. 2011;32(6):401-7. Epub 2012/02/09. doi: 10.1159/000335361. PubMed PMID: 22311341.
 11. Jacquin A, Binquet C, Rouaud O, Graule-Petot A, Daubail B, Osseby GV, Bonithon-Kopp C, Giroud M, Bejot Y. Post-stroke cognitive impairment: high prevalence and determining factors in a cohort of mild stroke. *J Alzheimers Dis*. 2014;40(4):1029-38. Epub 2014/03/01. doi: 10.3233/JAD-131580. PubMed PMID: 24577459.
 12. Erten-Lyons D, Woltjer R, Kaye J, Mattek N, Dodge HH, Green S, Tran H, Howieson DB, Wild K, Silbert LC. Neuropathologic basis of white matter hyperintensity accumulation with advanced age. *Neurology*. 2013;81(11):977-83. Epub 2013/08/13. doi: 10.1212/WNL.0b013e3182a43e45. PubMed PMID: 23935177; PMCID: 3888199.

13. Gouw AA, van der Flier WM, Fazekas F, van Straaten EC, Pantoni L, Poggesi A, Inzitari D, Erkinjuntti T, Wahlund LO, Waldemar G, Schmidt R, Scheltens P, Barkhof F. Progression of white matter hyperintensities and incidence of new lacunes over a 3-year period: the Leukoaraiosis and Disability study. *Stroke*. 2008;39(5):1414-20. Epub 2008/03/08. doi: 10.1161/STROKEAHA.107.498535. PubMed PMID: 18323505.
14. Benavente OR, Hart RG, McClure LA, Szychowski JM, Coffey CS, Pearce LA. Effects of clopidogrel added to aspirin in patients with recent lacunar stroke. *N Engl J Med*. 2012;367(9):817-25. Epub 2012/08/31. doi: 10.1056/NEJMoa1204133. PubMed PMID: 22931315.
15. Attems J, Jellinger KA. The overlap between vascular disease and Alzheimer's disease--lessons from pathology. *BMC Med*. 2014;12:206. Epub 2014/11/12. doi: 10.1186/s12916-014-0206-2. PubMed PMID: 25385447; PMCID: PMC4226890.
16. Ringman JM, Monsell S, Ng DW, Zhou Y, Nguyen A, Coppola G, Van Berlo V, Mendez MF, Tung S, Weintraub S, Mesulam MM, Bigio EH, Gitelman DR, Fisher-Hubbard AO, Albin RL, Vinters HV. Neuropathology of Autosomal Dominant Alzheimer Disease in the National Alzheimer Coordinating Center Database. *J Neuropathol Exp Neurol*. 2016;75(3):284-90. Epub 2016/02/19. doi: 10.1093/jnen/nlv028. PubMed PMID: 26888304; PMCID: PMC4934612.
17. McAleese KE, Firbank M, Dey M, Colloby SJ, Walker L, Johnson M, Beverley JR, Taylor JP, Thomas AJ, O'Brien JT, Attems J. Cortical tau load is associated with white matter hyperintensities. *Acta Neuropathol Commun*. 2015;3:60. Epub 2015/10/01. doi: 10.1186/s40478-015-0240-0. PubMed PMID: 26419828; PMCID: PMC4589169.
18. Kim HJ, Park S, Cho H, Jang YK, San Lee J, Jang H, Kim Y, Kim KW, Ryu YH, Choi JY, Moon SH, Weiner MW, Jagust WJ, Rabinovici GD, DeCarli C, Lyoo CH, Na DL, Seo SW. Assessment of Extent and Role of Tau in Subcortical Vascular Cognitive Impairment Using 18F-AV1451 Positron Emission Tomography Imaging. *JAMA Neurol*. 2018. Epub 2018/05/26. doi: 10.1001/jamaneurol.2018.0975. PubMed PMID: 29799981.

19. Matenia D, Mandelkow EM. The tau of MARK: a polarized view of the cytoskeleton. *Trends Biochem Sci.* 2009;34(7):332-42. Epub 2009/06/30. doi: 10.1016/j.tibs.2009.03.008. PubMed PMID: 19559622.
20. Lund H, Gustafsson E, Svensson A, Nilsson M, Berg M, Sunnemark D, von Euler G. MARK4 and MARK3 associate with early tau phosphorylation in Alzheimer's disease granulovacuolar degeneration bodies. *Acta Neuropathol Commun.* 2014;2:22. Epub 2014/02/19. doi: 10.1186/2051-5960-2-22. PubMed PMID: 24533944; PMCID: PMC4046661.
21. Seshadri S, Fitzpatrick AL, Ikram MA, DeStefano AL, Gudnason V, Boada M, Bis JC, Smith AV, Carassquillo MM, Lambert JC, Harold D, Schrijvers EM, Ramirez-Lorca R, Debette S, Longstreth WT, Jr., Janssens AC, Pankratz VS, Dartigues JF, Hollingworth P, Aspelund T, Hernandez I, Beiser A, Kuller LH, Koudstaal PJ, Dickson DW, Tzourio C, Abraham R, Antunez C, Du Y, Rotter JI, Aulchenko YS, Harris TB, Petersen RC, Berr C, Owen MJ, Lopez-Arrieta J, Varadarajan BN, Becker JT, Rivadeneira F, Nalls MA, Graff-Radford NR, Champion D, Auerbach S, Rice K, Hofman A, Jonsson PV, Schmidt H, Lathrop M, Mosley TH, Au R, Psaty BM, Uitterlinden AG, Farrer LA, Lumley T, Ruiz A, Williams J, Amouyel P, Younkin SG, Wolf PA, Launer LJ, Lopez OL, van Duijn CM, Breteler MM, Consortium C, Consortium G, Consortium E. Genome-wide analysis of genetic loci associated with Alzheimer disease. *JAMA.* 2010;303(18):1832-40. Epub 2010/05/13. doi: 10.1001/jama.2010.574. PubMed PMID: 20460622; PMCID: PMC2989531.
22. Gu GJ, Lund H, Wu D, Blokzijl A, Classon C, von Euler G, Landegren U, Sunnemark D, Kamali-Moghaddam M. Role of individual MARK isoforms in phosphorylation of tau at Ser(2)(6)(2) in Alzheimer's disease. *Neuromolecular Med.* 2013;15(3):458-69. Epub 2013/05/15. doi: 10.1007/s12017-013-8232-3. PubMed PMID: 23666762.
23. Augustinack JC, Schneider A, Mandelkow EM, Hyman BT. Specific tau phosphorylation sites correlate with severity of neuronal cytopathology in Alzheimer's disease. *Acta Neuropathol.* 2002;103(1):26-35. Epub 2002/02/12. PubMed PMID: 11837744.

24. Schneider A, Laage R, von Ahsen O, Fischer A, Rossner M, Scheek S, Grunewald S, Kuner R, Weber D, Kruger C, Klaussner B, Gotz B, Hiemisch H, Newrzella D, Martin-Villalba A, Bach A, Schwaninger M. Identification of regulated genes during permanent focal cerebral ischaemia: characterization of the protein kinase 9b5/MARKL1/MARK4. *J Neurochem.* 2004;88(5):1114-26. Epub 2004/03/11. PubMed PMID: 15009667.
25. Schneider A, Biernat J, von Bergen M, Mandelkow E, Mandelkow EM. Phosphorylation that detaches tau protein from microtubules (Ser262, Ser214) also protects it against aggregation into Alzheimer paired helical filaments. *Biochemistry.* 1999;38(12):3549-58. Epub 1999/03/26. doi: 10.1021/bi981874p. PubMed PMID: 10090741.
26. Despres C, Byrne C, Qi H, Cantrelle FX, Huvent I, Chambraud B, Baulieu EE, Jacquot Y, Landrieu I, Lippens G, Smet-Nocca C. Identification of the Tau phosphorylation pattern that drives its aggregation. *Proc Natl Acad Sci U S A.* 2017;114(34):9080-5. Epub 2017/08/09. doi: 10.1073/pnas.1708448114. PubMed PMID: 28784767; PMCID: PMC5576827.
27. Biernat J, Gustke N, Drewes G, Mandelkow EM, Mandelkow E. Phosphorylation of Ser262 strongly reduces binding of tau to microtubules: distinction between PHF-like immunoreactivity and microtubule binding. *Neuron.* 1993;11(1):153-63. Epub 1993/07/01. PubMed PMID: 8393323.
28. Ando K, Maruko-Otake A, Ohtake Y, Hayashishita M, Sekiya M, Iijima KM. Stabilization of Microtubule-Unbound Tau via Tau Phosphorylation at Ser262/356 by Par-1/MARK Contributes to Augmentation of AD-Related Phosphorylation and Abeta42-Induced Tau Toxicity. *PLoS Genet.* 2016;12(3):e1005917. Epub 2016/03/31. doi: 10.1371/journal.pgen.1005917. PubMed PMID: 27023670; PMCID: PMC4811436.
29. Hayden EY, Putman J, Nunez S, Shin WS, Oberoi M, Charreton M, Dutta S, Li Z, Komuro Y, Joy MT, Bitan G, MacKenzie-Graham A, Jiang L, Hinman JD. Ischemic axonal injury up-regulates MARK4 in cortical neurons and primes tau phosphorylation and aggregation. *Acta Neuropathol Commun.* 2019 Aug 20;7(1):135. doi: 10.1186/s40478-019-0783-6. PMID: 31429800; PMCID: PMC6700776.

30. Aneja B, Khan NS, Khan P, Queen A, Hussain A, Rehman MT, Alajmi MF, El-Seedi HR, Ali S, Hassan MI, Abid M. Design and development of Isatin-triazole hydrazones as potential inhibitors of microtubule affinity-regulating kinase 4 for the therapeutic management of cell proliferation and metastasis. *Eur J Med Chem.* 2019 Feb 1;163:840-852. doi: 10.1016/j.ejmech.2018.12.026. Epub 2018 Dec 13. PMID: 30579124.
31. Stroganov OV, Novikov FN, Stroylov VS, Kulkov V, Chilov GG. Lead finder: an approach to improve accuracy of protein-ligand docking, binding energy estimation, and virtual screening. *J Chem Inf Model.* 2008 Dec;48(12):2371-85. doi: 10.1021/ci800166p. PMID: 19007114.
32. Le Guilloux V, Schmidtke P, Tuffery P. Fpocket: an open source platform for ligand pocket detection. *BMC Bioinformatics.* 2009 Jun 2;10:168. doi: 10.1186/1471-2105-10-168. PMID: 19486540; PMCID: PMC2700099.
33. Schmidtke P, Bidon-Chanal A, Luque FJ, Barril X. MDpocket: open-source cavity detection and characterization on molecular dynamics trajectories. *Bioinformatics.* 2011 Dec 1;27(23):3276-85. doi: 10.1093/bioinformatics/btr550. Epub 2011 Oct 3. PMID: 21967761.
34. Sack JS, Gao M, Kiefer SE, Myers JE Jr, Newitt JA, Wu S, Yan C. Crystal structure of microtubule affinity-regulating kinase 4 catalytic domain in complex with a pyrazolopyrimidine inhibitor. *Acta Crystallogr F Struct Biol Commun.* 2016 Feb;72(Pt 2):129-34. doi: 10.1107/S2053230X15024747. Epub 2016 Jan 22. PMID: 26841763; PMCID: PMC4741193.
35. Sun D, Gao W, Hu H, Zhou S. Why 90% of clinical drug development fails and how to improve it? *Acta Pharm Sin B.* 2022 Jul;12(7):3049-3062. doi: 10.1016/j.apsb.2022.02.002. Epub 2022 Feb 11. PMID: 35865092; PMCID: PMC9293739.
36. Lipinski CA. Drug-like properties and the causes of poor solubility and poor permeability. *J Pharmacol Toxicol Methods.* 2000;44:235-49. PMID:11274893.
37. Lin JH and Lu AY. Role of pharmacokinetics and metabolism in drug discovery and development. *Pharmacol Rev.* 1997;49:403-49. PMID:9443165.

38. Wang J and Skolnik S. Recent advances in physicochemical and ADMET profiling in drug discovery. *Chem Biodivers.* 2009;6:1887-99. PMID:19937823.
39. Ha Ma Z, Cao X, Guo X, Wang M, Ren X, Dong R, Shao R, Zhu Y. Establishment and Validation of an In Vitro Screening Method for Traditional Chinese Medicine-Induced Nephrotoxicity. *Evid Based Complement Alternat Med.* 2018 Jun 28;2018:2461915. doi: 10.1155/2018/2461915. PMID: 30050583; PMCID: PMC6046169.
40. Ramirez T, Strigun A, Verlohner A, Huener HA, Peter E, Herold M, Bordag N, Mellert W, Walk T, Spitzer M, Jiang X, Sperber S, Hofmann T, Hartung T, Kamp H, van Ravenzwaay B. Prediction of liver toxicity and mode of action using metabolomics in vitro in HepG2 cells. *Arch Toxicol.* 2018 Feb;92(2):893-906. doi: 10.1007/s00204-017-2079-6. Epub 2017 Sep 30. PMID: 28965233; PMCID: PMC5818600.
41. Ghosh S, Wu MD, Shaftel SS, Kyrkanides S, LaFerla FM, Olschowka JA, O'Banion MK. Sustained interleukin-1 β overexpression exacerbates tau pathology despite reduced amyloid burden in an Alzheimer's mouse model. *J Neurosci.* 2013 Mar 13;33(11):5053-64. doi: 10.1523/JNEUROSCI.4361-12.2013. PMID: 23486975; PMCID: PMC3637949.
42. Kitazawa M, Cheng D, Tsukamoto MR, Koike MA, Wes PD, Vasilevko V, Cribbs DH, LaFerla FM. Blocking IL-1 signaling rescues cognition, attenuates tau pathology, and restores neuronal β -catenin pathway function in an Alzheimer's disease model. *J Immunol.* 2011 Dec 15;187(12):6539-49. doi: 10.4049/jimmunol.1100620. Epub 2011 Nov 16. PMID: 22095718; PMCID: PMC4072218.
43. Hinman JD, Rasband MN, Carmichael ST. Remodeling of the axon initial segment after focal cortical and white matter stroke. *Stroke.* 2013 Jan;44(1):182-9. doi: 10.1161/STROKEAHA.112.668749. Epub 2012 Dec 11. PMID: 23233385; PMCID: PMC3973016.
44. Nunez S, Doroudchi MM, Gleichman AJ, Ng KL, Llorente IL, Sozmen EG, Carmichael ST, Hinman JD. A Versatile Murine Model of Subcortical White Matter Stroke for the Study of Axonal

Degeneration and White Matter Neurobiology. J Vis Exp. 2016 Mar 17;(109):53404. doi:
10.3791/53404. PMID: 27023377; PMCID: PMC4829029.

CHAPTER 5

Hit-to-Lead Optimization and Molecular Target Identification of Small Molecule MYL2

Enhancers for Limb Girdle Muscular Dystrophy R1

Whitaker Cohn^{1,3}, Irina Kramerova², Alex Duong¹, Nicole Katzaroff¹, Parvez Alam¹, Jesus Campagna¹, Barbara Jagodinska¹, Julian Whitelegge³, Melissa J. Spencer², Varghese John¹

¹The Drug Discovery Lab, Mary S. Easton Center for Alzheimer's Disease Research, Department of Neurology, David Geffen School of Medicine, 710 Westwood Plaza, University of California Los Angeles, Los Angeles, CA 90095, USA

²Spencer Lab, Department of Neurology, David Geffen School of Medicine, 635 Charles Young Dr. S, University of California Los Angeles, Los Angeles, CA 90095, USA

³Pasarow Mass Spectrometry Laboratory, Jane and Terry Semel Institute for Neuroscience and Human Behavior, David Geffen School of Medicine, 760 Westwood Plaza, University of California Los Angeles, Los Angeles, CA 90095, USA

ABSTRACT

Limb-girdle muscular dystrophy type R1 (LGMDR1) is caused by autosomal recessive mutations in the gene encoding calpain 3 (CAPN3). As was shown in mouse model of LDMGR1 (C3KO mouse), CAPN3 is an essential component of the triad protein complex, which regulates calcium release in response to exercise and activates signaling pathways vital for muscle remodeling. As a result, C3KO mice have muscles that show diminished calcium/calmodulin-dependent protein kinase 2 (CAMKII) signaling during exercise. This leads to attenuated gene expression profiles characterized by a decreased expression of slow phenotype genes required for muscle growth and adaptation. Recently, a high-throughput screen identified a small molecule named AMBMP (2-Amino-4-[3,4-(methylenedioxy)benzylamino]-6-(3-methoxyphenyl)pyrimidine). This molecule was reported to activate CaMKII signaling and improve skeletal muscle health in an LGMDR1 mouse model. However, the therapeutic potential of AMBMP is hindered by its limited potency, bioavailability, and significant toxicity. In this study, we present an exploratory medicinal chemistry effort to develop more efficacious analogs of AMBMP. This is achieved using structure-activity relationship (SAR) analyses, *in-vitro* ADME characterization, and target engagement studies involving small molecule therapeutic-based affinity chromatography. Additionally, mass spectrometry-based global and phosphoproteomics studies were conducted to identify indirect drug targets. Through these efforts, we discovered analogs with increased activity, solubility, and metabolic stability compared to the original AMBMP molecule. Furthermore, we identified both direct and indirect molecular targets of AMBMP that play integral roles in enhancing CaMKII-mediated signaling, and myosin light chain 2 expression.

Key Words: AMBMP, Limb Girdle Muscular Dystrophy, Proteomics, Mechanism of Action

INTRODUCTION

Limb-girdle muscular dystrophies (LGMDs) constitute a group of genetically inherited neuromuscular disorders characterized by the progressive wasting of proximal muscles in the legs and arms (Ref. 1). Limb-girdle muscular dystrophy type R1 (LGMDR1) is one of the most prevalent forms of the LGMD and is caused by autosomal recessive mutations in the gene encoding calpain 3 (CAPN3), a calcium-dependent cysteine protease (Ref. 2-3). Individuals affected by LGMDR1 typically begin to show symptoms of muscle weakness in their second decade of life, and most will require the use of a wheelchair within 10-20 years after the first clinical signs of disease (Ref. 4). The muscle tissue of these patients is characterized by disrupted myofibrillar architecture, small fiber diameter, and abnormal mitochondrial structure/function (Ref. 5-8). Unfortunately, aside from physical therapy to help slow muscle wasting, there are currently no available treatment options that halt disease progression.

Muscle pathology in the muscles of CAPN3 knockout (C3KO) mice has many similarities with human LGMDR1 biopsies, and it is associated with reduced slow-oxidative (SO) fibers, mitochondrial abnormalities, and irregular lipid metabolism (Ref. 9-12). These deficits are likely related to the function of CAPN3 in maintaining the integrity of the triad protein complex. This complex regulates calcium release in response to exercise and activates signaling pathways vital for muscle remodeling (Ref. 13-15). The loss of CAPN3 in C3KO mice and LGMDR1 patient biopsies is associated with reduced triad components, namely ryanodine receptor 1 (RYR1) and calcium calmodulin kinase II β (CaMKII β). This reduction results in diminished CaMKII-mediated signaling (Ref. 11, 13). Consequently, in response to exercise, C3KO muscles exhibit attenuated

gene expression profiles characterized by a decreased expression of slow phenotype genes (Ref. 11-12). These findings underscore the specific impairment of CaMKII-mediated signaling in LGMDR1, which hinders downstream gene expression essential for muscle growth and adaptation.

Recently, a high-throughput screening effort was employed to identify small molecules capable of compensating for reduced CaMKII β signaling, aiming to counteract the impaired adaptive expression of slow oxidative SO genes observed in LGMDR1 (Ref. 16). This endeavor involved screening for compounds that increase the expression of one of the downstream transcriptional target of CaMKII β signaling, gene encoding a slow isoform of myosin light chain 2 (MYL2). This study identified several MYL2 enhancing compounds, including N4-(1,3-benzodioxol-5-ylmethyl)-6-(3-methoxyphenyl)-2,4-pyrimidinediamine hydrochloride (AMBMP). Encouragingly, AMBMP also demonstrated the ability to activate CaMKII β *in vivo*, stimulate the expression of slow genes, enhance oxidative metabolic capacity, and improve muscle function when administered to C3KO mice (Ref. 16). While it appears to be a highly promising candidate for treating LGMDR1, the therapeutic potential of AMBMP is impeded by its limited potency and bioavailability, along with significant toxicity. Furthermore, the precise molecular mechanism through which AMBMP activates CaMKII β signaling and increases MYL2 expression remains unknown.

This manuscript presents a comprehensive research program aimed at developing more biologically active and bioavailable analogs of AMBMP, as well as uncovering the mechanism of action (MOA) through which it increases MYL2 gene expression. An iterative medicinal chemistry approach involving structure-activity relationship (SAR) analyses was employed to design and

synthesize fourteen novel AMBMP analogs. Various *in-vitro* absorption, distribution, metabolism, and excretion (ADME) assays were then utilized to assess the drug-like properties of candidate MYL2-enhancing compounds as well as to identify lead candidate, AMBMP-13, which demonstrates both increased activity and bioavailability when compared to AMBMP. Furthermore, established methodologies such as small molecule therapeutic-based affinity chromatography and mass spectrometry-based global and phosphoproteomics were employed to identify both direct and indirect molecular targets of these MYL2 enhancing compounds. While the exact mechanism awaits validation, the findings suggest that AMBMP increases MYL2 expression through an S100A6-mediated mechanism that enhances CAMKII signaling and stabilizes the transcriptional coactivator PGC-1 α . Further exploration and validation of this mechanism promises to enhance our understanding of these compounds as modulators of CaMKII β signaling and slow oxidative (SO) gene expression, potentially unveiling novel therapeutic strategies for LGMD treatment.

METHODS

Synthesis of AMBMP Intermediate via C-N Cross Coupling

To a 50 mL round bottom flask equipped with a stir bar, 4,6-dichloropyrimidin-2-amine (500 mg, 3.05 mmol, 1 eq), benzo[d][1,3]dioxol-5-ylmethanamine (506 mg, 3.05 mmol, 1 eq), and N,N-Diisopropylethylamine (DIPEA) (591 mg, 4.56 mmol, 1.5 eq) in 10 mL of ethanol were added under N₂. The reaction mixture was stirred at 70 °C for 12 h. The mixture was concentrated under reduced pressure, washed with NaHCO₃ and extracted with ethyl acetate (4 x 30 mL). The organic layer was collected, dried with Na₂SO₄ and then purified by flash chromatography using a gradient

method with hexane and ethyl acetate. Fractions corresponding to the product peak were combined and concentrated to yield the final product.

Synthesis of AMBMP Analogs via Suzuki-Miyaura Coupling Reaction

N4-(benzo[d][1,3]dioxol-5-ylmethyl)-6-chloropyrimidine-2,4-diamine (1.0 eq), boronic acid-containing starting material (2.0 eq), sodium carbonate (4.0 eq) and tetrakis(triphenylphosphine)-palladium(0) (0.5 eq) were added to a 125 mL glass pressure and suspended in 25 mL of toluene-ethanol (2:1). The reaction mixture was stirred for 72 h at 110°C under nitrogen. Upon cooling, the crude product was filtered through celite and the filtrate was collected and concentrated under reduced pressure. The concentrate was then washed with NaHCO₃ and extracted with ethyl acetate (4 x 30 mL). The organic layer was collected, dried with Na₂SO₄ and then purified by flash chromatography using a gradient method with DCM and methanol. Fractions containing the product were combined and concentrated under reduced pressure to yield the final product.

Additional steps for synthesis of AMBMP14: To a round bottom flask equipped with a stir bar, N4-(benzo[d][1,3]dioxol-5-ylmethyl-6-3-((trimethylsilyl)ethynyl)phenyl)pyrimidine-2,4-diamine (AMBMP 14 Intermediate) and potassium carbonate were added under N₂. 2 mL of Degassed methanol was added to the flask and then the reaction was stirred for 2 h at room temperature. The reaction was monitored by TLC using 50:50 Ethyl Acetate: Hexane as the developing solvent. Once the reaction was complete, the reaction mixture was concentrated under reduced pressure and then further dried using the lyophilization to yield the final product.

Purity Analysis via Liquid Chromatography-Mass Spectrometry

Analysis of purity by liquid chromatography-mass spectrometry (LC-MS) was done at the UCLA Pasarow Mass Spectrometry Lab (PMSL; Julian Whitelegge, Ph.D., Director). DDL-672 was diluted to 10 mM in DMSO, then diluted 100-fold in in 50/50/0.1 Water/Acetonitrile/Formic Acid (100 μ M final concentration). An aliquot (10 μ L) was analyzed using a LTQ Orbitrap XL mass spectrometer (Thermo Fisher Scientific) coupled to an UltiMate 3000 HPLC (Thermo Fisher Scientific) with a Phenomenex analytical column (Kinetex 1.7 μ m C18 100 Å 100 x 2.1 mm). The mass spectrometer acquisition method scanned a mass range from 100 – 2000 m/z . The HPLC method utilized a mixture of solvent A (99.9/1 Water/Formic Acid) and solvent B (99.9/1 Acetonitrile/Formic Acid) and a gradient was use for the elution of the compounds (min/%B: 0/0, 3/0, 19/99, 20/99, 21/0, 30/0). An ion extracted chromatogram (IEC) using the m/z corresponding to the $[M+H]^+$ ion was utilized to identify the chromatographic peak for each compound. Purity was calculated by dividing the chromatographic peak area for each compound by the sum of all the non-background peak areas in the total ion chromatogram (TIC).

Purity Analysis via Magnetic Resonance Spectroscopy

Analysis of purity by magnetic resonance spectroscopy was done at the UCLA Molecular Instrumentation Center (MIC; Ignacio Martini, Ph.D., Director). Compounds were diluted in 600 μ L of $CDCl_3$ and analyzed using an AV400 NMR spectrometer (Bruker) containing a 5 mm broadband Z-gradient probe with Automatic Tune and Match (ATM). The analysis method consisted of a 64-scan proton NMR (1H -NMR) utilizing default parameters. Predicted 1H -NMR spectra were obtained using the ChemNMR 1H estimation function in ChemDraw (PerkinElmer). The experimental data were visualized and interpreted using Mnova (Mestrelab Research).

Compound Treatment of C2C12 Cells

C2C12 myoblasts were cultured in complete DMEM (Dulbecco's modified Eagle's medium, 10% fetal bovine serum (FBS), 2 mM L-glutamine, 100 units/mL penicillin G, 100 µg/mL streptomycin) until 90% confluent. Following one wash with phosphate buffered saline (PBS, pH 7.4), differentiation media (Dulbecco's modified Eagle's medium, 2% horse serum (Gibco), 2 mM L-glutamine, 100 units/mL penicillin G, 100 µg/mL streptomycin) was added containing compounds at different concentrations or 0.05% DMSO. For analysis of MYL2 mRNA levels: Forty-eight hours later, cells were harvested for RNA extraction and qPCR analysis. For analysis of protein and protein phosphorylation: After 3 min, 15 min, 60 min or 24 hours, the cells were washed once with ice-cold PBS with Halt™ Protease and Phosphatase Inhibitor Cocktail (Thermo Scientific, Waltham, MA)) and then collected via scraping with ice-cold lysis buffer (1 mL, 12 mM sodium lauroyl sarcosine, 0.5% sodium deoxycholate, 50 mM triethylammonium bicarbonate (TEAB)), Halt™ Protease and Phosphatase Inhibitor Cocktail (Thermo Scientific, Waltham, MA)).

Real-Time PCR

Total RNAs were isolated from cells or tissues using Trizol. cDNA was generated using iScript Reverse Transcriptase Supermix (Cat#1708841, Bio-Rad) and was used for real-time PCR with iTaq Universal SYBR Green Supermix (Cat#1725124, BioRad) according to the manufacturer's instructions. All real-time PCR reactions were run in CFX Connect Real-Time PCR System (Bio-Rad). The primers used in these experiments are shown below:

RT-PCR Myl2 forward 5'- AGTTCAAGGAAGCCTTCACAATC-3'

RT-PCR Myl2 reverse 5'- ATTGGACCTGGAGCCTCTTTGAT-3'

Cell Viability and Toxicity Analysis

Cell viability and toxicity were simultaneously assessed using the MultiTox-Fluor Multiplex Cytotoxicity Assay (Cat# PRG9200, Fisher Scientific) according to the manufacturer's protocol.

Liver Microsome Stability Assay

An aliquot (1 μ L) of test compound (1 mM, 100% DMSO) was added to an aqueous liver microsome solution (1000 μ L, PBS pH 7.4, 0.5mg/mL human liver microsomes (Cat#HMMPL, Thermo Fisher Scientific), 2 mM NADPH, 2 mM MgCl₂) and incubated at 37 °C for 120 min. Aliquots (50 μ L) of the microsome solution were taken at various time points (0, 5, 10, 15, 30, 60, 90, 120 min) and added to a reaction quenching solution (200 μ L 100% Acetonitrile) containing an internal standard. Solutions were clarified by centrifugation (16,000 x g, 5 min), and the supernatants were transferred to new tubes and lyophilized. Samples were reconstituted in 100 μ L of 50/50/0.1 (Water/Acetonitrile/Formic Acid) prior to analysis via liquid chromatography-tandem mass spectrometry (LC-MS/MS). Chromatographic peak areas normalized to the internal standard were plotted at each time point and the half-life ($t_{1/2}$) of compound in liver microsomes was determined by using the trendline equation to calculate the time at which compound abundance was 50% of that at time point 0 (t_0).

Plasma and Muscle Tissue Binding Assays

Muscle tissue was homogenized in PBS (pH 7.4) (1: 3 weight(mg)/volume(μ L)) and the protein concentration was determined using the Micro BCA™ Protein Assay Kit (Cat#23235, Thermo Fisher Scientific). Muscle homogenate was clarified and diluted to 20 mg/mL in PBS (pH 7.4).

Either muscle homogenate or plasma was added to Slide-A-Lyzer™ MINI Dialysis Devices, 10K MWCO dialysis cups (Cat#PI88401, Thermo Fisher Scientific) in a 48-well plate containing PBS (500 µL; pH 7.4). 1 µL of 1 mM compound was added to the muscle homogenate (Final Concentration: 2 µM compound, 0.5% DMSO) and incubated on a rocker for 4.5 hours at 37 °C. 50 µL of muscle homogenate or plasma (within the dialysis cup) and PBS (within the 48-well plate) were transferred to new microcentrifuge tubes containing 400 µL of quenching reagent (100% Acetonitrile) containing internal standard. Solutions were clarified by centrifugation (16,000 x g, 5 min), and the supernatants were transferred to new tubes and lyophilized. Samples were reconstituted in 100 µL of 50/50/0.1 (Water/Acetonitrile/Formic Acid) prior to analysis via LC-MS/MS. The % of the unbound drug ($f_{u, \text{bound}}$) was calculated using the following equation:

$$\% \text{ Bound} = [1 - (\text{PBS chromatographic peak area} / \text{muscle homogenate or plasma chromatographic peak area})] \times 100$$

In-Vivo Pharmacokinetics

Following oral administration of compound, mouse muscle tissue and plasma were collected after euthanasia and perfusion at 1, 2, 4 and 6 hours. muscle tissue was homogenized in a bead beater using 5 volumes of ice-cold 80% acetonitrile (1/5; mg of brain/µL of 80% ACN). Plasma analytes were extracted using 4 volumes of ice-cold acetonitrile (1/4; µL of plasma/µL of ACN). Solutions were clarified by centrifugation (16,000 x g, 5 min) and the supernatants were transferred to new tubes and lyophilized. Samples were reconstituted in 100 µL of 50/50/0.1 (Water/Acetonitrile/Formic Acid) prior to analysis via LC-MS/MS. An internal standard (IS) was added to every sample to account for compound loss during sample processing. Standards were made in drug naïve plasma or muscle lysates with increasing amounts of analyte (S1,S2: 0 pmol/

S3,S4: 1 pmol/ S5,S6: 10 pmol/ S7,S8: 100 pmol, S9,S10: 1000 pmol). The standard curve was made by plotting the known amount of analyte per standard vs. the ratio of measured chromatographic peak areas corresponding to the analyte over that of the IS (analyte/IS). The trendline equation was then used to calculate the absolute concentrations of each compound in plasma and muscle tissue.

Kinetic Solubility

Test compound (10 mM, 100% DMSO) was diluted separately into aqueous buffer (100 μ M; PBS pH 7.4) and DMSO at various concentrations (500, 250, 125, 62.5, 31.3, 15.6, 7.8, 3.9, 2, 1 μ M). The solutions were then incubated at 37 °C for 90 min and centrifuged (16000xg, 5 min). An aliquot of each supernatant is analyzed by UV/Vis (if possible) or LC-MS/MS. A standard curve was made by plotting the known amount of analyte per standard in DMSO vs. absorbance or chromatographic peak area. Aqueous Kinetic solubility (mM) was calculated using the trendline equation with maximum absorbance or chromatographic peak area observed in the aqueous sample.

Small Molecule Analysis via Liquid Chromatography-Tandem Mass Spectrometry

A targeted LC-MS/MS assay was developed for each compound using the multiple reaction monitoring (MRM) acquisition method on a 6460 triple quadrupole mass spectrometer (Agilent Technologies) coupled to a 1290 Infinity HPLC system (Agilent Technologies) with a Phenomenex analytical column (Kinetex 1.7 μ m C18 100 Å 100 x 2.1 mm). The HPLC method utilized a mixture of solvent A (99.9/1 Water/Formic Acid) and solvent B (99.9/1 Acetonitrile/Formic Acid) and a gradient was used for the elution of the compounds (min/%B: 0/1,

3/1, 19/99, 20/1, 30/1). Two fragment ions originating from each compound were monitored at specific LC retention times to ensure specificity and accurate quantification in the complex biological samples. The normalized chromatographic peak areas were determined by taking the ratio of measured chromatographic peak areas corresponding to each compound over that of the internal standard (Analyte/IS).

Synthesis of AMBMP-14 Agarose Beads

Disulfide azide agarose (1 equiv., Cat# 1238-2, Click Chemistry Tools) was incubated with AMBMP-14 (2 equiv.) and bromotris(triphenylphosphine)copper(I) (0.2 equiv., Cat# 572144, Sigma Aldrich) in the presence of dimethylformamide (DMF, 2 mL) and triethylamine (TEA, 1 equiv.). The reaction mixture was stirred at 60 °C for 16 hours. Following centrifugation (1,000 x g, 2 min), the supernatant was discarded, and the agarose beads were washed with DMF 12 times and then with PBS 6 times. Each wash consisted of a 2-minute incubation, centrifugation (1,000 x g, 2 min), and removal of the supernatant. A small aliquot of beads (20 uL) was taken for validation of successful coupling via mass spectrometry following incubation with tris (2-carboxyethyl) phosphine (TCEP, 20 mM, 10 min). Control agarose beads were subject to the all the same reactions and wash conditions, except without the addition of AMBMP-14.

Small-Molecule Affinity Purification

Differentiated C2C12 myotubes (10 cm dish) were washed once with ice-cold PBS, then collected via scraping with ice-cold lysis buffer (1 mL, M-PER™ Mammalian Protein Extraction Reagent with Halt™ Protease and Phosphatase Inhibitor Cocktail (Thermo Fisher Scientific). The lysates were clarified via centrifugation (16,000 x g) and protein concentration was assessed using a Micro

BCA™ Protein Assay Kit (Thermo Fisher Scientific) according to the manufacturer's protocol. All samples were diluted in lysis buffer to an equal volume (1 mL) and concentration (1 mg/mL). Either AMBMP-14 agarose beads or control agarose beads (100 uL, n=4 per lysate) were added to each sample and incubated with very gentle mixing on an end-over-end rotator at 4 °C for two hours. Following centrifugation (1,000 x g, 2 min), the supernatant was discarded, and the agarose beads were washed with ice-cold lysis buffer 8 times. Each wash consisted of a 5-minute incubation at 4 °C, centrifugation (1,000 x g, 2 min), and removal of the supernatant. Bound proteins were then eluted off the agarose beads with tris (2-carboxyethyl) phosphine (200 uL, 10 mM in lysis buffer, 30 min) and the supernatant was collected and processed for proteomics analysis via mass spectrometry.

Proteomics Sample Processing

Samples were treated with tris (2-carboxyethyl) phosphine (10 mM) and chloroacetamide (40 mM) in 50 mM triethyl ammonium bicarbonate (TEAB) at 95° C for 30 min. They were then diluted 5-fold with aqueous 50 mM TEAB and incubated overnight with Sequencing Grade Modified Trypsin (1 ug in 10 uL of 50 mM TEAB; Promega, Madison, WI). Following this an equal volume of ethyl acetate/trifluoroacetic acid (TFA, 100/1, v/v) was added and after vigorous mixing (5 min) and centrifugation (13,000 x g, 5 min), the supernatants were discarded, and the lower phases were dried in a centrifugal vacuum concentrator. The samples were then desalted using a modified version of Rappsilber's protocol in which the dried samples were reconstituted in acetonitrile/water/TFA (solvent A, 100 uL, 2/98/0.1, v/v/v) and then loaded onto a small portion of a C18-silica disk (3M, Maplewood, MN) that was placed in a 200 uL pipette tip (Ref. 17). Prior to sample loading the C18 disk was prepared by sequential treatment with methanol (20 uL),

acetonitrile/water/TFA (solvent B, 20 uL, 80/20/0.1, v/v/v) and finally with solvent A (20 uL). After loading the sample, the disc was washed with solvent A (20 uL, eluent discarded) and eluted with solvent B (40 uL). The collected eluent was dried in a centrifugal vacuum concentrator and reconstituted in water/acetonitrile/FA (solvent E, 10 uL, 98/2/0.1, v/v/v). Additional Steps for Global and Phosphoproteomics of AMBMP13 treated C2C12 Cells: Tryptic peptides were isotopically labeled (TMT18plex Isobaric Label Reagent Set, Thermo Fisher Scientific) according to the manufacturer's protocol to provide relative quantitation between samples. Phosphorylated peptides were sequentially enriched using two complementary affinity resins (Thermo Scientific™ High-Select™ TiO₂ Phosphopeptide Enrichment kit and High-Select™ Fe-NTA Phosphopeptide Enrichment kit) according to manufacturer's protocols. The phosphopeptide-enriched eluate and flow-through were fractionated separately via high pH reversed-phase chromatography (Pierce™ High pH Reversed-Phase Peptide Fractionation Kit) according to the manufacturer's protocol for increased proteome coverage.

Peptide Analysis via Liquid Chromatography-Tandem Mass Spectrometry

Aliquots (5 uL) were injected onto a reverse phase nanobore HPLC column (AcuTech Scientific, C18, 1.8um particle size, 360 um x 20 cm, 150 um ID), equilibrated in solvent C and eluted (500 nL/min) with an increasing concentration of solvent D (acetonitrile/water/FA, 98/2/0.1, v/v/v: min/% F; 0/0, 5/3, 18/7, 74/12, 144/24, 153/27, 162/40, 164/80, 174/80, 176/0, 180/0) using an EASY-nLC II (Thermo Fisher Scientific). The effluent from the column was directed to a nanospray ionization source connected to a hybrid quadrupole-Orbitrap mass spectrometer (Q Exactive Plus, Thermo Fisher Scientific) acquiring mass spectra in a data-dependent mode alternating between a full scan (m/z 350-1700, automated gain control (AGC) target 3 x 10⁶, 50

ms maximum injection time, FWHM resolution 70,000 at m/z 200) and up to 15 MS/MS scans (quadrupole isolation of charge states 2-7, isolation window 0.7 m/z) with previously optimized fragmentation conditions (normalized collision energy of 32, dynamic exclusion of 30 s, AGC target 1 x 10⁵, 100 ms maximum injection time, FWHM resolution 35,000 at m/z 200).

Proteomics Data Analysis

Raw proteomic data were searched against a Uniprot database containing the complete human proteome using SEQUEST-HT (including dynamic modifications: oxidation (+15.995) on M, deamidation (+0.984) on N/Q, and carbamidomethyl on C (+57.021), phosphorylation on S/T/Y (+79.966)) in Proteome Discoverer (Version 2.4, Thermo Scientific), which provided the relative abundances of the identified peptides. Decoy database searching was used to generate high confidence tryptic peptides (FDR < 1%) (Ref. 18). Tryptic peptides containing amino acid sequences unique to individual proteins were used to identify and provide relative quantification between different proteins in each sample. Post-translationally modified peptides from each protein were normalized to protein abundance in each sample. Peptides exhibiting a p-value ≤ 0.05 with a log₂-fold change ≥ 0.5 were analyzed using a series of bioinformatics tools including functional protein association network analysis, comprehensive gene set enrichment gene ontology (GO) classification and pathway analysis, as well as kinase substrate enrichment analyses (Ref. 19-22)

RESULTS

Hit-to-Lead Optimization Identifies More Biologically Active and Bioavailable MYL2 Enhancers

The general approach utilized to synthesize novel analogs of AMBMP consisted of two consecutive reactions (**Fig. 1A**). Briefly, the AMBMP intermediate, N4-(benzo[d][1,3]dioxol-5-ylmethyl)-6-chloropyrimidine-2,4-diamine, was synthesized by performing a C-N cross-coupling reaction between 4,6-dichloropyrimidin-2-amine (1 equiv) and benzo[d][1,3]dioxol-5-ylmethanamine (1 equiv) in the presence of N,N-Diisopropylethylamine (DIPEA; 1.5 equiv) at 70 °C for 12 hours. Next, each analog was synthesized by performing a Suzuki-Miyaura coupling reaction between the AMBMP intermediate (1 equiv) and a boronic acid-containing substituent (2 equiv), in the presence of sodium carbonate (4.0 equiv) and tetrakis(triphenylphosphine)-palladium(0) (0.5 equiv) at 110°C for 72 hours. Optimization efforts led to the synthesis of fourteen new chemical entities (NCEs): AMBMP-1 – AMBMP-14 (**Fig. 1B**). Three of these analogs (AMBMP-6, -13, & -14) were determined to increase MYL2 mRNA expression more than the original HTS hit, AMBMP (**Fig. 1C**).

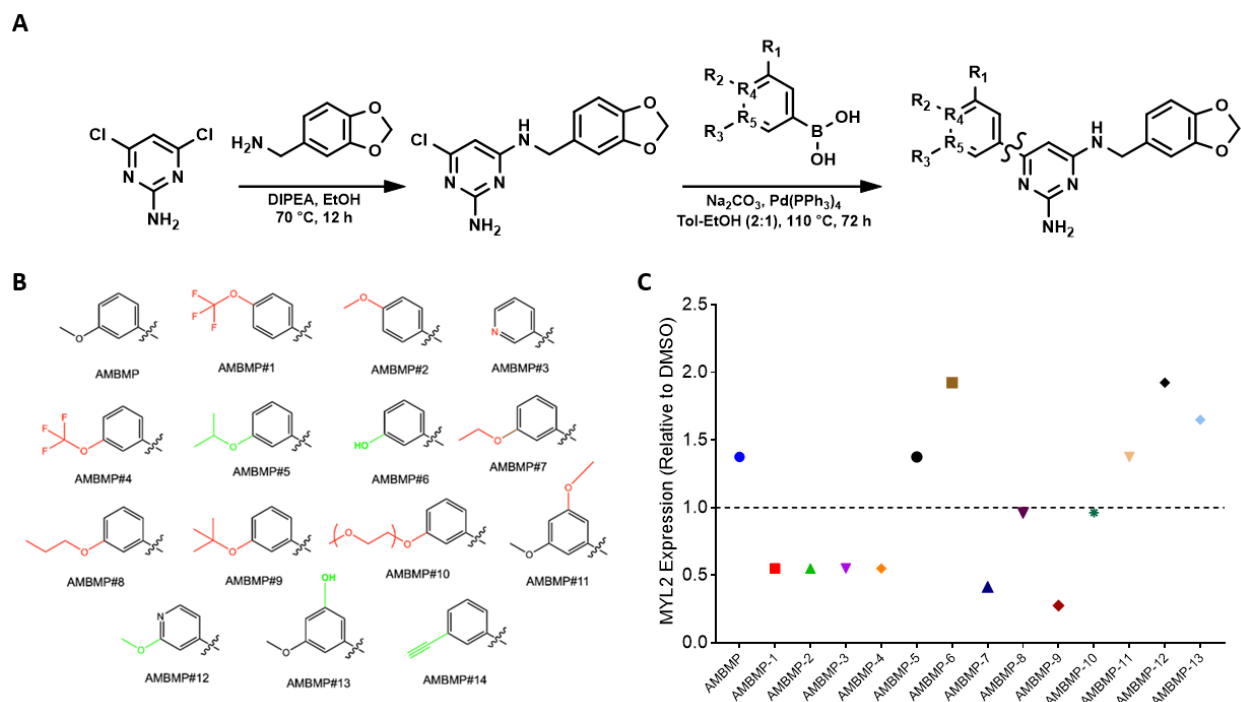
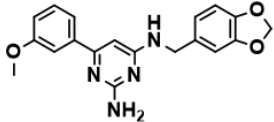
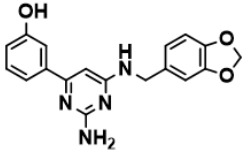
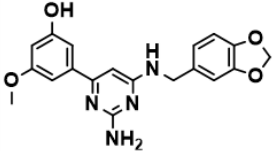


Figure 1. *Synthesis and testing of novel AMBMP analogs.* (a) General synthetic scheme used for the synthesis of novel analogs of AMBMP. (b) Chemical subgroups for AMBMP and the fourteen new chemical entities (NCEs): AMBMP-1 – AMBMP-14. Green indicates a modification that resulted in equal or increased MYL2 expression, relative to AMBMP. Red indicates a modification that resulted in decreased MYL2 expression, relative to AMBMP. (c) MYL2 expression in C2C12 cells following a 48-hour treatment with AMBMP or analogs 1 – 14.

To determine which compounds were likely to be successful therapeutics *in-vivo*, AMBMP and the two most active analogs were subjected to various *in-vitro* assays to determine the physicochemical properties that influence compound absorption, distribution, metabolism, excretion (ADME) (**Table 1**). This included the assessment of kinetic solubility, liver microsome stability, plasma and muscle tissue binding, and cell toxicity (**Table 1**). Desired *in-vitro* ADME property values are as follows: Kinetic Solubility > 50 μM ; Liver Microsomal Stability $t_{1/2}$ > 1 hour; Plasma Binding < 95%; Cell Toxicity (C_{tox}) > 20 μM ; Muscle Tissue Binding < 80%. While AMBMP exhibited favorable muscle tissue binding properties, it had relatively poor kinetic solubility (43 μM), high plasma binding (99.7%), significant cellular toxicity (19 μM), and a short half-life in liver microsomes (55 min). Interestingly, both NCEs, AMBMP-6 and -13, had significantly improved kinetic solubility (94 μM) and metabolic stability in liver microsomes (>120 min), relative to AMBMP. Additionally, AMBMP-13 was determined to be approximately 1.6-fold less toxic (30 μM). A structure-activity relationship analysis of the synthesized analogs revealed structural elements required for activity and/or enhanced MYL2 expression (**Fig. 2**). The most notable finding was that the addition of a hydroxyl moiety at either positions R¹ or R³ were able to significantly increase compound activity, solubility, and metabolic stability. Additionally,

it is important to note that bulky substitutions in these positions or at R² resulted decreased or no activity. Based on these results, AMBMP-13, was chosen as the lead candidate for further evaluation *in-vivo*.

Compound	Structure	Molecular Weight [Da]	Kinetic Solubility [μ M]	Liver Microsome Stability [$t_{1/2}$ (min)]	Plasma Binding [% bound]	Muscle Tissue Binding [% bound]	Cell Toxicity [Ctox (μ M)]
AMBMP		350.4	43	55	99.7	37.4	19
AMBMP-6		336.3	94	>120	99.1	29.4	14
AMBMP-13		366.38	94	>120	99.6	45.1	30

*Desired ADME property values: Kinetic Solubility > 50 μ M; Microsomal Stability $t_{1/2}$ > 1 hour; Plasma Binding < 95%; Muscle Tissue Binding < 80%; Cell Toxicity > 20 μ M

Table 1. *In-vitro* ADME properties of candidate MYL2 enhancers. Red font represents undesirable ADME property values.

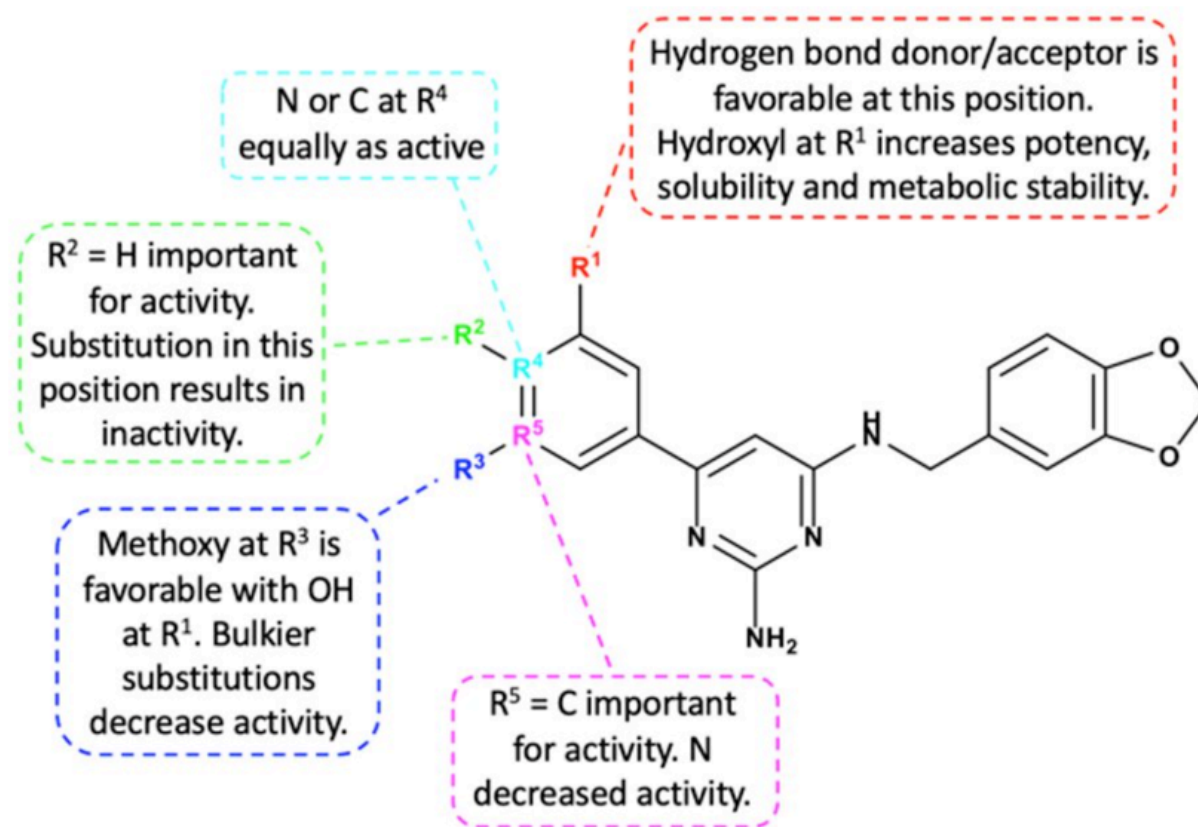


Figure 2. Key structure-activity relationship control elements for MYL2 activity, solubility, and metabolic stability.

Identification of Direct and Indirect Molecular Targets of AMBMP

Copper (I)-catalyzed click chemistry was employed to couple an alkyne-containing analog of AMBMP, AMBMP-14, to azide-containing agarose beads, creating a small molecule-based affinity probe for enriching direct molecular targets (**Fig. 3A**). Successful coupling was confirmed via liquid chromatography-mass spectrometry (LC-MS) after releasing the bound small molecule with a reducing agent (**Fig. 3B**). A subsequent affinity purification followed by mass spectrometry-based proteomics identified numerous proteins significantly enriched by the AMBMP-14 agarose, relative to control agarose beads, that were associated with disease and/or drug-relevant signaling

pathways (calcium/wnt signaling pathways) (**Fig. 3C**). Notably, one of the most abundant proteins from the affinity purification was S100 calcium binding protein (S100A6), a calcium-binding protein associated with various signaling pathways that regulate several important cellular functions, such as proliferation, apoptosis, and cytoskeleton dynamics (Ref. 23). Interestingly, S100A6 expression has been previously indicated to be increased in LGMDR1 patients (Ref. 24). This led to the hypothesis that S100A6 mediates drug-induced increases in MYL2 expression. Subsequent RNA interference-mediated protein knockdown of S100A6 expression in differentiating C2C12 cells was demonstrated to significantly increase MYL2 expression, relative to scramble siRNA treated controls (**Fig. 3D**).

Given that cell signaling via protein post-translational modifications (PTMs), such as phosphorylation, mediates the biological outcomes of many therapeutics, global and phosphoproteomics were utilized to identify indirect molecular targets of AMBMP that may serve as essential downstream effectors for enhancing MYL2 expression (Ref. 25). A phosphoproteomics analysis of differentiating C2C12 cells treated with the AMBMP-13 was conducted to identify kinases which showed significant changes in protein phosphorylation in response to drug treatment. Several time-points (3 min, 15 min, 60 min, 24 hours) were assessed relative to 0.05% DMSO treated controls (**Fig. 3E**). A substrate-specific kinase enrichment analysis utilizing this data identified several kinases that were significantly activated 15 minutes (CAMK2D, MAP2K1, PRKACA) and 60 minutes (CAMK2D, RPS6KA2, RPS6KA3, PRKACA) after AMBMP-13 treatment (**Fig. 3F**). A global proteomics analysis revealed significant changes in the abundance of numerous proteins 24 hours after AMBMP-13 treatment, relative to 0.05% DMSO treated controls (**Fig. 3G**). A transcription factor enrichment analysis was performed using

these data and identified several MYL2-associated and PGC1 α -activated transcription factors (**Fig. 3H**). Integrating the findings from the AMBMP-14 affinity purification and the AMBMP-13 global and phosphoproteomics analyses led to the predominant hypothesis that AMBMP increases MYL2 expression through an S100A6-mediated mechanism (**Fig. 3I**). Specifically, AMBMP may inhibit the interaction of S100A6 with the receptor for advanced glycation endproducts (RAGE), resulting in increased intracellular cyclic adenosine monophosphate (cAMP). Enhancing cAMP leads to activation of protein kinase A (PKA), CAMKII, and P38 α /mitogen-activated protein kinase 14 (MAPK14), leading to peroxisome proliferator-activated receptor gamma coactivator 1-alpha (PGC1 α)-mediated activation of MYL2-associated transcription factors, such as zinc finger protein 281 (ZNF281).

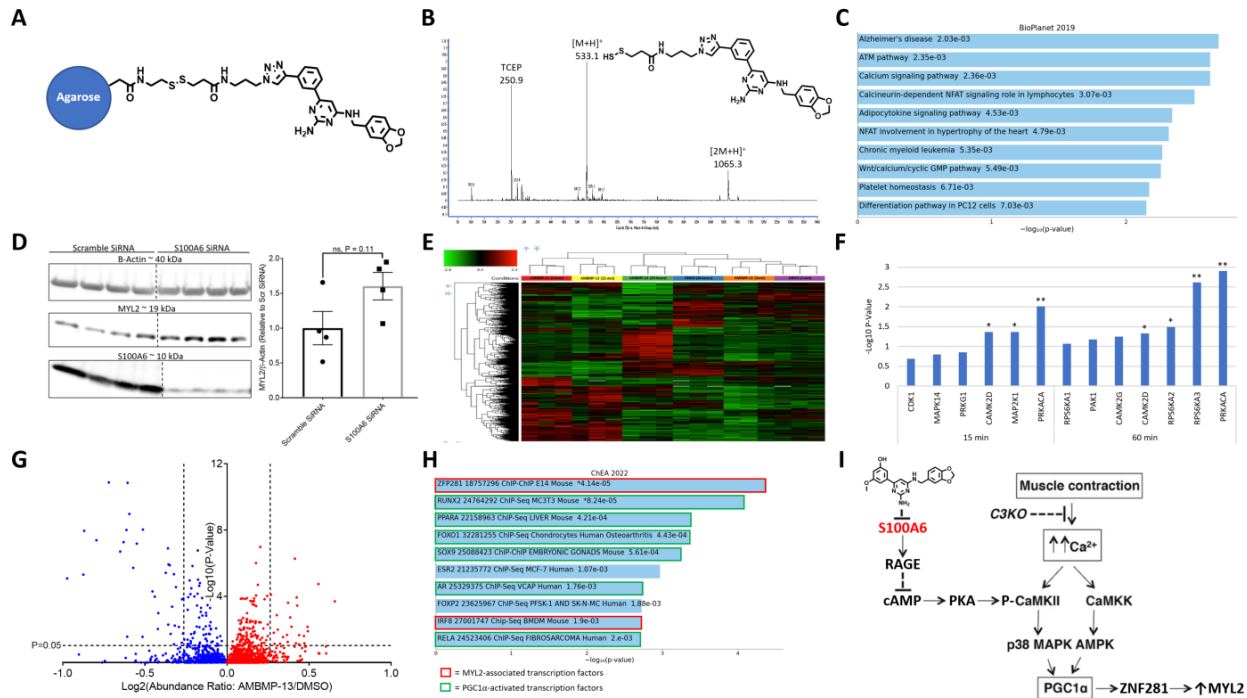


Figure 3. Identification of direct and indirect molecular targets of AMBMP. (a) A small molecule-based affinity probe for enriching direct molecular targets of AMBMP14. (B) A structure and mass

spectrum for the small molecule released from the affinity probe with a reducing agent. (C) Levels of significance (p-value) for cellular pathways in the National Center for Advancing Translational Sciences (NCATS) BioPlanet pathway database, using proteins identified in the AMBMP-14 affinity purification. (D) A western blot for β -Actin, MYL2, and S100A6, and densitometry quantified levels of MYL2/ β -Actin in C2C12 cells, following a 48-hour treatment with S100A6 siRNA or a scrambled siRNA control. (E) The relative abundance of phosphorylated peptides in C2C12 cells, following treatment with AMBMP-13 at a concentration of 2.5 μ M for 3, 15 or 60 minutes. (F) Levels of significance (p-value) for kinases in the Kinase Enrichment Analysis 2 (KEA2) database, activated 15 and 60 minutes after AMBMP-13 treatment. (G) Differences in the abundances of proteins, illustrated via volcano plot, in C2C12 cells 24-hours after AMBMP-13 treatment. The $-\log_{10}$ (p-value) is plotted against \log_{10} (abundance ratio: AMBMP-13/Vehicle). (H) Levels of significance (p-value) for transcription factors in the ChIP Enrichment Analysis (ChEA) 2022 database, activated 24 hours after AMBMP-13 treatment. (I) A hypothesized mechanism of action through which AMBMP and biological active analogs increase MYL2 expression.

Evaluation of S100A6 Levels and AMBMP-13 Efficacy In-Vivo

A gene expression analysis identified multiple S100 calcium binding proteins (S100A4, S100A6) to be significantly increased in the muscle LGMD2A patients, relative to healthy controls, supporting the idea that inhibiting S100A6 function may serve as a viable therapeutic strategy. (**Fig. 4A**). A proof-of-concept pharmacokinetic/pharmacodynamic (PK/PD) analyses was performed to see if the AMBMP-13 was orally bioavailable and increased MYL2 levels *in-vivo* in LGMDR1 mouse model. A pharmacokinetics analysis confirmed AMBMP-13 to be reasonably

bioavailable following oral administration via pipette feeding. AMBMP-13 reached a maximum muscle concentration of 348 nM, 1-hour post administration at a dose of 20 mg/kg (**Fig. 4B**). A short *in-vivo* study in LGMDR1 mouse model was performed at two doses of (10 and 20 mg/kg) utilizing intraperitoneal injection (IP) injection as the route of administration. Both doses induced significant increases MYL2 expression of approximately 2.7-fold (**Fig. 4C**).

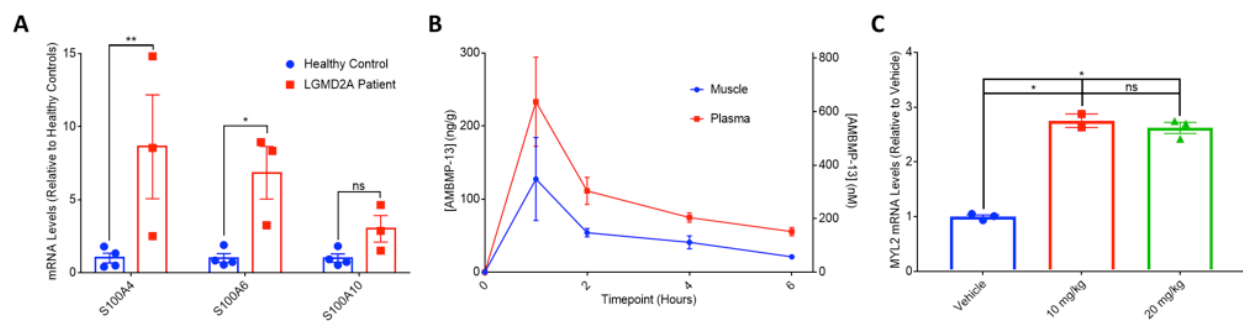


Figure 4. Evaluation of S100 protein levels in LGMD2A patients and AMBMP-13 efficacy *in-vivo* in LGMDR1 mouse model. (A) mRNA levels of S100 calcium binding proteins, S100A4, S100A6 and S100A10 in the muscle LGMD2A patients, relative to healthy controls. (B) AMBMP-13 plasma and muscle concentrations, 1, 2, 4 and 6 hours following oral administration at a dose of 20 mg/kg. (C) MYL2 mRNA levels in the muscles of CAPN3 knockout (C3KO) mice, following administration of vehicle or AMBMP-13 via intraperitoneal injection (IP) injection at a dose of 10 or 20 mg/kg, daily, for 5 days.

DISCUSSION

To the best of our knowledge, this study represents the first description of a medicinal chemistry effort to develop more biologically active and bioavailable analogs of AMBMP for the treatment of LGMDR1. This hit-to-lead optimization was performed by systematically altering chemical subgroups around the methoxyphenyl ring of the AMBMP molecule. The biological activity of

each analog was assessed and utilized to conduct a structure-activity-relationship analysis that guided further drug design. This approach enabled the identification of structural elements required for and contributing to biological activity, ultimately leading to the design and synthesis of two novel analogs, AMBMP-6 and AMBMP-13, that increase MYL2 mRNA expression more than AMBMP. To determine which of these compounds were likely to be successful therapeutics for treating muscular disorders *in-vivo*, various *in-vitro* assays were employed to evaluate physicochemical properties influencing drug ADME. While a compound may exhibit good *in-vitro* drug activity, it does not automatically guarantee favorable *in-vivo* activity unless it also possesses good bioavailability and half-life (Ref. 26). Moreover, the escalating costs associated with the development of novel therapeutics and the high rate of candidate attrition have prompted a shift in drug discovery strategies towards the simultaneous evaluation of comprehensive drug physicochemical properties alongside efficacy (Ref. 27). Notably, both AMBMP-6 and -13 exhibited considerably improved kinetic solubility (94 μM) and metabolic stability in liver microsomes (>120 min) compared to AMBMP. Moreover, AMBMP-13 was determined to be significantly less toxic (30 μM) than both AMBMP (19 μM) and AMBMP-6 (14 μM). Since drug toxicity is a key contributor to drug attrition in preclinical and clinical development, AMBMP-13 was selected as the lead drug candidate moving forward. Remarkably, the simple addition of a hydroxyl moiety to the 5-position of the 3-methoxyphenyl ring in AMBMP substantially increased biological activity, solubility, metabolic stability, as well as reduced cellular toxicity.

Determining the molecular mechanism through which a drug exerts its physiological effect is a central aspect of the drug discovery process, frequently utilized to develop more effective therapeutics. Knowledge of direct drug targets often facilitates the design of novel small molecules

that are more potent and selective (Ref. 28). Meanwhile, understanding of indirect drug targets can pinpoint downstream effectors suitable for alternative therapeutic strategies (Ref. 29). Therefore, an incomplete understanding of a drug's MOA can serve as a bottleneck, hindering the success rate during preclinical development. The synthesis of a biologically active alkyne-containing analog, AMBMP-14, capable of being linked to azide agarose beads, enabled the use of small molecule affinity chromatography to enrich direct targets these MYL2 enhancers. Interestingly, a subsequent affinity purification followed by mass spectrometry-based proteomics identified numerous proteins associated with calcium and WNT signaling pathways. This was interpreted as a validation of the experimental approach, as AMBMP has been previously documented as an activator of WNT signaling (Ref. 30). While we were encouraged by these results, this approach identified numerous direct targets of AMBMP that needed to be individually validated as modulators of MYL2 expression. Interestingly, an important calcium signaling protein, S100A6, was determined to be one of the most abundant proteins from the affinity purification. Additionally, S100A6 was confirmed to be increased in LGMDR1 patients, suggesting that the inhibition of S100A6 could serve as a valuable therapeutic approach for treating LGMDR1, and that it may be a direct pharmacological target of AMBMP. In subsequent experiments, siRNA-mediated knockdown of S100A6 expression was shown to increase MYL2 levels, confirming our hypothesis and demonstrating the value of chemoproteomics for identifying novel drug targets. This finding has important implications for the development of even more potent candidates, as *in-silico* molecular docking approaches can now be utilized to predict favorable S100A6-drug interactions, further guiding future drug design (Ref. 31).

Interestingly, changes in protein phosphorylation status following AMBMP-13 treatment suggested activation of the CAMKII-P38 MAPK signaling axis, which was previously identified to be diminished in C3KO muscles as well as essential for the transcription of genes required for muscle growth and adaptation (Ref. 12). This analysis also suggested activation of PKA, an upstream activator of CaMKII that can act through numerous mechanisms, including increasing calcium entry via the L-type calcium channel, increasing sarcoplasmic reticulum calcium release via RYR, and inhibiting CAMKII-targeting protein phosphatase 1 (PP1) (Ref. 32). Furthermore, administration of recombinant S100A6 has been demonstrated to decrease cAMP levels and PKA activity in a RAGE-dependent fashion (Ref. 33). These findings not only identify critical components of a potential AMBMP MOA, but also suggests the existence of multiple mechanisms through which increased expression of S100A6 can contribute to the diminished CAMKII signaling observed in LGMDR1. Further studies are required to validate proposed molecular mechanisms of S100A6 role in controlling CaMKII signaling.

Finally, a transcription factor enrichment analysis using upregulated proteins from the global proteomics analysis identified the activation of multiple MYL2-associated transcription factors. Interestingly, many of the enriched transcription factors are also known to be activated by PGC1 α , which was previously shown to be decreased in the muscles of C3KO mice (Ref. 12). Integration of these findings allowed us to establish a working MOA through which AMBMP enhances MYL2 expression. Specifically, we propose that AMBMP inhibits the interaction of S100A6 with RAGE, subsequently increasing cAMP-dependent activation of PKA, CAMKII, and P38 MAPK. This leads to the stabilization of the transcriptional co-activator PGC1 α , resulting in an increased transcription of SO genes, including MYL2. While validation of this mechanism is still ongoing,

this information may prove invaluable for identifying novel therapeutic approaches for treating LGMDR1. For instance, potent RAGE receptor antagonists, currently being investigated as treatments for both cancer and Alzheimer's disease, could ultimately be more efficacious activators of CaMKII signaling in LGMDR patients (Ref. 34-35).

In conclusion, the results presented here describe a successful research endeavor to develop more biologically active and bioavailable analogs of AMBMP as well as uncover the MOA through which these compounds increase MYL2 gene expression. The methodology involved an iterative medicinal chemistry approach employing structure-activity relationship (SAR) analyses to guide design of fourteen novel AMBMP analogs. Additionally, the drug-like attributes of potential MYL2-enhancing compounds were assessed using *in-vitro* ADME assays, resulting in the identification of a more biologically active and bioavailable lead candidate, AMBMP-13. Moreover, small molecule therapeutic-based affinity chromatography and mass spectrometry-based global and phosphoproteomics revealed both direct and indirect molecular targets influenced by these MYL2 enhancing compounds, suggesting a potential drug MOA as well as novel mechanisms through which S100A6 can contribute to the diminished CAMKII signaling. While the proposed pharmacological mechanism still necessitates validation, further investigation of these findings promises to aid in the development of more efficacious activators of CaMKII signaling that may one day be used to counteract impaired adaptive expression of SO genes in LGMDR1 patients.

AUTHOR CONTRIBUTIONS

WC, VJ, MS, JW, JC, BJ, IK participated in research design. WC, IK conducted experiments. WC, NK, AD, PA synthesized compounds. WC, IK performed data analysis. WC wrote the manuscript. VJ, MS, JC edited the manuscript.

ACKNOWLEDGEMENTS

The research described was supported by a seed grant funding from UCLA CTSI to the Spencer and John lab.

SUPPLEMENTARY ANALYTICAL MATERIAL

AMBMP Intermediate:

^1H NMR (400 MHz, CDCl_3) δ 6.78-6.73 (m, 3H), 5.95 (s, 2H), 5.78 (s, 1H), 4.93 (s, 2H), 4.38 (s, 2H), 1.69 (s, 1H). LC-MS, $[\text{M}+\text{H}]^+$, m/z: 279.0

AMBMP-6:

^1H NMR (400 MHz, MeOD) δ 7.23 (s, 3H), 6.85 (s, 3H), 6.77 (s, 1H), 6.17 (s, 1H), 5.91 (s, 2H), 4.47 (s, 2H). LC-MS $[\text{M}+\text{H}]^+$, m/z: 336.9

AMBMP-13:

^1H NMR (400 MHz, DMSO- d_6) δ 9.53 (s, 1H), 7.32 (s, 1H), 6.92-6.76 (m, $J=4.00$, 4.80, 8.00, 5H), 6.37 (t, $J=2.24$, 1H), 6.16 (s, 1H), 6.00 (s, 2H), 5.97 (s, 2H), 4.40-4.41 (d, $J=4.00$, 2H), 3.73 (s, 3H), 3.68 (s, 1H), 2.07 (s, 1H). LC-MS $[\text{M}+\text{H}]^+$, m/z: 367

AMBMP-14:

^1H NMR (400 MHz, MeOD) δ 7.92 (td, $J = 1.8, 0.6$ Hz, 1H), 7.80 (ddd, $J = 7.8, 1.8, 1.2$ Hz, 1H), 7.52 (dt, $J = 7.7, 1.4$ Hz, 1H), 7.41 (td, $J = 7.8, 0.6$ Hz, 1H), 6.88 – 6.80 (m, 2H), 6.79 – 6.74 (m, 1H), 6.22 (s, 1H), 5.91 (s, 2H), 4.48 (s, 2H), 3.35 (s, 1H). LC-MS $[\text{M}+\text{H}]^+$, m/z : 345.1

REFERENCES

1. Taghizadeh, E., Rezaee, M., Barreto, G. E., & Sahebkar, A. (2019). Prevalence, pathological mechanisms, and genetic basis of limb-girdle muscular dystrophies: A review. *Journal of cellular physiology*, 234(6), 7874-7884.
2. Richard, I., Broux, O., Allamand, V., Fougereousse, F., Chiannilkulchai, N., Bourg, N., ... & Beckmann, J. S. (1995). Mutations in the proteolytic enzyme calpain 3 cause limb-girdle muscular dystrophy type 2A. *Cell*, 81(1), 27-40.
3. Sorimachi H., Hata S., Ono Y. Expanding members and roles of the calpain superfamily and their genetically modified animals. *Exp. Anim.* 2010;59:549–566. doi:10.1538/expanim.59.549.
4. Sáenz, A., Leturcq, F., Cobo, A. M., Poza, J. J., Ferrer, X., Otaegui, D., Camaño, P., Urtasun, M., Vílchez, J., Gutiérrez-Rivas, E., Emparanza, J., Merlini, L., Paisán, C., Goicoechea, M., Blázquez, L., Eymard, B., Lochmuller, H., Walter, M., Bonnemann, C., Figarella-Branger, D., ... López de Munain, A. (2005). LGMD2A: genotype-phenotype correlations based on a large mutational survey on the calpain 3 gene. *Brain : a journal of neurology*, 128(Pt 4), 732–742.
5. Fanin, M., Nascimbeni, A. C., & Angelini, C. (2013). Muscle atrophy in Limb Girdle Muscular Dystrophy 2 A: a morphometric and molecular study. *Neuropathology and Applied Neurobiology*, 39(7), 762-771.
6. Fanin, M., & Angelini, C. (2015). Protein and genetic diagnosis of limb girdle muscular dystrophy type 2A: the yield and the pitfalls. *Muscle & nerve*, 52(2), 163-173.
7. Guglieri, M., Magri, F., D'Angelo, M. G., Prella, A., Morandi, L., Rodolico, C., ... & Comi, G. P. (2008). Clinical, molecular, and protein correlations in a large sample of genetically diagnosed Italian limb girdle muscular dystrophy patients. *Human mutation*, 29(2), 258-266.
8. El-Khoury, R., Traboulsi, S., Hamad, T., Lamaa, M., Sawaya, R., & Ahdab-Barmada, M. (2019). Divergent features of mitochondrial deficiencies in LGMD2A associated with novel calpain-3 mutations. *Journal of Neuropathology & Experimental Neurology*, 78(1), 88-98.

9. Kramerova, I., Kudryashova, E., Tidball, J. G., & Spencer, M. J. (2004). Null mutation of calpain 3 (p94) in mice causes abnormal sarcomere formation in vivo and in vitro. *Human molecular genetics*, *13*(13), 1373-1388.
10. Kramerova, I., Kudryashova, E., Wu, B., Germain, S., Vandeborne, K., Romain, N., ... & Spencer, M. J. (2009). Mitochondrial abnormalities, energy deficit and oxidative stress are features of calpain 3 deficiency in skeletal muscle. *Human Molecular Genetics*, *18*(17), 3194-3205.
11. Kramerova, I., Kudryashova, E., Ermolova, N., Saenz, A., Jaka, O., Lopez de Munain, A., & Spencer, M. J. (2012). Impaired calcium calmodulin kinase signaling and muscle adaptation response in the absence of calpain 3. *Human Molecular Genetics*, *21*(14), 3193-3204.
12. Kramerova, I., Ermolova, N., Eskin, A., Hevener, A., Quehenberger, O., Armando, A. M., ... & Spencer, M. J. (2016). Failure to up-regulate transcription of genes necessary for muscle adaptation underlies limb girdle muscular dystrophy 2A (calpainopathy). *Human molecular genetics*, *25*(11), 2194-2207.
13. Kramerova, I., Kudryashova, E., Wu, B., Ottenheijm, C., Granzier, H., & Spencer, M. J. (2008). Novel role of calpain-3 in the triad-associated protein complex regulating calcium release in skeletal muscle. *Human molecular genetics*, *17*(21), 3271-3280.
14. Franzini-Armstrong, C., & Jorgensen, A. O. (1994). Structure and development of EC coupling units in skeletal muscle. *Annual review of physiology*, *56*(1), 509-534.
15. Chin, E. R. (2005). Role of Ca²⁺/calmodulin-dependent kinases in skeletal muscle plasticity. *Journal of applied Physiology*, *99*(2), 414-423.
16. Liu, J., Campagna, J., John, V., Damoiseaux, R., Mokhonova, E., Becerra, D., Meng, H., McNally, E. M., Pyle, A. D., Kramerova, I., & Spencer, M. J. (2020). A Small-Molecule Approach to Restore a Slow-Oxidative Phenotype and Defective CaMKII β Signaling in Limb Girdle Muscular Dystrophy. *Cell reports. Medicine*, *1*(7), 100122.

17. Rappsilber, J., Mann, M., & Ishihama, Y. (2007). Protocol for micro-purification, enrichment, pre-fractionation and storage of peptides for proteomics using StageTips. *Nature protocols*, 2(8), 1896–1906.
18. Orsburn B. C. (2021). Proteome Discoverer-A Community Enhanced Data Processing Suite for Protein Informatics. *Proteomes*, 9(1), 15.
19. Xie, Z., Bailey, A., Kuleshov, M. V., Clarke, D. J. B., Evangelista, J. E., Jenkins, S. L., Lachmann, A., Wojciechowicz, M. L., Kropiwnicki, E., Jagodnik, K. M., Jeon, M., & Ma'ayan, A. (2021). Gene Set Knowledge Discovery with Enrichr. *Current protocols*, 1(3), e90.
20. Huang, R., Grishagin, I., Wang, Y., Zhao, T., Greene, J., Obenauer, J. C., Ngan, D., Nguyen, D. T., Guha, R., Jadhav, A., Southall, N., Simeonov, A., & Austin, C. P. (2019). The NCATS BioPlanet - An Integrated Platform for Exploring the Universe of Cellular Signaling Pathways for Toxicology, Systems Biology, and Chemical Genomics. *Frontiers in pharmacology*, 10, 445.
21. Lachmann, A., & Ma'ayan, A. (2009). KEA: kinase enrichment analysis. *Bioinformatics (Oxford, England)*, 25(5), 684–686.
22. Lachmann, A., Xu, H., Krishnan, J., Berger, S. I., Mazloom, A. R., & Ma'ayan, A. (2010). ChEA: transcription factor regulation inferred from integrating genome-wide ChIP-X experiments. *Bioinformatics (Oxford, England)*, 26(19), 2438–2444.
23. Donato, R., Sorci, G., & Giambanco, I. (2017). S100A6 protein: functional roles. *Cellular and molecular life sciences : CMLS*, 74(15), 2749–2760.
24. Sáenz, A., Azpitarte, M., Armañanzas, R., Leturcq, F., Alzualde, A., Inza, I., García-Bragado, F., De la Herran, G., Corcuera, J., Cabello, A., Navarro, C., De la Torre, C., Gallardo, E., Illa, I., & López de Munain, A. (2008). Gene expression profiling in limb-girdle muscular dystrophy 2A. *PloS one*, 3(11), e3750.
25. Needham, E. J., Parker, B. L., Burykin, T., James, D. E., & Humphrey, S. J. (2019). Illuminating the dark phosphoproteome. *Science signaling*, 12(565), eaau8645.

26. Lipinski C. A. (2000). Drug-like properties and the causes of poor solubility and poor permeability. *Journal of pharmacological and toxicological methods*, 44(1), 235–249.
27. Lin, J. H., & Lu, A. Y. (1997). Role of pharmacokinetics and metabolism in drug discovery and development. *Pharmacological reviews*, 49(4), 403–449.
28. Schenone, M., Dančák, V., Wagner, B. K., & Clemons, P. A. (2013). Target identification and mechanism of action in chemical biology and drug discovery. *Nature chemical biology*, 9(4), 232–240.
29. Douglass, E. F., Jr, Allaway, R. J., Szalai, B., Wang, W., Tian, T., Fernández-Torras, A., Realubit, R., Karan, C., Zheng, S., Pessia, A., Tanoli, Z., Jafari, M., Wan, F., Li, S., Xiong, Y., Duran-Frigola, M., Bertoni, M., Badia-I-Mompel, P., Mateo, L., Guitart-Pla, O., ... Califano, A. (2022). A community challenge for a pancancer drug mechanism of action inference from perturbational profile data. *Cell reports. Medicine*, 3(1), 100492.
30. Xia, Z., Qi, W., Xiaofeng, G., Jiguang, K., Hongfei, H., Yuchen, Z., Yihan, Z., Yan, W., Nannan, L., Yiwei, L., Hongsheng, B., & Xiaobai, L. (2020). AMBMP activates WNT pathway and alleviates stress-induced behaviors in maternal separation and chronic stress models. *European journal of pharmacology*, 881, 173192.
31. Pinzi, L., & Rastelli, G. (2019). Molecular Docking: Shifting Paradigms in Drug Discovery. *International journal of molecular sciences*, 20(18), 4331.
32. Grimm, M., & Brown, J. H. (2010). Beta-adrenergic receptor signaling in the heart: role of CaMKII. *Journal of molecular and cellular cardiology*, 48(2), 322–330.
33. Dogra, S., Das, D., Maity, S. K., Paul, A., Rawat, P., Daniel, P. V., Das, K., Mitra, S., Chakrabarti, P., & Mondal, P. (2022). Liver-Derived S100A6 Propels β -Cell Dysfunction in NAFLD. *Diabetes*, 71(11), 2284–2296.
34. Kwak, T., Drews-Elger, K., Ergonul, A., Miller, P. C., Braley, A., Hwang, G. H., ... & Hudson, B. I. (2017). Targeting of RAGE-ligand signaling impairs breast cancer cell invasion and metastasis. *Oncogene*, 36(11), 1559-1572.

35. Deane, R., Singh, I., Sagare, A. P., Bell, R. D., Ross, N. T., LaRue, B., ... & Zlokovic, B. V. (2012). A multimodal RAGE-specific inhibitor reduces amyloid β -mediated brain disorder in a mouse model of Alzheimer disease. *The Journal of clinical investigation*, 122(4), 1377-1392.

CHAPTER 6

Hit-to-Lead Optimization and Molecular Target Identification of Small Molecule

Sarcospan Enhancers for Duchenne Muscular Dystrophy

Whitaker Cohn^{1,3}, Dongwook Wi¹, Jesus Campagna¹, Ravinder Malik², Ekaterina Mokhonova², Hafsa Mamsa², Barbara Jagodzinska¹, Julian Whitelegge³, Rachele H. Crosbie², Varghese John¹

¹The Drug Discovery Lab, Mary S. Easton Center for Alzheimer's Disease Research, Department of Neurology, David Geffen School of Medicine, 710 Westwood Plaza, University of California Los Angeles, Los Angeles, CA 90095, USA

²Crosbie Lab, Department of Integrative Biology and Physiology, University of California Los Angeles, 610 Charles E. Young Drive East, Terasaki Life Sciences Building, Los Angeles, CA 90095 USA

³Pasarow Mass Spectrometry Laboratory, Jane and Terry Semel Institute for Neuroscience and Human Behavior, David Geffen School of Medicine, 760 Westwood Plaza, University of California Los Angeles, Los Angeles, CA 90095, USA

ABSTRACT

Duchenne muscular dystrophy (DMD) is a severe genetic disorder affecting about 1 in 5700 males globally, leading to childhood muscle atrophy, progressive motor function decline, and premature cardiac and respiratory failure. Despite advancements in DMD research, current treatments have limited efficacy, underscoring the need for new therapeutic targets. DMD arises from mutations in the dystrophin gene, which encodes for a protein that is vital for muscle cell stability during contractions. Dystrophin interacts with sarcospan (SSPN) and other glycoproteins, forming a complex that connects the cytoskeleton, cell membrane, and extracellular matrix. The absence of dystrophin and the related complex results in muscle damage, deterioration, and loss of function. Intriguingly, increasing SSPN expression in the mdx mouse model of DMD reduces muscle pathology and enhances function by improving membrane localization of compensatory adhesion complexes. Recently, a small molecule enhancer of SSPN, OT-9, was identified to increase SSPN protein levels in dystrophin-deficient myotubes. This manuscript presents a comprehensive research initiative aimed at developing more potent and bioavailable analogs of OT-9, as well as uncovering the mechanism of action (MOA) by which these compounds enhance SSPN gene expression. Through iterative medicinal chemistry and *in-vitro* ADME assays, two new OT-9 analogs, DDL-449 and DDL-472, were identified to increase SSPN levels *in-vivo*. Additionally, utilizing methods such as drug-affinity chromatography and mass spectrometry-based proteomics, both direct and indirect molecular targets of OT-9 analogs were identified, suggesting that CREB1 activation via AKT signaling likely contributes to the mechanism of action leading to enhanced SSPN expression. Further exploration and validation of this molecular mechanism promises to help identify novel therapeutic avenues for treating DMD.

Key Words: Sarcospan, Duchenne Muscular Dystrophy, Proteomics, Mechanism of Action

INTRODUCTION

Duchenne muscular dystrophy (DMD) is a severe genetic disorder that affects approximately 1 in 5700 males globally (Ref. 1). This debilitating ailment initiates muscle atrophy in childhood, leading to a gradual decline in motor function and, eventually, premature death due to cardiac and respiratory failure (Ref. 2). Despite substantial progress in DMD research, current treatments only minimally impede disease progression, highlighting the necessity for new therapeutic targets (Ref. 3-4).

DMD arises from mutations in the dystrophin gene, which encodes the essential dystrophin protein, crucial for stabilizing healthy muscle cells during contractions. Within muscle fibers, dystrophin interacts with sarcospan (SSPN) and various glycoproteins, forming an important adhesion complex that connects the actin cytoskeleton, cell membrane (sarcolemma), and extracellular matrix (ECM) (Ref. 5-6). In DMD, the absence of dystrophin and the dystrophin-glycoprotein complex (DGC) leads to damage upon muscle fiber contraction and subsequent muscle deterioration (Ref. 7). Intriguingly, increasing expression of SSPN, a scaffold protein in the adhesion complex, has been shown to reduce muscle pathology in a dystrophin deficient mouse model of DMD (MDX) (Ref. 8-10). This improvement in muscle function is attributed to the ability of SSPN to facilitate the membrane localization of two alternative adhesion complexes—the utrophin-glycoprotein complex (UGC) and the $\alpha7\beta1D$ -integrin complex—that compensate for DGC loss (Ref. 8-9).

Recently, a high-throughput screening effort was employed to identify small molecules capable of increasing SSPN expression, with the hope of identifying novel therapeutics that may be used to

treat DMD (Ref. 11-12). This study resulted in the identification of OT-9, which was confirmed to increase SSPN gene expression and protein levels in dystrophin-deficient mouse and human myotubes (Ref. 12). Furthermore, OT-9 increased the abundance of laminin-binding adhesion complexes, restoring membrane stability to these cells. Encouragingly, intramuscular injection of OT-9 into DMD mice induced no adverse effects and significantly increased SSPN expression *in vivo* (Ref. 12). While it appears to be a highly promising candidate for treating DMD, its therapeutic potential is impeded by its limited potency and bioavailability. Furthermore, the precise molecular mechanism through which OT-9 increases SSPN expression remains unknown.

This manuscript presents a comprehensive research initiative aimed at developing more potent and bioavailable analogs of OT-9, as well as uncovering the mechanism of action (MOA) by which OT-9 analogs increase SSPN gene expression. An iterative medicinal chemistry hit-to-lead optimization approach involving structure-activity relationship (SAR) analyses was employed to design and synthesize thirty-four novel OT-9 analogs. Various *in-vitro* absorption, distribution, metabolism, and excretion (ADME) assays were then utilized to assess the drug-like properties of candidate SSPN-enhancing compounds, DDL-449 and DDL-472, both of which significantly increased SSPN levels in DMD mice following oral administration. Furthermore, established methodologies such as small molecule therapeutic-based affinity chromatography and mass spectrometry-based global and phosphoproteomics were employed to identify both direct and indirect molecular targets of OT-9 analogs. While the exact mechanism awaits validation, findings indicate that cAMP responsive element binding protein 1 (CREB1) activation through AKT signaling likely contributes to increased SSPN expression. Further exploration and validation of this molecular mechanism promises to enhance our understanding of how these compounds

modulate SSPN expression and may potentially unveil novel therapeutic strategies for treating DMD.

METHODS

Compound Synthesis via Amide Coupling

Carboxylic acid-containing 2-oxo-1,2-dihydroquinoline-chromane or -2-oxo-2*H*-chromene substituent (1 equiv.), amine-containing substituent (4-aminophenyl) (1,4-oxazepan-4-yl) methanone (1 equiv.), 1-ethyl-3-(3-dimethylaminopropyl)carbodiimide (EDC; 1.2 equiv.), hydroxybenzotriazole (HOBt; 1.1 equiv.), and N-N, diisopropylethylamine (DIPEA; 2 equiv.) were added to a round bottom flask. The reagents were solubilized using anhydrous dichloromethane and the reaction mixture was stirred at 23 °C for 16 hours. The crude product was concentrated in vacuo, reconstituted with ethyl acetate, and an aqueous work-up was performed in a separatory funnel using hydrochloric acid (0.5 M), followed by a saturated sodium bicarbonate solution. The retained organic phase was dried with anhydrous sodium sulphate, concentrated in vacuo, and then purified via flash column chromatography using a 4 g silica flash column with a mobile phase of hexanes:ethyl acetate (time/% ethyl acetate: 0/0, 2/0, 10/100, 15/100), followed by DCM: MeOH (time/% MeOH: 0/0, 2/0, 20/10, 30/20). Identity and purity of each compound was confirmed via LC-MS, LC-UV/Vis and ¹H NMR.

DDL-449 In-Vivo Study

4-5 weeks old mdx mice were treated with DDL-449 at 60 mg/kg, daily, for two weeks by pipet feeding. Vehicle: 50%PEG-200/25% strawberry syrup. Tissues were harvested on day 15 for analysis (at 2 hours after last compound administration). Gene expression was normalized to β-

actin and SSPN transcript level in vehicle-treated mice. Data on the graph represents individual replicates, mean value per treated group and SD. Mean value of SSPN mRNA in vehicle-treated group is represented by green line. ****p<0.0001.

DDL-472 In-Vivo Study

3-4 weeks old mdx mice were treated with DDL-472 at 20 mg/kg, daily, for three weeks by pipet feeding. Vehicle: 50%PEG-200/25% strawberry syrup. Tissues were harvested on day 22 for analysis (at 2 hours after last compound administration). Gene expression was normalized to β -actin, mouse weight and SSPN transcript level in vehicle-treated mice. Data on the graph represents individual replicates, mean value per treated group and SD. Mean value of SSPN mRNA in vehicle-treated group is represented by green line. **p<0.01.

Gene Expression Analysis

Snap-frozen muscles (Tibialis Anterior) from treated mice were pulverized in liquid nitrogen. Total RNA was extracted using Trizol-based (Thermo Fisher Scientific) phase separation. RNA concentrations were determined using a NanoDrop 1000 (Thermo Fisher Scientific) and 750 ng of RNA in a 20 μ l reaction was reverse transcribed using iScript cDNA synthesis (Bio-Rad) with the following cycling conditions: 25°C for 5 mins, 42°C for 30 mins, 85°C for 5 mins. For qPCR analysis, SsoFast EvaGreen Supermix (Bio-Rad), 400 nM of each optimized forward and reverse primer (SSPN F: 5' TGCTAGTCAGAGATACTCCGTTTC 3', SSPN R: 5' GTCCTCTCGTCAACTTGGTATG 3', BACT F: 5' GAGCACCCCTGTGCTGCTCACCG 3', BACT R: 5' CAATGCCTGTGGTACGACCA 3'), and cDNA corresponding to 37.5 ng RNA were used to amplify cDNA measured by QuantStudio 5 Real-Time PCR System (Thermo Fisher

Scientific) with the following reaction conditions: 55°C for 2 mins, 95°C for 2 mins, 40 cycles of 95°C for 10 seconds and 62°C for 30 seconds, and dissociation stage. Each sample was run in triplicate. Data was analyzed using the ddCT method and normalized to reference gene ACTB with vehicle-treated samples serving as the calibrator (relative expression of vehicle control = 1).

Immunofluorescence Imaging of SSPN in Quadriceps Cryo-Sections

10µm quadriceps cryo-sections were stained with SSPN rabbit mAb 10B8 (Crosbie Lab).

In detail: Tissue was frozen in liquid nitrogen cooled isopentane and mounted on OCT (Tissue Tek) and stored at -80°C. Transverse cryosections (10µm) were blocked with 3% BSA at room temperature, followed by incubation with avidin/biotin blocking kit (Vector Laboratories). Sections were washed with PBS and primary antibodies were detected with species specific biotinylated antibodies for 1 hour at room temperature. Bound antibodies were visualized by incubation with Fluorescein-conjugated Avidin D (Vector Laboratories). Slides were wet mounted in Vectashield with or without DAPI (Vector Laboratories) before analysis by microscopy on Zeiss Axio Observer 7 or Axio Imager M2 (Carl Zeiss). Images were captured with Hamamatsu ORCA-Flash 4.0 V3 digital complementary metal oxide semiconductor camera and either EC Plan-Neofluar 10x/0.30 Ph1 or Plan-Aprochromat 20x/0.8 M27 objectives. All measurements were performed using Image J software (NIH).

Synthesis of Alkyne-Containing Analog, DDL-489

A solution of 3-(ethylamino) phenol (3.644 mmol, 1 Equiv.) and propargyl bromide (0.524 mmol, 1.2 Equiv.), and Potassium carbonate (4.3728 mmol, 1.5 Equiv.) in acetonitrile was stirred at RT for 16 hr. The reaction mixture was added to water and extracted with EtOAc. The combined

organic phases were washed with water and brine and dried over sodium sulfate. The resultant crude compound was purified by using a 4 g silica flash column, eluted with Hexanes: EtOAc (time (min) /% MeOH: 2/0, 20/50, 40/100), and dried under a vacuum to afford DDL 489 Intermediate 1 (INT1, 210mg, 32.7 %, brown oil). Next, POCl₃(0.6847 mmol, 4 Equiv.) was added dropwise to DMF on ice and the solution stirred for 1hr. A solution of INT 1 (0.4649 mmol, 1 Equiv.) was added and the reaction mixture was stirred at room temperature for 1 h, then heated at 75 °C for 1 h. After cooling, water was added and the mixture was stirred at room temperature, neutralized, and extracted with ethyl acetate. The organic layer was washed with brine, dried over Na₂SO₄, filtered, and the solvent evaporated. The resultant crude mixture was purified by using a 4 g silica flash column, eluted with Hexanes: EtOAc (time (min) /% EtOAc: 2/0, 20/50, 40/100) to give a DDL 489 INT2 (70.54mg, 65.2 %, light pink solid). Then, [Intermediate 2] (63.25mg, 0.3112 mmol, 1 Equiv.), 2,2-dimethyl-1,3-dioxane-4,6-dione (67.28 mg, 0.4668 mmol, 1.5 Equiv.) and triethylamine (14.45μL, 0.1037 mmol, 0.33 Equiv.) were combined in EtOH (3 mL). The mixture was heated at 60 °C for 24h. The mixture was cooled to room temperature and filtered. The collected material was washed with EtOH and dried under a vacuum to afford DDL 489 carboxylic acid (57.83mg, 68.5 %, yellow solid). DDL489 COOH (55.58mg, 0.205mmol, 1 Equiv.), HOBt (30.47mg, 0.2255 mmol, 1.1 Equiv.), and EDC (47.13 mg, 0.2458 mmol, 1.2 Equiv.) were added into the round bottom flask with a stir bar. 10 mL of anhydrous DCM and 2.5 eq. of DIPEA were added to the round bottom flask, and (4-aminophenyl) (1,4-oxazepan-4-yl)-methanone (1 Equiv.) was then added to the round bottom flask and stir for overnight. After being stirred overnight, the solution changed colors to yellowish. Atmospheric pressure chemical ionization was performed to check the reaction. The reaction mixture was reconstituted using DCM and transferred to a separatory funnel, the water layer was extracted and combined organic

layers were collected. The organic phase was washed with sodium bicarbonate (2 x 15 mL), and brine solution (15 mL), dried with anhydrous Na₂SO₄, filtered, concentrated, and evaporated. The resultant crude compound was purified by using a 4 g silica flash column, eluted with Hexane: ethyl acetate (time /% ethyl acetate: 0/0, 5/0, 25/100), and eluted with DCM: MeOH (time/% MeOH: 0/0, 5/0, 15/10, 25/20, 40/100) afforded DDL 489. The fractions that were corresponding to the interest peaks were dried in a speed vacuum to yield (50.88 mg of DDL 489, light yellow powder, 52.4 %). ¹H NMR (400 MHz, CDCl₃) δ 10.99 (s, 1H), 8.84 (s, 1H), 7.80-6.70 (m, 7H), 4.14 (s, 2H), 3.84-3.66 (m, 8H), 3.6 (q, J=8Hz, 2H), 2.30 (s, 1H), 2.05-1.85 (m, 2H), 1.31 (t, J=6Hz, 3H), LC-MS m/z [M+H]⁺ 474.25. An ion-extracted chromatogram (IEC) using the m/z corresponding to the [M+H]⁺ ion (474.25) was utilized to identify the chromatographic peak for each compound. Furthermore, the purity percent was calculated by dividing the chromatographic peak area for each compound by the sum of all the non-background peak areas in the UV-Vis absorption spectrum.

Purity Analysis via Liquid Chromatography-Mass Spectrometry

Analysis of purity by liquid chromatography-mass spectrometry (LC-MS) was done at the UCLA Pasarow Mass Spectrometry Lab (PMSL; Julian Whitelegge, Ph.D., Director). Compounds were diluted to 10 mM in DMSO, then diluted 100-fold in in 50/50/0.1 Water/Acetonitrile/Formic Acid (100 μM final concentration). An aliquot (10 μL) was analyzed using a LTQ Orbitrap XL mass spectrometer (Thermo Fisher Scientific) coupled to an UltiMate 3000 HPLC (Thermo Fisher Scientific) with a Phenomenex analytical column (Kinetex 1.7 μm C18 100 Å 100 x 2.1 mm). The mass spectrometer acquisition method scanned a mass range from 100 – 2000 m/z. The HPLC method utilized a mixture of solvent A (99.9/1 Water/Formic Acid) and solvent B (99.9/1

Acetonitrile/Formic Acid) and a gradient was used for the elution of the compounds (min/%B: 0/0, 3/0, 19/99, 20/99, 21/0, 30/0). An ion extracted chromatogram (IEC) using the m/z corresponding to the $[M+H]^+$ ion was utilized to identify the chromatographic peak for each compound. Purity was calculated by dividing the chromatographic peak area for each compound by the sum of all the non-background peak areas in the total ion chromatogram (TIC).

Purity Analysis via Magnetic Resonance Spectroscopy

DDL 489 (6 mg) was diluted in 600 μL of CDCl_3 and analyzed using an AV400 NMR spectrometer (Bruker) containing a 5 mm broadband Z-gradient probe with Automatic Tune and Match (ATM). The analysis method consisted of a 64-scan proton NMR ($^1\text{H-NMR}$) utilizing default parameters. Predicted $^1\text{H-NMR}$ spectra were obtained using the ChemNMR ^1H estimation function in ChemDraw (PerkinElmer). The experimental data were visualized and interpreted using Mnova (Mestrelab Research).

Synthesis of DDL-489 Agarose Beads

Disulfide azide agarose (1 equiv., Cat# 1238-2, Click Chemistry Tools) was incubated with DDL-489 (2 equiv.) and bromotris(triphenylphosphine)copper(I) (0.2 equiv., Cat# 572144, Sigma Aldrich) in the presence of dimethylformamide (DMF, 2 mL) and triethylamine (TEA, 1 equiv.). The reaction mixture was stirred at 60 $^\circ\text{C}$ for 16 hours. Following centrifugation (1,000 x g, 2 min), the supernatant was discarded, and the agarose beads were washed with DMF 12 times and then with PBS 6 times. Each wash consisted of a 2-minute incubation, centrifugation (1,000 x g, 2 min), and removal of the supernatant. A small aliquot of beads (20 μL) was taken for validation of successful coupling via mass spectrometry following incubation with tris (2-carboxyethyl)

phosphine (TCEP, 20 mM, 10 min). Control agarose beads were subject to the all the same reaction and wash conditions, except without the addition of DDL-489.

Small Molecule Affinity Purification

Differentiated myotubes (MDX or C2C12, 10 cm dish) were washed once with ice-cold PBS, then collected via scraping with ice-cold lysis buffer (1 mL, M-PER™ Mammalian Protein Extraction Reagent with Halt™ Protease and Phosphatase Inhibitor Cocktail (Thermo Fisher Scientific)). Muscle tissue samples were homogenized in a bead beater using 5 volumes of ice-cold lysis buffer (1/5; mg of tissue/uL of buffer). The lysates were clarified via centrifugation (16,000 x g) and protein concentration was assessed using a Micro BCA™ Protein Assay Kit (Thermo Fisher Scientific) according to the manufacturer's protocol. All samples were diluted in lysis buffer to an equal volume (1 mL) and concentration (1 mg/mL). Either DDL-489 agarose beads or control agarose beads (100 uL, n=4 per lysate) were added to each sample and incubated with very gentle mixing on an end-over-end rotator at 4 °C for two hours. Following centrifugation (1,000 x g, 2 min), the supernatant was discarded, and the agarose beads were washed with ice-cold lysis buffer 8 times. Each wash consisted of a 5-minute incubation at 4 °C, centrifugation (1,000 x g, 2 min), and removal of the supernatant. Bound proteins were then eluted off of the agarose beads with tris (2-carboxyethyl) phosphine (200 uL, 10 mM in lysis buffer, 30 min) and the supernatant was collected and processed for proteomics analysis via mass spectrometry.

MDX Myotube Drug Treatment

Differentiated MDX myotubes were treated with DDL-449 (5 uM) or 0.05% DMSO in supplemented cell culture media. After 10 min, 60 min or 24 hours, the cells were washed once

with ice-cold PBS with Halt™ Protease and Phosphatase Inhibitor Cocktail (Thermo Scientific, Waltham, MA)) and then collected via scraping with ice-cold lysis buffer (1 mL, 12 mM sodium lauroyl sarcosine, 0.5% sodium deoxycholate, 50 mM triethylammonium bicarbonate (TEAB)), Halt™ Protease and Phosphatase Inhibitor Cocktail (Thermo Scientific, Waltham, MA)).

Proteomics

Samples were treated with tris (2-carboxyethyl) phosphine (10 mM) and chloroacetamide (40 mM) in 50 mM triethyl ammonium bicarbonate (TEAB)) at 95° C for 30 min. They were then diluted 5-fold with aqueous 50 mM TEAB and incubated overnight with Sequencing Grade Modified Trypsin (1 ug in 10 uL of 50 mM TEAB; Promega, Madison, WI). Following this an equal volume of ethyl acetate/trifluoroacetic acid (TFA, 100/1, v/v) was added and after vigorous mixing (5 min) and centrifugation (13,000 x g, 5 min), the supernatants were discarded, and the lower phases were dried in a centrifugal vacuum concentrator. The samples were then desalted using a modified version of Rappsilber's protocol in which the dried samples were reconstituted in acetonitrile/water/TFA (solvent A, 100 uL, 2/98/0.1, v/v/v) and then loaded onto a small portion of a C18-silica disk (3M, Maplewood, MN) placed in a 200 uL pipette tip (Ref. 13). Prior to sample loading the C18 disk was prepared by sequential treatment with methanol (20 uL), acetonitrile/water/TFA (solvent B, 20 uL, 80/20/0.1, v/v/v) and finally with solvent A (20 uL). After loading the sample, the disc was washed with solvent A (20 uL, eluent discarded) and eluted with solvent B (40 uL). The collected eluent was dried in a centrifugal vacuum concentrator and reconstituted in water/acetonitrile/FA (solvent E, 10 uL, 98/2/0.1, v/v/v).

Additional Steps for Global and Phosphoproteomics of DDL-449 treated MDX Cells: Tryptic peptides were isotopically labeled (TMT18plex Isobaric Label Reagent Set, Thermo Fisher Scientific) according to the manufacturer's protocol to provide relative quantitation between samples. Phosphorylated peptides were sequentially enriched using two complementary affinity resins (Thermo Scientific™ High-Select™ TiO₂ Phosphopeptide Enrichment kit and High-Select™ Fe-NTA Phosphopeptide Enrichment kit) according to manufacturer's protocols. The phosphopeptide-enriched eluate and flow-through were fractionated separately via high pH reversed-phase chromatography (Pierce™ High pH Reversed-Phase Peptide Fractionation Kit) according to the manufacturer's protocol for increased proteome coverage.

Liquid Chromatography-Tandem Mass Spectrometry

Aliquots (5 μ L) were injected onto a reverse phase nanobore HPLC column (AcuTech Scientific, C18, 1.8 μ m particle size, 360 μ m x 20 cm, 150 μ m ID), equilibrated in solvent C and eluted (500 nL/min) with an increasing concentration of solvent D (acetonitrile/water/FA, 98/2/0.1, v/v/v: min/% F; 0/0, 5/3, 18/7, 74/12, 144/24, 153/27, 162/40, 164/80, 174/80, 176/0, 180/0) using an EASY-nLC II (Thermo Fisher Scientific). The effluent from the column was directed to a nanospray ionization source connected to a hybrid quadrupole-Orbitrap mass spectrometer (Q Exactive Plus, Thermo Fisher Scientific) acquiring mass spectra in a data-dependent mode alternating between a full scan (m/z 350-1700, automated gain control (AGC) target 3×10^6 , 50 ms maximum injection time, FWHM resolution 70,000 at m/z 200) and up to 15 MS/MS scans (quadrupole isolation of charge states 2-7, isolation window 0.7 m/z) with previously optimized fragmentation conditions (normalized collision energy of 32, dynamic exclusion of 30 s, AGC target 1×10^5 , 100 ms maximum injection time, FWHM resolution 35,000 at m/z 200).

Proteomics Data Analysis

Raw proteomic data were searched against a Uniprot database containing the complete human proteome using SEQUEST-HT (including dynamic modifications: oxidation (+15.995) on M, deamidation (+0.984) on N/Q, and carbamidomethyl on C (+57.021), phosphorylation on S/T/Y (+79.966)) in Proteome Discoverer (Version 2.4, Thermo Scientific), which provided measurements of relative abundance of the identified peptides. Decoy database searching was used to generate high confidence tryptic peptides (FDR < 1%) (Ref. 14). Tryptic peptides containing amino acid sequences unique to individual proteins were used to identify and provide relative quantification between different proteins in each sample. Post-translationally modified peptides from each protein will be normalized to protein abundance in each sample. Peptides exhibiting a p-value ≤ 0.05 with a log₂-fold change ≥ 0.5 will be analyzed using a series of bioinformatics tools including functional protein association network analysis, comprehensive gene set enrichment gene ontology (GO) classification and pathway analysis, as well as kinase substrate enrichment analyses (Ref. 15-21).

RESULTS

Hit-to-Lead Optimization Identifies Key Structural Elements for SSPN Enhancer Activity

The general synthetic approach utilized to synthesize the majority of novel OT-9 analogs required the coupling of amine and carboxylic acid containing starting materials (**Fig. 1A**). Briefly, each compound was synthesized by performing a coupling reaction between a carboxylic acid-containing substituent (1 equiv.) and an amine-containing substituent (1 equiv.) in the presence of 1-ethyl-3-(3-dimethylaminopropyl)carbodiimide (EDC; 1.2 equiv.), hydroxybenzotriazole

(HOBt; 1.1 equiv.) and N-N, diisopropylethylamine (DIPEA; 2 equiv.) at 23 °C for 16 hours. Optimization efforts led to the synthesis and testing of thirty-four new chemical entities (NCEs) to date (**Fig. 1B**). Five of these analogs (DDL-449, -463, -465, -472 and -489) were determined to increase SSPN expression 1.5-fold or greater in C2C12 cells (**Fig. 1B**). Following repeated testing, quinolone-containing analog, DDL-449, and coumarin-containing analog, DDL-472, were chosen as lead candidates moving forward (**Fig. 1C**). A subsequent dose response analysis in C2C12 cells identified DDL-449 to be more potent than DDL-472, increasing SSPN protein levels with EC₅₀'s of approximately 2200 nM and 5200 nM, respectively (**Fig. 1D**). Continued evaluation of these compounds identified them to be significantly more potent in disease-relevant H2K mdx and Mouly DMD myotubes when compared to C2C12 cells, increasing SSPN expression with EC₅₀ values in the nanomolar range (**Fig. 1E, 1F**).

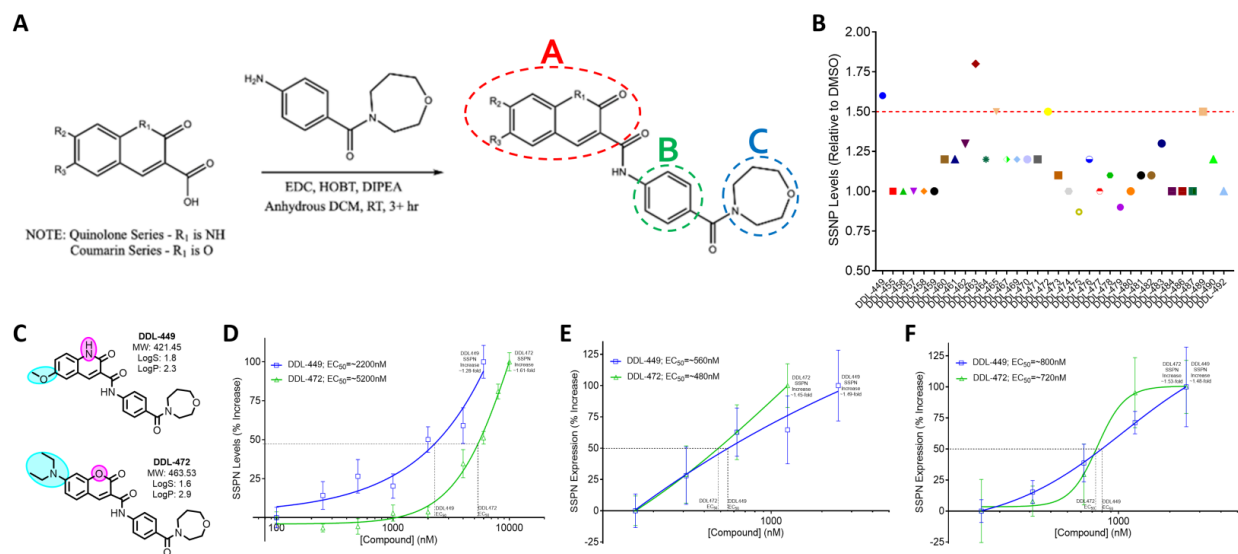
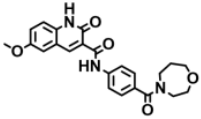
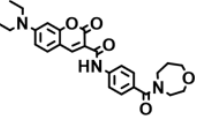


Figure 1. Synthesis and testing of novel SSPN enhancers. (a) General synthetic scheme used to synthesize most novel OT-9 analogs. Different regions of the molecule to be modified are A (red), B (green) and C (blue). (B) Maximal SSPN expression in C2C12 cells following a 24-hour

treatment with each OT-9 analog. (C) Structures of lead candidates, DDL-449 and DDL-472. (D) Dose-response curves showing SSPN protein levels (% increase) and calculated EC₅₀ values for DDL-449 and DDL-472, following treatment of C2C12 cells at concentrations of 100, 250, 500, 1000, 2000, 4000, 6000, 8000, 10000, and 30000 nM. (E) Dose-response curves showing SSPN mRNA levels (% increase) and calculated EC₅₀ values for DDL-449 and DDL-472, following treatment of H2K MDX myotubes concentrations of 156, 313, 625, 1250, 2500, and 5000 nM. (F) Dose-response curves showing SSPN mRNA levels (% increase) and calculated EC₅₀ values for DDL-449 and DDL-472, following treatment of Mouly DMD myotubes concentrations of 156, 313, 625, 1250, 2500, and 5000 nM.

To determine which compound was likely to be the more successful therapeutic *in-vivo*, DDL-449 and DDL-472 were subject to various *in-vitro* assays used to determine physiochemical properties that influence compound absorption, distribution, metabolism, excretion (ADME) (**Table 1**). This included the assessment of kinetic solubility, liver microsome stability, plasma and muscle tissue binding, and cell toxicity (**Table 1**). Desired *in-vitro* ADME property values are as follows: Kinetic Solubility > 50 μ M; Liver Microsomal Stability $t_{1/2}$ > 1 hour; Plasma Binding < 95%; Muscle Tissue Binding < 80%; Cell Toxicity (C_{tox}) > 20 μ M. Unfortunately, both compounds had fairly poor kinetic solubility and high plasma binding values. Though, interestingly, DDL-449 had significantly better metabolic stability in liver microsomes (84 min) and lower muscle tissue binding (48.8%), relative to DDL-472. A structure-activity relationship analysis of all the synthesized analogs revealed structural elements required for biological activity and/or enhanced SSPN expression (**Fig. 2**). The most notable finding was how the incorporation of a quinolone or coumarin influences drug regioselectivity. This is, the activity of coumarin-containing analogs

were increased by the addition of a functional group, such as a diethyl amino, at the 7-position of the coumarin ring. Whereas quinolone-containing analogs exhibited increased potency with substitutions, such as a methoxy group or a halogen, at the 6-position of the ring. Additionally, it is important to note that changes to the oxazepane or central phenyl ring resulted in decreased or no activity.

Compound	Structure	Molecular Weight (Da)	Kinetic Solubility [μM]	Liver Microsome Stability [$t_{1/2}$ (min)]	Plasma Binding [% bound]	Muscle Tissue Binding [% bound]	In-vitro Efficacious Dose in H2K MDX [EC_{50} (nM)]	Cell Toxicity (C_{tox} [μM])
DDL-449		421.45	2	84	97.9	48.8	560	>50
DDL-472		463.53	3	17	99.4	77.2	480	>50

*Desired ADME property values: Kinetic Solubility > 50 μM ; Microsomal Stability $t_{1/2}$ > 1 hrs; Plasma Binding < 95%; Muscle Tissue Binding < 80%; In-Vitro Efficacious Dose < 1 μM ; Cell Toxicity > 20 μM

Table 1. *In-vitro* ADME properties of candidate SSPN enhancers.

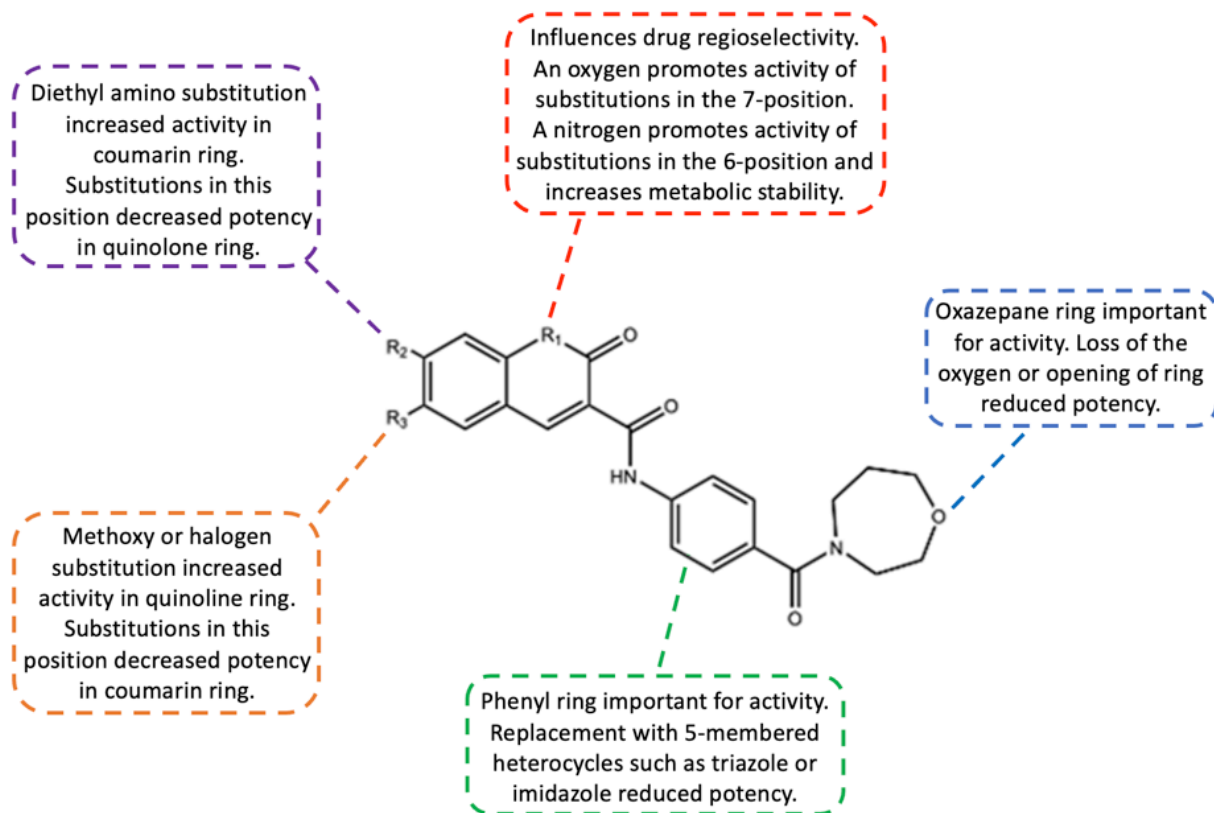


Figure 2. Key structure-activity relationship control elements for SSPN activity and metabolic stability.

Lead Candidates DDL-449 and DDL-472 Increase SSPN In-Vivo

Proof-of-concept pharmacokinetic/pharmacodynamic (PK/PD) analyses were subsequently performed to see if DDL-449 and DDL-472 were orally bioavailable and increased SSPN levels *in-vivo*. A pharmacokinetics analysis identified DDL-472 to be significantly more bioavailable following oral administration, reaching a maximum muscle concentration of 4000 nM, two hours post administration at a dose of 60 mg/kg (**Fig. 3A**) Whereas DDL-449 only reached a concentration of 400 nM (**Fig. 3A**). Subsequently, treatment with DDL-449 at a dose of 60 mg/kg or DDL-472 at a dose of 20 mg/kg was shown to increase expression of SSPN in the quadriceps of MDX mice 1.8-fold and 1.5-fold, respectively, relative to vehicle treated controls (**Fig. 3B, 3C**).

Cryo-sections stained with a SSPN antibody also confirmed increased levels of the SSPN protein localized to the sarcolemma (**Fig. 3D, 3E, 3F**).

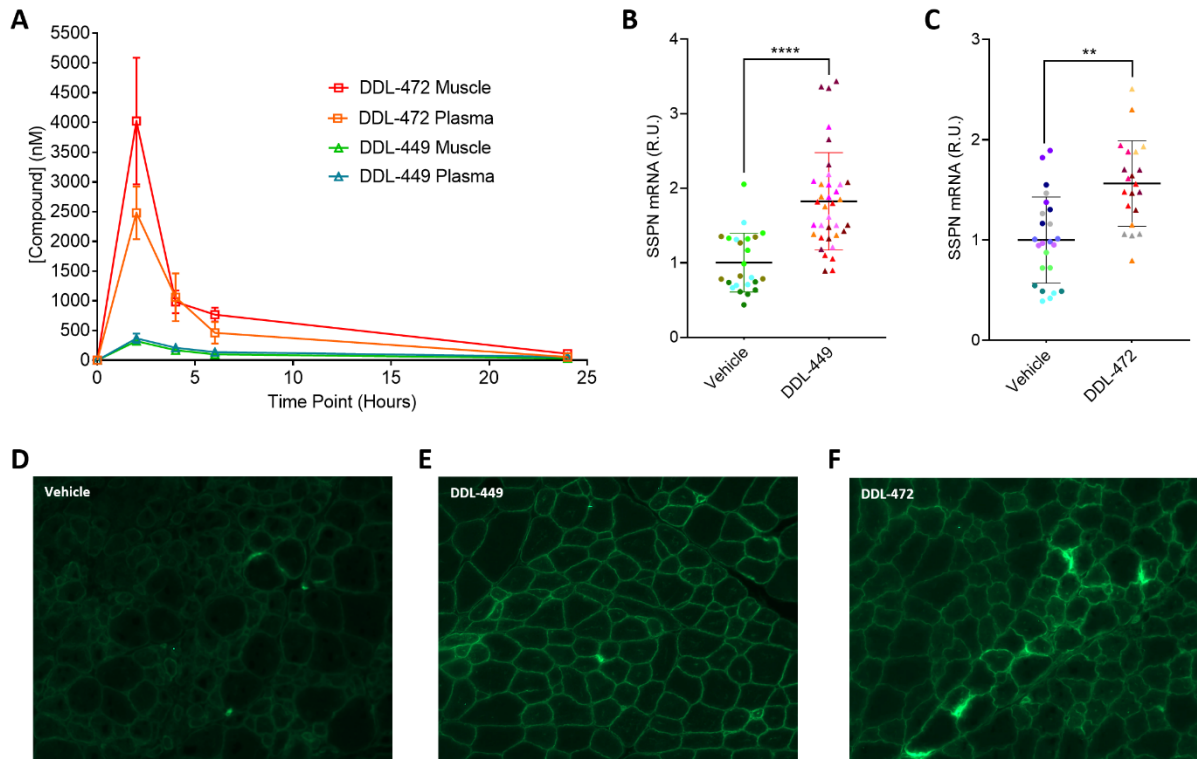


Figure 3. Lead candidates *DDL-449* and *DDL-472* increase *SSPN* in-vivo. (A) *DDL-449* and *DDL-472* plasma and muscle concentrations, 2, 4, 6 and 24 hours following oral administration at a dose of 60 mg/kg. (B) *SSPN* mRNA levels in the quadriceps of dystrophin deficient (MDX) mice, following administration of vehicle or *DDL-449* via oral gavage at a dose of 60 mg/kg, daily, for two weeks. (C) *SSPN* mRNA levels in the quadriceps of dystrophin deficient (MDX) mice, following administration of vehicle or *DDL-472* via oral gavage at a dose of 20 mg/kg, daily, for three weeks. (D) *SSPN* antibody stained quadriceps cryosection in vehicle treated mice. (E) *SSPN* antibody stained quadriceps cryosection in *DDL-449* treated mice. (F) *SSPN* antibody stained quadriceps cryosection in *DDL-472* treated mice.

Identification of Direct and Indirect Molecular Targets of OT-9

Copper (I)-catalyzed click chemistry was employed to couple a biologically active, alkyne-containing analog of OT-9, DDL-489, to azide-containing agarose beads, creating a small molecule-based affinity probe for enriching direct molecular targets of these SSPN enhancers (**Fig. 4A**). Successful coupling was confirmed via liquid chromatography-mass spectrometry (LC-MS) after releasing the bound small molecule with a reducing agent (**Fig. 4B**). An affinity purification followed by mass spectrometry-based proteomics identified numerous proteins significantly enriched by the DDL-489 agarose relative to control agarose beads, that are associated with drug metabolism and/or disease-relevant signaling pathways (xenobiotic metabolism, EGFR/integrin signaling pathways) (**Fig. 4C**). A phosphoproteomics analysis on differentiating C2C12 cells treated with DDL-449 identified significant changes in protein phosphorylation at various time-points (10 min, 60 min, 24 hours), relative to 0.05% DMSO treated controls (**Fig. 4D**). Substrate-specific and gene level kinase enrichment analyses using this data identified several kinases significantly activated 10 minutes (CDK2) and 60 minutes (MAPK9, MAPK8, GSK3B, RPS6KA3, AKT) after DDL-449 treatment (**Fig. 4E**). A global proteomics analysis also revealed significant changes in the abundance of numerous proteins 24 hours after DDL-449 treatment, relative to 0.05% DMSO treated controls (**Fig. 4F**). A transcription factor enrichment analysis using this data identified activation of several SSPN-associated transcription factors (ZFX, RUNX2, CREB1) (**Fig. 4G**). A gene set enrichment analysis using the differentially phosphorylated proteins, altered kinases, SSPN associated transcription factors and affinity purified molecular targets, identified DDL-449 mediated signaling pathways (**Fig. 4H**). Integrating findings from the DDL-489 affinity purification and the DDL-449 global and

phosphoproteomics analyses led to a hypothesis that DDL-449 increases SSPN expression through an PP2A-mediated mechanism (**Fig. 3I**). Specifically, DDL-449 may direct inhibit the activity of PP2A, and subsequently promote activation of AKT and RSK2, which then enhances activation of SSPN-associated transcription factors, such as CREB1.

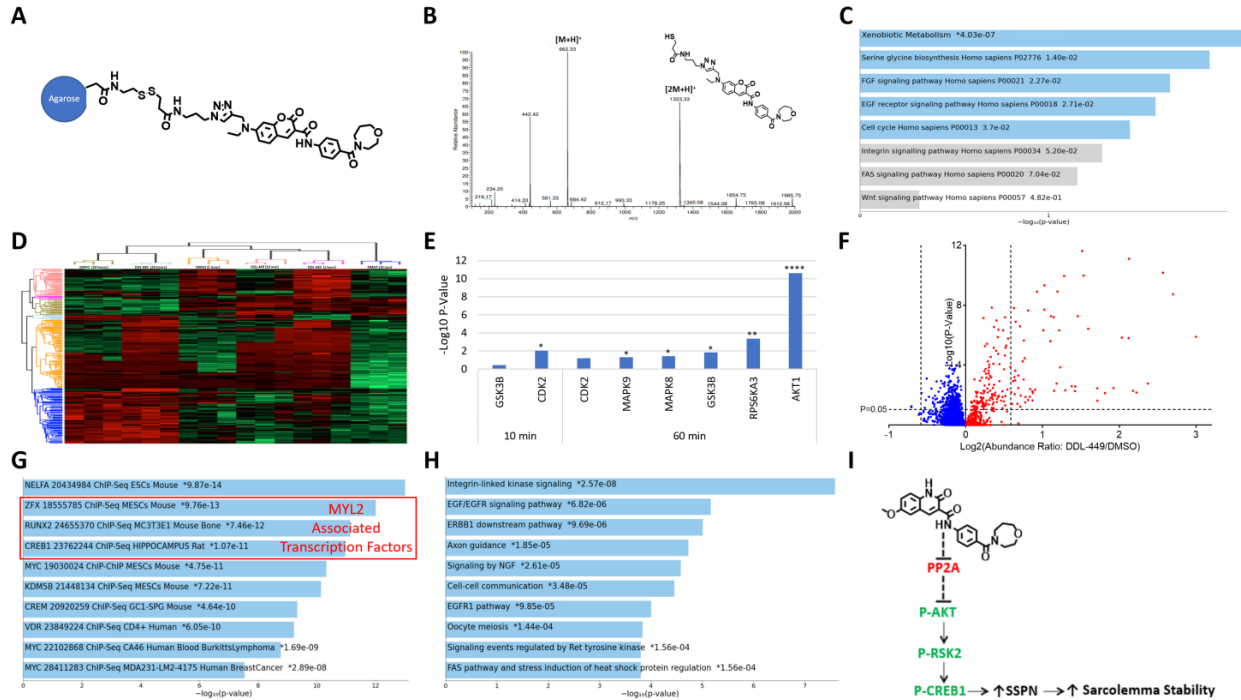


Figure 4. Identification of direct and indirect molecular targets of OT-9 analogs. (a) A small molecule-based affinity probe for enriching direct molecular targets of DDL-489. (B) A structure and mass spectrum for the small molecule released from the affinity probe with a reducing agent. (C) Levels of significance (p-value) for biological processes and cellular pathways in the Molecular Signatures Database (MSigDB) and Panther pathway database, using proteins identified in the AMBMP-14 affinity purification. (D) The relative abundance of phosphorylated peptides in MDX cells, following treatment with DDL-449 at a concentration of 5 μ M for 10 or 60 minutes. (E) Levels of significance (p-value) for kinases in the Kinase Enrichment Analysis 2 and 3 (KEA2,

KEA3) databases, activated 10 and 60 minutes after DDL-449 treatment. (F) Differences in the abundances of proteins, illustrated via volcano plot, in MDX cells 24-hours after DDL-449 treatment. The $-\log_{10}$ (p-value) is plotted against \log_{10} (abundance ratio: DDL-449/Vehicle). (G) Levels of significance (p-value) for transcription factors in the ChIP Enrichment Analysis (ChEA) 2022 database, activated 24 hours after DDL-449 treatment. (H) Levels of significance (p-value) for cellular pathways in the National Center for Advancing Translational Sciences (NCATS) BioPlanet pathway database, using differentially phosphorylated proteins, altered kinases, SSPN associated transcription factors and affinity purified molecular targets. (I) A hypothesized mechanism of action through which OT-9 and biological active analogs increase SSPN expression.

DISCUSSION

To the best of our knowledge, this study represents the first description of a medicinal chemistry effort to develop potent and bioavailable SSPN enhancers for the treatment of DMD. This hit-to-lead optimization was performed by systematically altering chemical subgroups in various regions of the OT-9, a SSPN enhancing compound previously identified in a HTS. The biological activity of each analog was assessed and utilized to conduct a structure-activity-relationship analysis that guided further drug design. While most alterations to the OT-9 scaffold resulted in decreased potency, this approach enabled the identification of structural elements required for and contributing to biological activity, ultimately leading to the design and synthesis of several compounds capable of increasing SSPN by 1.5-fold or greater *in-vitro*. After repeated testing, the coumarin-containing analog, DDL449, and the quinolone-containing analog, DDL472, were chosen as the most promising drug candidates moving forward. Interestingly, subsequent dose response analyses identified DDL-449 and DDL-472 to be significantly more potent SSPN

enhancers in disease-relevant myotubes when compared to wild-type cells. This could suggest that the mechanism through which these compounds increase SSPN expression is associated with molecular pathways dysregulated during DMD pathogenesis, and that treatment with these novel SSPN enhancers reverses this perturbation.

To determine which of these compounds was more likely to be a successful therapeutic for treating muscular disorders *in-vivo*, various *in-vitro* assays were employed to evaluate physicochemical properties influencing drug ADME. While a compound may exhibit good *in-vitro* drug activity, it does not automatically guarantee favorable *in-vivo* activity unless it also possesses good bioavailability and half-life (Ref. 22). Moreover, the escalating costs associated with the development of novel therapeutics and the high rate of candidate attrition have prompted a shift in drug discovery strategies towards the simultaneous evaluation of comprehensive drug physicochemical properties alongside efficacy (Ref. 23). Notably, DDL-449 exhibited considerably lower muscle tissue binding and greater metabolic stability in liver microsomes compared to DDL-472. Unfortunately, both compounds exhibited poor kinetic solubility and high plasma binding, which would be expected to restrict bioavailability. While this is not ideal, these experiments demonstrate the value of *in-vitro* ADME characterization for facilitating drug development, as this information highlights important areas of focus when designing future OT-9 analogs. However, it is important to note that additional medicinal chemistry efforts to improve these physicochemical properties may be hindered by the limited capacity with which the OT-9 scaffold can be altered without diminishing biological activity.

Proof-of-concept pharmacokinetic and pharmacodynamic analyses were subsequently conducted to determine if DDL-449 or DDL-472 could reach therapeutically relevant concentrations in the muscle and effectively increase SSPN levels. Interestingly, DDL-472 was determined to be significantly more bioavailable than DDL-449, reaching a concentration of approximately 4 μ M two hours after oral administration at a dose of 60 mg/kg. This dramatic difference in bioavailability can likely be attributed to the increased muscle tissue binding capacity of DDL-472. However, it is important to note that when DDL-472 muscle tissue binding (77.2%) is taken into account, the concentration of unbound drug that is free to interact with the pharmacological target is closer to 1 μ M. Encouragingly, this is still double the concentration shown to increase SSPN 50% *in-vitro* in H2K mdx myotubes. Based on these data, the dose could be lowered to 30 mg/kg and one would still expect to see significant increases in SSPN levels *in-vivo*. This highlights the utility of integrating *in-vitro* biological activity testing, ADME property analyses and *in-vivo* pharmacokinetics for establishing proper dosing to ensure drug efficacy *in-vivo*. As expected, both compounds were subsequently shown to induce significant increases in SSPN gene and protein expression in the muscles of MDX mice after only a few weeks of treatment. While our ultimate goal is to always to identify even more potent and bioavailable SSPN enhancers, this discovery certainly warrants further evaluation of these compounds as novel therapeutics for treating DMD.

Determining the molecular mechanism through which a drug exerts its physiological effect is a central aspect of the drug discovery process, frequently utilized to develop more effective therapeutics. Knowledge of direct drug targets often facilitates the design of novel small molecules that are more potent and selective (Ref. 24). Meanwhile, understanding of indirect drug targets can

pinpoint downstream effectors suitable for alternative therapeutic strategies (Ref. 25). Therefore, an incomplete understanding of a drug's MOA can serve as a bottleneck, hindering the success rate during preclinical development. The synthesis of a biologically active alkyne-containing analog, DDL-489, capable of being linked to azide agarose beads, enabled the use of small molecule affinity chromatography to enrich for direct targets of DDL-489. Interestingly, this affinity purification followed by mass spectrometry-based proteomics identified numerous proteins associated with xenobiotic metabolism, which could be interpreted as a validation of the experimental approach. While we were encouraged by these findings, this enrichment of drug metabolizing enzymes may also indicate that DDL-489 and associated analogs are more prone to rapid biotransformation and clearance within muscle cells. Notably, there was also enrichment of several proteins associated with regulating DMD-relevant signaling pathways. This included a regulatory subunit of protein phosphatase 2A (PP2A), a direct inhibitor of protein kinase B (PKB or AKT) (Ref. 26). Interestingly, activation of AKT signaling, in some cases achieved specifically through the inhibition of AKT-targeting phosphatases, has been consistently described as a promising therapeutic approach for treating DMD (Ref. 27-30). Similarly to the activation of AKT signaling, inhibitors of PP2A are known to increase the expression of utrophin-glycoprotein complex proteins important for maintaining sarcolemma stability in muscular dystrophy (Ref. 30-31). Several other proteins known to indirectly modulate AKT activity, such as phosphatidylethanolamine-binding protein-1 (PEBP1), and ILK signaling pathway components, α -parvin (PARVA) and integrin α -2 (ITGA2), were also identified (Ref. 32-35).

Given that cell signaling via protein post-translational modifications (PTMs), such as phosphorylation, mediates the biological outcomes of many therapeutics, global and

phosphoproteomics were utilized to identify indirect molecular targets of DDL-449 that may serve as essential downstream effectors for enhancing SSPN expression (Ref. 36). Residue-specific changes in protein phosphorylation status following DDL-449 treatment suggested significant activation of ribosomal protein S6 kinase A3 (RPS6KA3 or RSK2). This analysis also indicated increases in CDK2, GSK3 β , MAPK8, and MAPK9 activity. However, due to the high degree of overlapping substrates between these proteins, it is nearly impossible to determine if only one or all kinases are activated in response to DDL-449 treatment. Interestingly, when a kinase enrichment analysis was performed at the gene level using an alternative platform, AKT1 was the most significantly enriched kinase, interacting with 48 of the 89 protein substrates. It is important to note that bioinformatics tools used to predict kinase activity associated with either sets of genes or specific phosphorylation sites are both commonly used, and each has advantages and disadvantages. While site-specific analyses are widely accepted as more reliable, they are limited by the availability of extensively annotated phosphoproteome databases. That being said, the majority of the identified phosphorylation sites cannot be mapped back to a specific kinase, especially in non-human datasets, and, therefore, go unused. Conversely, kinase enrichment analyses at the gene level permit the use of most, if not all phosphoproteomics data, but is prone to a higher rate of false positives. Needless to say, all indications of kinase activity derived from proteomics data using inference-based platforms necessitate validation using a secondary approach.

Finally, a transcription factor enrichment analysis using upregulated proteins from the global proteomics analysis was utilized to predict activated transcription factors. Encouragingly, this included several SSPN-associated transcription factors, including cAMP-responsive element-

binding protein 1 (CREB1), which has been shown to stimulate skeletal muscle regeneration (Ref. 37). Interestingly, CREB1 is also known to be directly activated by RSK2, which itself is downstream of AKT signaling (Ref. 38-39). Integration of these findings suggests that DDL-449 may increase SSPN expression through direct inhibition of PP2A and subsequent activation of the AKT-RSK2-CREB1 signaling axis. While this hypothesis necessitates validation, this information may prove invaluable for identifying novel therapeutic approaches for treating DMD. For instance, testing and analoging of alternative PP2A inhibitors, such as those currently being investigated as treatments for cancer, could ultimately lead to the development of more potent and bioavailable SSPN enhancers (Ref. 40).

In conclusion, the results here describe a research endeavor to develop potent and bioavailable analogs of OT-9, and to uncover the pharmacological mechanism through which these compounds increase SSPN expression. The methodology involved an iterative medicinal chemistry approach employing structure-activity relationship analyses to guide the design of thirty-four NCEs to date. Additionally, *in-vitro* ADME assays were used to assess the drug-like properties of lead candidates, DDL-449 and DDL-472, highlighting areas for improvement when designing future OT-9 analogs. Encouragingly, both compounds significantly increased SSPN expression *in-vivo* following oral administration. Furthermore, small molecule therapeutic-based affinity chromatography and mass spectrometry-based global and phosphoproteomics revealed both direct and indirect molecular targets of OT-9 analogs, suggesting a potential mechanism of drug action resembling previously described pharmacological approaches to treating DMD through inhibition of AKT-targeting phosphatases. While the exact pharmacological mechanism still requires validation, further investigation of this mechanism promises to aid in the development of more

efficacious SSPN enhancers that may one day be used to enhance sarcolemma repair mechanisms in DMD patients.

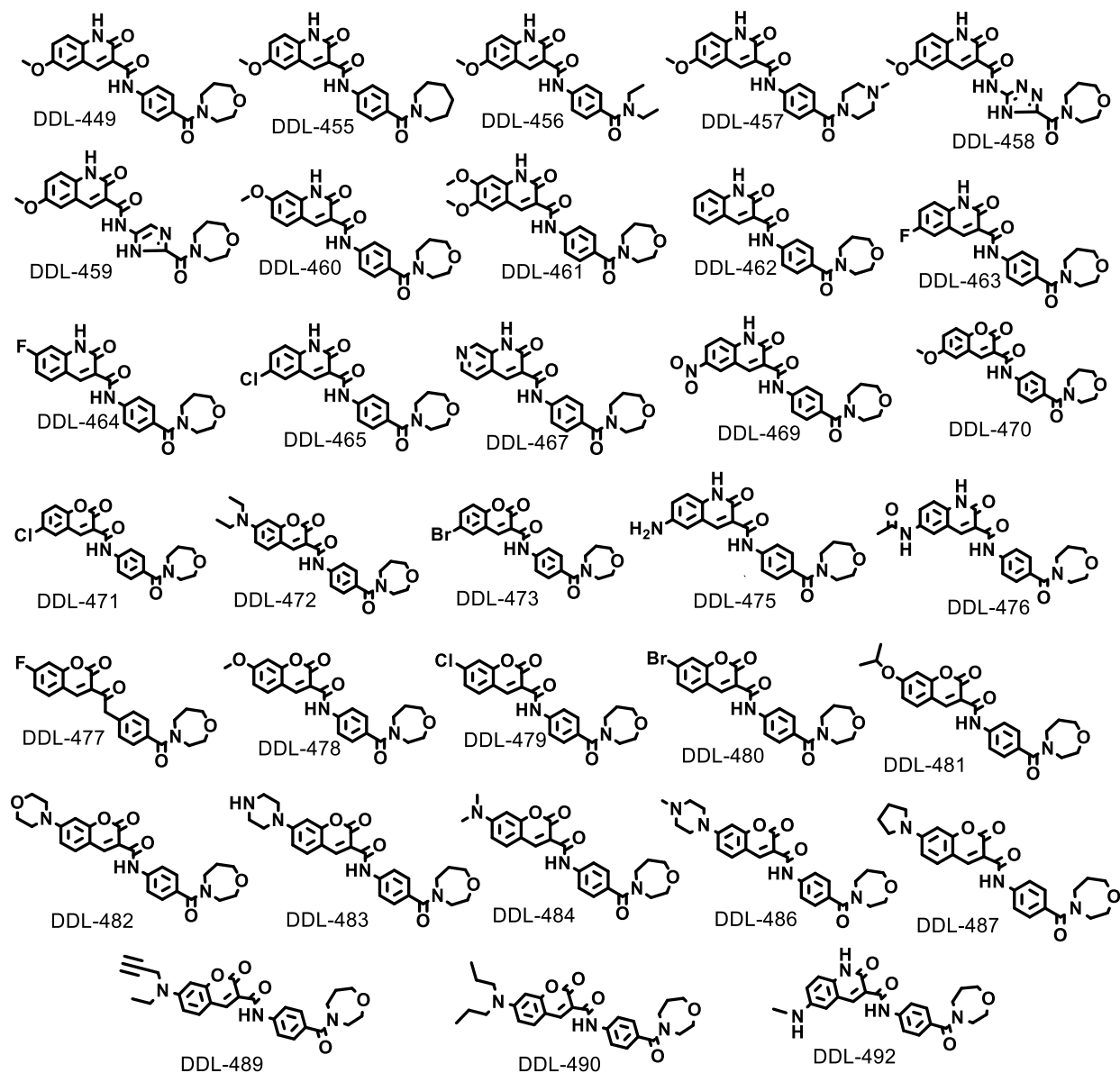
AUTHOR CONTRIBUTIONS

WC, VJ, RC, JW, JC, BJ, EM, RM, HM, DW participated in research design. WC, RM, EM conducted experiments. WC, DW synthesized compounds. WC, RM, EM, HM performed data analysis. WC wrote the manuscript. VJ, RC, JC edited the manuscript.

ACKNOWLEDGEMENTS

Support from lab members of the Crosbie and John labs and the sponsored research collaboration.

SUPPLEMENTARY FIGURES



Supplementary Figure S1. Chemical structures of all new chemical entities synthesized.

SUPPLEMENTARY ANALYTICAL INFORMATION

DDL-449:

$^1\text{H NMR}$ (400 MHz, DMSO- d_6) δ 12.57 (s, 1H), 12.40 (s, 1H), 8.92 (s, 1H) 7.76-7.32 (m, 7H), 3.79 (s, 3H), 3.65-3.44 (m, 8H), 1.84-1.71 (m, 2H). LC-MS m/z $[\text{M}+\text{H}]^+$ 422.25.

DDL-460:

^1H NMR (400 MHz, DMSO) δ 12.47 (s, 1H), 12.21 (s, 1H), 8.86 (s, 1H), 7.90 (s, 1H), 7.88 (s, 1H), 7.74 (s, 1H), 7.72 (s, 1H), 7.38 (d, $J = 8.6$ Hz, 2H), 6.90 (d, $J = 4.6$ Hz, 1H), 3.83 (s, 3H), 3.65 (s, 4H), 3.57 (s, 2H), 3.44 (s, 2H), 1.84 (s, 1H), 1.71 (s, 1H). LC-MS m/z $[\text{M}+\text{H}]^+$ 422.33.

DDL-461

^1H NMR (400 MHz, DMSO) δ 12.47 (s, 1H), 12.38 (s, 1H), 8.85 (s, 1H), 7.73 (d, $J = 8.3$ Hz, 2H), 7.50 (s, 1H), 7.38 (d, $J = 8.6$ Hz, 2H), 6.95 (s, 1H), 3.85 (s, 3H), 3.79 (s, 3H), 3.61 (d, $J = 29.9$ Hz, 6H), 3.45 (s, 2H), 1.84 (s, 1H), 1.71 (s, 1H). LC-MS m/z $[\text{M}+\text{H}]^+$ 452.25.

DDL-462

^1H -NMR (400 MHz, DMSO- d_6) δ 12.64 (s, 1H), 12.25 (s, 1H), 8.96 (s, 1H), 7.98 (d, $J = 9.3$ Hz, 1H), 7.75 (d, $J = 8.3$ Hz, 2H), 7.72 – 7.63 (m, 1H), 7.45 (d, $J = 8.3$ Hz, 1H), 7.39 (d, $J = 8.6$ Hz, 2H), 7.30 (t, $J = 7.0$ Hz, 1H), 3.58 (s, 1H), 3.44 (s, 2H), 3.28 (s, 3H), 2.50 (s, 3H), 1.71 (s, 1H). ; LC-MS m/z $[\text{M}+\text{H}]^+$ 392.17.

DDL-463

^1H NMR (400 MHz, DMSO- d_6) 12.73 (1 H, s), 12.24 (1 H, s), 8.96 (1 H, s), 7.89 (1 H, d, J 9.0), 7.75 (2 H, d, J 8.3), 7.59 (1 H, td, J 8.9, 2.9), 7.47 (1 H, dd, J 9.1, 4.8), 7.39 (2 H, d, J 6.7), 3.51 (4 H, d, J 53.5), 3.28 (4 H, s), 1.84 (1 H, s), 1.71 (1 H, s) ; LC-MS m/z $[\text{M}+\text{H}]^+$ 410.25.

DDL-464

¹H NMR (400 MHz, DMSO-*d*₆) δ 12.70 (s, 1H), 12.09 (s, 1H), 8.97 (s, 1H), 8.09 (dd, *J* = 8.8, 6.1 Hz, 1H), 7.75 (d, *J* = 8.3 Hz, 2H), 7.43 – 7.35 (m, 2H), 7.25 – 7.12 (m, 2H), 3.57 (s, 2H), 3.44 (s, 4H), 3.29 (s, 2H), 1.84 (s, 1H), 1.71 (s, 1H). ; LC-MS *m/z* [M+H]⁺ 410.17.

DDL-465

¹H NMR (400 MHz, DMSO) δ 12.75 (s, 1H), 12.18 (s, 1H), 8.93 (s, 1H), 8.13 (d, *J* = 4 Hz, 1H), 7.75 (d, *J* = 8.0 Hz, 1H), 7.71 (d, *J* = 4.0 Hz, 1H), 7.69 (d, *J* = 4 Hz, 1H), 7.44 (d, *J* = 8.0 Hz, 1H), 7.40 (s, 1H), 7.38 (s, 1H), 1.71-3.65 (m, 10H). LC-MS *m/z* [M+H]⁺ 426.17.

DDL-467

¹H NMR (400 MHz, DMSO) δ 12.08 (s, 1H), 8.94 (s, 1H), 8.80 (s, 1H), 8.425 (d, *J* = 4 Hz, 1H), 7.90 (dd, *J* = 8 Hz, 1H), 7.75 (d, *J* = 8 Hz, 2H), 7.40 (d, *J* = 12 Hz, 2H), 3.44-3.70 (m, 8H), 1.84 (s, 1H), 1.71 (s, 1H). LC-MS *m/z* [M+H]⁺ 393.17.

DDL-469

¹H NMR (400 MHz, DMSO) δ 13.07 (s, 1H), 11.91 (s, 1H), 9.13 (s, 1H), 9.02 (s, 1H), 8.445 (d, *J* = 4 Hz, 1H), 8.42 (d, 1H), 7.76 (d, *J* = 8.0 Hz, 2H), 7.56 (d, *J* = 8.0 Hz, 1H), 7.40 (d, *J* = 8.0 Hz, 1H), 1.71-3.65 (m, 10H). LC-MS *m/z* [M+H]⁺ 437.17.

DDL-475

¹H NMR (400 MHz, *d*₆-DMSO) δ 12.55 (s, 1H), 8.69 (s, 1H), 7.75-6.48 (m, 8H), 5.40 (s, 1H), 5.23 (s, 1H), 3.64-3.45 (m, 8H), 2.03-1.80 (m, 2H). LC-MS *m/z* [M+H]⁺ 407.25.

DDL-476

^1H NMR (400 MHz, $\text{d}_6\text{-DMSO}$) δ 12.35 (s, 1H), 10.14 (s, 1H), 8.84 (s, 1H), 8.14-7.37 (m, 7H), 4.05 (s, 1H), 3.65-3.44 (m, 8H), 2.04 (s, 3H), 1.83-1.71 (m, 2H). LC-MS m/z $[\text{M}+\text{H}]^+$ 449.25.

DDL-492

^1H NMR (400 MHz, CDCl_3) δ 12.51 (s, 1H), 8.70 (s, 1H), 7.77-7.00 (m, 8H), 3.70 (s, 3H), 3.65-3.45 (m, 8H), 1.84-1.71 (m, 2H). LC-MS m/z $[\text{M}+\text{H}]^+$ 421.25

DDI-470

^1H NMR (400 MHz, DMSO) δ 10.78 (s, 1H), 8.85 (s, 1H), 7.75 (d, $J = 8\text{Hz}$, 2H), 7.555 (d, $J = 4.0\text{ Hz}$, 1H), 7.47 (d, $J = 8\text{ Hz}$, 1H), 7.39 (d, $J = 8\text{ Hz}$, 1H), 7.35 (d, 1H), 7.325 (d, $J = 4.0\text{ Hz}$, 1H), 3.80 (s, 3H), 3.70 (s, 1H), 3.65 (s, 4H), 3.57 (s, 1H), 3.43 (s, 2H), 1.84 (s, 1H), 1.70 (s, 1H). LC-MS m/z $[\text{M}+\text{H}]^+$ 423.17.

DDL-471

^1H NMR (400 MHz, DMSO) δ 10.69 (s, 1H), 8.82 (s, 1H), 8.12 (d, $J = 4\text{ Hz}$, 1H), 7.79 (d, 1H), 7.765 (d, $J = 4\text{ Hz}$, 1H), 7.75, (s, 1H), 7.74 (d, $J = 8\text{ Hz}$, 1H), 7.57 (d, $J = 8\text{ Hz}$, 1H), 7.39 (d, $J = 8\text{ Hz}$, 1H), 3.70 (s, 2H), 3.65 (s, 3H), 3.57 (s, 1H), 3.43 (s, 2H), 1.84 (s, 1H), 1.70 (s, 1H). LC-MS m/z $[\text{M}+\text{H}]^+$ 427.25.

DDL-472

^1H NMR (400 MHz, DMSO) δ 10.81 (s, 1H), 8.74 (s, $J = 0.6\text{ Hz}$, 1H), 7.73 (d, $J = 8\text{ Hz}$, 2H), 7.36 (d, $J = 8\text{ Hz}$, 2H), 6.83 (d, $J = 4\text{ Hz}$, 1H), 6.80 (d, $J = 4\text{ Hz}$, 1H), 6.64 (d, 1H), 3.65 (m, 8H), 3.47

(q, $J = 8.0$ Hz, 4H), 1.83 (s, 1H), 1.70 (s, 1H), 1.11 (t, $J = 6.0$ Hz, 6H). LC-MS m/z $[M+H]^+$ 464.43.

DDL-473

^1H NMR (400 MHz, DMSO) δ 10.69 (s, 1H), 8.81 (s, 1H), 8.24 (d, $J = 2.4$ Hz, 1H), 7.89 (dd, $J = 8.8, 2.4$ Hz, 1H), 7.74 (d, $J = 8.2$ Hz, 2H), 7.50 (d, $J = 8.9$ Hz, 1H), 7.39 (d, $J = 8.6$ Hz, 2H), 3.69 (s, 2H), 3.65 (s, 3H), 3.57 (s, 1H), 3.43 (s, 2H), 1.84 (s, 1H), 1.70 (s, 1H).

DDL-477

^1H NMR (400 MHz, DMSO) δ 8.97 (s, 1H), 8.09 (d, $J = 4$ Hz, 1H), 7.75 (d, $J = 12.0$ Hz, 2H), 7.39 (d, $J = 8.0$ Hz, 2H), 7.25 – 7.10 (m, 2H), 1.71-3.65 (m, 10H). LC-MS m/z $[M+H]^+$ 411.17.

DDL-478

^1H NMR (400 MHz, CDCl_3) δ 10.92 (s, 1H), 8.94 (s, 1H), 7.78 (d, $J = 8.0$ Hz, 2H), 7.63 (d, $J = 8.0$ Hz, 1H), 7.43 (d, $J = 8.0$ Hz, 2H), 6.97 (dd, $J = 8.7, 2.4$ Hz, 1H), 6.90 (d, 1H), 3.93 (s, 3H), 3.89 – 3.43 (m, 8H), 2.11 – 1.24 (m, 2H) LC-MS m/z $[M+H]^+$ 423.17.

DDL-479

^1H NMR (400 MHz, CDCl_3) δ 10.84 (s, 1H), 8.98 (s, 1H), 7.78-7.40 (m, 7H), 3.85-3.56 (m, 8H), 2.05-1.85 (m, 2H). LC-MS m/z $[M+H]^+$ 427.17.

DDL-480

^1H NMR (400 MHz, CDCl_3) δ 10.84 (s, 1H), 8.97 (s, 1H), 7.79-7.43 (m, 7H), 3.85-3.56 (m, 8H), 2.05 (m, 2H). LC-MS m/z $[\text{M}+2\text{H}]^+$ 473.42.

DDL-481

^1H NMR (400 MHz, CDCl_3) δ 10.93 (s, 1H), 8.92 (d, 1H), 7.78 (d, $J = 8$ Hz, 2H), 7.61 (d, $J = 8$ Hz, 1H), 7.43 (d, $J = 8$ Hz, 2H), 6.92 (dd, $J = 8.7, 2.4$ Hz, 1H), 6.87 (d, $J = 2$ Hz, 1H), 4.67 (hept, $J = 12$ Hz, 1H), 3.97 – 2.05 (m, 10H), 1.41 (d, $J = 8$ Hz, 6H). LC-MS m/z $[\text{M}+\text{H}]^+$ 451.25.

DDL-482

^1H NMR (400 MHz, d_6 -DMSO) δ 10.78 (s, 1H), 8.79 (s, 1H), 7.79-6.93 (m, 7H), 3.70-3.69 (m, 4H), 3.69-3.57 (m, 6H) 3.44-3.43 (m, 4H), 3.41-3.35 (m, 2H) 1.83-1.70 (m, 2H). LC-MS m/z $[\text{M}+\text{H}]^+$ 478.58.

DDL-483

^1H NMR (400 MHz, DMSO) δ 10.76 (s, 1H), 8.81 (s, 1H), 7.84-7.03 (m, 7H), 3.69-3.64 (m, 8H), 3.57-3.43 (m, 4H), 1.83-1.70 (m, 2H), 1.49-1.19 (m, 4H).

DDL-484

^1H NMR (400 MHz, CDCl_3) δ 11.00 (s, 1H), 8.80 (s, 1H), 7.79-6.53 (m, 7H), 3.83-3.57 (m, 8H) 3.14 (s, 6H), 2.05-1.85 (m, 2H). LC-MS m/z $[\text{M}+\text{H}]^+$ 436.75.

DDL-486

^1H NMR (400 MHz, CDCl_3) δ 10.97 (s, 1H), 8.82 (s, 1H), 7.79-6.72 (m, 7H), 3.83-3.57 (m, 8H), 3.48 (t, $J=4\text{Hz}$, 4H), 2.56 (t, $J=4\text{Hz}$, 4H), 2.36 (s, 3H), 2.05-1.85 (m, 2H). LC-MS m/z $[\text{M}+\text{H}]^+$ 491.58.

DDL-487

^1H NMR (400 MHz, CDCl_3) δ 11.00 (s, 1H), 8.79 (s, 1H), 7.79-6.41 (m, 7H), 3.83-3.57 (m, 8H), 3.43 (t, $J=4\text{Hz}$, 4H), 2.09 (t, $J=4\text{Hz}$, 4H), 2.05-1.85 (m, 2H). LC-MS m/z $[\text{M}+\text{H}]^+$ 462.83.

DDL-489

^1H NMR (400 MHz, CDCl_3) δ 10.99 (s, 1H), 8.84 (s, 1H), 7.80-6.70 (m, 7H), 4.14 (s, 2H), 3.84-3.66 (m, 8H), 3.6 (q, $J=8\text{Hz}$, 2H), 2.30 (s, 1H), 2.05-1.85 (m, 2H), 1.31 (t, $J=6\text{Hz}$, 3H), LC-MS m/z $[\text{M}+\text{H}]^+$ 474.25.

DDL-490

^1H NMR (400 MHz, CDCl_3) δ 11.00 (s, 1H), 8.79 (s, 1H), 7.80-6.52 (m, 7H), 3.82-3.57 (m, 8H), 3.36 (t, $J=8\text{Hz}$, 4H), 1.85-1.71 (m, 2H), 1.37 (t, $J=8\text{Hz}$, 4H), 0.98 (t, $J=8\text{Hz}$, 6H). LC-MS m/z $[\text{M}+\text{H}]^+$ 492.00.

REFERENCES

1. Ryder S, Leadley RM, Armstrong N, Westwood M, de Kock S, Butt T, et al. The burden, epidemiology, costs and treatment for Duchenne muscular dystrophy: an evidence review. *Orphanet J Rare Dis.* 2017;12(1):79.
2. Wahlgren L, Kroksmark AK, Tulinius M, Sofou K. One in five patients with Duchenne muscular dystrophy dies from other causes than cardiac or respiratory failure. *Eur J Epidemiol.* 2022;37(2):147-156.
3. Schnell F, Donoghue C, Dworzak J, Charleston J, Frank D, Wilton S, et al. Development of a validated Western blot method for quantification of human dystrophin protein used in Phase II and III clinical trials of eteplirsen for the treatment of Duchenne muscular dystrophy (DMD) (P5.105). *Neurology.* 2017;88(16 Supplement):P5.105.
4. Moxley RT, Pandya S, Ciafaloni E, Fox DJ, Campbell K. Change in natural history of Duchenne muscular dystrophy with long-term corticosteroid treatment: implications for management. *J Child Neurol.* 2010;25(9):1116–1129.
5. Hoffman EP, Brown RH, Kunkel LM. Dystrophin: the protein product of the Duchenne muscular dystrophy locus. *Cell.* 1987;51(6):919–928.
6. Campbell KP, Kahl SD. Association of dystrophin and an integral membrane glycoprotein. *Nature.* 1989;338(6212):259–262.
7. Bonilla E, Samitt CE, Miranda AF, Hays AP, Salviati G, DiMauro S, et al. Duchenne muscular dystrophy: deficiency of dystrophin at the muscle cell surface. *Cell.* 1988;54(4):447–452.
8. Peter AK, Marshall JL, Crosbie RH. Sarcospan reduces dystrophic pathology: stabilization of the utrophin-glycoprotein complex. *J Cell Biol.* 2008;183(3):419–427.

9. Marshall JL, Oh J, Chou E, Lee JA, Holmberg J, Burkin DJ, et al. Sarcospan integration into laminin-binding adhesion complexes that ameliorate muscular dystrophy requires utrophin and $\alpha 7$ integrin. *Hum Mol Genet.* 2015;24(7):2011–2022.
10. Gibbs EM, Marshall JL, Ma E, Nguyen TM, Hong G, Lam JS, et al. High levels of sarcospan are well tolerated and act as a sarcolemmal stabilizer to address skeletal muscle and pulmonary dysfunction in DMD. *Hum Mol Genet.* 2016;25(24):5395–5406.
11. Shu, C., Mokhonova, E., & Crosbie, R. H. (2023). High-Throughput Screening to Identify Modulators of Sarcospan. *Methods in molecular biology (Clifton, N.J.)*, 2587, 479–493.
12. Shu C, Parfenova L, Mokhonova E, et al. High-throughput screening identifies modulators of sarcospan that stabilize muscle cells and exhibit activity in the mouse model of Duchenne muscular dystrophy. *Skelet Muscle.* 2020;10(1):26.
13. Rappsilber, J., Mann, M., & Ishihama, Y. (2007). Protocol for micro-purification, enrichment, pre-fractionation and storage of peptides for proteomics using StageTips. *Nature protocols*, 2(8), 1896–1906.
14. Orsburn B. C. (2021). Proteome Discoverer-A Community Enhanced Data Processing Suite for Protein Informatics. *Proteomes*, 9(1), 15.
15. Xie, Z., Bailey, A., Kuleshov, M. V., Clarke, D. J. B., Evangelista, J. E., Jenkins, S. L., Lachmann, A., Wojciechowicz, M. L., Kropiwnicki, E., Jagodnik, K. M., Jeon, M., & Ma'ayan, A. (2021). Gene Set Knowledge Discovery with Enrichr. *Current protocols*, 1(3), e90.
16. Liberzon, A., Birger, C., Thorvaldsdóttir, H., Ghandi, M., Mesirov, J. P., & Tamayo, P. (2015). The Molecular Signatures Database (MSigDB) hallmark gene set collection. *Cell systems*, 1(6), 417–425.

17. Mi, H., & Thomas, P. (2009). PANTHER pathway: an ontology-based pathway database coupled with data analysis tools. *Methods in molecular biology (Clifton, N.J.)*, 563, 123–140.
18. Huang, R., Grishagin, I., Wang, Y., Zhao, T., Greene, J., Obenauer, J. C., Ngan, D., Nguyen, D. T., Guha, R., Jadhav, A., Southall, N., Simeonov, A., & Austin, C. P. (2019). The NCATS BioPlanet - An Integrated Platform for Exploring the Universe of Cellular Signaling Pathways for Toxicology, Systems Biology, and Chemical Genomics. *Frontiers in pharmacology*, 10, 445.
19. Lachmann, A., & Ma'ayan, A. (2009). KEA: kinase enrichment analysis. *Bioinformatics (Oxford, England)*, 25(5), 684–686.
20. Lachmann, A., Xu, H., Krishnan, J., Berger, S. I., Mazloom, A. R., & Ma'ayan, A. (2010). ChEA: transcription factor regulation inferred from integrating genome-wide ChIP-X experiments. *Bioinformatics (Oxford, England)*, 26(19), 2438–2444.
21. Szklarczyk D, Morris JH, Cook H, Kuhn M, Wyder S, Simonovic M, Santos A, Doncheva NT, Roth A, Bork P, Jensen LJ and von Mering C. The STRING database in 2017: quality-controlled protein-protein association networks, made broadly accessible. *Nucleic Acids Res.* 2017;45:D362-D368.
22. Lipinski C. A. (2000). Drug-like properties and the causes of poor solubility and poor permeability. *Journal of pharmacological and toxicological methods*, 44(1), 235–249.
23. Lin, J. H., & Lu, A. Y. (1997). Role of pharmacokinetics and metabolism in drug discovery and development. *Pharmacological reviews*, 49(4), 403–449.

24. Schenone, M., Dančík, V., Wagner, B. K., & Clemons, P. A. (2013). Target identification and mechanism of action in chemical biology and drug discovery. *Nature chemical biology*, 9(4), 232–240.
25. Douglass, E. F., Jr, Allaway, R. J., Szalai, B., Wang, W., Tian, T., Fernández-Torras, A., Realubit, R., Karan, C., Zheng, S., Pessia, A., Tanoli, Z., Jafari, M., Wan, F., Li, S., Xiong, Y., Duran-Frigola, M., Bertoni, M., Badia-I-Mompel, P., Mateo, L., Guitart-Pla, O., ... Califano, A. (2022). A community challenge for a pancancer drug mechanism of action inference from perturbational profile data. *Cell reports. Medicine*, 3(1), 100492.
26. Wlodarchak, N., & Xing, Y. (2016). PP2A as a master regulator of the cell cycle. *Critical reviews in biochemistry and molecular biology*, 51(3), 162–184.
27. Boppart, M. D., Burkin, D. J., & Kaufman, S. J. (2011). Activation of AKT signaling promotes cell growth and survival in $\alpha7\beta1$ integrin-mediated alleviation of muscular dystrophy. *Biochimica et biophysica acta*, 1812(4), 439–446.
28. Gurpur, P. B., Liu, J., Burkin, D. J., & Kaufman, S. J. (2009). Valproic acid activates the PI3K/Akt/mTOR pathway in muscle and ameliorates pathology in a mouse model of Duchenne muscular dystrophy. *The American journal of pathology*, 174(3), 999–1008.
29. Parveen, A., Wen, Y., Roy, A., & Kumar, A. (2021). Therapeutic Targeting of PTEN in Duchenne Muscular Dystrophy. *Molecular therapy : the journal of the American Society of Gene Therapy*, 29(1), 8–9.
30. Peter, A. K., Ko, C. Y., Kim, M. H., Hsu, N., Ouchi, N., Rhie, S., Izumiya, Y., Zeng, L., Walsh, K., & Crosbie, R. H. (2009). Myogenic Akt signaling upregulates the utrophin-glycoprotein complex and promotes sarcolemma stability in muscular dystrophy. *Human molecular genetics*, 18(2), 318–327.

31. Rodova, M., Brownback, K., & Werle, M. J. (2004). Okadaic acid augments utrophin in myogenic cells. *Neuroscience letters*, *363*(2), 163–167.
32. Zaravinos, A., Bonavida, B., Chatzaki, E., & Baritaki, S. (2018). RKIP: A Key Regulator in Tumor Metastasis Initiation and Resistance to Apoptosis: Therapeutic Targeting and Impact. *Cancers*, *10*(9), 287.
33. Huang, A. H., Pan, S. H., Chang, W. H., Hong, Q. S., Chen, J. J., & Yu, S. L. (2015). PARVA promotes metastasis by modulating ILK signalling pathway in lung adenocarcinoma. *PloS one*, *10*(3), e0118530.
34. Liu, F., Tong, D., Li, H., Liu, M., Li, J., Wang, Z., & Cheng, X. (2016). Bufalin enhances antitumor effect of paclitaxel on cervical tumorigenesis via inhibiting the integrin $\alpha 2/\beta 5$ /FAK signaling pathway. *Oncotarget*, *7*(8), 8896–8907.
35. Li, G., Li, Y. Y., Sun, J. E., Lin, W. H., & Zhou, R. X. (2016). ILK-PI3K/AKT pathway participates in cutaneous wound contraction by regulating fibroblast migration and differentiation to myofibroblast. *Laboratory investigation; a journal of technical methods and pathology*, *96*(7), 741–751.
36. Needham, E. J., Parker, B. L., Burykin, T., James, D. E., & Humphrey, S. J. (2019). Illuminating the dark phosphoproteome. *Science signaling*, *12*(565), eaau8645.
37. Stewart, R., Flechner, L., Montminy, M., & Berdeaux, R. (2011). CREB is activated by muscle injury and promotes muscle regeneration. *PloS one*, *6*(9), e24714.
38. Liu, R. Y., Zhang, Y., Smolen, P., Cleary, L. J., & Byrne, J. H. (2020). Role of p90 ribosomal S6 kinase in long-term synaptic facilitation and enhanced neuronal excitability. *Scientific reports*, *10*(1), 608.

39. Choi, J. S., & Cho, Y. Y. (2023). Novel wiring of the AKT-RSK2 signaling pathway plays an essential role in cancer cell proliferation via a G₁/S cell cycle transition. *Biochemical and biophysical research communications*, 642, 66–74.
40. Ho, W. S., Wang, H., Maggio, D., Kovach, J. S., Zhang, Q., Song, Q., Marincola, F. M., Heiss, J. D., Gilbert, M. R., Lu, R., & Zhuang, Z. (2018). Pharmacologic inhibition of protein phosphatase-2A achieves durable immune-mediated antitumor activity when combined with PD-1 blockade. *Nature communications*, 9(1), 2126.

CONCLUDING REMARKS

The experience of attaining my doctoral degree has been a remarkable one, involving both truly amazing research projects and people. I feel blessed to have been able to collaborate with so many gifted researchers, who themselves are distinguished leaders in their respective fields. I am immensely appreciative for the knowledge that I have gained about the drug discovery process as well as intricate mechanisms underlying the pathology of the neurological and muscular disorders discussed here. My hope is that this research has facilitated the identification of novel drug candidates and/or therapeutic approaches that may one day be used to treat patients suffering from these devastating diseases.